

THÈSE

En vue de l'obtention du

DOCTORAT DE L'UNIVERSITÉ DE TOULOUSE

Délivré par :

Institut National Polytechnique de Toulouse (Toulouse INP)

Discipline ou spécialité :

Dynamique des fluides

Présentée et soutenue par :

M. LAURENT MUSCAT

le mardi 12 mars 2019

Titre :

Coupling of time integration schemes for compressible unsteady flows

---

Ecole doctorale :

Mécanique, Energétique, Génie civil, Procédés (MEGeP)

Unité de recherche :

Centre Européen de Recherche et Formation Avancées en Calcul Scientifique (CERFACS)

Directeur(s) de Thèse :

M. GUILLAUME PUIGT

M. MARC MONTAGNAC

Rapporteurs :

M. CHRISTOPHE BERTHON, UNIVERSITE DE NANTES

M. RODOLPHE TURPAULT, INP BORDEAUX

Membre(s) du jury :

M. BRUNO KOOBUS, UNIVERSITE DE MONTPELLIER, Président

M. GUILLAUME PUIGT, CERFACS, Membre

M. MARC MONTAGNAC, CERFACS, Membre

Mme MARTA DE LA LLAVE PLATA, ONERA, Membre

Remerciements

À mon père, ma mère, et à la mémoire de mon oncle Jean-Pierre.

Je tiens tout d'abors à remercier Monsieur Bruno Koobus qui m'a fait l'honneur de présider mon jury de thèse. Je remercie tout particulièrement Marta de la Llave Plata, Christophe Berton et Rodolphe Turpault pour leur rôle d'examinateurs et de rapporteurs, pour l'intérêt qu'ils ont porté à mes travaux de thèse et pour m'avoir fait part de leurs remarques constructives. Mon jury a pu me faire profiter d'un point de vue autant industriel qu'académique parfaitement en adéquation avec le contexte de ma thèse.

Je remercie particulièrement ma famille. D'abord mes parents pour tous les sacrifices qu'ils ont faits pour qu'aujourd'hui leur fils puisse défendre sa thèse. Je ne serai jamais assez reconnaissant de tout ce que vous avez fait pour moi et ça depuis toujours. Ensuite, la femme qui m'accompagne depuis maintenant 8 ans, Jena, on s'est nous nous sommes supportés dans les bons et les mauvais moments et je suis immensément fière du chemin qu'on a parcouru ensemble. Sans oublier, mes filleuls, Lorenzo et Lorik qui m'ont permis de vivre des moments de bonheur pendant ces 3 ans et forcément je me dois de remercier ma marraine, pour toutes l'affection qu'elle me porte depuis tant d'années. Je n'oublie pas aussi tous les autres membres de ma famille, les présents comme les absents. Mon plus grand souhait est de vous avoir rendu fier, autant que je le suis, de faire partie de cette famille.

Je remercie aussi tout particulièrement mes tuteurs industriels, Grégoire et Pierre. Je n'arrive pas à trouver les mots pour définir à quel point je suis reconnaissant envers vous. Je suis admiratif de votre travail et de vos convictions envers pour FLUSEPA. Pendant ces trois ans, j'ai eu vraiment l'impression de faire partie d'une équipe. Et c'est ce qui m'a poussé à me battre pour arriver aux objectifs que vous m'aviez fixés. Même s'il y a eu beaucoup de moment de doute au départ, je ne serai jamais arrivé jusqu'au bout, sans votre soutien (ou vos coups de pression en fait je ne sais plus).

Je tiens évidemment à remercier tous les autres membres d'ArianeGroup, je ne vais pas tous les citer par peur d'en oublier, mais je n'oublierai pas nos moments partagés dans l'OpenSpace du B51. Tous ces moments de doute, auraient été insurmontables sans ma petite Amandine. On a débarqué au même moment en thèse, nos galères ainsi que nos moments de fou rire ont soudé notre amitié, et maintenant nous voilà docteur tous les deux. Et bien sûr, comment oublier notre petit stagiaire de 3ème, Kevin. Tu es une personne formidable et je suis heureux et fier d'être ton ami. Je n'oublierai jamais nos moments vécus tous ensemble avec Arthur, PA, Adrien, Matthieu, Anthony, etc. Je tiens à remercier nos grands frères de thèse Bobby et Lorris. Je vous félicite encore pour vos superbes thèses.

Je remercie aussi tous les membres du CERFACS, Jean-François Boussuge qui a cru en moi et qui m'a permis d'avoir cette thèse, Thierry Poinsot, les thésards, les stagiaires, les seniors, les membres de l'administration, Super MARIE et Super CHANTAL, merci pour vos sourires, pour votre bonne humeur et pour vos cadeaux, je vous ai laissé une bouteille de champagne dans le frigo du CERFACS rien que pour vous deux (à condition que Chantal n'ait pas oublié mes mandarines de Tunisie).

J'ai une pensée particulière pour Christophe Coreixas, Gauthier Wissocq, Julien Vanharen, Pamphile Roy (Batman), Robin Campet (Robin du coup), Romain Bizzari (mon binôme adoré), Adèle Veilleux (ma calimero de co-bureau), Matthieu Catchirayer, et j'en oublie tant...

Je finirai bien-évidemment par les deux personnes à qui je dois tout durant ces 3 ans, Marc et Guillaume, mes deux patrons. Que cela fut dur pour vous de me supporter et de m'accompagner pendant ces années, je n'ose l'imaginer. Je n'ai pas de mots pour vous dire à quel point je vous suis reconnaissant d'avoir cru en moi et de m'avoir guidé jusqu'à la fin. Tout ce que je souhaite, c'est que vous soyez fier du travail accompli et de pouvoir, de nouveau, un jour, travailler avec vous deux.

Merci pour tout.

Symbols and mathematical notations

Basic physical quantities

The physical domain of interest is assumed to be the open space Ω of $\mathbb{R}^n$ ($n = 2$ or $n = 3$), with $\mathbb{R}$ the space of real numbers, and it is analysed during a time interval $[0,T']$. The following symbols will represent physical quantities:

- $x \in \Omega$: a point inside Ω defined by its coordinates,
- $t \in [0, T']$: a time instant,
- $(t, x) \in [0, T'] \times \Omega$ is the couple to define any quantity depending on both space position and time instant,
- $\rho(t, x) \in \mathbb{R}_+^*$: density in $kg.m^{-3}$,
- $u(t, x) \in \mathbb{R}^k$: velocity vector in $m.s^{-1}$,
- $p(t, x) \in \mathbb{R}_+^*$: pressure in Pa,
- $e(t, x) \in \mathbb{R}_+^*$: specific internal energy in $m^2.s^{-2}.kg^{-1}$,
- $T(t, x) \in \mathbb{R}_+^*$: temperature associated with internal energy in K,
- $g(t, x) \in \mathbb{R}$: the body acceleration in $m.s^{-2}$,
- q_r: the radiation heat flux in $W.m^{-2}$,
- q: the heat flux from Fourier law in $W.m^{-2}$,
- τ: the deviatoric stress tensor in Pa,
- W_{tm}: the turbulent variables (ex : (k, ε)),
- $W(t, x)$ or $W(t)$ or $W(x)$: the conservative variables $(\rho, \rho u, \rho E, W_{tm})$,
- $R(t, W(t))$ or $R(W(t))$ the residual

The following symbols will represent physical quantities spatially and temporally discretized:

- x_i : coordinate of center of gravity of cell i,
- Δt : time step,
- t^n : discretized time such as $t^{n+1} = t^n + \Delta t$,
- $W_i^n = W(t^n, x_i)$: conservation variable at instant t^n and cell i,
- $R_i^n = R(t^n, W(t^n, x_i))$: residual at instant t^n and cell i

Mathematical functions / operators

This thesis is devoted to the analysis of partial differential equations which are composed of different mathematical operators. In this section, f represents a function, g and l are vectors (whose components are g_i and l_i respectively) and $\mathbf{A}$ and $\mathbf{B}$ are two matrices. All quantities are assumed to depend on both space and time. Let:

- $\partial_t f = \dfrac{\partial f}{\partial t}$ represent the derivative of f with respect to the time t,
- $\partial_j f = \dfrac{\partial f}{\partial x_j}$ represent the derivative of f with respect to the $j-th$ space direction,
- ∇f be the gradient of f, a vector which components are the derivatives of f with respect to all space directions,
- $\nabla \cdot \vec{g}$ be the divergence of $\vec{g}$: $\nabla \cdot \vec{g} = \sum_i \partial_i g_i$,
- $\nabla \cdot \mathbf{A}$ be a vector which *j-th* component is: $\sum_i \partial_i a_{ji}$,
- $g \cdot l$ be the scalar product: $g \cdot l = \sum_i g_i l_i$,
- $g \cdot \nabla f = \sum_i g_i \partial_i f$,
- $\mathbf{A} : \mathbf{B} = \sum_{ij} a_{ij} b_{ji}$,
- $g \otimes l$ be the second order tensor: $(g \otimes l)_{ij} = g_i \, l_j$,
- Δf be the Laplacian (scalar) of f defined by: $\Delta f = \nabla \cdot (\nabla f)$,
- $\|g\|$ represents the length of g (L^2 norm of g): $\|g\|^2 = \sum_i g_i^2$.
- $\widehat{g}$ represents the Fourier transform of g: $\widehat{g}(t) = \int_{-\infty}^{+\infty} g \exp(-2\pi f \mathfrak{i} x) dx$.
- The inverse Fourier transform of g: $\widehat{g}^{-1}(t) = g(x,t) = \int_{-\infty}^{+\infty} \widehat{g} \exp(-2\pi f \mathfrak{i} x) df$.
- with $\mathfrak{i}$ the complex number such as: $\mathfrak{i}^2 = -1$

Remark: *The Einstein summation convention is applied to the whole document: summation over a set of indexed terms in a formula is implicit.*

Symbol Definitions

Subscript and upper script symbols

x^n	x at instant t^n
$\overline{x}$	mean quantity of x over a control volume
x'	temporal derivation of x
x''	second temporal derivation of x

Acronysm

LES	Large Eddy Simulation
RANS	Reynolds Averaged Navier-Stokes
URANS	Unsteady Reynolds Averaged Navier-Stokes
CFL	Courant–Friedrichs–Lewy
DDES	Delayed Detached Eddy Simulation
RKn	n-stage Runge Kutta
IRKn	n-stage Implicit Runge Kutta
DIRK	Diagonally Implicit Runge Kutta
ARK	Additive Runge Kutta
IMEX	IMplicit EXplicit
IMEXP	Preconditioned IMplicit EXplicit
MUSCL	Monotonic Upstream-Centered Scheme for Conservation Laws
ODE	Ordinary Differential Equation
PDE	Partial Differential Equation
ETD	Exponential Time Differencing
IRS	Implicit Residual Smoothing
BDF	Backward Differentiation Formula
ROW	ROsenbrock Wanner
CFD	Computational Fluid Dynamics
TVD	Total Variation Diminishing
TN	Timofeev and Norouzi
SSP	Strong Stability Properties
HCS	Hybrid Coupling Scheme
CCG	Collins, Colella, Glaz
AION	Another tIme integratiON
HLL	Harten, Lax, van Leer
HRL	Hybrid RANS/LES

Contents

Part I: Introduction 1

1 Introduction 3
- 1.1 Physical Problem and ArianeGroup Solution . . . 3
- 1.2 Position of the Study . . . 4
- 1.3 From the Models to the Cauchy Problem . . . 6
  - 1.3.1 Navier-Stokes Equations . . . 6
  - 1.3.2 Finite Volume Formulation . . . 7
  - 1.3.3 k-exact Reconstruction . . . 8
  - 1.3.4 Cauchy Problem . . . 10
  - 1.3.5 Description of Model Problems . . . 10

Part II: Mathematical background for time integration analysis 13

2 Mathematical Background for Time Integration Analysis 15
- 2.1 Notion of Stability . . . 15
- 2.2 Notion of Stiffness . . . 17
- 2.3 Notion of Order of Accuracy . . . 17
- 2.4 Spectral Analysis: Dispersion and Dissipation . . . 19
- 2.5 Space-Time Analysis and q-waves . . . 21
- 2.6 Total Variation Diminishing (TVD) Property . . . 22
- 2.7 Explicit and Implicit Time Integrators . . . 22
- 2.8 Theoretical Results for a First-order Accurate Time Integrator . . . 23

Part III: Review on Time Integration 25

3 Explicit Time Integration 27
- 3.1 Adams-Bashforth Scheme . . . 27

3.1.1 Principle . . . 27
3.1.2 Formulation . . . 27
3.1.3 Stability Properties . . . 28
3.2 Explicit Runge-Kutta Method . . . 29
3.2.1 Principle . . . 29
3.2.2 Formulation . . . 29
3.2.3 Stability Properties . . . 30
3.2.4 Order Condition for RK Method . . . 32
3.2.5 Partial Conclusion on the Explicit Runge-Kutta Methods . . . 32
3.3 Exponential Integrators . . . 32
3.3.1 Principle . . . 32
3.3.2 Formulation for Linear Equations . . . 32
3.3.3 Formulation for Non-linear Equations . . . 34
3.4 Implicit Residual Smoothing Time Scheme . . . 35
3.4.1 Principle . . . 35
3.4.2 Formulation . . . 36
3.4.3 Stability Properties . . . 37
3.5 Conclusion on Explicit Time Integration . . . 38

4 Implicit Method for Time Integration **39**
4.1 Backward Differentiation Formula Method . . . 39
4.1.1 Principle . . . 39
4.1.2 Formulation . . . 39
4.1.3 Stability Properties . . . 40
4.2 Adams-Moulton Scheme . . . 41
4.2.1 Principle . . . 41
4.2.2 Formulation . . . 41
4.2.3 Stability Properties . . . 41
4.3 Implicit Runge-Kutta Method . . . 42
4.3.1 Principle . . . 42
4.3.2 Formulation . . . 42
4.3.3 Stability Issue . . . 44
4.4 Rosenbrock Method . . . 45
4.4.1 Principle . . . 45
4.4.2 Formulation . . . 46
4.4.3 Stability Properties . . . 46
4.5 Conclusion on Implicit Time Integration . . . 46

5 Hybrid Explicit-Implicit Methods **47**
5.1 Additive Runge-Kutta Methods . . . 47
5.1.1 Principle . . . 47
5.1.2 Formulation . . . 47
5.1.3 Stability Properties . . . 48
5.2 IMEX Scheme (IMplicit-EXplicit Scheme) . . . 48
5.2.1 Principle . . . 48
5.2.2 Formulation . . . 49
5.2.3 Stability Properties . . . 50
5.3 Spatial Coupling of Time Integrators . . . 50
5.3.1 Principle . . . 50
5.3.2 Formulation . . . 51
5.4 Flux Bounding Method . . . 55

5.4.1 Principle . . . 55
5.4.2 Formulation . . . 55
5.5 Conclusion on Hybrid Time Integration . . . 56

6 Temporal Adaptive Method **57**
6.1 Temporal Adaptive . . . 59
6.1.1 Principle . . . 59
6.1.2 Update of the Solution . . . 60
6.1.3 Conservation Property . . . 63
6.2 Accuracy and Spectral Analysis of Temporal Adaptive Method . . . 64
6.2.1 Time Accuracy . . . 64
6.2.2 Numerical Assessment of the Theoretical Behaviour . . . 67
6.2.3 Space-Time Von Neumann Analysis . . . 68
6.2.4 Analysis of $q-$waves . . . 72
6.3 Partial Conclusion . . . 73

7 Partial conclusion on review of time integrators **75**

Part IV: A New Time Integrator **77**

8 First Hybrid Coupled Scheme **79**
8.1 Methodology of First Hybrid Coupling Scheme (HCS1) . . . 79
8.2 Space-Time Von Neumann Analysis . . . 80
8.2.1 Analysis at CFL=0.1 . . . 81
8.2.2 Analysis at CFL=0.6 . . . 83
8.3 Conclusion . . . 83

9 Another tIme integratiON (AION) Scheme **85**
9.1 Introduction . . . 85
9.2 Formulation . . . 85
9.3 Space-Time Stability Analysis . . . 86
9.3.1 Analysis of the Hyb/IRK2 and IRK2/Hyb Transitions . . . 86
9.3.2 Analysis of $q-$waves . . . 89
9.4 Partial conclusion . . . 94
9.5 Validation . . . 94
9.5.1 Order of Accuracy . . . 94
9.5.2 Sod's Tube . . . 104
9.5.3 Two-dimensional Linear Advection of an Isentropic Vortex . . . 109
9.5.4 Three-dimensional Taylor Green Vortex . . . 114
9.6 Partial Conclusion . . . 115

10 Temporal Adaptive Method with AION Scheme **117**
10.1 Update of the Solution for Hybrid Time Integration . . . 117
10.2 Conservation and Adaptive Time Accuracy . . . 118
10.2.1 Conservation Property . . . 118
10.2.2 Time Accuracy . . . 119
10.2.3 Numerical Assessment of the Theoretical Behaviour . . . 122
10.2.4 Space-Time Von Neumann Analysis . . . 123

10.2.5 Analysis of $q-$Waves 127
10.3 Validation of Temporal Adaptive Method with AION Scheme 130
10.3.1 Wave Propagation Problem 130
10.3.2 Sod's Tube 133
10.3.3 Two-dimensional Linear Advection of an Isentropic Vortex 137

11 AION Time Integration with RANS/LES Simulation **141**
11.1 Introduction 141
11.2 Two-dimensional Backward Facing Step 142

Part V: Conclusion & Perspectives **147**

12 Conclusion **149**

13 Perspectives **151**

Part VI: Appendices **153**

A TVD property of hybrid part of AION scheme **155**

Part VII: Bibliography **159**

I Introduction

1 Introduction **3**
1.1 Physical Problem and ArianeGroup Solution
1.2 Position of the Study
1.3 From the Models to the Cauchy Problem

1 Introduction

1.1 Physical Problem and ArianeGroup Solution

The simulation of the high energy flows encountered by space launchers is of great importance to achieve a robust design. Indeed, during take-off or re-entry, a launcher is subjected to several complex and extremely violent physical phenomena: first, during take-off, engines emit overheated gas flow to ensure a high level of thrust. Under these conditions, very powerful acoustic waves are generated, which can damage the launcher structure and even its payload. In addition, re-burning phenomena of these highly reducing gases can also worsen this problem. Then, during the hypersonic flight phases or atmospheric re-entry, friction and shocks into the gas become very important and the kinetic energy is converted into heat. This process of energy conversion causes chemical reactions in the flow itself (dissociation of polyatomic gases by shocks) or near the wall (recombination, ablation, pyrolysis, etc). Due to the violence of the phenomena encountered, it was imperative to develop really robust numerical schemes for the modelling of all flight phases encountered by space launchers.

For nearly 30 years, ArianeGroup has been developing its own CFD solution, **FLUSEPA**©[1], to simulate the aero-propulsive environment of space launchers. The first type of application concerned the modelling of stages separation. To do this, the different parts of the launcher are meshed independently and unified / interconnected in the same grid using a chimera-like technique (based on geometric intersections) that allows taking into account the relative motions. Gradually, most phases of flight, whether transient or stationary, occurring during the life of launchers and re-entry vehicles are modelled using new developments.

In practice, **FLUSEPA**© uses unstructured general grids (mainly made of hexahedra to enforce accuracy). As far as the modelling is concerned, reactive compressible and turbulent flows loaded with particles are treated by means of a Finite Volume formulation. As will be presented hereafter, spatial discretisation schemes based on the Godunov method use high order k-exact reconstructions. A specific issue concerns conservation which remains a key point to deal with complex physical phenomena (and in particular shock waves) and the chimera method implemented in **FLUSEPA**© is based on a original treatment that makes it totally conservative. This is called the geometric intersection of grids [1, 2].

More recently, improvements have been initiated to make some simulations feasible and in particular the simulation of the unsteady phenomena associated with the "large scales" of turbulence. This remains a key point because they play a leading role, for example in the correct modelling of detached flows such as those encountered at the base of launchers where classical models are known not to behave very well.

Four main axis of improvement were defined in order to reach this objective. The first concerns modelling with the definition and the implementation of new models both for aerodynamics (Pont [3]) and for combustion (Charrier *et al.* [4]), the challenge being that the new models implemented are neither too complex nor too specialized to remain effective. The second improvement concerns the computational architecture of the code and its evolution towards massively parallel architectures (Couteyen [5]). Here, one of the major challenges is to build a platform that can also evolve during the calculation. The third concerns dynamic

[1] FR4009261, 27/07/2013

mesh adaptation: Limare [6] implemented an Adaptive Meshing Refinement (AMR) technique that preserves accuracy and also guarantees conservation in refined areas. Here again, the goal is global efficiency: number of cells reduction and automation must not reduce the computational efficiency. Finally, the last point of improvement deals with numerical schemes. Indeed, modelling the boundary layers can need up to 80% of the total mesh size for a standard Reynolds Averaged Navier-Stokes (RANS) simulation. Menasria *et al.* [7] work on improving the space accuracy of the wall discretisation. The second research area for schemes concerns the hybridization between implicit and explicit temporal integration schemes. It is the core of the research work presented in this PhD thesis.

1.2 Position of the Study

Turbulence is characterized by a quasi-fractal cascade of vortices distributed over a wide range of temporal and spatial scales. As illustrated in Fig. 1.1, the vortices structures follow an energy

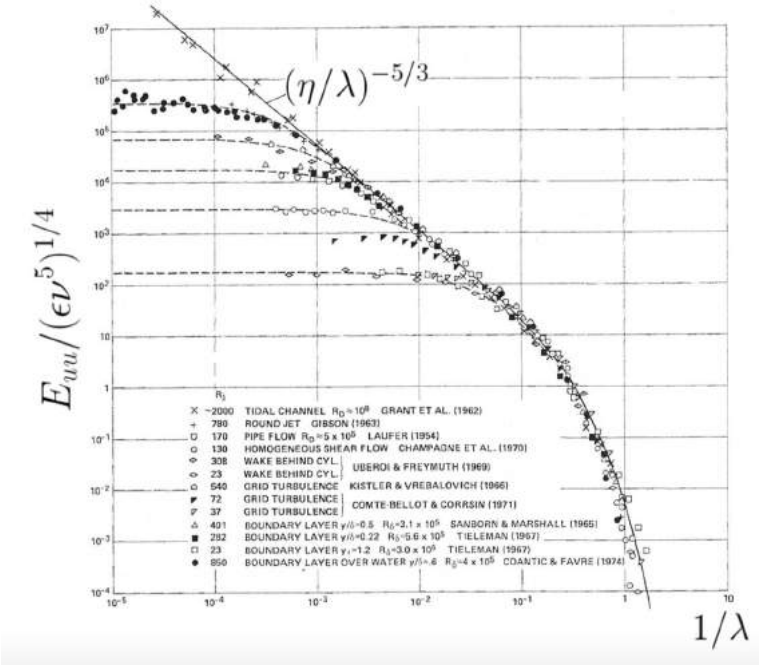

Fig. 1.1. Non dimensioned energy spectrum for several flows, adapted from Chapman [8]

cascade from large structures to the smallest ones and at the lowest scales, viscous effects produce their dissipation. For the physical problems of interest in this thesis, capturing all the turbulence scales is today out of the capability of the strongest supercomputers and for industry, two approaches are retained for the simulation of turbulence.

A first technique consists in computing the mean effects of the turbulence on the flow, following the Reynolds Averaged Navier-Stokes Equations (RANS). In this case, an averaging procedure is applied to the Navier-Stokes equations and extra terms produced by the non-linear convection terms are modelled in the final system of equations. Since the turbulence quantities are essentially averaged by the modelling procedure, the RANS approach is essentially applied to stationary models. When the flow contains an unsteadiness not related to turbulence (vortex shedding, etc), the hypothesis of ergodicity enables to compute such flows by means of Unsteady RANS (URANS) equations. RANS and URANS procedures are applied to industrial configurations due to their ability to accurately capture boundary layers.

The second technique consists in computing the largest scales of the turbulence and in modelling the smallest ones. In this case, a filter is applied to the Navier-Stokes equations and

extra terms produced by non-linear convection terms are modelled. Formally, the procedure looks like the one for RANS equations but the equations obtained after the modelling procedure are now highly unsteady. This is called the Large Eddy Simulation procedure (LES). It is assumed that the lowest scales of turbulence have a general behaviour and they can be modelled using the same closure terms for any configuration (see Sagaut [9] and Garnier *et al.* [10]). LES are entering industry today, due to their capability in capturing large turbulence scales. However, it can be demonstrated that the LES has limitations in Reynolds number due to the number of grid points to capture accurately the boundary layer. There exists several techniques to overcome this problem.

Among them, ArianeGroup is involved in the coupling of RANS and LES methods. The idea is to solve the boundary layer using the RANS approach and to switch to LES in regions with many unsteady phenomena, such as boundary-layer separation or turbulent shear-layer, where the resolution has to be fine enough [11]. This coupling approach is possible thank to the fact that the RANS and LES equations are formally the same, only the scale separator changes. It is possible to simply illustrate the interest of coupling both approaches on a backward facing step flow (Fig. 1.2). The analysis of RANS / LES coupling for **FLUSEPA**© was done recently, during the PhD of Pont [3].

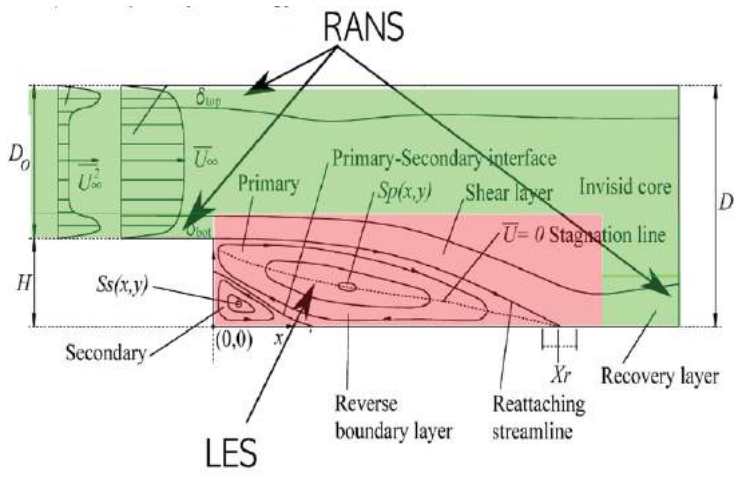

Fig. 1.2. Mean flow over a backward facing step (from Hall *et al.* [12]).

The unsteady zone characterized by a recirculation region is simulated by the LES method and the steady part of the flow, in the boundary layer, is computed by the RANS method. It is significant to use a fine grid in order to simulate the phenomena near the facing step with accuracy, and to play with an explicit time integration method, as generally done with LES. Indeed, LES accuracy depends strongly on the capability of the scheme to capture the energy cascade. Any diffusive scheme adds a numerical diffusion which effects can be larger than the ones of the flow. In the later condition, accuracy is lost. For controlling efficiently both the spectral properties of the scheme (dissipation and dispersion) and its accuracy, explicit schemes are considered due to an easier control of their properties. However, explicit time integration methods may lead to very small time step in order to satisfy the Courant–Friedrichs–Lewy (CFL) condition for stability. Remind that the CFL condition is a necessary condition for convergence towards the solution of the discretised partial differential equations.

Implicit time integrators may be considered in some cases since they allow large time steps for unsteady flows. Indeed, implicit schemes are generally chosen so to be linearly unconditionally stable. Nevertheless implicit time integration is generally used only for fast convergence to steady-state solutions. This type of integrators generally downgrades the quality of unsteady solution. To overcome this issue, high-order time accurate implicit integrators

are often used, but represent a huge CPU cost due to resolution of a linear system and also because the largest stable time step (stability constraint) becomes more and more restrictive once the order of accuracy of the implicit time integrator is increased (Dahlquist [13]). Formula describing several ways of coupling RANS and LES models can be found in the literature to simulate a quasi-steady solution through the (U)RANS formulation within boundary layers while performing an accurate simulation of the unsteady solution with LES model outside (see Wall-Modelled LES [14] or the Detached Eddy Simulation [15, 16] among others).

The main objective of this thesis is to propose and analyse methods that allow a larger time step for unsteady simulation while keeping a second-order time accuracy. Before entering into the details of the PhD, let's begin by focusing attention on the discretisation method.

1.3 From the Models to the Cauchy Problem

1.3.1 Navier-Stokes Equations

ArianeGroup studies space launchers during take-off and re-entry. The flow is solution of the compressible Navier-Stokes equations including reactive species. The Navier-Stokes equation can be derived from principle of mass, species, momentum and energy conservation:

Mass Conservation:

Principle of mass conservation may be described as:

$$\frac{\partial \rho}{\partial t} + \nabla \cdot (\rho u) = 0, \tag{1.1}$$

with ρ the density, and u the flow velocity

Species Conservation:

For flows with N_e reactive species, N_e equations of species transport may be expressed and the sum corresponds to the previous mass conservation equation.

$$\frac{\partial \rho Y_i}{\partial t} + \nabla \cdot (\rho u Y_i) = -\nabla(\rho d_i Y_i) + \rho \dot{h}_i, \tag{1.2}$$

with d_i the diffusion speed of the species i, and $\dot{h}_i$ the production/diffusion rates of species i.

Movement Quantity Conservation:

According to Newton's law, momentum of a system is varying thanks to the forces applied to it, such as:

$$\frac{\partial (\rho u)}{\partial t} + \nabla \cdot [\rho u \otimes u] = \quad -\nabla p + \nabla \cdot \tau + S_{qdm}, \tag{1.3}$$

with Y_i the mass fraction, p the pressure, τ the deviatoric stress tensor and:

$$S_{qdm} = \rho \sum_{i=1}^{N_e} Y_i f_i, \tag{1.4}$$

with f_i the volumetric forces applied to species i.

Total Energy Conservation:

The total energy conservation is written as:

$$\frac{\partial (\rho E)}{\partial t} + \nabla \cdot ((\rho E + p)u) = \quad \nabla \cdot (\tau \cdot u) - \nabla \cdot (J_E) + S_E, \tag{1.5}$$

with E the total energy, J_E the total energy flux and S_E the energy source term such as:

$$S_E = S_E(S_{qdm}, q, q_r) \tag{1.6}$$

with q the heat flux (Fourier Law) and q_r the radiation heat flux (neglected in the following). For the purpose of this PhD thesis (and especially for the equations), air is assumed to be a perfect gas with constant capacities, and gravity effects are neglected too, which leads to some simplifications in the following set of Navier-Stokes equations:

$$\begin{cases} \dfrac{\partial \rho}{\partial t} + \nabla \cdot (\rho u) & = & 0, \\ \dfrac{\partial (\rho u)}{\partial t} + \nabla \cdot [\rho u \otimes u] & = & -\nabla p + \nabla \cdot \tau, \\ \dfrac{\partial (\rho E)}{\partial t} + \nabla \cdot ((\rho E + p) u) & = & \nabla \cdot (\tau \cdot u) + \nabla \cdot (q). \end{cases} \tag{1.7}$$

The first equation represents the mass conservation, the second equation reflects momentum conservation and finally, the last equation deals with energy conservation. In Eq. (1.7), standard CFD notations are chosen: ρ is the density, u the flow velocity, p the pressure, τ the deviatoric stress tensor, E the total energy, q the heat flux. In addition, three mathematical operators are mandatory: ∇ the gradient operator, $\nabla\cdot$ the divergence operator and $\otimes$ the outer vectors product. For RANS simulations, the previous equations are modified according to an averaging procedure that splits the unknowns into averaged quantities and fluctuations. Fluctuations and averaging procedure introduce additional terms in the non linear part of the equations that need to be modeled by means of a turbulence model. A turbulence model is defined from convection / diffusion equations, with specific terms for the production and the destruction of the turbulence. In addition, turbulence induces modifications in the shear stress tensor and in the heat flux. The LES equations are derived from the Navier-Stokes equations by means of a filtering procedure in order to separate the different scales of the flow. This process leads formally to the very same equations on the mean flow conservative variables as the RANS model, but the closure is specific to LES. Here again, a turbulence closure is mandatory but it is generally based on algebraic expressions and it is no longer needed to solve transport equations for the turbulence quantities.

The full set of Navier-Stokes equations, (including turbulent equations), can be expressed by the following vector-valued system of equations:

$$\frac{\partial W}{\partial t} + \nabla \cdot \big(F(W, \nabla W)\big) = S(W), \tag{1.8}$$

with $W = (\rho, \rho u, \rho E)$, F is the flux density and S the source term vector. In the following, the compact form (1.8) will be considered for brevity. This system of equation must be discretised and the finite volume formulation described in Sec. 1.3.2 is retained.

1.3.2 Finite Volume Formulation

The Navier-Stokes equations (1.8) are now discretised by a finite volume formulation. The goal is to define first the computational domain, to split it into several non overlapping cells and to integrate the Navier-Stokes equations on all cells. Gauss' relation then links the volume integrals of the divergence terms and the interface fluxes. In a compact form, it leads to:

$$\frac{d}{dt} \iiint_{\Omega_j} W d\Omega = - \oiint_{A_j} F(W, \nabla W).\vec{n} dS + \iiint_{\Omega_j} S d\Omega, \tag{1.9}$$

where Ω_j is the control volume of cell j, with border A_j, $\vec{n}$ is the outgoing unit normal vector. The flux density F depends on both the solution W and its gradient ∇W. From now on, it is possible to define the mean quantity of the conservative variables:

$$\overline{W}_j = \frac{1}{|\Omega_j|} \iiint_{\Omega_j} W d\Omega. \tag{1.10}$$

This representation allows to rewrite equations with a finite volume formulation:

$$|\Omega_j|\frac{d\overline{W}_j}{dt} = R(\overline{W}_j), \tag{1.11}$$

where it is recalled that $\overline{W}$ depends on time and R the right part containing contribution of flux and source term. Actually, the residual is defined as the sum of the flux contributions over the whole boundary of any cell. In **FLUSEPA**© convection and diffusion fluxes are discretised by means of a k-exact formulation.

1.3.3 k-exact Reconstruction

The accuracy of the solution of the Navier-Stokes equations strongly depends on the flux computed on the cell interface. This flux can need extrapolated quantities that are computed from the averaged quantities. In order to provide a flexible and efficient way to handle any accuracy of the solution, a k-exact formulation was implemented in **FLUSEPA**©.

For a hyperbolic equation, a standard first-order accurate scheme is obtained if the flux computation is based on the averaged quantities in the control volumes located on both sides of the interface.

The MUSCL formulation enables a second order of accuracy by a linear extrapolation of the unknowns from their cell-centred approximation and their gradients. Following this idea, the goal of the k-exact reconstruction is to define a Taylor expansion of the unknowns that allows a $(k+1)$-th order accurate reconstruction of the solution. Indeed for two-dimensional representation of the solution W_j at cell j (with (x_j, y_j) coordinates of the gravity centre of cell j), the Taylor expansion of $W^{\mathcal{R}}(x-x_j, y-y_j)$ is:

$$\begin{aligned} W_j^{\mathcal{R}}(x-x_j, y-y_j) =& W_j + \frac{\partial W}{\partial x}\bigg|_j (x-x_j) + \frac{\partial W}{\partial y}\bigg|_j (y-y_j) \\ &+ \frac{\partial^2 W}{\partial x^2}\bigg|_j \frac{(x-x_j)^2}{2} + \frac{\partial^2 W}{\partial x \partial y}\bigg|_j (x-x_j)(y-y_j) + ... \end{aligned} \tag{1.12}$$

This reconstruction formulation may be expressed as an approximation of the solution in a cell j. But all quantities are nodal in this case. The objective is to calculate any unknown (W_j and corresponding derivatives) from the mean quantities $\overline{W}_j$ and $\overline{W}_i$, where cells i are the neighbouring cells of volume j. Then, the mean quantity of the conservative variables on the control volume (averaged quantities) is required to be recovered:

$$\overline{W}_j = \frac{1}{|\Omega_j|}\iint_{\Omega_j} W_j^{\mathcal{R}} d\Omega = W_j + \frac{\partial W}{\partial x}\bigg|_j \overline{x_j} + \frac{\partial W}{\partial y}\bigg|_j \overline{y_j} + \frac{\partial^2 W}{\partial x^2}\bigg|_j \frac{\overline{x_j^2}}{2} + \frac{\partial^2 W}{\partial x \partial y}\bigg|_j \overline{x_j y_j} + ..., \tag{1.13}$$

with :

$$\overline{x_j^n y_j^m} = \frac{1}{|\Omega_j|}\iint_{\Omega_j} (x-x_j)^n (y-y_j)^m d\Omega. \tag{1.14}$$

Now, it is important to express the averaged quantities on cells i around j for the computation of the derivatives:

$$\begin{aligned} |\Omega_i|\overline{W}_i = \iint_{\Omega_i} W_j^{\mathcal{R}} d\Omega =& W_j + \frac{\partial W}{\partial x}\bigg|_j \iint_{\Omega_i} (x-x_j) d\Omega + \frac{\partial W}{\partial y}\bigg|_j \iint_{\Omega_i} (y-y_j) d\Omega \\ &+ \frac{\partial^2 W}{\partial x^2}\bigg|_j \frac{1}{2}\iint_{\Omega_i} (x-x_j)^2 d\Omega + \frac{\partial^2 W}{\partial x \partial y}\bigg|_j \iint_{\Omega_i} (x-x_j)(y-y_j) d\Omega + ..., \end{aligned}$$

(1.15)

Gooch and Van Altena [17] decided to susbitute $(x - x_j)$ and $(y - y_j)$ with $(x - x_i) + (x_j - x_i)$ and $(y - y_i) + (y_j - y_i)$ respectively, in order to avoid computing moments of each cell i around j. Introducing these geometric terms:

$$\widehat{x^n y^m_{ji}} = \frac{1}{|\Omega_i|} \iint_{\Omega_i} ((x - x_i) + (x_j - x_i))^n . ((y - y_i) + (y_j - y_i))^m d\Omega. \tag{1.16}$$

Then the previous Eq. (1.15) may be rewritten as:

$$\frac{1}{|\Omega_i|} \iint_{\Omega_i} W_j^{\mathcal{R}} d\Omega = W_j + \frac{\partial W}{\partial x}\bigg|_j \widehat{x_{ji}} + \frac{\partial W}{\partial y}\bigg|_j \widehat{y_{ji}} + \frac{\partial^2 W}{\partial x^2}\bigg|_j \frac{\widehat{x^2_{ji}}}{2} + \frac{\partial^2 W}{\partial x \partial y}\bigg|_j \widehat{xy_{ji}} + ..., \tag{1.17}$$

Finally, the next constraint is to compute the previous moments $\widehat{x^n y^m}_{ij}$ on cells i. These moments are important for the computation of derivatives. Ollivier-Gooch and Van Altena [17] solve the linear system (not square in general) by a least-square method:

$$\begin{pmatrix} 1 & \overline{x}_j & \overline{y}_j & \overline{x_j^2} & \overline{xy_j} & \dots \\ w_{j1} & w_{j1}\widehat{x_{j,1}} & w_{j1}\widehat{y_{j,1}} & w_{j1}\widehat{x^2_{j,1}} & w_{j1}\widehat{xy_{j,1}} & \dots \\ w_{j2} & w_{j2}\widehat{x_{j,2}} & w_{j2}\widehat{y_{j,2}} & w_{j2}\widehat{x^2_{j,2}} & w_{j2}\widehat{xy_{j,2}} & \dots \\ \vdots & \vdots & \vdots & \vdots & \vdots & \vdots \\ w_{jN} & w_{jN}\widehat{x_{j,N}} & w_{jN}\widehat{y_{j,N}} & w_{jN}\widehat{x^2_{j,N}} & w_{jN}\widehat{xy_{j,N}} & \dots \end{pmatrix} \begin{pmatrix} W_j \\ \partial W/\partial x \\ \partial W/\partial y \\ \frac{1}{2}\partial^2 W/\partial x^2 \\ \partial^2 W/\partial x \partial y \\ \vdots \end{pmatrix} = \begin{pmatrix} \overline{W}_j \\ w_{j1}\overline{W}_1 \\ w_{j2}\overline{W}_2 \\ w_{j3}\overline{W}_3 \\ \vdots \\ w_{jN}\overline{W}_N \end{pmatrix}, \tag{1.18}$$

for N nearby cells in the stencil for the k-exact reconstruction, and the weights:

$$w_{ij} = \frac{1}{(x_j - x_i)^2 + (y_j - y_i)^2} \tag{1.19}$$

Haider *et al.* [18] and Pont *et al.* [19] use a successive correction in order to perform the k-exact reconstruction. The main objective is to perform a recursive algorithm in order to increase the order of accuracy of l-th derivative operator with the previous $(l-1)$-th derivative. For example, the algorithm starts with the definition of a local first derivative operator $\mathcal{D}$ (of first order accuracy) which performs a non exact second derivative operator $\mathcal{D}^2$, this operator is corrected to obtain a first-order accurate second derivative. Then the corrected second derivative operator is used to define a first derivative at second order of accuracy. Hence this method is done recursively to get high-order accurate derivatives. The main objective is to approximate derivatives until the $(k+1)$ order of accuracy of the reconstruction. In other terms the reconstruction can be said to be k-exact or $(k+1)$ order accurate, if:

$$W^{\mathcal{R}}(x - x_j, y - y_j) = W(x, y) + O(\Delta x^{k+1}, \Delta y^{k+1}). \tag{1.20}$$

The successive reconstruction correction was designed to avoid geometrical reconstruction in order to define the required stencil in a parallel environnement. The number of ghost cells is limited to the minimum (only one ghost cell per face at the boundary). Starting from the solution, the polynomial reconstruction is built using truncation error of Taylor expansion by increasing the order of the approximation. Of course, since the truncation error must be computed, it is necessary to exchange locally the set of local derivatives (first, the gradients, then the second-order derivatives, then the third-order derivatives and so on).

A MUSCL reconstruction is also introduced to cope with the TVD property. For a second-order scheme, the flux on an interface is estimated using an affine extrapolation of the cell-centred unknowns onto the interface. If f denotes a mesh interface located between the left cell i to the right cell j and if C_i, C_j and C_f denote the cell centres and the face centre, the standard reconstruction is simply:

$$\begin{aligned} W^L &= W_j^n + (\nabla W)_j^n \cdot \overrightarrow{C_i C_f}, \\ W^R &= W_i^n + (\nabla W)_i^n \cdot \overrightarrow{C_j C_f}, \end{aligned} \tag{1.21}$$

where the gradient ∇W needs to be computed with the k-exact reconstruction. These gradients are also used to compute the viscous flux.
The following work focuses on the time integration procedure and the space discretisation methods implemented in **FLUSEPA**© will not be further developed in this thesis.

1.3.4 Cauchy Problem

Our interest will be focused on the treatment of the left-hand side of the Navier Stokes equation ($\overline{W}' = \frac{d\overline{W}}{dt}$) for the time integration. The finite volume formulation of the equations can be expressed as the following Cauchy problem:

$$\begin{cases} \dfrac{d\overline{W}_j}{dt} = R(t, \overline{W}_j) \\ \overline{W}_j(0) = W_j^0, \quad \forall j \in \{1, ..., N\}. \end{cases} \tag{1.22}$$

In the right-hand side, the residual R is defined by the spatial scheme. It depends also on the space derivatives of the state variables. In the left-hand side, the time derivative will be discretised to compute the solution at instant t^{n+1} from the previous one at t^n.

For the sake of clarity, the averaging symbol for the conservative quantities will be dropped, and W will represent the averaged quantities over the control volumes.

1.3.5 Description of Model Problems

All the time integrators that will be presented in the following, are implemented in an one-dimensional prototype. In order to test and validate different kinds of time integrators, several physical models need to be introduced. Another interest is the possibility to obtain an analytical solution of such models (far from boundaries):

One-dimensional Advection Equation

$$\frac{\partial W}{\partial t} + c\frac{\partial W}{\partial x} = 0, \tag{1.23}$$

with c the constant advection velocity. Hence for a Gaussian hump initialisation, the analytical solution correspond to a Gaussian convected with the velocity c.

One-dimensional Advection-Diffusion Equation

The equation reads:

$$\frac{\partial W}{\partial t} + c\frac{\partial W}{\partial x} = D\frac{\partial^2 W}{\partial x^2}, \tag{1.24}$$

with D the constant diffusivity. Here for a Gaussian hump initialisation, the analytical solution corresponds to a Gaussian function convected with the velocity c and diffused with diffusivity D. The analytical solution for $(t, x) \in [0, +\infty] \times [0, 1]$ with the initial condition $W(0, x) = \sin(2\pi x)$ is:

$$W(t, x) = \sin\big(2\pi x\big) e^{-4\pi^2 D t}. \tag{1.25}$$

Then for the advection-diffusion equation, one obtains:

$$W(t,x) = \sin\big(2\pi(x-ct)\big)e^{-4\pi^2 Dt}. \tag{1.26}$$

Scalar One-dimensional Conservation Law

$$\frac{\partial W}{\partial t} + \frac{\partial f(W)}{\partial x} = 0. \tag{1.27}$$

A conservation law states that a particular measurable property of a system does not change as the system evolves over time. Exact conservation laws may include conservation of energy, conservation of linear momentum, conservation of angular momentum, etc.

Euler Equations

The Euler equations represent the motion of an inviscid perfect gas fluid:

$$\begin{aligned}
&\frac{\partial \rho}{\partial t} + \nabla\cdot(\rho u) = 0,\\
&\frac{\partial (\rho u)}{\partial t} + \nabla\cdot[\rho u\otimes u] = -\nabla p,\\
&\frac{\partial (\rho e)}{\partial t} + \nabla\cdot((\rho e + p)u) = 0.
\end{aligned} \tag{1.28}$$

These non-linear equations are a simplification of Navier-Stokes equations. The proposed formulation does not account for gravity since the force associated to gravity differs with the pressure force by several orders of magnitude and can be neglected.

After introducing several significant notions in Chap. 2, in the following of this report, state of the art methods to time integrate unsteady compressible flows with global time step will be also introduced. In Chap. 3, explicit methods are discussed, together with a method that enhances a standard explicit approach. Implicit time integrators will be presented in Chap. 4. Then, the hybrid method that blends explicit and implicit schemes for time integration are given in Chap. 5. Furthermore a method that allows a time integration with consistent local time stepping will be introduced in Chap. 6. To finish, the "philosophy" resulting from the chosen methodology for hybrid coupling of time integrators implemented in **FLUSEPA**© will be presented, with also the extension to local time stepping approach and the extension to Hybrid RANS/LES simulation in Chap. 10.

II Mathematical background for time integration analysis

2 Mathematical Background for Time Integration Analysis 15

2.1 Notion of Stability
2.2 Notion of Stiffness
2.3 Notion of Order of Accuracy
2.4 Spectral Analysis: Dispersion and Dissipation
2.5 Space-Time Analysis and q-waves
2.6 Total Variation Diminishing (TVD) Property
2.7 Explicit and Implicit Time Integrators
2.8 Theoretical Results for a First-order Accurate Time Integrator

2 Mathematical background for time integration analysis

Numerical schemes are the basic ingredients for the definition of the discrete approximations of the partial derivatives from the initial set of equations. In fact, several notions are mandatory to explain some theoretical properties of the discrete approximation. For this reason, this chapter is devoted to the introduction of mathematical notions that will be useful in the PhD thesis.

In this report, the notions introduced are related to the time integration of the equations in order to time-march the initial solution towards either the converged solution or its approximation at a given time instant. Among the necessary notions, stability, stiffness, order of accuracy and the Von Neumann analysis will be introduced.

2.1 Notion of Stability

The first notion to introduce is stability.

Notion 2.1.1 — Stability. Beyond its stability domain, a scheme allows unfortunately an important propagation of numerical discretisation errors. These errors can lead to the divergence of the computation or to non physical values. In the following, the stability domain of a time integrator is introduced and two cases must be considered for the following general model equation $\partial W/\partial t = R(t, W)$.

In the linear case, the operator $R(t, W)$ depends linearly on W and one obtains:

$$\frac{\partial W}{\partial t} = \mathbf{A}W. \tag{2.1}$$

Considering a time integration procedure such as:

$$W^{n+1} = G(\Delta t \mathbf{A})W^n, \tag{2.2}$$

the behaviour of Eq. (2.1) is explained through the analysis of the Jacobian $\mathbf{A}$ of the initial equation $R(t, W)$. It will be supposed that the Jacobian $\mathbf{A}$ is diagonalizable with the eigenvectors $v_1, ..., v_m$ associated with the eigenvalues $\lambda_1, ..., \lambda_m$. Eigenvectors are supposed to fill entirely the set of vectors in which the solution of Eq. (2.1) is sought. As a consequence, the eigenvectors define a basis of the set of solutions and W^0 is expressed in this basis:

$$W^0 = \sum_{i=1}^{m} \alpha_i v_i, \tag{2.3}$$

so:

$$W^n = \sum_{i=1}^{m} (G(\Delta t \lambda_i))^n \alpha_i v_i. \tag{2.4}$$

The expression of W^n in Eq. (2.4) stays limited for $n \to \infty$ if and only if, for the eigenvalues λ_i, $|G(\Delta t \lambda_i)| \leq 1$. $G(\Delta t \lambda_i)$ is a function of the eigenvalue that depends on the time integration procedure and is called the stability function of the method. It can be interpreted as the numerical solution after one step of the following Dahlquist test equation:

$$\begin{cases} \dfrac{\partial W}{\partial t} = \lambda W \\ W^0 = 1. \end{cases} \tag{2.5}$$

The ensemble $\mathcal{S} = \{z \in \mathbb{C}, |G(z)| < 1\}$ is called the stability domain of the method.

In the non-linear case, the procedure can formally be kept unchanged but the main difference appears in the fact that $\mathbf{A}$ is not with constant coefficients.

First, it is important to introduce the stability for the general Cauchy's problem (with non-linear R):

Definition 2.1.1 — Stability with Cauchy's problem. For the following Cauchy's problem:

$$\begin{cases} \dfrac{\partial W}{\partial t} = R(t, W(t)), \forall t \in [0, T] \\ W(0) = W^0. \end{cases} \tag{2.6}$$

The problem is stable according to Liapunov for a norm $||\cdot||$, if $\forall \epsilon > 0$ there is $\delta(\epsilon) > 0$ such that $||W(0)|| < \delta(\epsilon) \Rightarrow ||W(t)|| < \epsilon, \forall t > 0$.

Definition 2.1.2 — Stability of the linearized version of the non-linear problem. In the case of non-linearity of the residual R and considering a discrete representation of the Cauchy problem in a grid of N elements (with $i \in [1...N]$), such as:

$$\begin{cases} \dfrac{\partial W_i}{\partial t} = R_i(t, W(t)) \\ W_i(0) = W_i^0 \end{cases} \tag{2.7}$$

The following linearised system will be considered:

$$\begin{cases} \dfrac{\partial W_i}{\partial t} = \displaystyle\sum_{j=1}^{N} a_{ij} W_j \\ a_{ij} = \dfrac{\partial R_i}{\partial W_j}(0) \end{cases} \tag{2.8}$$

where $\mathbf{A}$ is a square matrix (a_{ij}) with $i, j \in \{1, ..., N\}$. This linearised system is stable (according to Liapunov) if and only if :

1. all the roots λ of the characteristic polynomial:

$$det(\lambda \mathbf{I} - \mathbf{A}) = 0 \tag{2.9}$$

have a negative real part, $\mathcal{R}e(\lambda) \leq 0$

2. all multiple roots have a strictly negative real part, $\mathcal{R}e(\lambda) < 0$.

2.2 Notion of Stiffness

An additional restriction on the largest stable time step can occur due to the notion of stiffness for the system of equations. Stiffness can also create instability and divergence of the numerical simulation. Hence, it is significant to understand the principle of stiffness and also to find a method that allows to overcome this problem.

Notion 2.2.1 — Stiffness. *"The essence of stiffness appears when stability is more of a constraint than accuracy"* (cited from [20]). Undeniably, the problem of stiffness leads to computational difficulty in many practical problems. This may appear when fast evolution phenomenum tends slowly to equilibrium.

Sources of stiffness include acoustic waves for low Mach number flows, viscous effect, source terms [21] and large variations of mesh size.

It appears that when problems are stiff, a numerical method with left-half plane included in its stability region is needed, and this type of method is called A-stable.

Definition 2.2.1 — A-stability. A method is called A-stable if the stability domain $\mathcal{S}$ is such as:

$$\{z \in \mathbb{C}, \mathcal{R}e(z) < 0\} \subset \mathcal{S}. \tag{2.10}$$

Definition 2.2.2 — L-stability. A method is called L-stable if:

- the method is A-stable
- $\lim_{z \to \infty} G(z) = 0$

For a L-stable method, the point at infinity ($z \longrightarrow \infty$) is in the stability region of the method. A L-stable method is interesting for computing some situations where rapid transient solution appears without very small time steps, characteristic of stiff problems.

2.3 Notion of Order of Accuracy

After introducing the notion of stability of a numerical method, it is important to consider the concept of order of accuracy for a numerical scheme. Indeed, it is important to be able to control and quantify the accuracy of the numerical simulation. First, the local and global error is introduced:

Definition 2.3.1 — Local and global error. For any numerical method that provides a numerical approximation W of an exact solution $\mathcal{W}$ of the Cauchy's problem at time step t^{n+1}, the local error $e(W^{n+1})$ at the discrete time $n+1$ is defined as:

$$e(W^{n+1}) = \mathcal{W}^{n+1} - W^{n+1} \tag{2.11}$$

The global error E is the accumulation of the local error over all the iterations, considering an exact solution at the initial time step.

Considering a one step numerical method that solves the Cauchy's problem such as:

$$W^{n+1} = W^n + \Delta t D^n(W^{n+1}, W^n, ..., W^0, R), \tag{2.12}$$

the function D will be considered as an increment function. Then, the local error $e(W^{n+1})$ at the discrete time instant $n+1$ (considering that previous numerical states are exact and that the increment function is compute thanks to exact states) can be defined by:

$$e(W^{n+1}) = \mathcal{W}^{n+1} - \mathcal{W}^n - \Delta t D^n\left(\mathcal{W}^{n+1}, \mathcal{W}^n, ..., \mathcal{W}^0, R\right) \tag{2.13}$$

and the truncation error is defined as:

$$T^{n+1} = \frac{\mathcal{W}^{n+1} - \mathcal{W}^n}{\Delta t} - D^n\left(\mathcal{W}^{n+1}, \mathcal{W}^n, ..., \mathcal{W}^0, R\right) \tag{2.14}$$

The numerical method is convergent if the truncation error tends to zero as the time step size tends to zero:

$$\lim_{\Delta t \to 0}\left(\max_n \left|T^{n+1}\right|\right) = 0. \tag{2.15}$$

Rewriting (2.14) as:

$$\mathcal{W}^{n+1} = \mathcal{W}^n + \Delta t D^n\left(\mathcal{W}^{n+1}, \mathcal{W}^n, ..., \mathcal{W}^0, R\right) + \Delta t T^{n+1} \tag{2.16}$$

and substracting Eq. (2.12) from Eq. (2.16) gives:

$$\begin{aligned} e(W^{n+1}) =& e(W^n) + \\ & \Delta t\left(D^n\left(\mathcal{W}^{n+1}, \mathcal{W}^n, ..., \mathcal{W}^0, R\right) - D^n\left(W^{n+1}, W^n, ..., W^0, R\right)\right) + \Delta t T^{n+1} \end{aligned} \tag{2.17}$$

Considering that the increment function is Lipschitz continuous, there exists a constant L such as for any instants $t_1 > 0$ and $t_2 > 0$ with their respective solutions W_1 and W_2:

$$\left|D^n\left(W_1^{n+1}, W_1^n, ..., W_1^0, R\right) - D^n\left(W_2^{n+1}, W_2^n, ..., W_2^0, R\right)\right| \leq L\left|W_1^{n+1} - W_2^{n+1}\right|. \tag{2.18}$$

According to Theorem 12.2 from [22], the global error E satisfies the bound:

$$\left|E\right| \leq \frac{\max\limits_{k \leq n}(T^{k+1})}{L}\left(exp\left(L(t^n - t^0)\right) - 1\right). \tag{2.19}$$

Then according to Theorem 3.6 [23] and for :

$$\left|e(W^{n+1})\right| \leq K\Delta t^{p+1}, \tag{2.20}$$

with K a real constant independant of Δt, the truncation error is bounded by:

$$\left|T^{n+1}\right| \leq K\Delta t^p. \tag{2.21}$$

And the global error (order of accuracy) can be estimated as:

$$\left|E\right| \leq \frac{K\Delta t^p}{L}\left(\exp\left(L(t^n - t^0)\right) - 1\right). \tag{2.22}$$

Hence, the numerical method is consistent if $e(W^{n+1}) = \mathcal{O}(\Delta t)$ and it has order of accuracy p if:

$$e(W^{n+1}) = \mathcal{O}(\Delta t^{p+1}) = C_{order}\Delta t^{p+1}. \tag{2.23}$$

with C_{order} the error constant independant of Δt.

2.4 Spectral Analysis: Dispersion and Dissipation

The analysis of the order of accuracy gives the behaviour of the discretisation when time and space steps tend to zero. They do not introduce any information on the behaviour of the solution regarding its Fourier approximation, mode per mode. This is the goal of the Von Neumann stability analysis. In addition, the Von Neumann analysis is also a tool to estimate *a priori* both dissipation and dispersion induced by the numerical schemes.

The principle of Von Neumann analysis starts from a given initial value at the instant t^n. This solution can be expressed using the Fourier transform through its projection onto the Fourier modes:

$$W(t^n, x) = \int_{-\infty}^{+\infty} S_W(f) \exp(2\mathrm{i}\pi f x) dx, \tag{2.24}$$

where $S_W(f)$ is a complex number than represents the mode associated to the (space) frequency f. $S_W(f)$ and $W(t^n, x)$ are linked by a Fourier transform:

$$S_W(f) = \int_{-\infty}^{+\infty} W(t^n, x) \exp(-2\mathrm{i}\pi f x) dx. \tag{2.25}$$

The goal is to express the solution at the time instant t^{n+1} from the solution at time t^n by means of the projection onto the Fourier basis / modes.

Numerically, it is impossible to deal with an infinite number of modes. The finite volume approximation of the initial solution is by nature defined by N degrees of freedom, N being the number of mesh cells for the one-dimensional problem. Moreover, according to the Shannon's theorem, almost two points are needed to define properly the Fourier coefficients on a given mode. It results that there is a finite number of modes that can be characterised spatially over the mesh. Injecting this Discrete Fourier solution into the discrete schemes gives a transfer function between the solutions at two successive time instants. At this point, an important issue needs to be highlighted: our standard problems are by nature hyperbolic and non linear. By essence, non linearity effects are able to transfer energy between modes and a non-linear equation makes the transfer function complex to define and to analyse. For this reason, the process is generally applied to a linear equation, typically the advection equation at constant velocity c.

The linear advection equation at constant velocity c is solved using a harmonic wave as initial solution $W(0, x) = a \exp(\mathrm{i}kx)$ with $k \in \mathbb{R}$ the wavenumber and $a \in \mathbb{C}$ on an uniform one-dimensional mesh for which mesh size is Δx. The analytical solution is $W(t, x) = a \exp(\mathrm{i}(kx - \omega t))$ with $\omega = ck$. Numerically, the discrete solution at the time instants t^n and t^{n+1} are such that:

$$\begin{aligned} W_j^n &= a^n \exp(\mathrm{i}kx_j) \\ W_j^{n+1} &= a^{n+1} \exp(\mathrm{i}kx_j) = G W_j^n \ , \end{aligned} \tag{2.26}$$

where a^n and a^{n+1} are complex numbers and $x_{j+1} = x_j + \Delta x$.

The amplification factor $G \in \mathbb{C}$ is:

$$G = \frac{a^{n+1}}{a^n} = G(k, \Delta t, \Delta x) \tag{2.27}$$

and depends therefore on the time step, the initial wave number (or frequency) and the mesh size. The Von Neumann criterion for stability between two consecutive time steps is:

$$|G| \leq 1. \tag{2.28}$$

Thanks to the amplification factor of Eq. (2.27), it is possible to define the numerical dissipation and the numerical dispersion. The numerical dissipation can be seen as the lost in energy between two consecutive solutions, while dispersion is a phase shift introduced by the schemes.

The same amplification factor can be introduced easily for the exact analytical problem. It will be referred as $\tilde{G}$ in the following. A phase shift also appears in the analytical solution due to the term in ωt in the analytical expression. The theoretical phase shift between solutions at time t^{n+1} and t^n is denoted $\tilde{\Phi}$.

Definition 2.4.1 — Von Neumann analysis. Dissipation error can be defined as the error in amplitude, defined by the ratio of the numerical amplitude to the exact amplitude:

$$\epsilon_D = \frac{|G|}{|\tilde{G}|}. \tag{2.29}$$

And dispersion error is defined by the difference between the phases:

$$\epsilon_\phi = \Phi - \tilde{\Phi}, \tag{2.30}$$

for pure parabolic problems, where there is absence of convective terms in equation. For convection-dominated problems the expression:

$$\epsilon_\phi = \frac{\Phi}{\tilde{\Phi}}, \tag{2.31}$$

is more adapted.

In a standard way, the spectral analysis with Von Neumann method tends to be performed for spatial or temporal schemes independently: for spatial schemes, the time integration is assumed to be perfect (analytical) and the spatial derivation is assumed exact for time schemes. But, the procedure can be extended for the coupled space-time discretisation. Sengupta *et al.* show in many recent papers [24, 25, 26] for instance, that studying the behaviour obtained by a coupled analysis involving both space and time discretisation is strongly significant.

Takacs [27] presented another method in order to obtain dissipation and dispersion error. This method allows to calculate dissipation and dispersion thanks to the theory of probability.

Definition 2.4.2 — Takacs analysis. If the total error of the numerical scheme is defined as the mean square error for the exact solution, given by:

$$E_{tot} = \frac{1}{N}\sum_j (W_j - \mathcal{W}_j)^2 \tag{2.32}$$

with N the number of grid points. This error may be expressed as the addition of the variance of $(W - \mathcal{W})$ and the difference of the squared means:

$$\frac{1}{N}\sum_j (W_j - \mathcal{W}_j)^2 = \sigma^2(W - \mathcal{W}) + (\overline{W} - \overline{\mathcal{W}})^2 \tag{2.33}$$

It may be shown that:

$$\begin{aligned} E_{tot} &= \sigma^2(W) + \sigma^2(\mathcal{W}) - 2Cov(W, \mathcal{W}) + (\overline{W} - \overline{\mathcal{W}})^2 \\ &= \sigma^2(W) + \sigma^2(\mathcal{W}) - 2r\sigma(W)\sigma(\mathcal{W}) + (\overline{W} - \overline{\mathcal{W}})^2 \\ &= \big(\sigma(W) - \sigma(\mathcal{W})\big)^2 + (\overline{W} - \overline{\mathcal{W}})^2 + 2(1 - r)\sigma(W)\sigma(\mathcal{W}) \\ &= E_{diss} + E_{disp} \end{aligned} \tag{2.34}$$

$Cov(W, \mathcal{W})$ is the covariance between the numerical solution W and the exact solution $\mathcal{W}$, r is defined as the correlation between W and $\mathcal{W}$. And:

$$\begin{aligned} E_{diss} &= \big(\sigma(W) - \sigma(\mathcal{W})\big)^2 + (\overline{W} - \overline{\mathcal{W}})^2 \\ E_{disp} &= 2(1-r)\sigma(W)\sigma(\mathcal{W}) \end{aligned} \tag{2.35}$$

If W and $\mathcal{W}$ are exactly correlated then $r = 1$. The notion of non correlation between W and $\mathcal{W}$ is equivalent to the notion of dispersion. In case of irregular mesh Total error, variance and covariance are defined such as:

$$\begin{aligned} E_{tot} &= \left(\sum_j (W_j - \tilde{W}_j)^2 dx_j\right)^2 \\ \sigma(W) &= \sum_j (W_j - \overline{W}_j)^2 dx_j \\ Cov(W, \tilde{W}) &= \sum_j (W_j - \overline{W}_j)(\tilde{W}_j - \overline{\tilde{W}}_j) dx_j \end{aligned} \tag{2.36}$$

Remark: The standard Von Neumann analysis can be applied to a mesh with constant mesh size and for a given time step. It is not usable when mesh size varies. Takacs analysis can be seen in the later case as an extension of the standard analysis. Information is no longer local but averaged over the whole computational domain.

2.5 Space-Time Analysis and q-waves

The one-dimensional linear advection equation with a constant velocity c is a basic hyperbolic equation. By nature, the solution of the equation is the initial condition transported at the velocity c: if $u_0(x)$ is the initial condition, then $u(x,t) = u_0(x - ct)$. In certain conditions, several authors mentioned the existence of waves traveling in the opposite direction. The existence of such numerical waves was observed by Poinsot and Veynante for combustion [28] or by Trefethen [29]. Vichnevetsky and Bowles [30] reported, during specific computation, the creation of physical and spurious (non-physical) waves.

Notion 2.5.1 — p-waves and q-waves. For the linear advection at constant velocity c in a one-dimensional configuration, all waves must theoretically be transported at the velocity c. Numerically, two kinds of waves can be encountered: the p-waves are physical waves transported at the same direction as the one given by c, whereas the q-waves are the non-physical waves transported in the opposite direction. q-waves are due to the numerical space-time discretisation. Sengupta *et al.* [24] related the numerical group velocity to existence of q-waves.

The coupled space-time discretisation is applied to the one-dimensional advection equation Eq. (1.23) at constant velocity c. One looks for the unsteady solution that is assumed to be a single wave associated to the wavenumber k: $W(t,x) = \exp(\mathrm{i}(kx - \omega t))$. The discretised solution must satisfy some relations. First, the exact dispersion relation is obtained:

$$\tilde{\omega} = \tilde{k}c. \tag{2.37}$$

It expresses the fact that the wavenumber is changed by the scheme, thus associated to dispersion and the corresponding ω is also changed for compatibility issue. Eq. (2.37) introduced the phase shift by the change in wavenumber but phase shift can also be a consequence to the transport at a velocity that differs with c, hence leading to:

$$\omega = kc_N. \tag{2.38}$$

Here c_N is the numerical wavenumber dependent phase speed, distinct from the advection velocity c. The numerical phase speed is related to β as:

$$c_N = \frac{\beta}{k\Delta t} \tag{2.39}$$

and the numerical group velocity:

$$V^{gN} = \frac{d\beta}{dk}\frac{c}{\text{CFL}\ \Delta x} \tag{2.40}$$

According to Sengupta *et al.* [24], creation of q-waves is related to numerical waves propagating upstream (when the group velocity is negative) even if the physics requires downstream movement. It is important to notice that the negative group velocity is only a necessary condition for apparition of q-waves. Indeed observation of q-waves also depends upon the real and imaginary part of the amplification factor of the space-time discretisation. For excessive dissipation, filtering or damping, the q-waves may be removed in a few points of the mesh. It is important to notice that, according to Sengupta *et al.* [24], initial condition, grid resolution and multi-dimensional case have also effects on q-waves.

2.6 Total Variation Diminishing (TVD) Property

By considering a scalar one-dimensional hyperbolic non-linear conservation law (defined in space and time), Lax made the observation that the total increasing and decreasing variations of a differentiable solution between any pair of characteristics are conserved. Indeed, in presence of shock wave discontinuities, information is lost and the total variation decreases. This theoretical property must be recovered by the discrete approximation of the initial equation.

Definition 2.6.1 — TVD. For the one-dimensional advection equation on $\mathbb{R}$, the total variation of the numerical solution is defined as:

$$TV(W) = \sum_j |W_{j+1} - W_j| \tag{2.41}$$

and the discrete total variation non-increasing bound condition:

$$TV(W^{n+1}) \leq TV(W^n), \tag{2.42}$$

needs to be verified by numerical discretisation for non-linear conservation laws [31, 32, 33].

2.7 Explicit and Implicit Time Integrators

After introducing the different desired properties of numerical schemes, it is important to present and classify time integration methods. Indeed numerical simulation of turbulence in our domain may be performed by a hybrid RANS/LES simulation (coupling of LES and RANS method) as mentioned previously. For the time integration of this kind of turbulence simulation, two standard approaches may be chosen. An explicit time integrator is a method that computes the state W^{n+1} thanks to the previous states of the system. So W^{n+1} may be expressed, for an explicit scheme, such as:

$$W^{n+1} = Q_E(W^n, W^{n-1}, ..., W^0). \tag{2.43}$$

The second standard approach is the implicit time integration. Contrary to explicit one, the computation of numerical solution W^{n+1} requires to solve the following system

$$W^{n+1} = Q_I(W^{n+1}, W^n, ..., W^0). \tag{2.44}$$

The solution of Eq. (2.44) can be found as a fixed-point equation solved using the Newton's approach. This means that this kind of integrator involves a linear system to invert. It leads to the computation of matrix-vector products which may represent a significant computational cost and an explicit time integration approach is generally cheaper than an implicit formulation. Nevertheless, if the chosen implicit method is unconditionally stable, the time step can be chosen large and the overhead of the linear system solution can be counterbalanced by a huge reduction of the number of time steps necessary to attain the desired final time.

2.8 Theoretical Results for a First-order Accurate Time Integrator

Starting from the Taylor expansion in time of the solution W of the one-dimensional linear advection equation at constant velocity c in Eq. (1.23), it comes:

$$W(t+\Delta t) = W(t) + \Delta t \frac{\partial W}{\partial t} + \frac{\Delta t^2}{2}\frac{\partial^2 W}{\partial t^2} + O(\Delta t^3) \tag{2.45}$$

and so:

$$\frac{\partial W}{\partial t} = \frac{W(t+\Delta t) - W(t)}{\Delta t} - \frac{1}{2}\Delta t \frac{\partial^2 W}{\partial t^2} + O(\Delta t^2). \tag{2.46}$$

Discretizing (1.23) by the proposed first-order approximation:

$$\frac{W(t+\Delta t) - W(t)}{\Delta t} + c\frac{\partial W}{\partial x} = 0 \tag{2.47}$$

and injecting (2.46) into (2.47), the modified equation is obtained:

$$\frac{\partial W}{\partial t} + c\frac{\partial W}{\partial x} = -c^2 \frac{\Delta t}{2}\frac{\partial^2 W}{\partial x^2} + O(\Delta t^2), \tag{2.48}$$

Hence, the time integration of the advection equation with the first-order scheme gives the solution of the advection-diffusion equation with an advection velocity c and a negative diffusivity $\nu = -c^2\frac{\Delta t}{2}$. Now our goal is to estimate the L^2 error ε_r of the solution. To do this we consider the exact advective solution and the numerical advection/diffusion solution with ν viscosity.

Now solving:

$$\frac{\partial W}{\partial t} + c\frac{\partial W}{\partial x} = \nu\frac{\partial^2 W}{\partial x^2}, \tag{2.49}$$

for $(x,t) \in [0,1] \times [0,+\infty]$ with the initial condition $W(x,0) = \sin(2\pi x)$, the analytic L^2 error ε_r can be computed exactly:

$$\begin{aligned} \varepsilon_r^2 &= \int_0^1 \Bigg(\underbrace{\sin\big(2\pi(x-ct)\big)\exp(-4\pi^2\nu t)}_{adv./diff.} - \underbrace{\sin\big(2\pi(x-ct)\big)}_{adv.} \Bigg)^2 dx \\ &= \big[\exp(-4\pi^2\nu t) - 1\big]^2 \left\{ \frac{1}{2} - \frac{1}{8\pi}\big[\sin\big(4\pi(1-ct)\big) + \sin\big(4\pi ct\big)\big] \right\} \end{aligned} \tag{2.50}$$

This analysis will be useful in the last chapters of the document.

III Review on Time Integration

3 Explicit Time Integration 27
3.1 Adams-Bashforth Scheme
3.2 Explicit Runge-Kutta Method
3.3 Exponential Integrators
3.4 Implicit Residual Smoothing Time Scheme
3.5 Conclusion on Explicit Time Integration

4 Implicit Method for Time Integration 39
4.1 Backward Differentiation Formula Method
4.2 Adams-Moulton Scheme
4.3 Implicit Runge-Kutta Method
4.4 Rosenbrock Method
4.5 Conclusion on Implicit Time Integration

5 Hybrid Explicit-Implicit Methods 47
5.1 Additive Runge-Kutta Methods
5.2 IMEX Scheme (IMplicit-EXplicit Scheme)
5.3 Spatial Coupling of Time Integrators
5.4 Flux Bounding Method
5.5 Conclusion on Hybrid Time Integration

6 Temporal Adaptive Method 57
6.1 Temporal Adaptive
6.2 Accuracy and Spectral Analysis of Temporal Adaptive Method
6.3 Partial Conclusion

7 Partial conclusion on review of time integrators 75

3 Explicit time integration

In the following, several explicit time integrators will be introduced. Explicit schemes are currently time integrators often used in standard unsteady compressible flow solvers. They are simple to implement and they are associated to a lower computational cost than other time integrators such as implicit ones. Explicit methods are very effective for accurate transport of flow physics. Nevertheless, the main drawback of explicit time integrators is the stability limit. The maximum stable time step used depends on flow physics and on a CFL condition due to the scheme. In this chapter, several methods for time-integrating explicitly the Navier-Stokes equation will be formulated, such as Heun's scheme, Adams-Bashforth's scheme and explicit Runge-Kutta's scheme. Moreover, in order to overcome the stability limitation of standard explicit time integrators, the literature review will also introduce alternatives enabling larger time steps, such as exponential integrators and implicit residual smoothing.

3.1 Adams-Bashforth Scheme

3.1.1 Principle

The Adams-Bashforth methods [34] are part of linear multistep methods adapted for numerical resolution of ODE and PDE. This kind of method is interesting thanks to its relative simplicity and one evaluation of the residual is needed at each step, which results in a low computational cost. Indeed, an Adams-Bashforth method of s steps will use s evaluations of the residual.

3.1.2 Formulation

Let's start from the exact integration of the standard PDE written in the compact form, between times t^n and t^{n+1}:

$$W(t^{n+1}) - W(t^n) = \int_{t^n}^{t^{n+1}} R(l, W(l))dl. \tag{3.1}$$

The principle of the time-integration of the Adams-Bashforth scheme is to provide an approximation of the integral in the right-hand side of Eq. (3.1). To approximate the integral it is assumed that $W(t^{n-i})$ and $R^{n-i} = R(t^{n-i}, W(t^{n-i}))$ are known and evaluated for the $s-1$ previous time steps $n-s+1 \leq i \leq n$. The interpolation polynomial P^s of R^n is defined as:

$$P(l) = P(t^n + k\Delta t) = \sum_{i=0}^{s-1} (-1)^i \binom{-k}{i} \nabla^i R(t^n), \tag{3.2}$$

considering that :

$$\begin{aligned} &\nabla^0 R(t^n) = R(t^n) \\ &\nabla^{j+1} R(t^n) = \nabla^j R(t^n) - \nabla^j R(t^{n-1}) \end{aligned} \tag{3.3}$$

and the following approximation is used:

$$W(t^{n+1}) \approx W(t^n) + \int_{t^n}^{t^{n+1}} P(l)dl = W(t^n) + \Delta t \sum_{i=0}^{s-1} \gamma_i \nabla^i R(t^n). \tag{3.4}$$

with the coefficient γ_i defined as:

$$\gamma_i = (-1)^i \int_0^1 \binom{-k}{i} dk \tag{3.5}$$

The equation (3.4) is the general formulation of Adams-Bashforth's method with s steps
Remark: It is of strong importance to remind that the approximation of the residual is based on the s previous residuals obtained at the s previous (physical) time steps.

3.1.3 Stability Properties

A s-step Adams-Bashforth' scheme applied to Dahlquist test equation (2.5) leads to:

$$W^{n+1} = W^n + \lambda \Delta t \sum_{i=0}^{s-1} \gamma_i \nabla^i W(t^n). \tag{3.6}$$

Considering:

$$\begin{aligned} &\kappa = \exp(\mathrm{i}\theta) \quad \text{for } \theta \in [0, 2\pi], \\ &\kappa^j = \exp(j\mathrm{i}\theta). \end{aligned} \tag{3.7}$$

Then by applying $W^j = \kappa^j$ in Eq. (3.6) and dividing by κ^n, given a polynomial $p(z)$ with $z = \lambda \Delta t$ and the following root locus:

$$z = \frac{\kappa - 1}{\sum_{i=0}^{s-1} \gamma_i (1 - \frac{1}{\kappa})^i} \tag{3.8}$$

The root locus corresponds to the points of z which can constitute the boundary of the stability region.

Theorem 3.1.1 — Root locus. The boundary of the stability domain $\mathcal{S}$ consists of parts of the root locus curve c given by: $\theta \mapsto z(e^{\mathrm{i}\theta})$. If the method is consistent and all "parasitic" roots of $p(\zeta) = 0$ lie inside the unit disc (*I.E.*, the method is "strictly stable"), at least a small disc:

$$\{z \in \mathbb{C}, |z - \delta| \leq \delta\} \quad \text{With} \quad \delta > 0 \tag{3.9}$$

lies inside the stability domain $\mathcal{S}$. According to the definition of the stability domain:

$$\begin{aligned} \mathcal{S} = \{&z \in \mathbb{C}, \text{simple roots } \kappa(z) \text{ of (3.6) satisfy } |\zeta(z)| \leq 1, \\ &\text{multiple roots satisfy } |\zeta(z)| < 1\} \end{aligned} \tag{3.10}$$

For $s = 1$, this is the circle of Euler's method centred at -1. But for $s = 2, 3, ..., 6$ the stability domains size is rapidly decreasing. Then these methods are surely not appropriate for resolution of stiff problem and thus not A-stable (see Fig. 3.1).

As an example, the stability of the second-order accurate Adams-Bashforth' scheme:

$$W^{n+1} = W^n + \Delta t (\frac{3}{2} R(t^n, W^n) - \frac{1}{2} R(t^{n-1}, W^{n-1})), \tag{3.11}$$

will be studied. Hence for the Dahlquist test equation (2.5)

$$W^{n+1} = (1 + \frac{3}{2} \lambda \Delta t) W^n - \frac{1}{2} \lambda \Delta t W^{n-1}. \tag{3.12}$$

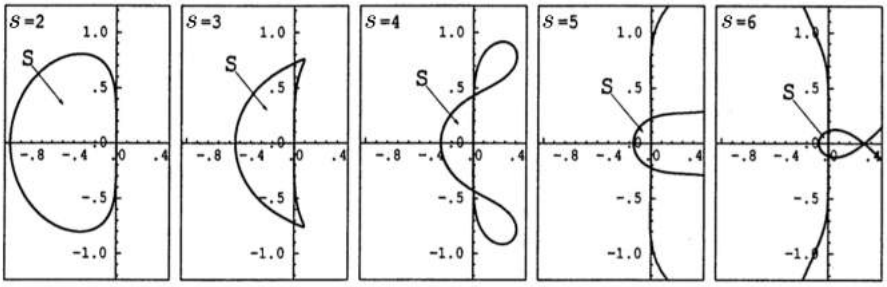

Fig. 3.1. Stability domains for Adams-Bashforth schemes from [35]

and by substitution of $W^n = \kappa^n$:

$$\kappa^2 - (1 + \frac{3}{2}\lambda\Delta t)\kappa + \frac{1}{2}\lambda\Delta t = 0. \tag{3.13}$$

Hence the previous equation has two roots:

$$\begin{aligned} \kappa_1(\lambda) &= \frac{1}{2}\left((1 + \frac{3}{2}\lambda\Delta t) + \sqrt{(1 + \frac{3}{2}\lambda\Delta t)^2 - 2\lambda\Delta t}\right), \\ \kappa_2(\lambda) &= \frac{1}{2}\left((1 + \frac{3}{2}\lambda\Delta t) - \sqrt{(1 + \frac{3}{2}\lambda\Delta t)^2 - 2\lambda\Delta t}\right). \end{aligned} \tag{3.14}$$

Thus, the stability region is characterized by the following ensemble $\mathcal{S}$:

$$\mathcal{S} = \{z \in \mathbb{C}, |\kappa_1(z)| \leq 1 \text{ and } |\kappa_2(z)| \leq 1\}. \tag{3.15}$$

3.2 Explicit Runge-Kutta Method

3.2.1 Principle

These methods were developed by C. Runge [36] and M. W. Kutta [37]. The Runge-Kutta (RK) methods are qualified as one-step and multi-stage methods contrary to linear multistep methods such as Adams-Bashforth methods. Instead of using more than one previous solution state, a RK method uses only the previous state W^n and some stage values that can be viewed as intermediate values of the solution $W(t)$ at the times $t^n + c_i\Delta t$ to define W^{n+1}. These values are computed within each integration step. The number s of a RK method is the number of stage values that are used and the residual computed at these stages are denoted by k_i for $i = 1, ..., s$. The explicit RK method has the property that all stages k_i are explicit. Indeed each stage depends on the previous solution W^n and on the previous computed stage k_j for $j = 1, ..., i-1$.

3.2.2 Formulation

As presented previously, all explanations will follow the notations introduced for the generic Cauchy problem defined in Eq. (2.6). Here, s intermediate points are introduced in the interval $[t^n, t^{n+1}]$ and they are denoted $t^{n,1}, t^{n,2}, ..., t^{n,s}$. $c_1, c_2, ..., c_s$ are real numbers in the interval $[0, 1]$ and $t^{n,i} = t^n + c_i\Delta t$ for $i \in \{1, ..., s\}$. The discrete values $W(t^{n,i})$ must verify:

$$W(t^{n,i}) = W(t^n) + \int_{t^n}^{t^{n,i}} R(l, W(l))dl \tag{3.16}$$

with a change in variables, for each stage of the explicit RK method:

$$W(t^{n,i}) = W(t^n) + \Delta t \int_0^{c_i} R(t^n + \tau\Delta t, W(t^n + \tau\Delta t))d\tau. \tag{3.17}$$

and also (for external iteration in order to obtain the solution W^{n+1} at t^{n+1}):

$$W(t^{n+1}) = W(t^n) + \Delta t \int_0^{1} R(t^n + \tau\Delta t, W(t^n + \tau\Delta t))d\tau. \tag{3.18}$$

So, $s+1$ quadrature methods are chosen with s quadrature points in order to approximate (3.17) and (3.18). As a consequence, taking $s(s+1)$ parameters $(a_{ij})_{1\leq i,j\leq s}$ called *internal coefficients* and $(b_i)_{1\leq i\leq s}$ called *weights* is equivalent if:

$$\begin{aligned}
&\int_0^{c_i} R(t^n + \tau\Delta t, W(t^n + \tau\Delta t))d\tau \to \sum_{j=1}^{s} a_{ij} R(t^n + \tau\Delta t, W(t^n + \tau\Delta t)) \\
&\int_0^{1} R(t^n + \tau\Delta t, W(t^n + \tau\Delta t))d\tau \to \sum_{j=1}^{s} b_i R(t^n + \tau\Delta t, W(t^n + \tau\Delta t)).
\end{aligned} \tag{3.19}$$

Then the formulation of the Runge-Kutta explicit iteration method is:

$$\begin{cases}
W^0 \text{ known} \\
k_i = R(t^n + c_i\Delta t, W^n + \sum_{j=1}^{i-1} a_{ij}k_j),\ i = 1, ..., s \\
W^{n+1} = W^n + \Delta t \sum_{i=1}^{s} b_i k_i.
\end{cases} \tag{3.20}$$

The method is characterised by parameters (a_{ij}), (b_i) and (c_i). These data are usually arranged in a mnemonic device, known as the Butcher tableau [38]:

c_1	a_{11}	a_{12}	$\cdots$	a_{1s-1}	a_{1s}
c_2	a_{21}	a_{22}	$\cdots$	a_{2s-1}	a_{2s}
$\vdots$	$\vdots$	$\vdots$		$\vdots$	$\vdots$
c_s	a_{s1}	a_{s2}	$\cdots$	$a_{s,s-1}$	$a_{s,s}$
	b_1	b_2	$\cdots$	b_{s-1}	b_s

Tab. 3.1. The Butcher tableau for the Runge-Kutta method.

3.2.3 Stability Properties

If a Runge-Kutta integrator is applied to the resolution of Dahlquist linear equation (2.5), the formulation of such method is:

$$\begin{cases}
W^{(i)} = W^n + \lambda\Delta t \sum_{j=1}^{i-1} a_{ij} W^{(j)},\ i = 1, ..., s \\
W^{n+1} = W^n + \lambda\Delta t \sum_{i=1}^{s} b_i W^{(i)}
\end{cases} \tag{3.21}$$

Hence:

$$W_{n+1} = G(\lambda \Delta t) W_n \tag{3.22}$$

where the stability function G is defined as the following polynomial of degree $< s$ for a s-stage RK method:

$$G(z) = 1 + z \sum_j b_j + z^2 \sum_{j,k} b_j a_{jk} + z^3 \sum_{j,k,l} b_j a_{jk} a_{kl} + ... \tag{3.23}$$

According to Hairer and Wanner [35], for a RK method of order p the stability function can be defined as:

$$G(z) = 1 + z + \frac{z^2}{2!} + ... + \frac{z^p}{p!} + O(z^{p+1}) \tag{3.24}$$

An example of four-stage Runge-Kutta (RK4) algorithm is the one presented by Jameson *et al.* [39] of fourth-order accuracy for linear problems and second-order accurate in general, with the following formulation:

$$\begin{cases} W^0 \text{ known} \\ k_1 = R(t^n, W^n) \\ k_2 = R(t^n + \frac{\Delta t}{2}, W^n + \frac{k_1}{2}) \\ k_3 = R(t^n + \frac{\Delta t}{2}, W^n + \frac{k_2}{2}) \\ k_4 = R(t^n + \Delta t, W^n + k_3) \\ W^{n+1} = W^n + \frac{1}{6}\Delta t(k_1 + 2k_2 + 2k_3 + k_4). \end{cases} \tag{3.25}$$

Another example of simple second-order Runge-Kutta scheme is Heun's scheme (with two stages). Heun's scheme [40] employs a predictor-corrector formulation: the value of the state W^{n+1} will be predicted and then corrected by a trapezoidal rule. The explicit Heun's scheme may be written as (for temporal integration):

- A predictor stage : $\widehat{W} = W^n + \Delta t R(t^n, W^n)$
- A corrector stage : $W^{n+1} = W^n + \frac{\Delta t}{2}\big(R(t^n, W^n) + R(t^n, \widehat{W})\big)$

Heun's scheme is characterised by the following Butcher tableau:

0	0	
1	1	0
	$\frac{1}{2}$	$\frac{1}{2}$

Tab. 3.2. The Butcher tableau for the explicit Heun's scheme.

In order to study the stability of Heun's scheme, the integrator is applied to the Dahlquist test equation (2.5). Then one obtains:

$$W^{n+1} = \big(\frac{\lambda^2 \Delta t^2}{2} + \lambda \Delta t + 1\big) W^n. \tag{3.26}$$

Hence the stability region of Heun's scheme is:

$$\mathcal{S} = \{z \in \mathbb{C}, |\frac{z^2}{2} + z + 1| \leq 1\}. \tag{3.27}$$

3.2.4 Order Condition for RK Method

The Butcher tableau represents the different coefficients for a given RK method and it is important to remind that there is a kind of consistency between the coefficients:

$$c_i = \sum_{j=1}^{s} a_{ij}. \tag{3.28}$$

In order to be at least of the first order of accuracy, the coefficients b_i of the RK method must satisfy the following equation:

$$\sum_{i=1}^{s} b_i = 1. \tag{3.29}$$

So any RK method that satisfies both conditions is called consistent and at least first-order accurate. For RK method of higher order, the algebraic conditions on the coefficients of the method become increasingly complicated [23, 35, 41].

3.2.5 Partial Conclusion on the Explicit Runge-Kutta Methods

Explicit Runge-Kutta methods are particularly appreciated for their stability domains which are larger than the majority of explicit methods. Nevertheless, high-order Runge-Kutta scheme may be very expensive in term of computational cost. Indeed the number of stages increases non-linearly with the order of accuracy. In this context, Williamson [42] designed low-storage Runge-Kutta schemes up to the fourth order with only two stages. High-order Runge-Kutta scheme with TVD properties was investigated by Jameson *et al.* [39] and Shou and Osher [43]. The explicit methods presented previously are conditionally stable, and of course they may have a very restrictive constraint. This is also a drawback for unsteady simulations for which the transient regime can be long and time-consuming and unconditionally stable methods should be preferred. Regardless issues of stability and computational cost, it is relevant that explicit schemes may be restricted to resolution of non-stiff problem since any stiff problem induces a significant decrease of the time step (as an example chemical effects have to be resolved with a smaller time step than aerodynamic ones). The following methods tends to extend explicit method to resolve these kinds of problem.

3.3 Exponential Integrators

3.3.1 Principle

As it was presented in chapter 1, several phenomena, often encountered in aero-space domain, may be interpreted as physically stiff. And as presented previously, stiffness translates, in a practical point of view, into a time step in agreement with this local transient phenomenon which can be characterised by a very small characteristic time. In this context, any explicit temporal integrator is controlled by severe time-step restrictions in order to maintain numerical stability. In such case, a matrix exponential formulation may have the potential to greatly overcome this time-step restriction.

The first exponential integrators were designed by Certaine [44] and will be introduced for linear and non-linear equations.

3.3.2 Formulation for Linear Equations

Exponential integrators attempt to solve Cauchy's problem by the decomposition of the right-hand part (the residual R) into a linear contribution (matrix-vector product) and an external driving force such as:

$$\begin{cases} W'(t) = R(t, W(t)) = \mathbf{B}W(t) + q(t) \\ W(0) = W^0. \end{cases} \tag{3.30}$$

It is a linear and autonomous problem with $\mathbf{B}$ the matrix system and $\mathbf{q}$ an external driving force. The solution of this previous system is expressed analytically:

$$W(t) = \exp(t\mathbf{B})W^0 + \int_0^t \exp\big((t-s)\mathbf{B}\big)q(s)ds. \tag{3.31}$$

First, the homogeneous case with no driving force ($q = 0$) will be considered. The main effort on computation will be on the product of the exponential matrix by the vector ($\exp(t\mathbf{B})W^0$). Thanks to Taylor's expansion of the exponential function, it is possible to express $\exp(t\mathbf{B})W^0$ such as:

$$\exp(t\mathbf{B})W^0 = \sum_{n=0}^{\infty} \frac{1}{n!}(t\mathbf{B})^n W^0, \tag{3.32}$$

An approximation of this product can be found with a general polynomial approximation of the form:

$$\exp(t\mathbf{B})W^0 \approx p_{m-1}(t\mathbf{B})W^0, \tag{3.33}$$

with p_{m-1} a polynomial of degree $(m-1)$. So as presented previously, this kind of formulation introduces a matrix-vector product. The solution $W(t)$ at a given time t is not computed directly by the exponential integrator from the initial solution. Indeed, the exponential integrator solves the following iterative problem over one time step $[t^n, t^n + \Delta t]$:

$$\begin{cases} W(t^n + \Delta t) = \exp((t^n + \Delta t)\mathbf{B})W^0 = \exp(\Delta t\mathbf{B})W(t^n) \\ W(0) = W^0. \end{cases} \tag{3.34}$$

Nevertheless, for various flow configurations, the system of governing equations is non-homogeneous, *i.e.* the source term $q(t)$ is non-zero. Then if we consider the external-driving force, attention will be paid on the approximation of the integral part in (3.31). It is possible to rewrite the general solution (3.31) with the assumption that $q(t) = q(t^0)$ such as

$$W(t) = \exp(t\mathbf{B})W^0 + t\varphi_1(t\mathbf{B})q(t^0), \tag{3.35}$$

with:

$$\varphi_1(z) = \frac{\exp(z) - 1}{z}. \tag{3.36}$$

Then for one time step:

$$W^{n+1} = \exp(\Delta t\mathbf{B})W^n + \Delta t\varphi_1(\Delta t\mathbf{B})q(t^n), \tag{3.37}$$

This time integration is also called the explicit exponential Euler method or Exponential Time Differencing (ETD) method. With some manipulations and according to Eq. (3.36), the following formulation is obtained:

$$\begin{aligned} W^{n+1} &= \exp(\Delta t\mathbf{B})W^n + \Delta t\varphi_1(\Delta t\mathbf{B})q(t^n) \\ &= (\Delta t\mathbf{B}\varphi_1(\Delta t\mathbf{B}) + \mathbf{I})W^n + \Delta t\varphi_1(\Delta t\mathbf{B})q(t^n), \\ &= W^n + \Delta t\varphi_1(\Delta t\mathbf{B})(\mathbf{B}W^n + q(t^n)). \end{aligned} \tag{3.38}$$

So the only remaining expensive operation is to evaluate $\varphi_1(t\mathbf{B})W^0$.

The treatment of the non linear term q can lead to many other possible formulations. For instance, the non linear term q can be treated implicitly, leading to the implicit version of the ETD Euler method :

$$W^{n+1} = \exp(\Delta t\mathbf{B})W^n + \Delta t\varphi_1(\Delta t\mathbf{B})\mathbf{q}(t^{n+1}). \tag{3.39}$$

There are also the ETD linear multistep methods with an algebraic polynomial approximation of the non-linear term, such as the ETD Adams-Bashforth methods with the following formulation [45]:

$$W^{n+1} = \exp(\Delta t \mathbf{B}) W^n + \Delta t \sum_{i=0}^{q-1} \alpha_i(\Delta t \mathbf{B}) \nabla^i q(t^n), \tag{3.40}$$

where $\nabla^0 q(t^n) = q(t^n)$ and $\nabla^{i+1} q(t^n) = \nabla^i q(t^n) - \nabla^i q(t^{n-1})$ and the related function $\alpha_i(x)$ needs to satisfy the following recurrence relations:

$$\begin{aligned} x\alpha_0(x) &= \exp(x) - 1 \\ x\alpha_{i+1}(x) + 1 &= \alpha_i(x) + \frac{1}{2}\alpha_{i-1}(x) + \frac{1}{3}\alpha_{i-2}(x) + ... + \frac{1}{i+1}\alpha_0(x). \end{aligned} \tag{3.41}$$

Beylkin *et al.* [46] provide a second representation of the ETD Adams-Bashforth with the related functions called φ-functions, defined as:

$$\varphi_l(x\mathbf{B}) = \frac{1}{x^l} \int_0^x \exp(x-\tau)\mathbf{B} \frac{\tau^{l-1}}{(l-1)!} d\tau, \quad l \geq 1 \tag{3.42}$$

with the recurrence relation:

$$\varphi_{l+1}(x) = \frac{\varphi_l(x) - \frac{1}{l!}}{x}, \quad \varphi_l(0) = \frac{1}{l!} \tag{3.43}$$

An exponential time integrator can also be based on a single-step method such as the standard Runge-Kutta schemes, for instance using the following formulation:

$$\begin{aligned} k_i &= \sum_{j=1}^{s} a_{ij}(\Delta t \mathbf{B}) \Delta t q(k_j) + \exp(c_i \Delta t \mathbf{B}) W^n, \quad i = 1, 2, ..., s, \\ W^{n+1} &= \sum_{i=1}^{s} b_i(\Delta t \mathbf{B}) \Delta t q(k_i) + \exp(\Delta t \mathbf{B}) W^n. \end{aligned} \tag{3.44}$$

Examples of an approximate ETD Runge-Kutta method were proposed by Ehle and Lawson [47], then by van der Houwen [48] and Verwer [49]. In their schemes, exponential and related functions are approximated rather than exactly computed. More methods based on the Runge-Kutta framework were presented and compared in the review paper of Minchev and Wright [50]. More recently, Huang and Shu proposed a bound preserving ETD Runge-Kutta applied to discontinous Galerkin methods for the computation of a scalar hyperbolic equation with stiff source terms [51]. It is mentioned in their paper that the method should be applied to high order finite volume schemes.

3.3.3 Formulation for Non-linear Equations

It is necessary to employ some modifications for the resolution of non-linear governing equation as Navier-Stokes equations. Indeed if the general non-linear initial-value problem Eq. (3.1) is considered, a linearisation of the residual R with respect to the state W^n leads to:

$$R(W(t)) = R(W(t^n)) + \left.\frac{\partial R}{\partial W}\right|_{W(t^n)} (W(t) - W(t^n)) + r_e(W(t)), \tag{3.45}$$

with the remainder term $r_e(W(t))$ and the Jacobian matrix:

$$\mathbf{B} = \left.\frac{\partial R}{\partial W}\right|_{W(t^n)}. \tag{3.46}$$

So the Cauchy problem may be written such as:

$$\frac{dW}{dt} = R(W(t^n)) + \mathbf{B}(W(t) - W(t^n)) + r_e(W(t)). \tag{3.47}$$

Then if we introduce an exponential integrator $\exp(-t\mathbf{B})$ in previous equation and integrate over the time interval $[t^n, t^{n+1}]$, the solution $W(t^{n+1})$ can be written as:

$$W(t^{n+1}) = W(t^n) + (\exp(\Delta t\mathbf{B}) - \mathbf{I})\mathbf{B}^{-1}R(W(t^n)) + \int_{t^n}^{t^{n+1}} \exp((t^n + \Delta t - s)\mathbf{B})r_e(W(s))ds, \tag{3.48}$$

This represents the *exact solution* at t^{n+1} of the given problem (3.1). It is necessary to compute numerically the integral in (3.48) that involves remainder term for an accurate time integration. Nevertheless, according to Schulze *et al.* [52], the error caused by omitting the integral is comparable to the one induced by a standard explicit Runge-Kutta method with three stages (see [53] and [54]). So if the integral is set to zero, the previous equation may be expressed such as:

$$W(t^{n+1}) = W(t^n) + \Delta t\varphi_1(\Delta t\mathbf{B})R(W(t^n)). \tag{3.49}$$

This expression may be related to previous one (3.37). A formulation of exponential time integrator for periodic cases was proposed by Montanelli and Bootland [55] thanks to different ETD method first introduced by Minchev and Wright [50]. About the stability of such method, for the Dahlquist linear equation (2.5) it appears that exponential integrators are exact. Then the left half-plane of the complex space is totally covered. Thus exponential integrators are A-stable.

In the following, another technique in order to extend explicit method to solve stiff problem will be presented. This kind of method have some characteristics identical to implicit time integrators but this method is not part of them.

3.4 Implicit Residual Smoothing Time Scheme

3.4.1 Principle

The following method allows to perform an explicit Runge-Kutta' scheme beyond its stability limit by computation of a matrix-vector product. This kind of method is not considered as a pure implicit method. In fact the main idea behind this technique is to smooth the residual R over a set of neighbouring cells. This method is called implicit residual smoothing. Here, the inner-loop used to solve the matrix-product term will be called implicit stage and the scheme that approximates the residual will be called explicit stage. It is necessary to introduce the amplification matrix factor $\mathbf{G}$ that compares the space discretisation for the implicit stage and the explicit stage:

$$\mathbf{G} = \mathbf{I} - \mathbf{H}^{-1}\mathbf{K}, \tag{3.50}$$

with $\mathbf{H}$ and $\mathbf{K}$ respectively the space discretisation operators for the implicit stage and the explicit stage.

3.4.2 Formulation

Standard explicit Runge-Kutta's time integrator (3.20) may be re-formulated as:

$$\begin{cases} W^{(0)} = W^n \\ W^{(i)} = W^{(0)} + \Delta t \sum_{j=1}^{i-1} a_{ij} R(t^n + c_j \Delta t, W^{(j)}),\ i = 1, ..., s \\ W^{n+1} = W^n + \Delta t \sum_{i=1}^{s} b_i R(t^n + c_i h, W^{(i)}). \end{cases} \tag{3.51}$$

It is possible to enlarge the stability domain of the explicit Runge-Kutta schemes. This enhancement is performed by an implicit residual smoothing (IRS) technique. The operator will be applied to inviscid fluxes contribution. It is sometimes called Lax-Wendroff-like implicit operator [56] and it is applied to any stage of the Runge-Kutta' scheme:

$$\begin{cases} W^{(0)} = W^n \\ J(W^{(i)} - W^{(0)}) = \Delta t \sum_{j=1}^{i-1} a_{ij} R(t^n + c_j \Delta t, W^{(j)}),\ i = 1, ..., s \\ W^{n+1} = W^n + \Delta t \sum_{i=1}^{s} b_i R(t^n + c_i \Delta t, W^{(i)}). \end{cases} \tag{3.52}$$

For a second-order implicit smoothing applied to a one-dimensional problem, the implicit operator is:

$$J = 1 - \theta \left(\frac{\Delta t}{\Delta x} \right)^2 \delta(\lambda^2 \delta), \tag{3.53}$$

where θ is a parameter, δ represents the difference operator and λ the spectral radius of the inviscid flux Jacobian (value of the largest eigenvalue, defined as the sum of velocity magnitude and speed of sound for Euler equations). In the case of a d-dimensional problem, the IRS operator is now:

$$J = \prod_{l=1}^{d} \left[1 - \theta \left(\frac{\Delta t}{\Delta x_l} \right)^2 \delta_l(\lambda_l^2 \delta_l) \right], \tag{3.54}$$

with Δx_l, δ_l and λ_l, respectively, the space step, the difference operator and the spectral radius of the flux Jacobian in the lth direction. The multidimensional IRS operator leads to a tridiagonal system inversion per mesh direction at each Runge-Kutta' stage. The truncation error induced by this implicit operator applied to:

$$\frac{dW}{dt} + \sum_d \frac{\partial f_d}{\partial x_d} = 0. \tag{3.55}$$

is equal to :

$$-\theta(\Delta t)^2 \sum_d (\lambda_d^2) \frac{\partial^3 f_d}{\partial x_d^3} + O(\Delta t^2). \tag{3.56}$$

This error is proportional to a third derivative of the flux f, it appears that the error has a dispersive nature. It is important to recognize θ as a smoothing coefficient that stabilizes the temporal scheme. The preceding second order IRS will be referred as IRS2. This type of smoothing operator could be expressed as a Laplacian filter after each Runge-Kutta stages. It is

possible to increase the accuracy of the implicit residual smoothing operator. The Laplacian filter may be substituted by a bilaplacian operator (referred as IRS4), approximated by fourth order central differences [57]. Hence for one-dimensional problem, the IRS4 operator is such as:

$$J = 1 + \theta\left(\frac{\Delta t}{\Delta x}\right)^4 \delta(\lambda^4 \delta^3). \tag{3.57}$$

And the associated truncation error induced by this operator applied to Eq. (3.55) is now:

$$-\frac{1}{12}\theta(\Delta t)^4 \sum_d (\lambda_d^4)\frac{\partial^5 f_d}{\partial x_d^5} + O(\Delta t^4). \tag{3.58}$$

As before with the IRS2, the IRS4 involves an error with a dispersive nature but leads to a higher order of accuracy than the previous one.

3.4.3 Stability Properties

Now the effect of the IRS operator on RK scheme stability will be introduced. So for standard RK stage:

$$W^{(i)} = W^{(0)} + \Delta t \sum_{j=1}^{i-1} a_{ij} R(t^n + c_j \Delta t, W^{(j)}),\ i = 1, ..., s. \tag{3.59}$$

For the Dahlquist test problem (2.5) and after a Fourier transform of the previous system (3.59), it is possible to express the amplification factor of RK scheme at ith stage $G^{(i)}$ as:

$$G^{(i)} = 1 - \Delta t \tilde{R} G^{(i-1)}, \tag{3.60}$$

where $G^{(0)} = 1$ and the complex $\tilde{R}$ is the Fourier symbol of the residual. In the case that an IRS operator is applied to any RK stage, it comes:

$$J(W^{(i)} - W^{(0)}) = \Delta t \sum_{j=1}^{i-1} a_{ij} R(t^n + c_j \Delta t, W^{(j)}),\ i = 1, ..., s, \tag{3.61}$$

and the previous amplification factors may be re-formulated:

$$G^{(i)} = 1 - \Delta t \frac{\tilde{R}}{\tilde{J}} G^{(i-1)}, \tag{3.62}$$

with $\tilde{J}$ the Fourier symbol of the scalar IRS operator. Then for the previous IRS2 ans IRS4 scheme:

$$\begin{aligned} \tilde{J}_{IRS2} &= 1 + 4\,\theta\, CFL^2 sin^2\left(\frac{k\Delta x}{2\pi}\right) \\ \tilde{J}_{IRS4} &= 1 + 16\,\theta\, CFL^4 sin^4\left(\frac{k\Delta x}{2\pi}\right), \end{aligned} \tag{3.63}$$

So for the Fourier implicit operator $\tilde{J}$ greater than one, the impact of $\tilde{R}$ on the amplification factor is reduced. This results in the increase of the maximum available time step for explicit RK time integrators thanks to the IRS technique. The stability region was studied by Cinnella and Content [57] for RK4 (Jameson *et al.* [39]) and RK6 (Bogey and Bailly [58]) with a MUSCL spatial scheme constructed by applying a ninth-order extrapolation to the fluxes. It appears that the IRS4 operator introduces a fourth order error of dispersion but this error remains smaller

than the one obtained with the baseline scheme (RK6 and RK4). Then, according to Cinnella and Content [57], an IRS method applied for the computation of turbulent compressible flows can allow to reduce the computational cost by a factor between 3 and 5, taking references from either the explicit RK4 scheme or the RK6 one. For the computation of a linear advection of a Gaussian hump, it reveals that the application of the IRS4 operator on the RK6 scheme (second order accurate) at $CFL = 10$ reduces by 30% the CPU cost of the simulation, with a reference cost obtained using the RK4 scheme at $CFL = 1$, while keeping a very similar accuracy. However, it is important that such application of a bi-Laplacian operator remains correct only for structured grids. Indeed in structured grid case, the smoothing direction (the direction on which the operator is applied) coincides with the grid lines. An application on unstructured grid was proposed by Catalano and Daloiso [59] by application of a new line-search (LS) algorithm.

3.5 Conclusion on Explicit Time Integration

Several methods were introduced for solving stiff and non-stiff problems. For non-stiff problems, explicit Runge-Kutta or linear multi-step methods lead to accurate results. Nevertheless, in case of stiffness, such standard explicit method suffer from instability. Several work was performed in order to enhance the standard explicit methods for stiffness, and few ones was presented in this report. Now, the attention will be paid on the implicit time integrator. Such integrator can lead to accurate results, even for stiff problems.

4 Implicit Method for Time Integration

Implicit time integrators are introduced in order to enable a fast convergence towards the steady solution using large time steps. For unsteady flows, implicit time integration schemes can also be considered for applying larger time steps than explicit ones respecting their stability property. If the use of the implicit formulation is cheaper than performing many explicit time steps, the overall CPU cost is therefore lower than when a pure explicit approach is chosen. In addition, implicit schemes may be an interesting approach for the computation of stiff physics, such as the flow around aero devices. Such a time integrator has the benefit of being either linearly unconditionally stable, or with a large stable time step. But, implicit methods have a negative effect on the overall CPU cost because they generally require an extra computational cost associated with the solution of a linear system of equations.

In this context, several implicit method for time integrating the Navier-Stokes equations will be formulated in this chapter, such as Backward Differentiation Formula method, Adams-Moulton's scheme, implicit Runge-Kutta's scheme and Rosenbrock's method.

4.1 Backward Differentiation Formula Method

4.1.1 Principle

Backward Differentiation Formula (BDF)-type time integrators are part of multistep methods. Adams-Bashforth methods are obtained by integration of an interpolation polynomial that approximates the residual, while BDF-type methods are obtained by differentiating an interpolation polynomial that approximates the solution W.

4.1.2 Formulation

The formulation is explained easily by considering two steps. The first step consists of approximating the solution W^{n+1} thanks to a Lagrange polynomial as:

$$P_s(t^n, W^{n+1}) = \sum_{i=0}^{s} W^{n+1-i} L^i(t^n). \tag{4.1}$$

with:

$$L^i(t^n) = \prod_{0 \leq j \leq s, j \neq i} \frac{t^n - t^{n-j}}{t^{n-i} - t^{n-j}}. \tag{4.2}$$

For the second step it is assumed that :

$$P_s'(t^{n+1}, W^{n+1}) = R^{n+1} \tag{4.3}$$

For $s = 1$:

$$P_1(t, W^{n+1}) = W^{n+1} + (t - t^{n+1}) \frac{W^{n+1} - W^n}{\Delta t} \tag{4.4}$$

According to the Eq. (4.3):

$$P_1'(t, W^{n+1}) = \frac{W^{n+1} - W^n}{\Delta t} = R^{n+1}, \tag{4.5}$$

then, it comes:

$$W^{n+1} = W^n + \Delta t R^{n+1} \tag{4.6}$$

and the implicit backward Euler method is recovered.

For $s = 2$:

$$P_2(t, W^{n+1}) = W^{n+1} + (t - t^{n+1})\left[\frac{W^{n+1} - W^n}{\Delta t} + (t - t^n)\frac{W^{n+1} - 2W^n + W^{n-1}}{2\Delta t^2}\right] \tag{4.7}$$

and considering again the Eq. (4.3):

$$P_2'(t, W^{n+1}) = \frac{3W^{n+1} - 4W^n + W^{n-1}}{2\Delta t} = R^{n+1}, \tag{4.8}$$

which leads to second order A-stable Gear's scheme [60]:

$$W^{n+1} = \frac{4}{3}W^n - \frac{1}{3}W^{n-1} + \frac{2}{3}\Delta t R^{n+1}. \tag{4.9}$$

The general formulation of a s-step BDF method is:

$$\sum_{j=1}^{s} \frac{1}{j}\nabla^j W^{n+1} = \Delta t R^{n+1} \tag{4.10}$$

with $\nabla^0 W^n = W^n$ and $\nabla^{j+1} W^n = \nabla^j W^n - \nabla^j W^{n-1}$.

4.1.3 Stability Properties

For the previous expression of BDF methods (4.10) applied to Dahlquist test equation (2.5), the following equation is obtained:

$$\sum_{j=1}^{s} \frac{1}{j}\nabla^j W^{n+1} = \lambda \Delta t W^{n+1}. \tag{4.11}$$

Now, the technique introduced in Sec. 3.1.3 for stability is applied to BDF scheme, leading to:

$$p(\kappa) = \sum_{j=1}^{s} \frac{1}{j}\kappa^{s-j}(\kappa - 1)^j. \tag{4.12}$$

It is more convenient to consider the polynomial:

$$\tilde{p}(z) = (1 - z)^s p\left(\frac{1}{1 - z}\right) \tag{4.13}$$

via the transformation $\kappa = 1/(1 - z)$. Then the s-step BDF method is stable if and only if all roots of the polynomial (4.13) are outside the disc $\{z \in \mathbb{C}, |z - 1| \leq 1\}$ with simple roots allowed on the boundary (cited from [23]). According to [35] a s-step BDF method is stable until $s < 7$

4.2 Adams-Moulton Scheme

4.2.1 Principle

The Adams-Moulton time integrators are built using the same philosophy as the explicit approach of Adams-Bashforth, but the solution W^{n+1} is used in the residual formulation, which changes the class of the method from explicit to implicit. The residual R is approximated by an interpolation polynomial at the time instant $t^{n+1}, t^n, ..., t^{n-s}$ (for a Adams-Moulton with s steps).

4.2.2 Formulation

A s-step Adams-Moulton's scheme is written as:

$$P^*(l) = P^*(t^n + k\Delta t) = \sum_{i=0}^{s} (-1)^i \binom{-k+1}{i} \nabla^i R(t^{n+1}), \tag{4.14}$$

and the following approximation is used:

$$W(t^{n+1}) \approx W(t^n) + \int_{t^n}^{t^{n+1}} P^*(l) dl = W(t^n) + \Delta t \sum_{i=0}^{s} \gamma_i^* \nabla^i R(t^{n+1}). \tag{4.15}$$

with the coefficient γ_i^* defined as:

$$\gamma_i^* = (-1)^i \int_0^1 \binom{-k+1}{i} dk \tag{4.16}$$

Equation (4.15) is the general formulation of Adams-Bashforth's method with s steps The second-order accurate Adams-Moulton scheme ($s = 1$) is equivalent to the Crank-Nicolson formulation [61] (called IRK2 in the following):

$$\frac{W^{n+1} - W^n}{\Delta t} = \frac{1}{2}(R^{n+1} + R^n). \tag{4.17}$$

4.2.3 Stability Properties

A s-step Adams-Moulton's scheme applied to Dahlquist's equation (2.5) leads to:

$$W^{n+1} = W^n + \lambda \Delta t \sum_{j=0}^{s} \gamma_j^* \nabla^j W^{n+1} \tag{4.18}$$

Applying the same procedure introduced in Sec. 3.1.3 for stability of Adam-Moulton's scheme, leads to a polynomial $p(z)$ with $z = \lambda \Delta t$. And finally, the root locus is as follows:

$$z = \frac{1 - \frac{1}{\kappa}}{\sum_{j=0}^{s} \tilde{\gamma}_j (1 - \frac{1}{\kappa})^j}, \tag{4.19}$$

For $s = 1$, the Adam-Moulton scheme is equivalent to the Crank-Nicolson scheme and this method is A-stable. But for $s = 2, 3, .., 6$ the stability domain is larger than one from the explicit Adams-Bashforth method but does not cover the left-half plane. Unfortunately the more the number of steps increases the less the method is stable (Fig. 4.1).

Theorem 4.2.1 — Dahlquist 1963. A multistep method cannot be A-stable if its order p verifies: $p > 2$. Moreover, any second-order multistep method is A-stable if and only if

$$C_{order} \leq -\frac{1}{12} \tag{4.20}$$

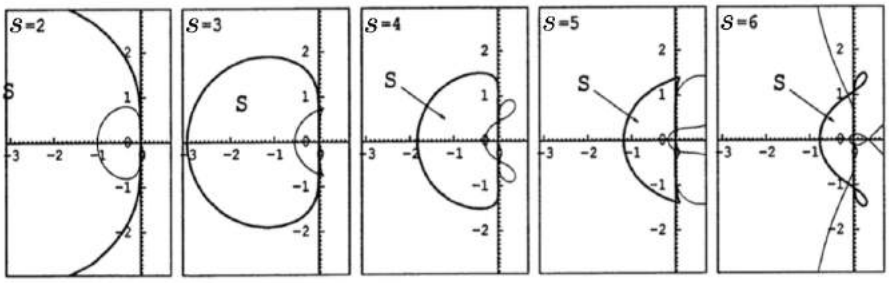

Fig. 4.1. Stability domains for Adams-Moulton schemes from [35]

C_{order} being defined in Eq. (2.23).

Remark: The second-order Crank-Nicholson's method is A-stable because $C_{order} = -\frac{1}{12}$.

4.3 Implicit Runge-Kutta Method

4.3.1 Principle

Implicit Runge-Kutta (IRK) methods (proposed by Kunstmann [62] and Butcher [63]) are multi-stage methods, contrary to previous Adams-Moulton time integrators. For an IRK method, any stage k_i depends on the previous ones but also on the local one. In explicit time integration, any stage k_i of a RK scheme depends only on the previous stages. As explicit RK method, implicit ones are represented by the set of real numbers $(\mathbf{A}, b, c)$ where $\mathbf{A}$ is the square matrix $(a_{ij})_{i,j=1,...,s}$ of dimension $s \times s$, b and c are two vectors of dimension s, $b^T = (b_1, ..., b_s)$ and $c = (c_1, ..., c_s)^T$.

4.3.2 Formulation

The first implicit Runge-Kutta scheme was introduced by Cauchy with the combination of the averaged value in the problem written with the Picard form (3.1):

$$W(t^{n+1}) = W(t^n) + \Delta t R(t^n + \theta \Delta t, W^n + \Theta(W^{n+1} - W^n)), \tag{4.21}$$

where $0 \leq \theta, \Theta \leq 1$.

If the relation is expressed using the implicit midpoint rule scheme with $\theta = \Theta = \frac{1}{2}$ and defining $k_1 = \frac{W^{n+1} - W^n}{\Delta t}$, it comes:

$$\begin{cases} k_1 = R(t^n + \dfrac{\Delta t}{2}, W^n + \dfrac{\Delta t}{2} k_1) \\ W^{n+1} = W^n + \Delta t k_1. \end{cases} \tag{4.22}$$

Another way to approximate Eq. (3.1) is to use the Radau quadrature [63]:

$$W^{n+1} - W^n = \int_{t^n}^{t^{n+1}} R(l, W(l)) dl \approx \frac{\Delta t}{2} \left(R(t^n, W^n) + 3R(t^n + \frac{2}{3}\Delta t, W(t^n + \frac{2}{3}\Delta t)) \right). \tag{4.23}$$

Definition 4.3.1 — Radau quadrature. The Radau quadrature is a formula for the numerical approximation of integrals. It requires $m + 1$ control points and fits all polynomials up-to degree $2m$. By nature, if the quadrature is written for the interval $[-1, 1]$, the point -1 is included in the set of control points, giving m free abscissas $(l_i)_{2 \leq i \leq m+1}$. For the function H

on the interval $[-1, 1]$, the general formula is:

$$\int_{-1}^{1} H(l)dl = w_1 H(-1) + \sum_{i=2}^{m+1} w_i H(l_i). \tag{4.24}$$

Starting from $l_1 = -1$, the free abscissas l_i for $i = 2, ..., m+1$ are the roots of the polynomial:

$$\frac{P_{m+1}(x) + P_m(x)}{1+x} \tag{4.25}$$

where $P_m(x)$ is the Legendre polynomial of degree m. The weights of the free abscissas are:

$$w_i = \frac{1 - l_i}{(m+1)^2 (P_m(l_i))^2}, \tag{4.26}$$

and for the endpoint:

$$w_1 = \frac{2}{(m+1)^2}. \tag{4.27}$$

The error term is given by :

$$E = \frac{2^{2m+1}(m+1)[m!]^4}{[(2m+1)!]^3} H^{(2m+1)}(\xi), \tag{4.28}$$

for ξ in $(-1, 1)$.

In order to approximate W at time $t^n + \frac{2}{3}\Delta t$, a quadratic interpolation is possible:

$$W(t^n + \frac{2}{3}\Delta t) = \frac{5}{9} W^n + \frac{4}{9} R(t^{n+1}, W^{n+1}) + \frac{2}{9}\Delta t R(t^n, W^n) + \mathcal{O}(\Delta t^4). \tag{4.29}$$

with $W^{n+1} = W^n + \frac{\Delta t}{4}(k_1 + 3k_2)$. Substituting W^{n+1} in the previous equation, the method of Hammer and Hollingsworth [64] is recovered:

$$\begin{cases} k_1 = R(t^n, W^n) \\ k_2 = R(t^n + \frac{2}{3}\Delta t, W^n + \frac{\Delta t}{3}(k_1 + k_2)) \\ W^{n+1} = W^n + \frac{\Delta t}{4}(k_1 + 3k_2). \end{cases} \tag{4.30}$$

The system (4.22) is defined by one intermediate stage, k_1. The previous system (4.30) is defined by two stages, k_1 and k_2. The construction can be extended to any system of s stage, with b_i, a_{ij} $(i = 1, ..., s)$ real and c_i defined as:

$$c_i = \sum_{j=1}^{i-1} a_{ij} \tag{4.31}$$

Then method:

$$\begin{cases} W^0 \ known \\ k_i = R(t^n + c_i \Delta t, W^n + \sum_{j=1}^{i} a_{ij} k_j), \ i = 1, ..., s \\ W^{n+1} = W^n + \Delta t \sum_{i=1}^{s} b_i k_i \end{cases} \tag{4.32}$$

is called an implicit Runge-Kutta iterative method with s-stages.

There are many ways to approximate the integral of Eq. (4.23) with quadrature rules such as Gauss, Radau and Labatto [35, 63, 65, 66].

4.3.3 Stability Issue

Starting from the implicit Euler method applied to Dahlquist's test problem (2.5) leads to:

$$\begin{aligned} &W^{n+1} = G(\lambda\Delta t)W^n \\ &\text{with } G(z) = \frac{1}{1-z}. \end{aligned} \tag{4.33}$$

For the implicit Euler method, the stability domain $\mathcal{S}$ is the region located out of the circle of centre $(1,0)$ and of radius 1. The stability domain covers the whole left-half plane $\mathbb{R} < 0$, which explains that the implicit Euler method is A-stable.

Considering the implicit Runge-Kutta method:

$$\begin{cases} k_i = W^n + \Delta t \sum_{j=1}^{i} a_{ij} R(t^n + c_j\Delta t, k_j),\ i = 1, ..., s \\ W^{n+1} = W^n + \sum_{j=1}^{s} b_j R(t^n + c_j\Delta t, k_j), \end{cases} \tag{4.34}$$

As expected, the system (4.34) becomes linear for the Dahlquist's problem:

$$\begin{cases} k_1 = W^n + \lambda\Delta t a_{11} k_1 \\ \quad\vdots \\ k_s = W^n + \lambda\Delta t \sum_{j=1}^{s} a_{sj} k_j. \end{cases} \tag{4.35}$$

The mathematical formulation can be simplified into the following relation:

$$\begin{pmatrix} k_1 \\ \vdots \\ k_s \end{pmatrix} = \left((\mathbf{I} - \lambda\Delta t\mathbf{A})^{-1} \right) W^n. \tag{4.36}$$

and Eq. (4.34) becomes:

$$W^{n+1} = W^n + \lambda\Delta t b^T \begin{pmatrix} k_1 \\ \vdots \\ k_s \end{pmatrix} = \left(1 + \lambda\Delta t b^T (\mathbf{I} - \lambda\Delta t\mathbf{A})^{-1} \right) W^n. \tag{4.37}$$

where $b^T = (b_1, ..., b_s)$, $\mathbf{A} = (a_{ij})_{i,j=1,...,s}$ and $e = (1, ..., 1)^T$. The stability function $G(z)$ satisfies:

$$G(z) = 1 + z b^T (\mathbf{I} - z\mathbf{A})^{-1} e \tag{4.38}$$

or:

$$G(z) = \frac{det(\mathbf{I} - z\mathbf{A} + z b^T e)}{det(\mathbf{I} - z\mathbf{A})}, \tag{4.39}$$

and this is directly due to Cramer's rule for the resolution of the linear systems:

$$\begin{pmatrix} \mathbf{I} - \mathbf{A}z & 0 \\ -z b^T & 1 \end{pmatrix} \begin{pmatrix} \underline{k} \\ W^{n+1} \end{pmatrix} = \begin{pmatrix} e \\ 1 \end{pmatrix}. \tag{4.40}$$

with $\underline{k} = (k_1, ..., k_s)^T$. Implicit Runge-Kutta methods based on Gauss, Lobatto and Radau rules (from Ehle [65] and Axelsson [66]) are A-stable. For any implicit Runge-Kutta method, with a matrix **A** non-singular, satisfying one of the following conditions:

$$a_{sj} = b_j, i = 1, ..., s \tag{4.41}$$

or:

$$a_{1j} = b_j, i = 1, ..., s \tag{4.42}$$

then $\lim_{z \to +\infty} R(z) = 0$ and the A-stable IRK method are L-stable.

It appears that integrating a system of q differential equation with a s-stage IRK method (implicit method with a full $s \times s$ matrix) requires the solution of qs simultaneous implicit non-linear equation at each time step. For lower triangular matrix $\mathbf{A} = (a_{ij})$ (where $a_{ij} = 0$ for $i < j$). The equations may then be solved in s successive stages with only a q-dimensional system to be solved at each stage. These kinds of method are called diagonally implicit Runge-Kutta (DIRK). For this type of methods, the stability function $G(z)$ for a s-stage DIRK method, may be expressed such as:

$$G(z) = \frac{P(z)}{H(z)} = \frac{P(z)}{(1 - a_{11}z)(1 - a_{22}z)...(1 - a_{ss}z)} \tag{4.43}$$

For a DIRK method with $a_{11} = ... = a_{ss} = \gamma$:

$$G(z) = \frac{P(z)}{(1 - \gamma z)^s} \tag{4.44}$$

with:

$$P(z) = (-1)^s \sum_{j=0}^{s} T_s^{s-j} \left(\frac{1}{\gamma}\right) (\gamma z)^j \tag{4.45}$$

where the polynomial $T(z)$ is defined as:

$$T_s(z) = \sum_{j=0}^{s} T^{s-j} (-1)^j \binom{s}{j} \frac{z^j}{j!} \tag{4.46}$$

This is the s-degree Laguerre polynomial and $T_s^k(z)$ represent the k-th derivative. The DIRK method is A-stable for :

$$H(i\delta)H(-i\delta) - P(i\delta)P(-i\delta) > 0 \ \ \forall \delta \in \mathbb{R} \tag{4.47}$$

4.4 Rosenbrock Method

4.4.1 Principle

In our physical context the residual R is strongly non-linear, Rosenbrock time integrators are approaches that try to avoid non-linear system by substituting them by a sequence of linear systems. There are sometimes named linearly implicit Runge-Kutta schemes. The main advantage of such method is to avoid computation of matrix-vector product that may represent a huge computation cost.

4.4.2 Formulation

The Cauchy problem integrated by an implicit s-stage RK method is considered. With the following stages:

$$k_i = R(t^n + c_i\Delta t, W^n + \sum_{j=1}^{i} a_{ij}k_j),\ i = 1, ..., s, \tag{4.48}$$

with the previous k_j stages for $j = 1, ..., i-1$ and

$$k_i^{(0)} = -\sum_{j=1}^{i-1} \gamma_{ij}\frac{k_j}{a_{ii}}, \tag{4.49}$$

used as a starting values. Then for one Newton-like iteration, we obtain:

$$(\mathbf{I} - a_{ii}\Delta t\mathbf{J})(k_i^{(1)} - k_i^{(0)}) = R(t^n + c_i\Delta t, y^n + \sum_{j=1}^{i}(a_{ij} - \gamma_{ij})k_j) - k_i^{(0)}, \tag{4.50}$$

with $\mathbf{J}$ an approximation to the Jacobian $\frac{\partial R}{\partial W}(t^n, W^n)$. For autonomous systems (as Cauchy (1.22)) and a Jacobian at fixed instant t^0, $\mathbf{J} = R'(t^0, W^0)$, Rosenbrock-Wanner (ROW) [67] methods are obtained:

$$\begin{cases} \left[I - \gamma\Delta t\mathbf{J}\right]k_i = R(t^n + c_i\Delta t, W^n + \sum_{j=1}^{i-1} a_{ij}k_j) + \Delta t\mathbf{J}\sum_{j=1}^{i-1}\gamma_{ij}k_j,\ i = 1, ..., s \\ \qquad W^{n+1} = W^n + \Delta t\sum_{i=1}^{s} b_i k_i, \end{cases} \tag{4.51}$$

also called semi-implicit Runge-Kutta methods.

4.4.3 Stability Properties

By applying the Rosenbrock method to Dahlquist test problem (2.5), the stability function $G(z)$ associated is:

$$G(z) = 1 + zb^T(\mathbf{I} - z\mathbf{A})^{-1}e, \tag{4.52}$$

where $b^T = (b_1, ..., b_s)$, $\mathbf{A} = (a_{ij} + \gamma_{ij})_{i,j=1,...,s}$ and $e = (1, ..., 1)^T$. Since the matrix $\mathbf{A}$ is a lower-triangular matrix the stability function is equal to the DIRK one presented previously in Sec. 4.3.3. Hence stability conditions are equivalent.

4.5 Conclusion on Implicit Time Integration

In this chapter several implicit time integrators were introduced. They are very efficient for simulating attached boundary layers and quasi-steady flows. It appears that they are interesting for the computation of stiff physics since many of these time integrators are A-stable or L-stable. The main issue of implicit time integrators is their large computational cost compared to the explicit methods, due to resolution of linear system (resolution of linear system in **FLUSEPA**© is ensure by GMRES/QR method [68, 69, 70]). However, it is important to note that explicit integrators are more interesting for calculating unsteady phenomena such as shocks and acoustic waves. Whatever the strengths and the weaknesses of the two types of conventional approaches, hybridation of these schemes was an important subject of research. In the following, several hybrid schemes will be presented. Any hybrid scheme tends to solve problems with stiff and non-stiff phenomena with the most appropriate scheme (explicit or implicit or both)

5 Hybrid Explicit-Implicit Methods

Numerous studies have been conducted to couple the RANS and LES techniques in order to capture the higher energy scales in isotropic and fine cell areas with the LES paradigm and to carry out RANS modeling elsewhere, in quasi-steady zones allowing more cells stretched. Depending on the behavior of physics (stiff or non-stiff phenomena), time integrators of explicit or implicit nature are more appropriate. It appears that implicit time integrators are suitable for stiff terms, while explicit time integrators can be preferred for non-stiff terms. Taking the specific example of the reactive Navier-Stokes equations, it can be of strong interest to couple explicit and implicit time integrators. Several techniques can be considered. One can apply a specific time integration scheme on the different parts of the equation residual. Another approach consists in blending the schemes according to the local stiffness of the physics.

5.1 Additive Runge-Kutta Methods

5.1.1 Principle

Additive Runge-Kutta methods (ARK_N) [71] allow to use several time integrators for updating the solution of the Cauchy problem (1.22): convection, diffusion and chemical reaction terms can be time-integrated with their own schemes. The schemes are then rolled in an individual method for the time integration of the full equation. The global scheme that blends several contributions associated with the partition of the residual according to the stiffness of the physics is called an additive method. Among the possible schemes, Runge-Kutta's scheme are the preferred technique since their design is straightforward and in addition, the definition of a stable high-order method is quite simple.

5.1.2 Formulation

A N-additive Runge-Kutta scheme (ARK_N) is used to solve equations of the form:

$$\frac{dW}{dt} = R(t, W(t)) = \sum_{\nu=1}^{N} R^{[\nu]}(t, W(t)) \tag{5.1}$$

where the residual $R(t, W(t))$ is composed of N terms, each of these having its own stiffness. The system can also be represented by Cauchy's problem as follows:

$$\begin{cases} W'(t) = \sum_{\nu=1}^{N} R^{[\nu]}(t, W(t)) \\ W(0) = W^0 \\ \text{Suitable boundary conditions} \end{cases} \tag{5.2}$$

Remark: It must be highlighted that the set of equations is no longer purely hyperbolic and suitable boundary conditions must be defined on the boundary.

The associated ARK_N algorithm is simply:

$$\begin{cases} W^0 \text{ known} \\ k_i^{[\nu]} = R^{[\nu]}(t^n + c_i^{[\nu]}\Delta t, W^n + \sum_{j=1}^{i} a_{ij}^{[\nu]} k_j^{[\nu]}) \ , i = 1, ...s \\ W^{n+1} = W^n + \Delta t \sum_{\nu=1}^{N} \sum_{i=1}^{s} b_i^{[\nu]} k_i^{[\nu]}. \end{cases} \tag{5.3}$$

Each term is integrated with its own s-stage Runge-Kutta method. Nevertheless, the respective Butcher coefficients $a_{ij}^{[\nu]}$, $b_i^{[\nu]}$, and $c_i^{[\nu]}$, $\nu = 1, 2, ..., N$ are constrained by the required order of accuracy and by stability considerations.

5.1.3 Stability Properties

The stability function of the ARK_N method is obtained on the linear test equation that looks like the Dahlquist equation (2.5):

$$W' = \sum_{\nu=1}^{N} \lambda^{[\nu]} W. \tag{5.4}$$

This means that the Dahlquist test equation (2.5) is performed for all parts of the residual. The associated stability function is then such as:

$$\begin{aligned} G(z^{[1]}, ..., z^{[N]}) &= \frac{P(z^{[1]}, ..., z^{[N]})}{H(z^{[1]}, ..., z^{[N]})}, \\ &= \frac{det\left[\mathbf{I} - \sum_{\nu=1}^{N}(z^{[\nu]}\mathbf{A}^{[\nu]}) + \sum_{\nu=1}^{N}(z^{[\nu]} e \otimes b^{[\nu]T})\right]}{det\left[\mathbf{I} - \sum_{\nu=1}^{N}(z^{[\nu]}\mathbf{A}^{[\nu]})\right]}, \end{aligned} \tag{5.5}$$

with $\mathbf{A}^{[\nu]} = a_{ij}^{[\nu]}$, $b^{[\nu]} = b_i^{[\nu]}$, $z^{[\nu]} = \lambda^{[\nu]}\Delta t$.

For instance, switching back to the reactive Navier-Stokes equations, the associated Dalhquist equation is:

$$\frac{dW}{dt} = \lambda^C W + \lambda^D W + \lambda^R W, \tag{5.6}$$

where

- $z^C = \lambda^C(\Delta t)$ reflects the eigenvalue associated with **convection**. This term is predominately *imaginary*,
- $z^D = \lambda^D(\Delta t)$ reflects the eigenvalue associated with **diffusion**. This term is predominately *real*,
- $z^R = \lambda^R(\Delta t)$ reflects the eigenvalues associated with **chemical reaction**. This term is mostly *real* and may be large value.

If the stability domain of the full integrator contains all values of z^C, z^D and z^R then it is stable.

5.2 IMEX Scheme (IMplicit-EXplicit Scheme)

5.2.1 Principle

The Implicit-Explicit (IMEX) scheme should be compared to ARK_2 scheme since this method also uses a partitioning of the residual into two distinct parts, a stiff one and a non-stiff one.

IMEX scheme have been widely used for the time integration of spatially discretised PDEs of diffusion-convection type. Usually an implicit scheme is used for the diffusion term (linear and stiff operator) and an explicit scheme is used for the convection term (non-linear and non-stiff operator).

5.2.2 Formulation

An IMEX scheme solves an equation of the form:

$$\frac{dW}{dt} = R(t, W(t)) = f(t, W(t)) + g(t, W(t)) \tag{5.7}$$

with $f(W)$ the non-linear term which has to be time-integrated by an explicit scheme and $g(W)$ the linear term which has to be time-integrated by an implicit scheme. Of course, an IMEX scheme is defined uniquely by the set of explicit and implicit integrators.

In a first step, the IMEX formulation can be defined from a general linear multi-step method: it is possible to apply a s-step IMEX scheme to Eq. (5.7) with $s \geq 1$. The scheme may be written as:

$$\frac{1}{\Delta t} W^{n+1} + \frac{1}{\Delta t} \sum_{j=0}^{s-1} a_j W^{n-j} = \sum_{j=0}^{s-1} b_j f(t^{n-j}, W^{n-j}) + \sum_{j=-1}^{s-1} c_j g(t^{n-j}, W^{n-j}), \tag{5.8}$$

where $c_{-1} \neq 0$ (see [72] for some stability and convergence results).

Considering specifically Eq. (5.7), one of the most popular IMEX scheme [73] is defined as a combination of the second order accurate Adams-Bashforth (explicit scheme) for the convection term and the Crank-Nicolson's implicit scheme for the diffusion term:

$$\frac{W^{n+1} - W^n}{\Delta t} = \frac{3}{2} f(t^n, W^n) - \frac{1}{2} f(t^{n-1}, W^{n-1}) + \frac{1}{2} \left(g(t^{n+1}, W^{n+1}) + g(t^n, W^n) \right) \tag{5.9}$$

The linear scheme presented below is a LM-based IMEX scheme. However, such scheme tends to have an undesirable time-step restriction for convection-diffusion problems.

The use of Runge-Kutta's schemes for the explicit part of the IMEX scheme was developped to take advantage of the great stability characteristics of Runge-Kutta's schemes. In the following, an implicit Runge-Kutta scheme is defined with parameters c_i, a_{ij} and b_j and its associated explicit Runge-Kutta scheme (in the IMEX framework) is defined with parameters $\widehat{c}_i$, $\widehat{a}_{ij}$ and $\widehat{b}_j$. For any time integration performed with a s-stage Runge-Kutta IMEX scheme, the first stage is always explicit and the remaining stages are pairwise implicit/explicit. The solution at time step $n+1$ is then a linear combination of the stages of both schemes. The method can be summarised as:

$\widehat{k}_1 = f(t^n, W^n)$
$k_1 = g(t^n, W^n)$
for $i = 2, s$ **do**
  $W^{[i]} = W^n + \Delta t \sum_{j=1}^{i} a_{ij} k_j + \Delta t \sum_{j=1}^{i-1} \widehat{a}_{ij} \widehat{k}_j.$
  $k_i = g(t^{[i]}, W^{[i]})$
  $\widehat{k}_{i+1} = f(t^{[i]}, W^{[i]}).$
end for
$W_{n+1} = W_n + \Delta t \sum_{j=1}^{s} b_j k_j + \Delta t \sum_{j=1}^{s+1} \widehat{b}_j \widehat{k}_j.$

It is important to notice that any of the s terms $k_i = g(t^{[i]}, W^{[i]})$ reflects a linear system to solve. A matrix-vector product needs to be computed, with the following matrix:

$$\mathbf{I} - \Delta t a_{ii} \frac{\partial g}{\partial W}. \tag{5.10}$$

5.2.3 Stability Properties

The stability analysis is performed following the same approach as for the ARK_N method, which leads to:

$$W' = \lambda^{[E]} W + \lambda^{[I]} W \tag{5.11}$$

and the resulting stability function is:

$$G(z^{[E]}, z^{[I]}) = \frac{det\left[\mathbf{I} - z^{[E]}\widehat{\mathbf{A}} - z^{[I]}\mathbf{A} + z^{[E]} e \otimes \widehat{b}^T + z^{[I]} e \otimes b^T\right]}{det\left[\mathbf{I} - z^{[E]}\widehat{\mathbf{A}} - z^{[I]}\mathbf{A}\right]} \tag{5.12}$$

As it should be expected, ARK_N and IMEX scheme have a stability function that depends on the respective stability functions of both explicit and implicit schemes considered in the definition of the full scheme. As mentioned previously, problems with several stiff terms remain difficult for the time integration. It appears that partitioning the problem in several time integrators (ARK_N, IMEX, etc) may be a solution.

But for some application, the performance of standard IMEX schemes suffers. For problems written as:

$$W' = R(t, W(t)) = \mathcal{L}(W) + \mathcal{N}(W), \tag{5.13}$$

with $\mathcal{L}$ the linear differential operator and $\mathcal{N}$ the non-linear differential operator, Uri *et al.* [74] performed a stability analysis and the conclusion is crude. If $\mathcal{L}$ is a stiff operator and $\mathcal{N}$ is not stiff, the standard IMEX schemes work well. But in many applications, both terms may introduce stiffness and this is encountered in many aplications such as electrochemistry, combustion and plasma physics. So the stiffness of the term $\mathcal{N}$ treated explicitly leads to large restriction on time step size, as shown in Chap. 3. Among the possible methods than enhance explicit schemes for stiff phenomena, exponential time integrators are good solutions and Luan *et al.* [75] presented recently a preconditioned implicit exponential integrator (IMEXP) for integration of stiff PDEs that uses an exponential integrator as a preconditioner.

The proposed hybrid methods tend to compute stiff problem using a partitioning of the residual, according to the different terms in the set of equations. Hereafter, an alternative hybrid method for time integration of stiff problems involving irregular grids or penalizing local flow features will be presented. Indeed it appears that standard explicit time integrators may suffer from very small time step in cells where the CFL stability condition may be highly restrictive.

5.3 Spatial Coupling of Time Integrators

5.3.1 Principle

The simulation of unsteady flows with small-scales features needs a very refined mesh. This is particularly truth for the simulation of the boundary layer, contact discontinuity or shock waves. In this context, the very small mesh cells lead to a very small time step for the unsteady simulation using an explicit scheme, since the time step must respect the CFL condition. Many implicit schemes (especially those that are unconditionally stable) can overcome this limitation at the expense of the CPU consumption. A hybrid scheme that blends explicit and implicit time integrations can be designed in order to allow large time step while maintaining the accuracy of the explicit method. The following hybrid schemes allow to switch between explicit and implicit approach on irregular (unstructured) grid. The hybridization is based on an hybrid reconstruction in the context of the finite volume discretization.

One of the first spatial hybridization of time integrators was proposed in 1986 by Fryxell *et al.* [76]. Their hybrid implicit-explicit method is built in order to perform one-dimensional Lagrangian hydrodynamic simulations. The hybrid scheme is based on the extension of a Godunov-type scheme to the implicit regime. The framework was then extended to Euler equations with an iterative approach by Dai and Woodward [77]. Their scheme is second-order accurate in time and space but remains quite complicated to implement. This complexity is a consequence of the requirement of solving the solution by an iterative process. In addition, the authors mention that the extension to multi-dimensional systems remains an open question.

A hybrid explicit-implicit scheme for Eulerian hydrodynamics, that ensures the total variation diminishing (TVD) property at all CFL numbers for a linear equation was proposed by Collins *et al.* [78] and it is denoted CCG from now on. This hybrid scheme allows a second order of accuracy in space and time on pure explicit mesh cells.

5.3.2 Formulation

CCG Scheme

For the linear advection equation in one dimension Eq. (1.23), the CCG scheme allows to compute W^{n+1} using a predictor-corrector formulation:

$$W_i^{n+1} = W_i^n - \frac{c\Delta t}{\Delta x_i}\left[W_{i+1/2} - W_{i-1/2}\right] \tag{5.14}$$

where state $W_{i+1/2}$ is calculated by use of different intervals of interpolation according to the value of the local CFL number (r_i), such as :

$$W_{i+1/2} = \begin{cases} W_i^n + \dfrac{1}{2}(1-r_i)(\nabla W)_i^n & \text{for } r_i \leq 1 \\ \dfrac{1}{r_i}W_i^n + \dfrac{(1-r_i)}{r_i}(\nabla W)_i^{n+1} & \text{for } r_i > 1 \end{cases} \tag{5.15}$$

with $r_i = \frac{a\Delta t}{\Delta x_i}$ and $(\nabla W)_i^n$ a finite difference approximation of $\partial W/\partial x \mid_{(x_i,t_n)}$. Unfortunately, the CCG scheme can lead to an incorrect numerical solution since it fails to maintain the TVD property for nonlinear equations. Men'shov and Nakamura [79] proposed an enhancement of this formulation: the TVD property is maintained for non-linear hyperbolic equations.

Men'shov and Nakamura scheme

Starting from the standard one-dimensional hyperbolic equation:

$$\frac{\partial W}{\partial t} + \frac{\partial F(W)}{\partial x} = 0, \tag{5.16}$$

the hybrid scheme allows to solve Eq. (5.16) discretized as:

$$W_i^{n+1} = W_i^n - \frac{\Delta t}{\Delta x_i}\left[F_{i+1/2} - F_{i-1/2}\right] \tag{5.17}$$

with $F_{i+1/2}$ a standard numerical flux at the interface $i+1/2$ associated with the function F that solves the Riemann problem using the reconstructed variables $W^L_{i+1/2}$ and $W^R_{i+1/2}$ as input arguments. Any scheme to solve the Riemann problem is a natural choice and in this context, all explanations are dedicated to the Harten, Lax, van Leer (HLL) scheme [80]:

$$F(W_1, W_2) = \frac{\left[s^+_{\frac{1}{2}} f_1 - s^-_{\frac{1}{2}} f_2 + s^+_{\frac{1}{2}} s^-_{\frac{1}{2}}(W_2 - W_1)\right]}{s^+_{\frac{1}{2}} - s^-_{\frac{1}{2}}} \tag{5.18}$$

with $f_k = f(W_k)$, $k = 1, 2$ and the numerical wave speeds $(s^+_{\frac{1}{2}}, s^-_{\frac{1}{2}})$ expressed such as:

$$\begin{aligned} s^+_{\frac{1}{2}} &= max(0, a_1, a_2) \\ s^-_{\frac{1}{2}} &= min(0, a_1, a_2) \end{aligned} \tag{5.19}$$

with $a_{1,2}$ the theoretical wave speeds of the hyperbolic equation. Then the interface variables are evaluated such as:

$$\begin{aligned} W^L_{i+1/2} &= W^\omega_i + \frac{1-\omega_i\beta^n_i}{2}(\nabla W)^n_i \\ W^R_{i+1/2} &= W^\omega_{i+1} + \frac{1+\omega_{i+1}\beta^n_{i+1}}{2}(\nabla W)^n_{i+1} \end{aligned} \tag{5.20}$$

where :

$$\beta^n_i = \frac{\Delta t}{\Delta x_i}\left(s^{+,n}_{i-\frac{1}{2}} - s^{-,n}_{i+\frac{1}{2}}\right) \text{ and } W^\omega_i = \omega_i W^n_i + (1-\omega_i)W^{n+1}_i. \tag{5.21}$$

ω_i is a blending parameter such that: $0 \leq \omega_i \leq 1$. As a consequence, the flux for the hybrid scheme is evaluated by composition of two components. The first one corresponds to an implicit scheme and the other one to a second order explicit scheme. The amount of explicit to implicit contributions is controlled by the parameter ω_i. In order to compute the interfaces values, the instant t^ω is introduced such as $t^\omega = t^n + (1-\omega)\Delta t$. Roughly speaking, the scheme is now composed of two steps. First, the intermediate state W^ω is evaluated by interpolation between values at the lower and upper time levels: $W^\omega = \omega_i W^n + (1-\omega)W^{n+1}$. For the second step, the explicit scheme is computed from the instant t^ω by the use of a space reconstruction performed at t^n.

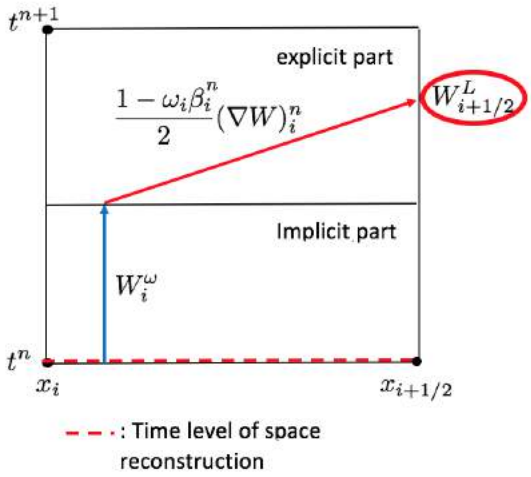

Fig. 5.1. Illustration of the hybridation principle for Men'shov and Nakamoura scheme.

Timofeev and Norouzi scheme

As said previously, this method is linearly unconditionally stable scheme with TVD property for non-linear case, and it could be extended to multidimensional unsteady compressible case. But the switching procedure of CCG and Men'shov and Nakamura schemes (from explicit to implicit and *vice versa*) cannot maintain a second order of accuracy in space and time over the whole computational domain. Timofeev and Norouzi [81] overcame this difficulty by

blending second-order accurate schemes (in space and time) for explicit, implicit and hybrid cells using a smooth parameter to couple the considered time integrators. Their method is one of the most advanced one since it maintains TVD properties. The hybrid scheme [81] denoted TN in the following, is applied to the Cauchy problem Eq. (1.22) and is defined through a predictor-corrector formulation:

$$\begin{cases} \text{Predictor step:} & \widehat{W}_j = W_j^n + \omega_j \Delta t R(W_j^n) \\ \text{Corrector step:} & W_j^{n+1} = W_j^n + \dfrac{\Delta t}{|\Omega_j|}(F_{j+\frac{1}{2}}^{Hybrid} - F_{j-\frac{1}{2}}^{Hybrid}) \end{cases} \quad \text{for } 0 \leq \omega_j \leq 1. \tag{5.22}$$

In the following a face f will be considered, with the face center C_f, separating two cells, i and j, with respectively cell centers C_i and C_j.

Here the predicted state is performed thanks to a residual computed without any Riemann solver, and $\widehat{W}_j$ is computed using a fully upwind scheme. So, the reconstruction state W_j^f in the flux $F(W_j^f)$ involved in the computation of the residual $R(W_j^n)$ of the cell j is computed by $W_j^f = W_j^n + (\widetilde{\nabla W})_j^n \cdot \overrightarrow{C_j C_f}$. As a consequence, the predictor step is not conservative. Furthermore, the gradient $\widetilde{\nabla W}$ is computed thanks to the standard gradient ∇W and a slope limiter.

At the corrector step, for any cell j, the hybrid flux F^{Hybrid} is computed using a (approximated) Riemann solver with the following reconstructed left and right states on a face:

$$\begin{aligned} W^L = \quad & \omega_j \left[\frac{W_j^n + \widehat{W}_j}{2} + (\widetilde{\nabla W})_j^n \cdot \overrightarrow{C_j C_f}\right] + \\ & (1-\omega_j) \left[W_j^{n+1} + (\widetilde{\nabla W})_j^{n+1} \cdot \overrightarrow{C_j C_f} - \frac{1-\omega_j}{2}(\widetilde{\Delta_t W})_j^{n+1}\right], \\ W^R = \quad & \omega_i \left[\frac{W_i^n + \widehat{W}_i}{2} + (\widetilde{\nabla W})_i^n \cdot \overrightarrow{C_i C_f}\right] + \\ & (1-\omega_i) \left[W_i^{n+1} + (\widetilde{\nabla W})_i^{n+1} \cdot \overrightarrow{C_i C_f} - \frac{1-\omega_i}{2}(\widetilde{\Delta_t W})_i^{n+1}\right]. \end{aligned} \tag{5.23}$$

In the specific case of the one-dimensional advection equation Eq. (1.23), the interfaces variables can be defined as:

$$\begin{aligned} W_{i+1/2}^L &= W_i^\omega - \frac{1-\omega_i}{2}(\widetilde{\Delta_t W})_i^{n+1} + \frac{1-\omega_i \nu_i}{2}(\nabla W)_i^\omega, \\ W_{i+1/2}^R &= W_{i+1}^\omega - \frac{1-\omega_{i+1}}{2}(\widetilde{\Delta_t W})_{i+1}^{n+1} + \frac{1+\omega_{i+1}\nu_{i+1}}{2}(\nabla W)_{i+1}^\omega, \end{aligned} \tag{5.24}$$

with $\nu_j = \frac{c_j \Delta t}{h_j}$. In Eq. 5.24, the term $\widetilde{\Delta_t W}$ plays the role of a time slope limiterand this is the main improvement of the TN scheme over the one of Men'shov and Nakamura. All details regarding this specific term and the proof of the TVD property are provided in thesis of Norouzy [82]. Furthermore, the space reconstruction ∇W is evaluated at instant t^ω instead of t^n (see Fig. 5.2).

The hybrid parameter ω_j, subsequently named cell status, is defined for each cell j such that $0 \leq \omega_j \leq 1$. It is used to switch smoothly from an explicit ($\omega_j = 1$) to an implicit ($\omega_j = 0$) time integration. And for $0 < \omega_j < 1$ the residual is computed thanks to the states at instant t^n and t^{n+1}. For numerical application, the cell status ω_j is locally adapted thanks to the flow and the stability constraint.

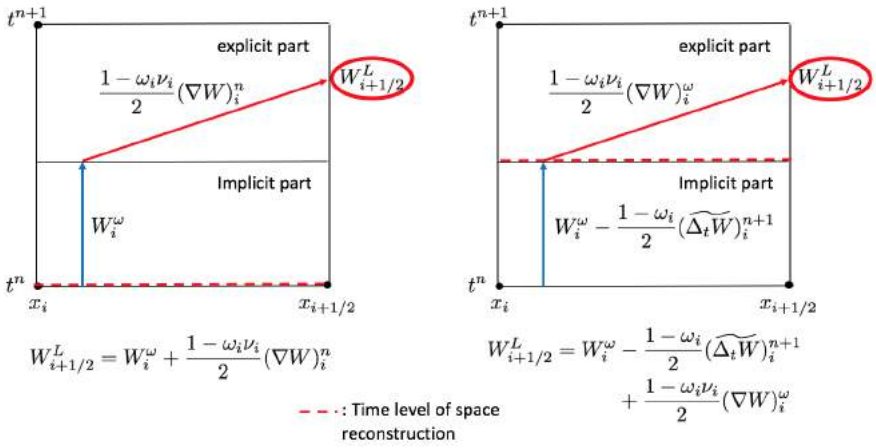

Fig. 5.2. Comparaison of hybridation principle for Men'shov and Nakmoura scheme (left) and Timofeev Narouzy scheme (right).

Definition of Additional Time Variables

First of all, the maximum global time step allowable according to the part $\mathcal{D}$ of the domain without source of stiffness is computed as:

$$\Delta t = \min_{j\in\mathcal{D}} \hat{v}\frac{h_j}{c_j}, \tag{5.25}$$

where $\hat{v} < 1$ plays the role of CFL number for the part of the computational domain where the scheme is explicit, h_j is a reference length scale and c_j is the largest wave speed associated with the hyperbolic equations in cell j. Then, the parameter ω_j is defined as:

$$\omega_j = \min\left(1, \frac{1}{\nu_j}\right). \tag{5.26}$$

In Eq. (5.23), the term $(\widetilde{\Delta_t W})_j^{n+1}$ represents the main inprovement of the formulation since it leads to the TVD property to the coupled space/time reconstruction. In practice, this term is given by Newton's algorithm which at any step s reads:

$$(\widetilde{\Delta_t W})_j^{n+1,s} = \begin{cases} \max\left[0, \min\left(\min_j[\beta(W_j^{n+1,s} - W_j^n) + (\widetilde{\Delta_t W})_j^{n+1,s-1}], W_j^{n+1,s} - W_j^n\right)\right] \\ \qquad\qquad \text{if } W_j^{n+1,s} - W_j^n \geq 0, \\ \min\left[0, \max\left(\max_j[\beta(W_j^{n+1,s} - W_j^n) + (\widetilde{\Delta_t W})_j^{n+1,s-1}], W_j^{n+1,s} - W_j^n\right)\right] \\ \qquad\qquad \text{if } W_j^{n+1,s} - W_j^n < 0. \end{cases} \tag{5.27}$$

The parameter β is computed from the local CFL number ν_j and ω_j at each step s:

$$\beta = \frac{2\left(1 - \omega_j^s\nu_j^s(2 - \omega_j^s\nu_j^s)\right)}{\nu_j^2(1-\omega_i^s)^2} \tag{5.28}$$

This method provides a second-order accuracy in space and time in full explicit, full implicit and hybrid explicit-implicit parts.

Remark: The key ingredient is for sure the time-limited reconstruction. To our knowledge, the number of studies on this specific point is really limited and an additional work should focus on improving the treatment while maintaining the TVD property.

This last hybrid scheme was extended to the two-dimensional case for Euler equations by Norouzy [81]. In 2006, second order accurate explicit and implicit time integrators were hybridized by Tóth *et al.* [83] and coupled with an adaptive mesh refinement (AMR) strategy for three-dimensional applications in magnetohydrodynamics using structured grids. The procedure is quite complex to implement and needs to blend the first and second order fluxes on the interfaces. In 2017, May and Berger [84] proposed a method to switch between explicit and implicit approaches called *flux bounding*. The coupling of explicit and implicit schemes is performed by the coupling of explicit and implicit flux contributions on the interface in the context of finite volume discretisation procedure.

5.4 Flux Bounding Method

5.4.1 Principle

The flux bounding technique is another way to couple spatially explicit and implicit time integrators and of course, this kind of approach is not based on the splitting of the residual term, as in the IMEX framework. The flux bounding method was introduced recently by May [84].

The principle is to split the mesh into 3 parts according to the way the interface flux is computed. In the first one, explicit time integration is performed on all interfaces of the cells. In the second one, an implicit time integration is performed on all the interfaces of the cells. Of course, in the finite volume framework, there are some volumes for which some fluxes are computed using an explicit formulation and other with an implicit formulation. These cells are in the third part of the mesh. This part of the mesh is called the transition part in the following.

5.4.2 Formulation

For the linear advection equation in one dimension (1.23), both explicit and implicit Euler schemes will be used to integrate the solution. All explanations will follow the test case defined in Fig. 5.3. it is important to remark that cell 0 is the smallest one, leading to the strongest CFL condition. As a consequence, it will be integrated implicitly in time. Cells -1 and 1 will be considered as transition cells and the rest of the mesh will be integrated explicitly.

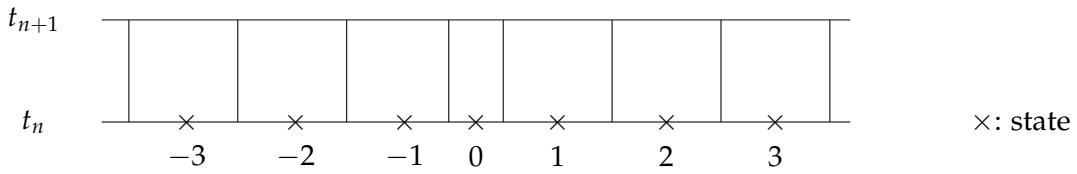

Fig. 5.3. Scheme of the computation of Flux bounding method (1/3).

The $\times$ symbol represents the state at instant t_n. In order to integrate each state at instant t_{n+1}, the explicit part will be integrated first because the whole necessary information to update the solution at time t_{n+1} is available at the time instant t_n. Here a finite volume formulation with flux reconstruction is used:

$$W_i^{n+1} = W_i^n - \frac{\Delta t}{\Delta x_i}\left[F_{i+1/2} - F_{i-1/2}\right] \tag{5.29}$$

with $F_{i+1/2}$ the flux through the border $i + 1/2$:

$$F_{i+1/2} = F(W_{i+1/2}^L, W_{i+1/2}^R). \tag{5.30}$$

It can be computed at the second order using the standard MUSCL reconstruction and a slope limiter. In the following, F^E will represent any flux computed with states at instant t^n and F^I will represent a flux computed with the state at instant t^{n+1} (Fig. 5.4).

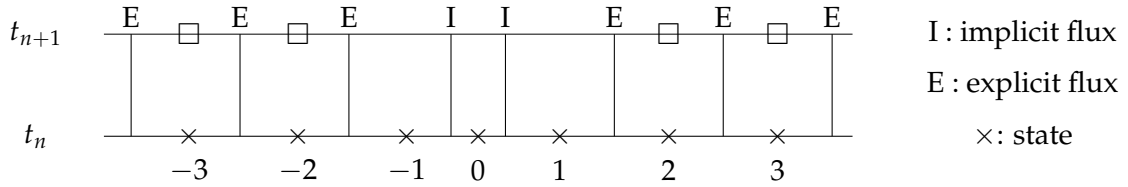

Fig. 5.4. Scheme of the computation of Flux bounding method (2/3).

As shown in Fig. 5.4, the explicit cells are time integrated to t^{n+1} but the process cannot be performed for implicit and transition cells. In this context, the time integration for cells -1, 0 and 1 is:

$$\begin{aligned} W_{-1}^{n+1} &= W_{-1}^{n} - \frac{\Delta t}{\Delta x}\left[F_{-1/2}^{I} - F_{-3/2}^{E}\right] \\ W_{0}^{n+1} &= W_{0}^{n} - \frac{\Delta t}{\alpha \Delta x}\left[F_{1/2}^{I} - F_{-1/2}^{I}\right] \\ W_{1}^{n+1} &= W_{1}^{n} - \frac{\Delta t}{\Delta x}\left[F_{3/2}^{I} - F_{1/2}^{E}\right] \end{aligned} \tag{5.31}$$

Finally, it is possible to time integrate the transient and the implicit cells until time instant t_{n+1} (see Fig. 5.5) by the standard rules for the implicit fluxes F^I.

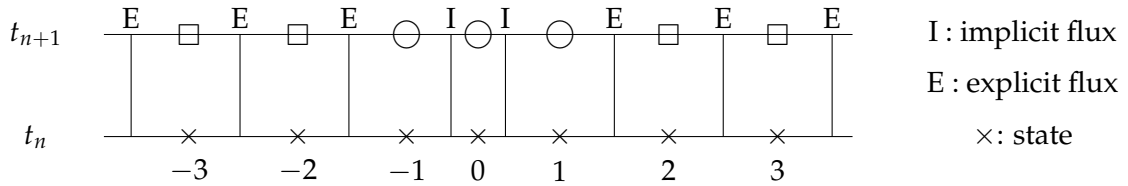

Fig. 5.5. Scheme of the computation of Flux bounding method (3/3).

The advantage of such method is to keep the TVD property. In addition, the procedure can be easily adapted to any multidimensional mesh. Such a method also allows to couple second order implicit and explicit schemes, such as Heun's (explicit) scheme and IRK2 (implicit) scheme. The key point is not time integration: it is the space reconstruction of the quantities in order to enable a MUSCL reconstruction coupled with a limiter. Unfortunately, it can be shown that the hybrid cells are not second-order accurate in time and the coupling procedure cannot maintain the accuracy of the initial explicit and implicit time integrators.

5.5 Conclusion on Hybrid Time Integration

A hybrid scheme as the one of Timofeev and Norouzi allows to blend spatially explicit and implicit time integrators. This family of schemes allows to recover the spectral properties of the explicit scheme in the explicit part of the mesh. This can be an advantage for the transport of unsteady physics since accuracy and spectral properties are easier to control with an explicit time integrator. In addition, a stiff phenomenon could be time-integrated with the implicit scheme, taking advantage of the good stability properties of implicit schemes.

In the next chapter, our attention will be beared on a method that overcomes limitation of explicit time integration for stiffness by use of a local time stepping approach.

6 Temporal Adaptive Method

One of the important ingredients of **FLUSEPA**© is the k-exact reconstruction that is applied to the computation of any term in any of the schemes. In particular, the reconstruction is necessary to increase the accuracy of the convection term and gives interface gradients for the diffusion flux. In addition, it also gives accurate cell centred gradients for the chemistry source terms. Although a particular attention has been paid to space discretisation schemes for accurately capturing unsteady phenomena, another source of improvement has been the implementation of an optimized time integration process. Actually, the k-exact reconstruction can be applied to any kind of mesh cell, and an adaptive mesh refinement allows a better capture of the physics. Without entering into details, an adaptive mesh refinement was applied to many problems in the past and the literature review of this method is out of the scope of the present PhD thesis. One must keep in mind that adaptive mesh refinement can easily be applied to Cartesian grids, allowing a local mesh refinement. The same kind of approach is available in **FLUSEPA**© and has been adapted to unstructured grids. While this process of adaptation is generally limited to spatial dimensions, it is interesting to extend the treatment to the temporal scheme, especially for the computation of unsteady flows. In the latter case, the spatial adaptation leads to very small cells that can lead to a large decrease of the maximum stable time step allowed. If a global time step approach is retained, it results that time integration of the biggest cells is performed by a fraction of the maximal allowable time step and this leads to useless computational costs. In this context, a time-adaptive scheme can help in reducing the CPU cost of the adaptive mesh refinement (AMR) algorithm.

Brenner [2] developed in **FLUSEPA**© an algorithm that allows to time integrate each cell of the mesh with its maximum time step allowable. This kind of method is named a time-adaptive scheme. The principle of time-adaptive schemes is to time-integrate the solution in each cell using its own time step according to the local CFL condition. Sub-cycling is used to time integrated smallest cells until the time step of the biggest ones. It appears that one of the main difficulty lies in the treatment of the boundary condition at the interface between a given grid refinement and a finer one.

A one-dimensional temporal adaptive algorithm was proposed by Sanders and Osher [85], leading to a first-order time accurate method applied to a scalar equation. Later on, the extension of the procedure to multi-dimensional problems was performed by Dawson [86]. Both papers used the same procedure in order to allow time synchronisation between cells time integrated with their own time step between t^n and t^{n+1}. In order to keep space-time conservation, the sum of fluxes on small cells is equal to the one of the larger cells at the interface between cells of different sizes. Nevertheless, this method leads to a first-order accurate reconstruction. Dawson and Kirby [87] proposed an extension to the second order of accuracy. They extended the procedure by means of Total Variation Diminishing (TVD) property. Constantinescu and Sandu [88] developed a set of Runge-Kutta integrators called Partitioned Runge-Kutta. The interest of these methods is their ability to be adapted to automatic mesh refinement and respect strong mathematical properties (Strong Stability Preserving). Later on, the same authors extended their procedure to the famous explicit Adams scheme [89].

Berger and Oliger [90] and Berger and Colella [91] proposed a different approach for both space and time refinements. Starting with the initial grid level indexed $l = 0$, several grid

levels $l = 1$,..., $l = l_{max}$ are introduced by local refinement (see Fig. 6.1). Here, ghost cells are introduced at the level l. For transferring information from coarse to fine grids, the values inside ghost cells are interpolated from the coarse grid $l - 1$. It must be noticed that these ghost cells can be considered on boundary conditions or inside the computational domain. The time integration remains the same in almost the whole domain which is the principal interest of such method. Indeed its implementation remains simple.

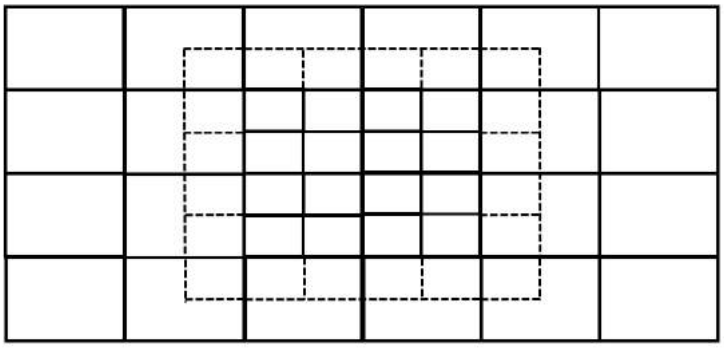

Fig. 6.1. Two grids of different level, dotted cells correspond to ghost cells for the finest grid.

Grids are considered by means of time classes, they are time integrated according to their level, starting from a coarse grid ($l = 0$) and finishing by the most refined level ($l = l_{max}$). On each grid level, the following steps are considered:

- time integrate cells of level l with local time step (Δt_l). If $l > 0$ the boundary information is collected from the next coarser level $l - 1$ by interpolation of the flux.
- synchronise cells of levels l and $l + 1$ and interpolate correction to finest cells (of level $[l + 2, ..., l_{max}]$).

According to such adaptive procedure, grids are time integrated according to their own time steps and the more the grids are refined the more they need time integration steps. The time synchronization is a correction step that allows consistency over the whole domain. Unfortunately, synchronisation and interpolation (for instance to fill ghost-cells) involve a loss of order of accuracy and conservation. Indeed there are several ways to define the computation of the flux on inter-level faces (see Fig. 6.2) and most of the time, the procedure is not conservative. Indeed, following Fig. 6.2, the ghost cell j_α allows to compute the flux $F(W_{j_\alpha}, W_k)$ for the cell k but, unfortunately, $F(W_{j_\alpha}, W_k) \neq F(W_k, W_j)$.

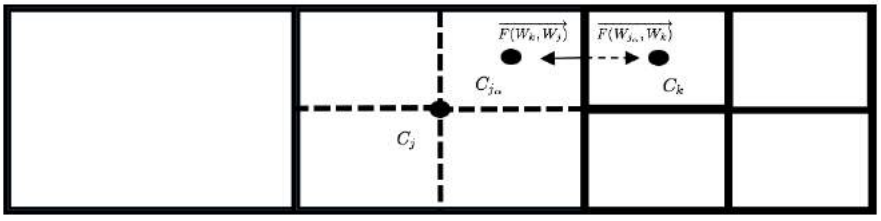

Fig. 6.2. Example of inter-level flux conservation issue.

Many methods were developed in order to limit the impact on the resulting loss of accuracy. A correction on the state W thanks to a passive scalar was introduced by Bell *et al.* [92]. According to the authors, this correction allows a fast convergence for quasi-steady state but the conservation of flux is not guaranteed and the errors on state are not reduced. Another

correction applied by Bell in [93] seen as a kind of "fixed" Dirichlet boundary condition involves unfortunately an inconsistency at the interface between grid levels.

The method implemented in **FLUSEPA**© is based on principles introduced by Kleb *et al.* [94]. They proposed a local time integration according to temporal classes. Indeed cells are ranked according to their maximum time step. The work in [94] is based on the explicit Euler time integration, leading to a first-order time accurate solution. Brenner [95] extended the method to second-order time accuracy thanks to the predictor-corrector formulation of Heun's scheme and it is designed in order to maintain time accuracy on a finite volume formulation. Krivodonova [96] uses an equivalent temporal adaptive scheme with the discontinuous Galerkin method [97] as Liu *et al.* in [98, 99] where a p-stage RK scheme is designed for non-uniform time step approach with high order spatial scheme.

The time-adaptive procedure proposed by Brenner and implemented in **FLUSEPA**© is used today for all industrial applications but the scheme was not fully described and was not analysed in details. The goal of the present chapter is to explain the adaptive time integration procedure and to give its main mathematical properties.

6.1 Temporal Adaptive

6.1.1 Principle

As presented previously the time adaptation procedure available in the **FLUSEPA**© is an extension to the method proposed by Kleb *et al.* [94]. The local time adaptive explicit Euler scheme proposed by Kleb *et al.* [94] is first-order accurate in time. The extension presented in [2] is based on Heun's integrator which is second-order accurate in time.

According to Kleb *et al.* [94], the local time step of each cell j is computed $\Delta\tau_j = \mathrm{CFL}\frac{h_j}{\|\vec{v}_j\|+c_j}$ where h_j is a reference length scale, $\vec{v}_j$ the velocity vector and c_j the speed of sound in cell j. Of course, this kind of relation is typically encountered for Euler flows and can be adapted for another kind of equations. The minimum value of the local time step, Δt_{min}, enables the definition of the time class of rank K, computed with

$$K = \left\lfloor \frac{\ln\left(\frac{\Delta\tau_j}{\Delta t_{min}}\right)}{\ln(2)} \right\rfloor, \tag{6.1}$$

from which the time step of the class denoted K is deduced:

$$\Delta t_K = 2^K \Delta t_{min}. \tag{6.2}$$

From Eq. (6.2), it is clear that the class of rank 0 is associated with the time step Δt_{min}.

Therefore the resulting higher ranked temporal classes are time integrated with associated time steps equal to $2\Delta t_{min}$, $4\Delta t_{min}$ and so on. In order to obtain time synchronisation, cells of class K must be time integrated one more time compared with cells of class $K+1$. Then cells of class 0 are time integrated $K_{max}+1$ times, with K_{max} the maximal level of temporal classes available.

In practice, it is also mandatory that the difference in class rank between two cells that share an interface is not greater than one. As a consequence, two adjacent cells are time integrated with the same time step (if they are in the same class) or with time steps which ratio is 2. This kind of procedure differs with the one presented in [100, 101, 102]: these methods allow to time integrated each cell of the mesh with its own maximal allowable time step.

In the following section, attention will be paid on the treatment of the flux between cells that belong to classes with different ranks since it is the key aspect to ensure time synchronisation with conservation [90, 91].

6.1.2 Update of the Solution

When two cells of different time classes share a common interface, the cell with the lower rank is iterated one more time than the cell with the higher rank. It is then mandatory to elaborate a specific treatment for computation of the flux on the interface between these two cells for time synchronisation with conservation while maintaining accuracy.

The method will be illustrated on a one-dimensional example with cells of class $K = 0$ and $K = 1$ in Fig. 6.3. The treatment is represented in the space / time framework, with space in the abscissa and time in the ordinate. The dashed lines represent the time at which the solution must be computed starting from the initial solution represented by •. The first-order time-accurate solutions using the predictor step of Heun's scheme will be represented by $\widehat{\times}$.

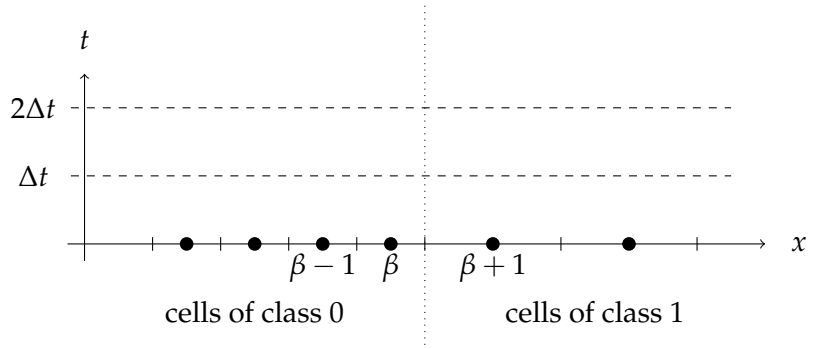

Fig. 6.3. 1D configuration consisting of a mesh composed of two classes. Initial solution is represented by the black circle. The key point will be the definition of the interface $F_{\beta+1/2}$

Starting from the initial time $t = 0$, all cells will be time integrated until $2\Delta t$, which is the time step of the class with the maximum rank, here $K = 1$, and then twice the time step of the cells with rank $K = 0$. In the following, $F_i^{k\Delta t}$ will represent the flux at the interface i (non integer index) at the time $k\Delta t$. If $k = 0$, the superscript will be simply 0. For a one-dimensional representation in the standard finite volume approximation, the local residual in cell index j is simply $R_j = F_{j+1/2} - F_{j-1/2}$.

The Heun's second-order time accurate explicit predictor-corrector scheme [40] is used. So, to reach $t = 2\Delta t$, cells with class rank 1 will undergo only two stages:

a-1. $\widehat{W}^{2\Delta t} = W^0 + 2\Delta t R(W^0)$

b-1. $W^{2\Delta t} = W^0 + \dfrac{2\Delta t}{2}\Big(R(W^0) + R(\widehat{W}^{2\Delta t})\Big)$,

but cells with class rank 0 will undergo four stages:

a-0. $\widehat{W}^{\Delta t} = W^0 + \Delta t R(W^0)$

b-0. $W^{\Delta t} = W^0 + \dfrac{\Delta t}{2}\Big(R(W^0) + R(\widehat{W}^{\Delta t})\Big)$

c-0. $\widehat{W}^{2\Delta t} = W^{\Delta t} + \Delta t R(W^{\Delta t})$

d-0. $W^{2\Delta t} = W^{\Delta t} + \dfrac{\Delta t}{2}\Big(R(W^{\Delta t}) + R(\widehat{W}^{2\Delta t})\Big)$.

• **Step 1:**

The residual $R(W^0)$ is computed using the initial solution and the predicted states are obtained for all cells (stages a-0 and b-0), as shown in Fig 6.4. For the following step of the treatment, it should be noticed that the stage b-1 needs the residual computed using $\widehat{W}^{2\Delta t}$ available only on the cells of class 1 (and not on class 0) and the stage b-0 needs the residual using $\widehat{W}^{\Delta t}$ available on the cells of class 0 (and not on class 1).

• **Step 2:**

The residual $R(\widehat{W}^{2\Delta t})$ needed by the stage b-1 is computed thanks to the predicted states on cells of rank 0 according to the required stencil to compute the interface flux (Fig. 6.5). For the

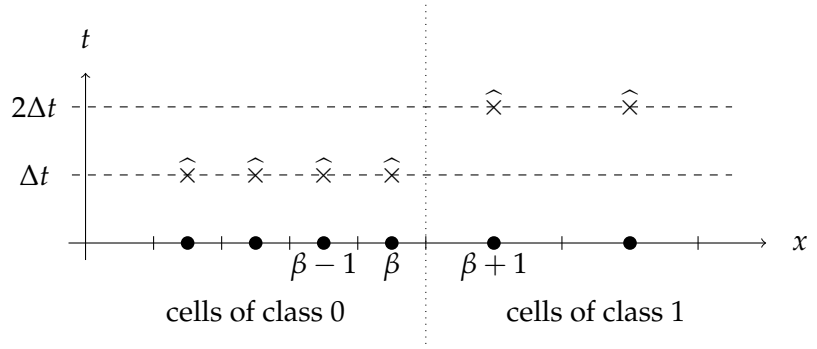

Fig. 6.4. Initial solution and predicted states using stages a-0 and b-0.

required cells with class rank 0, the estimated states are:

$$\begin{aligned} \widehat{W}_{\beta}^{2\Delta t} &= W_{\beta}^{0} + 2\Delta t R(W^{0}) \\ \widehat{W}_{\beta-1}^{2\Delta t} &= W_{\beta-1}^{0} + 2\Delta t R(W^{0}). \end{aligned} \tag{6.3}$$

These states are considered as extrapolated states since time integration until $2\Delta t$ violates the CFL stability condition for these cells ($2\Delta t$ is the time step of cells from class of rank 1).

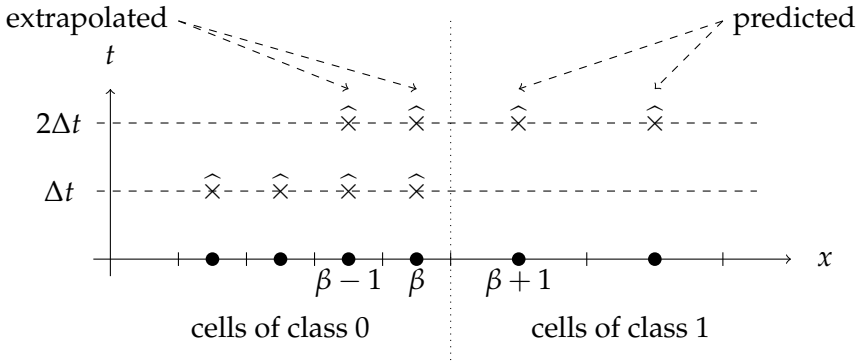

Fig. 6.5. Predicted or extrapolated states used for the computation of the flux $F_{\beta+1/2}$ t time $2\Delta t$

For cells of class rank 1, once the flux $F_{\beta+1/2}(\widehat{W}^{2\Delta t})$ is computed, the final state of stage b-1 can be computed at $t = 2\Delta t$ (Fig. 6.6).

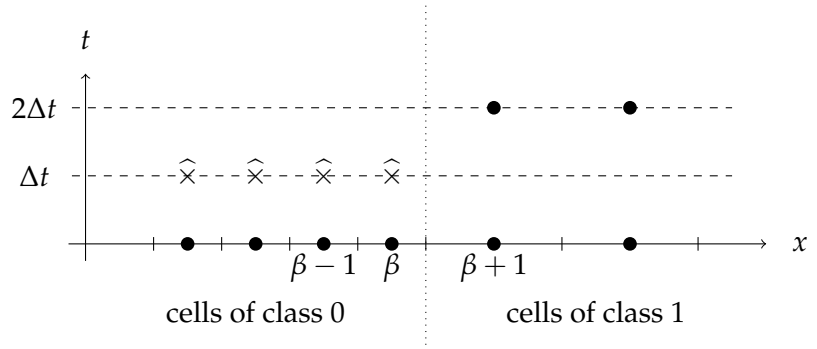

Fig. 6.6. Update of the solution for cells of class rank 1 at time $2\Delta t$

• **Step 3:**
For the cells of class rank 0 sharing a face with a cell of class rank 1, the update of the solution

associated with stage b-0 needs the definition of the flux at the interface (here identified as $\beta + 1/2$):

$$F_{\beta+1/2}(\widehat{W}^{\Delta t}) = \frac{1}{2}(F_{\beta+1/2}(W^0) + F_{\beta+1/2}(\widehat{W}^{2\Delta t})). \tag{6.4}$$

This interpolation is represented by means of arrows in Fig. 6.7.

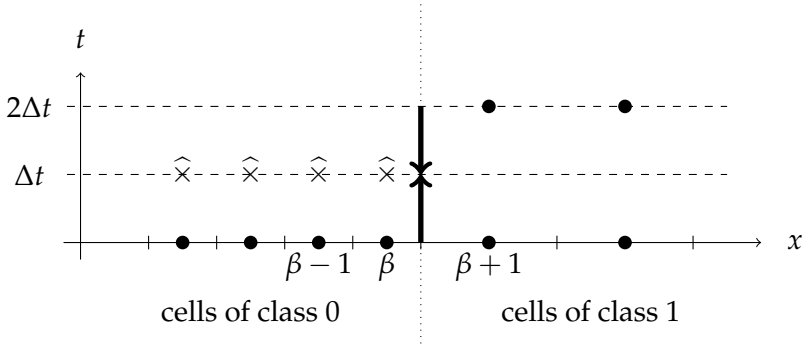

Fig. 6.7. Definition of the interpolated flux at the interface between cell classes

• **Step 4:**
The flux is directly given by Step 3 for the interface $\beta + 1/2$ but the computation of residual in cells β, $\beta - 1$,... may involve states in the cells of class 1. The number of cells in class of rank 1 involved in this treatment depends only on the stencil associated with the spatial scheme for the cells in class rank 0 (MUSCL formulation for instance). In order to compute the other corrected flux at $t = \Delta t$ for cells of class rank 0 located in the stencil of the spatial schemes (cell $\beta - 1$ for instance), it is necessary to predict the states in some cells of class rank 1 at $t = \Delta t$. A simple first-order accurate prediction would be

$$\widehat{W}^{\Delta t}_{\beta+1} = W^0_{\beta+1} + \Delta t R(W^0),$$

but in order to enforce less numerical error, a new procedure is chosen. So, the residual at time Δt is computed by a parabolic interpolation of the residual:

$$R^{\Delta t}_{\beta+1} = \frac{1}{4}R_{\beta+1}(\widehat{W}^{2\Delta t}) + \frac{3}{4}R_{\beta+1}(W^0) \tag{6.5}$$

and this residual is used to compute the predictor state at time Δt using:

$$\widehat{W}^{\Delta t}_{\beta+1} = W^0_{\beta+1} + \Delta t R^{\Delta t}_{\beta+1}. \tag{6.6}$$

The new estimated solution in cell $\beta + 1$ is represented as a predicted state in Fig. 6.8.

Using the new available predicted states, the cells of class rank 0 can be updated and the stage b-0 is completed. From now on, the variables $W^{\Delta t}$ are available for any cell of class rank 0 (Fig. 6.9). The last step is to apply stages c-0 and d-0, which consist to time integrated cells of class rank 0 from Δt to $2\Delta t$.

• **Step 5:**
Finally, to time-integrated the cells of class rank 0 from Δt to $2\Delta t$ (stages c-0 and d-0). There are two points to perform the time integration. First, it is mandatory to keep the interface flux constant for the Heun's stages: the flux computed using Eq. (6.4) is imposed to compute the residual in cell β for stages c-0 and d-0. Moreover, the high order spatial interpolation (for instance for interface $\beta - 1/2$) may need the fields in the cells of class rank 1 at time Δt. In that case, the data computed using Eq. (6.6) is kept constant for stages c-0 and d-0.

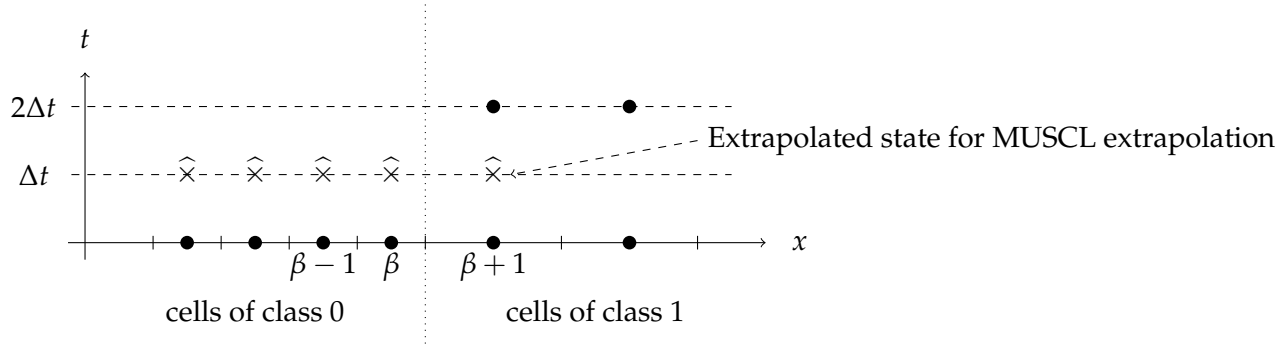

Fig. 6.8. Estimation of the states in class rank 1 for the intermediate time Δt

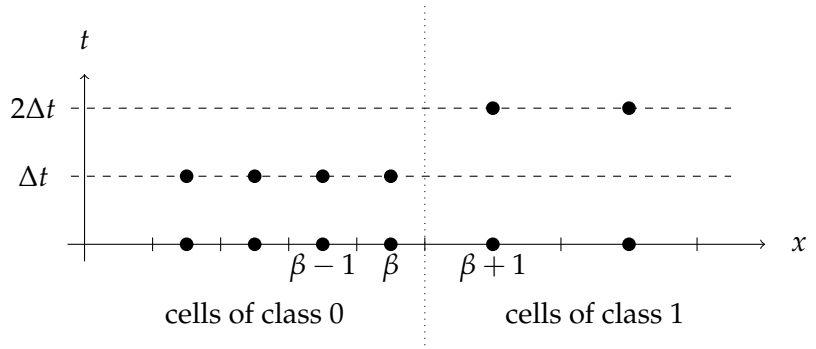

Fig. 6.9. Update of the solution of class 0 at time Δt. The states at time $2\Delta t$ for class rank 1 are available.

To conclude, thanks to the sub-cycling process, this temporal adaptation method makes it possible in a global iteration to integrate each cell with its own allowed time step. According to P.Brenner [95] for a maximal time step equal to $\Delta t_{max} = 2^K \Delta t_{min}$ and for most cells in time level K, the computational cost may be divided by 2^K in most favourable case. Then the present temporal adaptive method remains less expensive that the full explicit method.

6.1.3 Conservation Property

The main objective of the current section is the proof of conservation since it is a key ingredient for time adaptive methods. Considering an interface between cells of different temporal classes, conservation means that the time integration of the flux $F_{\beta+\frac{1}{2}}$ over the duration of $2\Delta t$ is identical for both cells around the interface indexed $\beta + \frac{1}{2}$. The demonstration will be attempted on one-dimensional configuration. According to the one-dimensional configuration presented in Sec. 6.1.2, the cell $\beta + 1$ of class rank 1 may be time integrated with predictor and corrector stages of Heun's scheme from $t = 0$ to $t = 2\Delta t$ as

$$\begin{aligned} \widehat{W}^{2\Delta t}_{\beta+1} &= W^0_{\beta+1} + \frac{2\Delta t}{\Delta x}\left(F_{\beta+\frac{3}{2}}(W^0) - F_{\beta+\frac{1}{2}}(W^0)\right) \\ W^{2\Delta t}_{\beta+1} &= W^0_{\beta+1} + \frac{2\Delta t}{2\Delta x}\left(F_{\beta+\frac{3}{2}}(\widehat{W}^{2\Delta t}) + F_{\beta+\frac{3}{2}}(W^0) - F_{\beta+\frac{1}{2}}(W^0) - F_{\beta+\frac{1}{2}}(\widehat{W}^{2\Delta t})\right). \end{aligned} \tag{6.7}$$

All negative contributions from the interface $\beta + \frac{1}{2}$ must be recovered in the flux balance of the cell β.

Then, the cell β of class rank 0 may be time-integrated from $t = 0$ to $t = 2\Delta t$ thanks to

Heun's scheme such as

$$\begin{aligned}\widehat{W}_\beta^{\Delta t} &= W_\beta^0 + \frac{\Delta t}{\Delta x}\big(F_{\beta+\frac{1}{2}}(W^0) - F_{\beta-\frac{1}{2}}(W^0)\big),\\ W_\beta^{\Delta t} &= W_\beta^0 + \frac{\Delta t}{2\Delta x}\big(F_{\beta+\frac{1}{2}}(\widehat{W}^{\Delta t}) + F_{\beta+\frac{1}{2}}(W^0) - F_{\beta-\frac{1}{2}}(W^0) - F_{\beta-\frac{1}{2}}(\widehat{W}^{\Delta t})\big)\end{aligned} \tag{6.8}$$

in a first phase, and

$$\begin{aligned}\widehat{W}_\beta^{2\Delta t} &= W_\beta^{\Delta t} + \frac{\Delta t}{\Delta x}\big(F_{\beta+\frac{1}{2}}(\widehat{W}^{\Delta t}) - F_{\beta-\frac{1}{2}}(W^{\Delta t})\big),\\ W_\beta^{2\Delta t} &= W_\beta^{\Delta t} + \frac{\Delta t}{2\Delta x}\big(F_{\beta+\frac{1}{2}}(\widehat{W}^{\Delta t}) + F_{\beta+\frac{1}{2}}(\widehat{W}^{2\Delta t}) - F_{\beta-\frac{1}{2}}(W^{\Delta t}) - F_{\beta-\frac{1}{2}}(\widehat{W}^{2\Delta t})\big),\end{aligned} \tag{6.9}$$

in a second phase. If $W_\beta^{\Delta t}$ of Eq. (6.8) is replaced in the second equation of (6.9), and reminding that Eq. (6.4) holds, then

$$\begin{aligned}W_\beta^{2\Delta t} = W_\beta^0 + \frac{\Delta t}{2\Delta x}\Big(&2\big(F_{\beta+\frac{1}{2}}(\widehat{W}^{2\Delta t}) + F_{\beta+\frac{1}{2}}(W^0)\big) - F_{\beta-\frac{1}{2}}(W^0)\\ &- F_{\beta-\frac{1}{2}}(\widehat{W}^{\Delta t}) - F_{\beta-\frac{1}{2}}(W^{\Delta t}) - F_{\beta-\frac{1}{2}}(\widehat{W}^{2\Delta t})\Big).\end{aligned} \tag{6.10}$$

Fortunately, cells β and $\beta+1$ that share the same interfaces $\beta+\frac{1}{2}$ are time integrated with the same interface flux from $t=0$ to $t=2\Delta t$.

6.2 Accuracy and Spectral Analysis of Temporal Adaptive Method

6.2.1 Time Accuracy

Local accuracy must be analysed for cells concerned by time synchronisation, which means that they belong to two different temporal classes and share a common interface. For the sake of clarity, demonstration is performed in one dimension but the proof remains relevant in multidimensional. The proof is made using a one-dimensional mesh with a fixed grid size Δx and the two temporal classes are imposed. A generic partial differential equation is integrated spatially using the standard finite volume formulation. Indeed, two relations are obtained, the first one being associated to the exact relation (using a spatial integration and Gauss theorem) and the second one to the approximated discrete version:

$$\begin{aligned}\Delta x\frac{d\mathcal{W}_j}{dt} &= \Delta x\mathcal{R}_j = \mathcal{F}_{j+\frac{1}{2}} - \mathcal{F}_{j-\frac{1}{2}},\\ \Delta x\frac{dW_j}{dt} &= \Delta x R_j = F_{j+\frac{1}{2}} - F_{j-\frac{1}{2}},\end{aligned} \tag{6.11}$$

with $\mathcal{W}$ the exact state, $\mathcal{R}$ the exact residual and $\mathcal{F}$ the exact flux. Then W represent the numerical state, R the numerical residual and F the numerical flux. In the following, the numerical error on cells of rank 0 and 1 between $t=0$ and $t=2\Delta t$ is formulated as

$$e(W^{2\Delta t}) = \mathcal{W}^{2\Delta t} - W^{2\Delta t}, \tag{6.12}$$

and the procedure consists in studying the error performed at each step of the temporal adaptive method presented in Sec. 6.1.2). In the following, the numerical flux will be assumed to be p^{th}-order accurate in space and a first-order finite difference relation approximates the time derivative:

$$\begin{aligned}F_{j+1/2} &= \mathcal{F}_{j+1/2} + \mathcal{O}(\Delta x^p),\\ \frac{\widehat{W}^{\Delta t} - W^0}{\Delta t} &= \frac{dW}{dt} = \frac{d\mathcal{W}}{dt} + \mathcal{O}(\Delta t)\end{aligned} \tag{6.13}$$

According to Eq. (6.11), it is clear that the residual behaves as $\mathcal{O}(\Delta x^{p-1})$ due to the relation between the residual and the flux. Using Eq. (6.13), Eq. (6.11) may be written as (omitting subscript j)

$$\begin{aligned} \frac{\widehat{W}^{\Delta t} - W^0}{\Delta t} &= \mathcal{R} + \mathcal{O}(\Delta x^{p-1}) + \mathcal{O}(\Delta t) \\ \widehat{W}^{\Delta t} &= W^0 + \Delta t\big(\mathcal{R} + \mathcal{O}(\Delta x^{p-1})\big) + \mathcal{O}(\Delta t^2) \\ &= W^0 + \Delta t\mathcal{R} + \mathcal{O}(\Delta t \Delta x^{p-1}, \Delta t^2). \end{aligned} \tag{6.14}$$

Equation (6.14) represents the time integration of state W during a predictor stage of Heun's scheme. Now, the numerical error attempted at cells of temporal classes rank 0 and 1 are computed. Let us first study the local error performed at cells of class rank 1.

Local Numerical Error of Cells of Class Rank 1

According to the numerical error performed at the predictor state from Eq. (6.14), and regardless the orders of accuracy of the space numerical scheme, the accuracy of the numerical residual at cells of temporal class rank 1 is studied with

$$\begin{aligned} R(\widehat{W}^{2\Delta t}) &= R(W^0 + 2\Delta t\mathcal{R} + \mathcal{O}(\Delta t \Delta x^{p-1}, \Delta t^2)) \\ &= \mathcal{R}(W^0 + 2\Delta t\mathcal{R} + \mathcal{O}(\Delta t \Delta x^{p-1}, \Delta t^2)) + \mathcal{O}(\Delta x^{p-1}) \end{aligned} \tag{6.15}$$

With the assumption that numerical state W at instant $t = 0$ is exact, i.e. $W^0 = \mathcal{W}^0$, the Taylor expansion of residual around W^0 gives

$$R(\widehat{W}^{2\Delta t}) = \mathcal{R}(W^0) + 2\Delta t \frac{\partial \mathcal{R}}{\partial \mathcal{W}} \mathcal{R}(W^0) + \mathcal{O}(\Delta t \Delta x^{p-2}, \frac{\Delta t^2}{\Delta x}, \Delta x^{p-1}). \tag{6.16}$$

Then the state W at cells of class rank 1 of the corrector stage is given by

$$\begin{aligned} W^{2\Delta t} &= W^0 + \frac{2\Delta t}{2}\big(R(W^0) + R(\widehat{W}^{2\Delta t})\big). \\ &= W^0 + \Delta t\big(\mathcal{R} + \mathcal{R} + 2\Delta t \frac{\partial \mathcal{R}}{\partial \mathcal{W}} \mathcal{R} + \mathcal{O}(\Delta t \Delta x^{p-2}, \frac{\Delta t^2}{\Delta x}, \Delta x^{p-1})\big). \end{aligned} \tag{6.17}$$

Finally, the numerical error of $W^{2\Delta t}$ at cells of class rank 1 (see Eq. (6.12)) may be formulated using the Taylor expansion of $\mathcal{W}^{2\Delta t}$ and Eqs. (6.16) and (6.17) such as,

$$e(W^{2\Delta t}) = \mathcal{W}^0 + 2\Delta t \frac{\partial \mathcal{W}}{\partial t} + 2\Delta t^2 \frac{\partial^2 \mathcal{W}}{\partial t^2} + \mathcal{O}(\Delta t^3) - W^{2\Delta t} = \mathcal{O}(\Delta t^3, \frac{\Delta t^3}{\Delta x}, \Delta t^2 \Delta x^{p-2}, \Delta t \Delta x^{p-1}). \tag{6.18}$$

Local Numerical Error due to Time Interpolation for Cells of Class Rank 1

As mentioned in the methodology of time synchronisation introduced previously, the flux at interface $\beta - \frac{1}{2}$ has a special treatment. Indeed, according to the MUSCL reconstruction and its stencil, special treatment of cells of class rank 1 are necessary for computation of flux $\beta - \frac{1}{2}$ (see Step 4 in Sec. 6.1.2). Here, only cell $\beta + 1$ of class rank 1 is considered, and then it is important to evaluate the error due to parabolic interpolation. Thanks to Eq. (6.16) the state $\widehat{W}^{\Delta t}_{\beta+1}$ may be formulated,

$$\begin{aligned} \widehat{W}^{\Delta t}_{\beta+1} &= W^0_{\beta+1} + \Delta t\left(\frac{3}{4}R(W^0) + \frac{1}{4}R(\widehat{W}^{2\Delta t})\right). \\ &= W^0_{\beta+1} + \Delta t\left(\frac{3}{4}\mathcal{R} + \frac{1}{4}(\mathcal{R} + 2\Delta t\mathcal{R}\frac{\partial \mathcal{R}}{\partial \mathcal{W}}) + \mathcal{O}(\frac{\Delta t^2}{\Delta x}, \Delta t \Delta x^{p-2}, \Delta x^{p-1})\right). \end{aligned} \tag{6.19}$$

Then the error $e(\widehat{W}^{\Delta t}_{\beta+1})$ according to parabolic interpolation, may be formulated as:

$$e(\widehat{W}^{\Delta t}_{\beta+1}) = \mathcal{W}^0_{\beta+1} + \Delta t\frac{\partial \mathcal{W}}{\partial t} + \frac{\Delta t^2}{2}\frac{\partial^2 \mathcal{W}}{\partial t^2} + \mathcal{O}(\Delta t^3) - \widehat{W}^{\Delta t}_{\beta+1} = \mathcal{O}(\Delta t^3, \frac{\Delta t^3}{\Delta x}, \Delta t^2\Delta x^{p-2}, \Delta t\Delta x^{p-1}). \tag{6.20}$$

Thanks to the numerical error formulation Eq. (6.20), the numerical flux at interface $\beta - \frac{1}{2}$ can be expressed as:

$$\begin{aligned} F_{\beta-\frac{1}{2}}(\widehat{W}^{\Delta t}) &= \mathcal{F}_{\beta-\frac{1}{2}} + \Delta t\mathcal{R}\frac{\partial \mathcal{F}_{\beta-\frac{1}{2}}}{\partial \mathcal{W}} + \mathcal{O}(\Delta t^3, \frac{\Delta t^3}{\Delta x}, \Delta t^2\Delta x^{p-2}, \Delta t\Delta x^{p-1}; \Delta x^p). \\ F_{\beta-\frac{1}{2}}(W^0) &= \mathcal{F}_{\beta-\frac{1}{2}} + \mathcal{O}(\Delta x^p). \end{aligned} \tag{6.21}$$

Now, the numerical error is studied for the cell β of class rank 0.

Local Numerical Error of Cells β of Class Rank 0

According to numerical error performed at the predictor stage $\widehat{W}^{2\Delta t}$ (see Eq. (6.14)) and using Taylor expansion of flux around W, it comes:

$$\begin{aligned} F_{\beta+\frac{1}{2}}(\widehat{W}^{2\Delta t}) &= \mathcal{F}_{\beta+\frac{1}{2}} + 2\Delta t\mathcal{R}\frac{\partial \mathcal{F}_{\beta+\frac{1}{2}}}{\partial \mathcal{W}} + \mathcal{O}(\Delta t^2, \Delta t\Delta x^{p-1}, \Delta x^p). \\ F_{\beta+\frac{1}{2}}(W^0) &= \mathcal{F}_{\beta+\frac{1}{2}} + \mathcal{O}(\Delta x^p). \end{aligned} \tag{6.22}$$

Then, the flux $F(\widehat{W}^{\Delta t})_{\beta+\frac{1}{2}}$ can be formulated as:

$$\begin{aligned} F_{\beta+\frac{1}{2}}(\widehat{W}^{\Delta t}) &= \frac{1}{2}\left(F_{\beta+\frac{1}{2}}(W^0) + F_{\beta+\frac{1}{2}}(\widehat{W}^{2\Delta t})\right) \\ &= \mathcal{F}_{\beta+\frac{1}{2}} + \Delta t\mathcal{R}\frac{\partial \mathcal{F}_{\beta+\frac{1}{2}}}{\partial \mathcal{W}} + \mathcal{O}(\Delta t^2, \Delta x^p, \Delta t\Delta x^{p-1}). \end{aligned} \tag{6.23}$$

Thanks to Eqs. (6.21), (6.23), (6.22), the state $W^{\Delta t}_\beta$ is such as:

$$\begin{aligned} W^{\Delta t}_\beta &= W^0_\beta + \frac{\Delta t}{2\Delta x}\left(F_{\beta+\frac{1}{2}}(W^0) + F_{\beta+\frac{1}{2}}(\widehat{W}^{\Delta t}) - F_{\beta-\frac{1}{2}}(\widehat{W}^{\Delta t}) - F_{\beta-\frac{1}{2}}(W^0)\right) \\ &= W^0_\beta + \frac{\Delta t}{2}\left(2\mathcal{R} + \Delta t\mathcal{R}\frac{\partial \mathcal{R}}{\partial \mathcal{W}}\right. \\ &\quad \left. + \mathcal{O}(\frac{\Delta t^2}{\Delta x}, \frac{\Delta t^3}{\Delta x^2}, \Delta t^2\Delta x^{p-3}, \Delta t\Delta x^{p-2}, \Delta x^{p-1})\right). \end{aligned} \tag{6.24}$$

Then the error $e(W^{\Delta t}_\beta)$ can be formulated such as:

$$\begin{aligned} e(W^{\Delta t}_\beta) &= \mathcal{W}^0_\beta + \Delta t\frac{\partial \mathcal{W}}{\partial t} + \frac{\Delta t^2}{2}\frac{\partial^2 \mathcal{W}}{\partial t^2} + \mathcal{O}(\Delta t^3) - W^{\Delta t}_\beta \\ &= \mathcal{O}(\Delta t^3, \frac{\Delta t^3}{\Delta x}, \frac{\Delta t^4}{\Delta x^2}, \Delta t^3\Delta x^{p-3}, \Delta t^2\Delta x^{p-2}, \Delta t\Delta x^{p-1}). \end{aligned} \tag{6.25}$$

According to the numerical local error $e(W^{\Delta t}_\beta)$ (see Eq. (6.25)), and the special treatment of cell $\beta + 1$ according to the stencil of MUSCL reconstruction (see error in Eq. (6.20)), the flux $F_{\beta-\frac{1}{2}}(W^{\Delta t})$ and $F_{\beta-\frac{1}{2}}(\widehat{W}^{\Delta t})$ is formulated as:

$$\begin{aligned} F_{\beta-\frac{1}{2}}(\widehat{W}^{2\Delta t}) &= \mathcal{F}_{\beta-\frac{1}{2}} + 2\Delta t\mathcal{R}\frac{\partial \mathcal{F}_{\beta-\frac{1}{2}}}{\partial \mathcal{W}} + \mathcal{O}(\Delta t^3, \frac{\Delta t^3}{\Delta x}, \frac{\Delta t^4}{\Delta x^2}, \Delta t^3\Delta x^{p-3}, \Delta t^2\Delta x^{p-2}, \Delta t\Delta x^{p-1}, \Delta x^p), \\ F_{\beta-\frac{1}{2}}(W^{\Delta t}) &= \mathcal{F}_{\beta-\frac{1}{2}} + \mathcal{O}(\Delta t^3, \frac{\Delta t^3}{\Delta x}, \frac{\Delta t^4}{\Delta x^2}, \Delta t^3\Delta x^{p-3}, \Delta t^2\Delta x^{p-2}, \Delta t\Delta x^{p-1}, \Delta x^p) \end{aligned}$$

(6.26)

Thanks to Eqs. (6.26), (6.23), (6.22), (6.25), the state $W_\beta^{2\Delta t}$ can be formulated as:

$$\begin{aligned} W_\beta^{2\Delta t} &= W_\beta^{\Delta t} + \frac{\Delta t}{2\Delta x}\Big(F_{\beta+\frac{1}{2}}(\widehat{W}^{2\Delta t}) + F_{\beta+\frac{1}{2}}(\widehat{W}^{\Delta t}) - F_{\beta-\frac{1}{2}}(\widehat{W}^{2\Delta t}) - F_{\beta-\frac{1}{2}}(W^{\Delta t})\Big). \\ &= \mathcal{W}_\beta^{\Delta t} + \mathcal{O}(\Delta t^3, \frac{\Delta t^3}{\Delta x}, \frac{\Delta t^4}{\Delta x^2}, \Delta t^3 \Delta x^{p-3}, \Delta t^2 \Delta x^{p-2}, \Delta t \Delta x^{p-1}) \\ &\quad + \frac{\Delta t}{2}\Bigg(2\mathcal{R} + 3\Delta t \mathcal{R}\frac{\partial \mathcal{F}_{\beta+\frac{1}{2}}/\Delta x}{\partial \mathcal{W}} - 2\Delta t \mathcal{R}\frac{\partial \mathcal{F}_{\beta-\frac{1}{2}}/\Delta x}{\partial \mathcal{W}} \\ &\quad + \mathcal{O}(\frac{\Delta t^2}{\Delta x}, \frac{\Delta t^3}{\Delta x^2}, \frac{\Delta t^4}{\Delta x^3}, \Delta t^3 \Delta x^{p-4}, \Delta t^2 \Delta x^{p-3}, \Delta t \Delta x^{p-2}, \Delta x^{p-1})\Bigg) \end{aligned} \tag{6.27}$$

Then the local error $e(W_\beta^{2\Delta t})$ is:

$$\begin{aligned} e(W_\beta^{2\Delta t}) &= \mathcal{W}_\beta^{\Delta t} + \Delta t \frac{\partial \mathcal{W}}{\partial t} + \frac{\Delta t^2}{2}\frac{\partial^2 \mathcal{W}}{\partial t^2} + \mathcal{O}(\Delta t^3) - W_\beta^{2\Delta t} \\ &= \mathcal{O}(\Delta t^2, \frac{\Delta t^3}{\Delta x}, \frac{\Delta t^4}{\Delta x^2}, \frac{\Delta t^5}{\Delta x^3}, \Delta t^4 \Delta x^{p-4}, \Delta t^3 \Delta x^{p-3}, \Delta t^2 \Delta x^{p-2}, \Delta t \Delta x^{p-1}) \end{aligned} \tag{6.28}$$

Fot the solution of a hyperbolic equation, the CFL number gives a linear relation between the grid spacing Δx and the time step Δt: $\Delta x \simeq \Delta t$. This assumption allows simplifications in the previous expressions. The local numerical error performed until $t = 2\Delta t$ on cell β of class rank 0 is $O(\Delta t^2, \Delta x^p)$, and the local numerical error at cells of class rank 1 is $O(\Delta t^2, \Delta x^p)$ too. As a consequence, the local time order of accuracy is kept unchanged at interface between cells of different temporal classes. In the following section, the influence of local numerical error due to temporal adaptive method on global error will be investigated.

6.2.2 Numerical Assessment of the Theoretical Behaviour

In order to study the impact of time synchronisation on global order of accuracy, a one-dimensional numerical analysis will be performed on the advection of a sinus wave inside a periodical domain of length $L = 1$ ($x \in [0, 1]$), with the following initial state:

$$W(x, t = 0) = sin(2\pi x) \tag{6.29}$$

A constant space step will be considered in a grid of N cells. Two temporal classes are imposed with 100 cells of class 0 ($\frac{N}{2} - 50 \leq j \leq \frac{N}{2} + 50$) and other cells belong to the temporal class of rank 1. For a fixed time step $\Delta t = 2.5 \cdot 10^{-5} s$ the computation is performed until $3s$ of physical time. A 1-exact spatial scheme is used for the computation. The accuracy of the temporal adaptive method with Heun's scheme (defined as "Heun+TA") is compared with the standard Heun's integrator. It appears that the temporal adaptive method coupled with a $1-$ exact reconstruction maintains the second order space-time accuracy of Heun's scheme according to Fig.6.10 and Tab. 9.1.

Time integrator	E_{tot} slope
Heun	1.97
Heun + TA	1.93

Tab. 6.1. Total error slopes

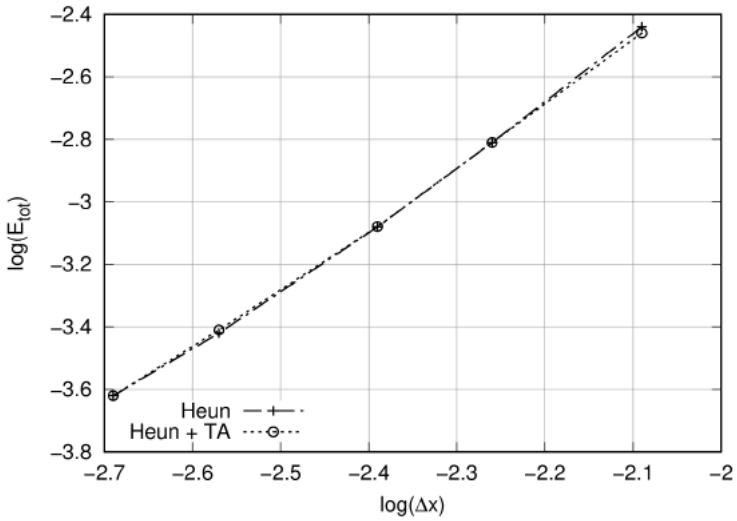

Fig. 6.10. Total error for a second order accurate spatial scheme

6.2.3 Space-Time Von Neumann Analysis

The von Neumann analysis presented in Sec. 2.4 is a powerful tool to analyse the spectral properties of any numerical scheme. In the following section a one-dimensional linear advection equation (6.30) with a harmonic initial condition and with periodic boundary conditions will be considered,

$$\begin{cases} W(x,0) = \exp(\mathrm{i}kx) & x \in [0,L] \\ W(0,t) = W(L,t) & t \in R^+ \end{cases} \tag{6.30}$$

The comparison between the exact theoretical solution and the numerical approximation gives information on both dissipation and dispersion of the fully discrete scheme thanks to the expression of the amplification factor (see Eq. (2.27)). The fully discrete relation obtained from Eq. (1.23) with harmonic initial condition and periodic boundary conditions (see Eqs. (6.30)) using a second-order finite volume scheme reads:

$$W_j^{n+1} = G_j W_j^n, \tag{6.31}$$

where W_j^n represents the harmonic (averaged) solution at discrete time n and in the center of cell j. It is recalled that the complex coefficient G_j represents the amplification factor between two consecutive time solutions. In the following, $\mu_j = |G_j|$ will be considered as the dissipation coefficient, and $\phi_j = arg(G_j)/\mathrm{CFL}$ as the dispersion coefficient.

As the temporal adaptive approach involves sub-cycling of time integrations, the space-time spectral analysis needs to be performed on several time steps. The space-time spectral analysis will be performed on two time steps for two classes of cells. With $c > 0$, two configurations of time synchronisation between classes will be studied and named as "step DOWN" and "step UP" (Fig. 6.11).

Remark: In the following the cell size Δx will be considered as fixed in the whole domain because a standard space-time spectral analysis with different Δx is cumbersome (see for instance [103]). This analysis will be performed numerically in Sec. 10.3.1 for the propagation of a wave packet. Attention will be paid on the numerical effect on numerical solution resulting from time synchronisation with irregular size of cells.

Remark: Since Δx is constant in the whole domain, for a time step Δt corresponding to CFL $= 0.5$ in cells of class rank 0, the time step $2\Delta t$ corresponds to CFL $= 1$ in cells of class rank 1 . Then the time step Δt must be chosen so that CFL < 0.5 to remain below the stability condition in class rank 1.

The domain configuration shown in Fig. 6.11 will be considered with $N = 300$ cells, in the following spectral analysis.

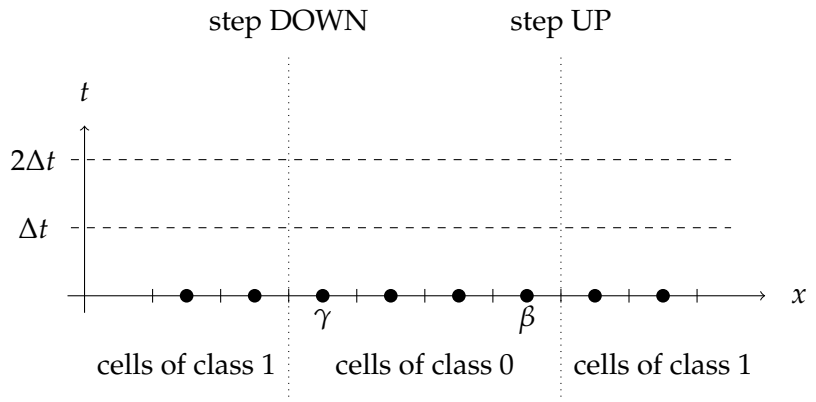

Fig. 6.11. Sketch of the whole domain configuration

The spectral analysis will focus on state W in cells β and γ from $t = 0$ to $t = 2\Delta t$ and will be compared to the standard Heun time integration of the state W at cell $\beta - 10$ (far from class transitions) from $t = 0$ to $t = 2\Delta t$.

Transfer Function for Heun's Scheme, Far From Class Transition

Heun's time integration at cell $\beta - 10$ (far from class transition) from $t = 0$ to $t = 2\Delta t$ is:

$$\begin{aligned} W_{\beta-10}^{\Delta t} &= W_{\beta-10}^{0} - \Delta t\left[\frac{1}{2}\left(R^{0} + \widehat{R}^{0}\right)\right] \\ W_{\beta-10}^{2\Delta t} &= W_{\beta-10}^{\Delta t} - \Delta t\left[\frac{1}{2}\left(R^{\Delta t} + \widehat{R}^{\Delta t}\right)\right] \end{aligned} \tag{6.32}$$

and by means of the finite volume formulation:

$$\begin{aligned} W_{\beta-10}^{2\Delta t} = W_{\beta-10}^{\Delta t} - \frac{\Delta t}{\Delta x}\Bigg[&\frac{1}{2}\left(F_{\beta-\frac{19}{2}}(\Delta t, W^{\Delta t}) + F_{\beta-\frac{19}{2}}(2\Delta t, \widehat{W}^{\Delta t})\right) \\ &- \frac{1}{2}\left(F_{\beta-\frac{21}{2}}(\Delta t, W^{\Delta t}) + F_{\beta-\frac{21}{2}}(2\Delta t, \widehat{W}^{\Delta t})\right)\Bigg] \end{aligned} \tag{6.33}$$

Analysis for the Cell β Near Step UP

The finite volume formulation of the state $W_{\beta}^{2\Delta t}$ at the cell β near the step UP is different due to time synchronisation:

$$\begin{aligned} W_{\beta}^{2\Delta t} = W_{\beta}^{\Delta t} - \frac{\Delta t}{\Delta x}\Bigg[&\frac{1}{2}\left(F_{\beta+\frac{1}{2}}(\Delta t, W^{\Delta t}) + F_{\beta+\frac{1}{2}}(2\Delta t, \widehat{W}^{2\Delta t})\right) \\ &- \frac{1}{2}\left(F_{\beta-\frac{1}{2}}(\Delta t, W^{\Delta t}) + F_{\beta-\frac{1}{2}}(2\Delta t, \widehat{W}^{2\Delta t})\right)\Bigg] \end{aligned} \tag{6.34}$$

Considering the MUSCL reconstruction for a simple advection from left to right in one dimension, the linear extrapolation of the unknown used for the flux computation reads

$$F(t, W) = c\, W^{L} = c\left(W + \frac{\Delta x}{2}(\nabla W)\right) \tag{6.35}$$

Then, by substitution in Eq.(6.34),

$$\begin{aligned} W_\beta^{2\Delta t} = W_\beta^{\Delta t} - \frac{c\Delta t}{\Delta x}\Bigg[&\frac{1}{2}\left(\frac{1}{2}\left(W_\beta^0 + \frac{\Delta x}{2}(\nabla W)_\beta^0\right) + \frac{1}{2}\left(\widehat{W}_\beta^{2\Delta t} + \frac{\Delta x}{2}(\widehat{\nabla W})_\beta^{2\Delta t}\right)\right) \\ &+ \frac{1}{2}\left(\widehat{W}_\beta^{2\Delta t} + \frac{\Delta x}{2}(\widehat{\nabla W})_\beta^{2\Delta t}\right) \\ &- \frac{1}{2}\left(W_{\beta-1}^{\Delta t} + \frac{\Delta x}{2}(\nabla W)_{\beta-1}^{\Delta t}\right) - \frac{1}{2}\left(\widehat{W}_{\beta-1}^{2\Delta t} + \frac{\Delta x}{2}(\widehat{\nabla W})_{\beta-1}^{2\Delta t}\right)\Bigg] \end{aligned} \tag{6.36}$$

It appears that terms $\widehat{W}_\beta^{2\Delta t}$ and $(\widehat{\nabla W})_\beta^{2\Delta t}$, may be source of instability because of the possible violation of the Courant condition for these cells.

Analysis for the Cell γ Near Step DOWN

In the configuration of the step DOWN at cells γ, the time integrations of the state W can be formulated such as:

$$\begin{aligned} W_\gamma^{2\Delta t} &= W_\gamma^{\Delta t} - \frac{\Delta t}{\Delta x}\Bigg[\frac{1}{2}\left(F_{\gamma+\frac{1}{2}}(\Delta t, W^{\Delta t}) + F_{\gamma+\frac{1}{2}}(2\Delta t, \widehat{W}^{\Delta t})\right) \\ &\qquad - \frac{1}{2}\left(F_{\gamma-\frac{1}{2}}(\Delta t, W^{\Delta t}) + F_{\gamma-\frac{1}{2}}(2\Delta t, \widehat{W}^{2\Delta t})\right)\Bigg] \\ W_\gamma^{2\Delta t} &= W_\gamma^{\Delta t} - \frac{c\Delta t}{\Delta x}\Bigg[\frac{1}{2}\left(W_\gamma^{\Delta t} + \frac{\Delta x}{2}(\nabla W)_\gamma^{\Delta t}\right) + \frac{1}{2}\left(\widehat{W}_\gamma^{2\Delta t} + \frac{\Delta x}{2}(\widehat{\nabla W})_\gamma^{2\Delta t}\right) \\ &\qquad - \frac{1}{2}\left(\frac{1}{2}\left(W_{\gamma-1}^0 + \frac{\Delta x}{2}(\nabla W)_{\gamma-1}^0\right) + \frac{1}{2}\left(\widehat{W}_{\gamma-1}^{2\Delta t} + \frac{\Delta x}{2}(\widehat{\nabla W})_{\gamma-1}^{2\Delta t}\right)\right) \\ &\qquad - \frac{1}{2}\left(\widehat{W}_{\gamma-1}^{2\Delta t} + \frac{\Delta x}{2}(\widehat{\nabla W})_{\gamma-1}^{2\Delta t}\right)\Bigg] \end{aligned} \tag{6.37}$$

In order to obtain the spectral behaviour resulting from time synchronisation the amplification factor G between $W^{2\Delta t}$ and W^0 have to be computed and all the terms in the previous Eqs. (6.33), (6.36) and (6.37) have to be be expressed according to W^0:

$$\begin{aligned} W^{\Delta t} &= G_1 W^0 \\ (\widehat{\nabla W})^{2\Delta t} &= G_2 W^0 \\ (\nabla W)^0 &= G_3 W^0 \\ \widehat{W}^{2\Delta t} &= G_4 W^0 \\ &... \end{aligned} \tag{6.38}$$

According to Figs. 6.12 and 6.13 amplification never occurs for step UP configuration. For the step DOWN configuration, it appears that the terms $\widehat{W}_{\gamma-1}^{2\Delta t}$ and $(\widehat{\nabla W})_{\gamma-1}^{2\Delta t}$ can create amplification as shown in Figs. 6.12 and 6.13.

For CFL= 0.6, both step UP and DOWN configurations present strong amplification according to Fig. 6.14, due to the fixed grid size Δx (cf. Remark of Sec. 6.2.3). It is important to remember that amplification in a certain range of wave numbers does not necessarily involve instability. Nevertheless, it is preferable not to allow this type of configuration in a large part of the computational domain. In particular, if several classes are located closely, a wave can be amplified at any step DOWN, then CFL below 0.6 is a better solution.

Morever, Figs. 6.12 and 6.14 reveal that the time synchronisation does no affect the dispersion behaviour of Heun's scheme. Nevertheless, keeping in mind that Heun's scheme is the reference, Fig. 6.13 shows that dispersion is changed for wavenumbers above $\frac{\pi}{2\Delta x}$.

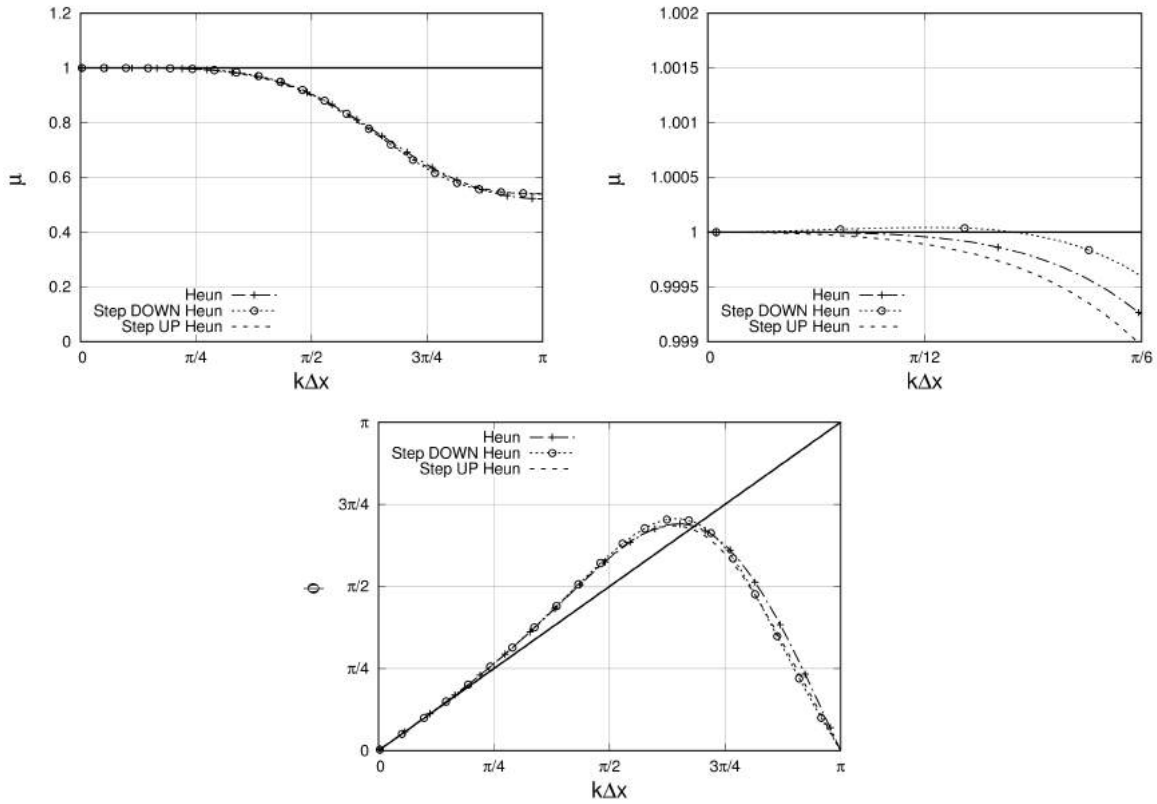

Fig. 6.12. Dissipation μ and dispersion ϕ for Heun's scheme with temporal adaptive approach at CFL=0.1

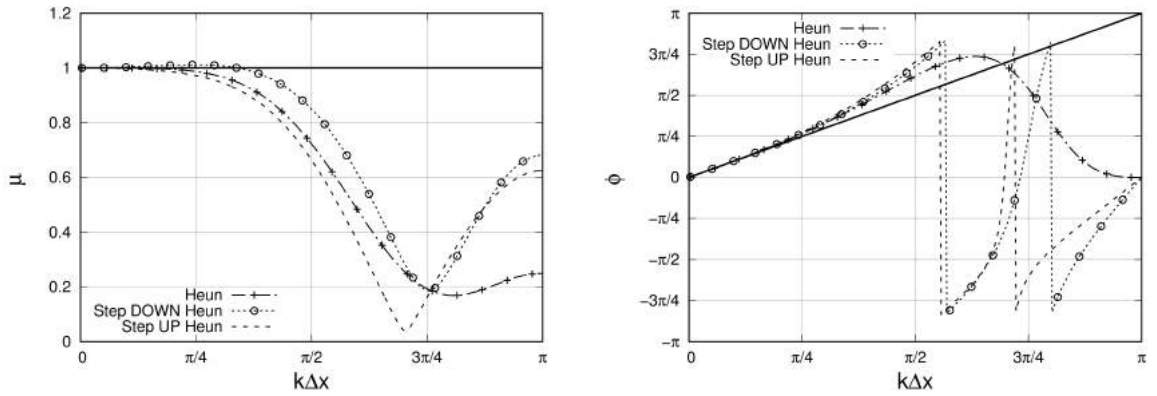

Fig. 6.13. Dissipation μ and dispersion ϕ for Heun's scheme with temporal adaptive approach at CFL=0.3

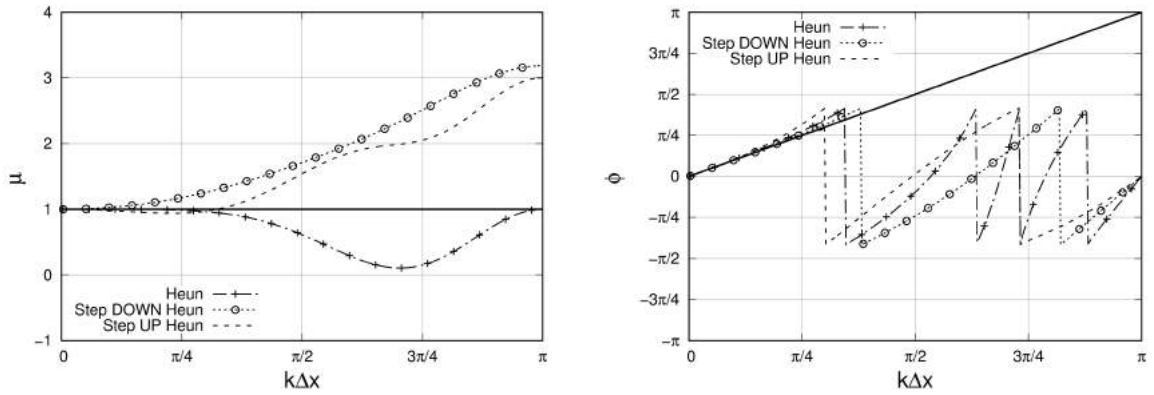

Fig. 6.14. Dissipation μ and dispersion ϕ for Heun's scheme with temporal adaptive approach at CFL=0.6

6.2.4 Analysis of $q-$waves

The analysis was described in Sec. 2.5 for a linear advection equation and it was highlighted that the key point is the region of negative group velocity. In the case of temporal adaptive method, the analysis of q-waves is performed on two consecutive time step (duration is $2\Delta t$) according to the configuration presented in previous Sec. 6.2.3.

Here cells β and γ which represent both configurations occurring during time synchronisation in temporal adaptive method (according to Sec. 6.2.3) are taken into account. Indeed the numerical phase speed c^N and the numerical group velocity V^{gN} are computed from G (Eq. 6.31) for cells β and γ . The analysis of $q-$waves is performed for CFL $\in [0,1]$. The dashed curves in Figs. 6.15 correspond to a discontinuity of dispersion ϕ ($|V^{gN}|/|c| >> 1$), and negative group velocity $V^{gN} < 0$ corresponding to grey zones.

Remark: In order to compare several configurations, the CFL domain $[0,1]$ is larger than the stability domain of Heun's scheme with a 1-exact spatial scheme. Indeed, amplification always occurs for CFL$>$ 0.6. But the analysis can still be performed for any value of the CFL number.

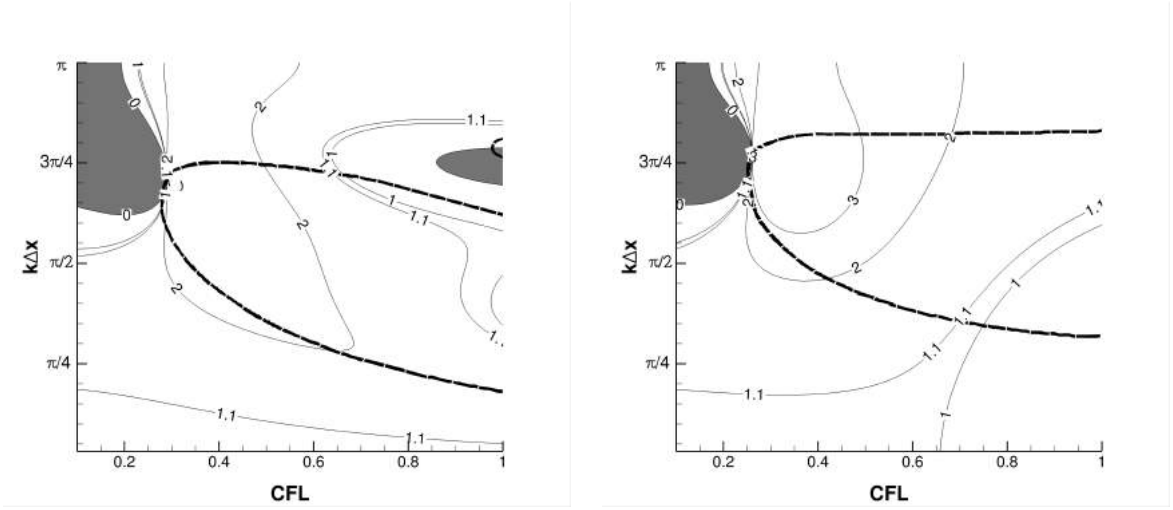

Fig. 6.15. Isocontours of V^{gN} for cell β (left - step UP) and γ (right - step DOWN)

According to Figs. 6.15, it appears that the size of grey zone (corresponding to areas of

negative-V^{gN} group velocity) in step UP and step DOWN configuration, is not varying a lot for CFL $\in [0, 0.8]$. Furthermore it can be noticed that, in step UP case, another negative-V^{gN} group velocity zone is present for $CFL > 0.9$. Now it is important to study the capability of the temporal adaptive method to damp possible $q-$waves. For that, it is mandatory to couple the observations on negative group velocity with the dissipation property of the time integration.

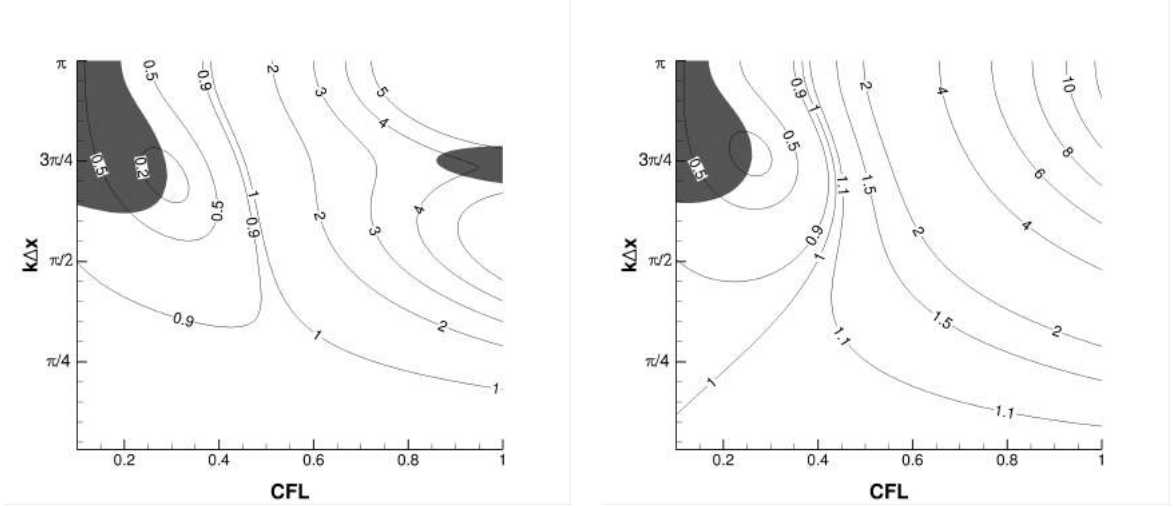

Fig. 6.16. Isocontours of the dissipation μ_β and μ_γ with grey zone for negative group velocity

According to Fig. 6.16, the negative-V^{gN} zone found for CFL$>$ 0.5 matches with the dissipation factor $\mu_\beta > 3$, leading to amplification. This is in agreement with the instability of the scheme for CFL$>$ 0.5 (mentioned in the remark of Sec. 6.2.3). Nevertheless, the zones of negative-V^{gN} for CFL$<$ 0.5 corresponds to $\mu < 0.5$ and the wave is partially dissipated in one iteration.

6.3 Partial Conclusion

This chapter was devoted to the last ingredient of **FLUSEPA**©: the adaptive time integration scheme. This scheme, based on Heun's scheme, was detailed to complement past papers. In addition, new results were presented (spectral analysis, q-waves, etc).

7 Partial conclusion on the review of time integrators

Several time integrators of different type were previously introduced, using either a global time stepping approach or a local time stepping approach with time adaptation. The industrial solver **FLUSEPA**© uses either a temporal adaptive procedure coupled with the explicit Heun's scheme previously introduced or a standard Euler implicit global time stepping method. Our goal is to design an approach that extends the stability properties of Heun's scheme coupled with temporal approach and that maintaining the spectral properties of the explicit time integration in order to ensure an accurate transport of unsteady physics. Several options were investigated:

- **Full implicit schemes** allow time integration with large time steps but their implementation for the transport of unsteady physics will impose a high-order time accurate approach with a very high CPU cost and a small stability region.
- **Implicit residual smoothing approach** allows to increase the stability region of the Runge-Kutta schemes for structured grids, which impose to test and implement an additional algorithm for the treatment of unstructured grids.
- **Exponential integrators** represent a very interesting option according to their capability to treat stiffness (A-stability) but their implementation will impose to split the residual (as for **IMEX approach**) in linear and non-linear parts. Such a procedure is not present using Heun's scheme and a first requirement is to avoid such a splitting procedure. Nevertheless, this kind of approach may be a good alternative to temporal adaptive approach in future developments.
- **The TN hybrid scheme** appears to be an interesting approach to investigate according to its stability properties, to its predictor-corrector approach (one-step/two-stages), to its time accuracy and it blends explicit and implicit time integrators.

In this context, the TN scheme methodology is based on a parameter that allows a smooth blending of time integrators. It will be at the genesis of our study to **couple explicit and implicit time integrators**.

Thanks to its A-stability property and its one-step/two-stage formulation, **the IRK2 scheme** will be our chosen candidate for the implicit time integration of our future coupling methods. Gear's scheme could be an alternative for implicit time integration (A-stable and second-order time accurate) but multi-step formulation is not adapted with chimera-like technique of **FLUSEPA**©, especially for moving domains. Hence this report will present the design of a time integration procedure that spatially couples explicit and implicit time integration and is adapted to the spatial coupling of RANS and LES regions according to the time integration procedure already included in **FLUSEPA**©.

In the next chapters, attention will be paid on the coupling procedure between Heun's and IRK2 schemes first, and then on the extension of the procedure to deal with time adaptation.

IV A New Time Integrator

8 First Hybrid Coupled Scheme 79
8.1 Methodology of First Hybrid Coupling Scheme (HCS1)
8.2 Space-Time Von Neumann Analysis
8.3 Conclusion

9 Another tIme integratiON (AION) Scheme ... 85
9.1 Introduction
9.2 Formulation
9.3 Space-Time Stability Analysis
9.4 Partial conclusion
9.5 Validation
9.6 Partial Conclusion

10 Temporal Adaptive Method with AION Scheme 117
10.1 Update of the Solution for Hybrid Time Integration
10.2 Conservation and Adaptive Time Accuracy
10.3 Validation of Temporal Adaptive Method with AION Scheme

11 AION Time Integration with RANS/LES Simulation 141
11.1 Introduction
11.2 Two-dimensional Backward Facing Step

8 First Hybrid Coupling Scheme

The standard explicit Heun's scheme is already implemented in **FLUSEPA**© solver. A first design of an hybrid solver based on the explicit scheme of Heun, the implicit time integrator IRK2 and the hybrid Timofeev and Norouzi (TN) [81] blending method is introduced. The main goals are to maintain the second order time accuracy, avoid downgrade of spectral properties and extend stability properties of standard Heun's time integration.

8.1 Methodology of First Hybrid Coupling Scheme (HCS1)

This section presents a first attempt to couple the three latter schemes. TN hybrid formulation is useful for a smooth transition between explicit and implicit time integrations. In order to ensure conservation, it is of strong importance to define an unique flux on any surface for the resulting numerical space/time integration. Indeed an interface may separate two cells with different status according to the parameter ω_j. The cell status is named Heun for $\omega_j = 1$, IRK2 for $\omega_j = 0$, and Hybrid otherwise, as shown by the one-dimensional example on Fig. 8.1. The

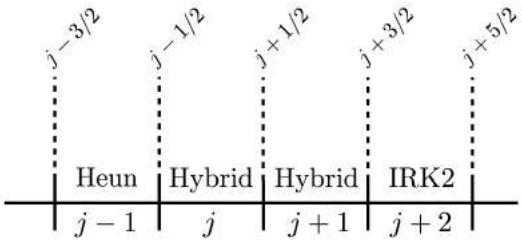

Fig. 8.1. One-dimensional example to explain cell status and the flux conservation property of the coupling scheme HCS1

type of reconstruction used for the flux computation at an interface that separates two cells depends on the status of these cells as shown in Tab. 8.1.

Left cell status \ Right cell status	Heun	Hybrid	IRK2
Heun	F^{Heun}	F^{Heun}	$\times$
Hybrid	F^{Heun}	F^{Hybrid}	F^{IRK2}
IRK2	$\times$	F^{IRK2}	F^{IRK2}

Tab. 8.1. Flux formula depending on neighbour cells. The table is "symmetrical": the flux between two cells is independent of the direction of information propagation.

For the one-dimensional example of cells status illustrated on Fig. 8.1, and according to the flux definition presented in Tab. 8.1, the first version of the coupling scheme, referred as HCS1,

is designed as,

$$\begin{cases} \text{Predictor step:} & \widehat{W_j} = W_j^n + \omega_j \Delta t R(W_j^n) \\ \text{Corrector step:} & \begin{cases} W_{j-1}^{n+1} = W_{j-1}^n + \dfrac{\Delta t}{2|\Omega_{j-1}|}(F_{j-\frac{1}{2}}^n + \widehat{F}_{j-\frac{1}{2}} - F_{j-\frac{3}{2}}^n - \widehat{F}_{j-\frac{3}{2}}) \\ W_j^{n+1} = W_j^n + \dfrac{\Delta t}{|\Omega_j|}(F_{j+\frac{1}{2}}^{Hybrid} - \dfrac{F_{j-\frac{1}{2}}^n + \widehat{F}_{j-\frac{1}{2}}}{2}) \\ W_{j+1}^{n+1} = W_{j+1}^n + \dfrac{\Delta t}{|\Omega_{j+1}|}(\dfrac{F_{j+\frac{3}{2}}^n + F_{j+\frac{3}{2}}^{n+1}}{2} - F_{j+\frac{1}{2}}^{Hybrid}) \\ W_{j+2}^{n+1} = W_{j+2}^n + \dfrac{\Delta t}{2|\Omega_{j+2}|}(F_{j+\frac{5}{2}}^n + F_{j+\frac{5}{2}}^{n+1} - F_{j+\frac{3}{2}}^n - F_{j+\frac{3}{2}}^{n+1}). \end{cases} \end{cases} \tag{8.1}$$

The flux defined as hybrid F^{Hybrid} is computed thanks to the state reconstruction method introduced in Eq. (5.23). The scheme of Eq. (8.1) ensures the uniqueness of the definition of the flux, and then flux conservation. The HCS1 scheme is designed with several differences compared to TN scheme. Indeed:

- A (approximated) Riemann solver is used at predictor step for the computation of the residual and hence, the predictor step is conservative.
- For $\omega_j = 1$ the Heun's scheme is used for time integration.
- For $\omega_j = 0$ the IRK2 scheme is used for time integration.

Remark 1: In practice the IRK2 time integration is performed when $\omega_j \leq 0.5$ in order to make transition between explicit and implicit scheme as fast as possible.
Remark 2: For the Navier-Stokes simulation, the standard diffusion scheme available in the code was used for the implicit and explicit regions. Whereas, in the hybrid regions, the definition of the cell-centered gradient is modified as

$$(\nabla W)_j^{hyb} = \omega_j \left(\frac{(\widetilde{\nabla W})_j^n + (\widetilde{\widetilde{\nabla W}})_j}{2} \right) + (1 - \omega_j)(\widetilde{\nabla W})_j^{n+1} \quad \text{for } 0.5 < \omega_j < 1. \tag{8.2}$$

This hybrid gradient computation is inspired from the hybrid treatment that allows a smooth transition between the time integrators available in the TN scheme. Any gradient in Eq. (8.2) is computed from the standard gradient and corrected using a slope limiter.

8.2 Space-Time Von Neumann Analysis

The same space-time von Neumann analysis provided in Sec. 6.2.3 for studying the temporal adaptive method will now be focused on the coupling of time integrators. For the standard von Neumann analysis, the study is ususally focused on a single scheme for space and time, which leads to an amplification factor that does not depend on the space position. However, in our case, several time discretisation schemes are coupled, and the global scheme has spectral properties that will depend on the cell status ω_j. The cell status can be linked to size of the cell in irregular grids. But taking into account irregular grids in the spectral analysis is difficult [103]. For a fixed mesh size Δx, a manufactured choice of ω_j keeps the analysis quite simple to perform and to observe the spectral behaviour of the HCS1 scheme. The number of

one-dimensional cells is fixed to $N = 300$ and the function ω_j is fixed as

$$\begin{cases} \omega_j = \alpha\, \omega_{j-1} & \text{for } \dfrac{N}{2} - 50 \leq j \leq \dfrac{N}{2} \\ \omega_j = \dfrac{1}{\alpha}\, \omega_{j-1} & \text{for } \dfrac{N}{2} + 1 \leq j \leq \dfrac{N}{2} + 50 \\ \omega_j = 1 & \text{elsewhere.} \end{cases} \tag{8.3}$$

with $\alpha = 0.90$. For a 1-exact space scheme, an amplification at certain range of wavenumber with Heun's explicit time integration appears at CFL over 0.6 and according to this observation, the spectral analysis will be performed for CFL=0.1 and CFL=0.6.

8.2.1 Analysis at CFL=0.1

Thanks to Figs. 8.2 and 8.3, it is possible to obtain information on both dissipation and dispersion for the coupled time/space HSC1 scheme according to the cell index j ranging from 1 to N and for the normalised wavenumber such as $0 \leq k\Delta x \leq \pi$. Here, CFL=0.1 is used to couple space and time discretization to update the solution.

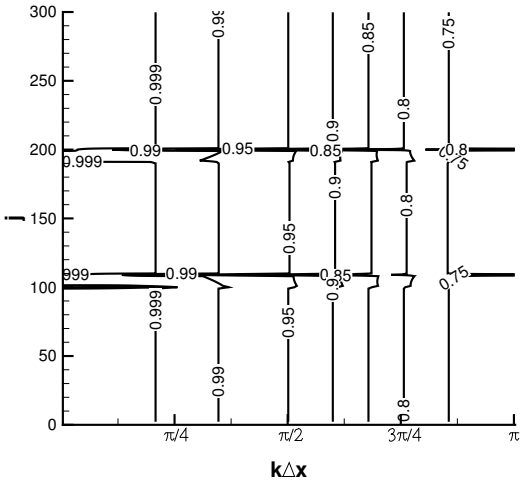

Fig. 8.2. Isocontours of the dissipation coefficient μ_j for the HCS1 scheme at CFL=0.1

The analysis using Figs. 8.2 and 9.2 is qualitative but not really accurate. Standard dissipation and dispersion curves give a valuable information and the analysis is performed on a set of points, following Tab. 8.2.

The standard curves (μ_j and ϕ_j as a function of $k\Delta x$) introduced in Figs. 8.4 and-8.5 allow to focus on the behaviour at the transitions between the different time integrations, taking the six specific discretization cells introduced in Tab. 8.2. The main consequences are:

- Normalised wavenumbers $k\Delta x \in [0, 0.6]$ are amplified for Heun/Hybrid cells, according to Fig. 8.4. Nevertheless, the rate of amplification is quite low and it is possible to assume that for a local treatment (on one cell in one-dimension), this amplification should not lead to the global divergence of the computation.
- An important rate of dispersion appears for cells with Hybrid/Heun and Hybrid/IRK2 fluxes, compared to other configurations (Fig. 8.5).

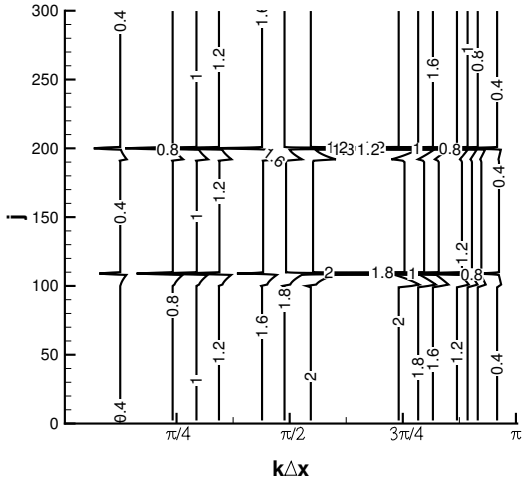

Fig. 8.3. Isocontours of the dispersion coefficient ϕ_j for the HCS1 scheme at CFL=0.1

Tab. 8.2. Cell position, legend, and associated flux types. Note that left and right sides concern a 1D domain with a positive advection speed.

Legend	Flux type on left interface	Flux type on right interface	Cell position
Heun	explicit	explicit	$j = 31$
Heun/Hyb	explicit	hybrid	$j = 100$
Hyb/IRK2	hybrid	implicit	$j = 104$
IRK2	implicit	implicit	$j = 150$
IRK2/Hyb	implicit	hybrid	$j = 196$
Hyb/Heun	hybrid	explicit	$j = 200$

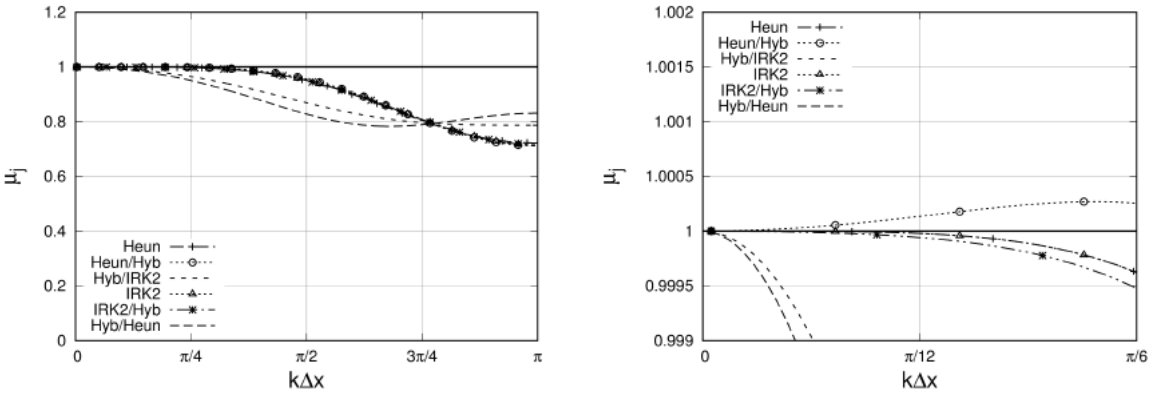

Fig. 8.4. Dissipation μ_j of the scheme HCS1 for all kinds of cells at CFL=0.1

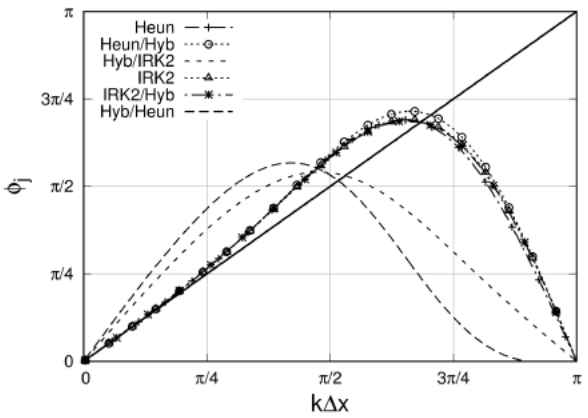

Fig. 8.5. Dispersion ϕ_j of the scheme HCS1 for all kinds of cells at CFL=0.1

8.2.2 Analysis at CFL=0.6

The same analysis is performed now at CFL=0.6, which is the stability limit for Heun's scheme since above it, amplification for some wavenumbers occurs. Dissipation and dispersion curves are given in Figs. 8.6 and 8.7 for the set of cells introduced in Tab. 8.2. The dispersion behaviour of the Heun/Hybrid scheme is quite similar to one of Heun's scheme and presents a change of phase sign for $k\Delta x \simeq 1.8$. The rate of amplification observed at CFL=0.6 is much higher than at CFL=0.1. The discrete jumps on dispersion curves in Fig. 8.7 at $k\Delta x \simeq 1.2, 1.6, 1.8, 2.2, 2.4,$ and 2.6. correspond to values of $k\Delta x$ with maxima of dispersion error, and due to values of normalised wavenumber $k\Delta x$ where $\mathcal{R}e(G_j) = 0$ (from Eq. 6.31).

Moreover, amplification occurs and the level of amplification is much higher than for the CFL=0.1 condition. In case of hybrid parameter ω_j defined to follow some physical features, such numerical amplification in stability range of Heun's explicit scheme may lead to an unacceptable flow or numerical divergence.

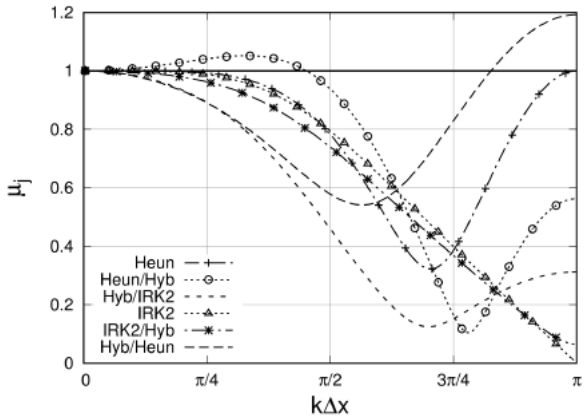

Fig. 8.6. Dissipation μ_j of the scheme HCS1 for all kinds of cells at CFL=0.6

8.3 Conclusion

The HCS1 presented in this chapter is a first tentative to couple IRK2 and Heun's schemes. The procedure is designed to maintain second-order of accuracy. However, the spectral analysis reveals that this straightforward coupling of Heun's, Crank-Nicolson's and TN schemes leads

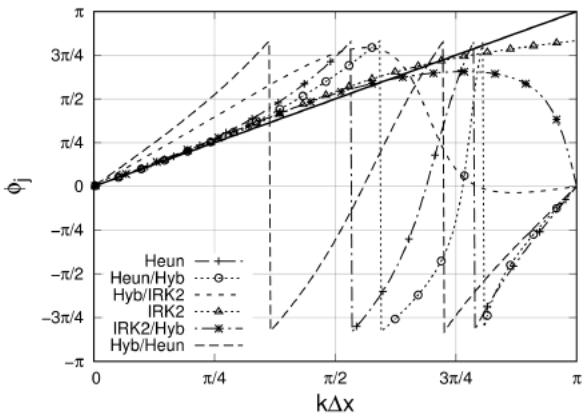

Fig. 8.7. Dispersion ϕ_j of the scheme HCS1 for all kinds of cells at CFL=0.6

to amplification. A new way to couple the desired explicit and implicit schemes is proposed in Sec. 9.

9 Another tIme integratiON (AION) Scheme

9.1 Introduction

In order to improve spectral characteristics observed with HCS1 scheme, a new hybrid scheme still based on both Heun's and Crank-Nicolson's schemes was designed. This new hybrid time integrator is named AION [104] (Another tIme integratiON). For illustration this scheme is applied to the Cauchy problem of Eq. (1.22).

9.2 Formulation

This hybrid scheme has a predictor-corrector formulation as TN's and Heun's schemes. Taking again Tab. 8.1 for the definition of the fluxes and the associated one-dimensional example given on Fig. 8.1, the AION scheme is designed as:

$$\left\{\begin{array}{ll} \text{Predictor step:} & \widehat{W}_j = W_j^n + \Delta t R(W_j^n) \\ \text{Corrector step:} & \left\{\begin{array}{l} W_{j-1}^{n+1} = W_{j-1}^n + \dfrac{\Delta t}{2|\Omega_{j-1}|}(F_{j-\frac{1}{2}}^n + \widehat{F}_{j-\frac{1}{2}} - F_{j-\frac{3}{2}}^n - \widehat{F}_{j-\frac{3}{2}}) \\ W_j^{n+1} = W_j^n + \dfrac{\Delta t}{|\Omega_j|}(F_{j+\frac{1}{2}}^{Hybrid} - \dfrac{F_{j-\frac{1}{2}}^n + \widehat{F}_{j-\frac{1}{2}}}{2}) \\ W_{j+1}^{n+1} = W_{j+1}^n + \dfrac{\Delta t}{|\Omega_{j+1}|}(\dfrac{F_{j+\frac{3}{2}}^n + F_{j+\frac{3}{2}}^{n+1}}{2} - F_{j+\frac{1}{2}}^{Hybrid}) \\ W_{j+2}^{n+1} = W_{j+2}^n + \dfrac{\Delta t}{2|\Omega_{j+2}|}(F_{j+\frac{5}{2}}^n + F_{j+\frac{5}{2}}^{n+1} - F_{j+\frac{3}{2}}^n - F_{j+\frac{3}{2}}^{n+1}). \end{array}\right. \end{array}\right. \tag{9.1}$$

There are two points of difference between AION and HCS1 time integration schemes:

- The residual $R(W_j^n)$, in the predictor step, is still computed thanks to an approximate Riemann solver, but the predictor state $\widehat{W}_j$ will be time-integrated until $\omega_j \Delta t$ only in the hybrid part of AION scheme (i.e. $\widehat{W}_j = W_j^n + \omega \Delta t R(W_j^n)$ for hybrid cells)
- The hybrid flux uses a different reconstruction and it is the key point to maintain stability without amplification.

In hybrid regime, the reconstructed states are defined as:

$$\begin{aligned} W^L = \; & \omega_j \left[\frac{W_j^n + \widehat{W}_j}{2}\right] + \frac{1}{2}(\widetilde{\nabla W})_j^n \cdot \overrightarrow{C_j C_f} + \left(\omega_j - \frac{1}{2}\right)(\widetilde{\widetilde{\nabla W}})_j \cdot \overrightarrow{C_j C_f} + \\ & (1-\omega_j)\left[W_j^{n+1} + (\widetilde{\nabla W})_j^{n+1} \cdot \overrightarrow{C_j C_f} - \frac{1-\omega_j}{2}(\widetilde{\Delta_t W})_j^{n+1}\right], \\ W^R = \; & \omega_i \left[\frac{W_i^n + \widehat{W}_i}{2}\right] + \frac{1}{2}(\widetilde{\nabla W})_i^n \cdot \overrightarrow{C_i C_f} + \left(\omega_i - \frac{1}{2}\right)(\widetilde{\widetilde{\nabla W}})_i \cdot \overrightarrow{C_i C_f} + \\ & (1-\omega_i)\left[W_i^{n+1} + (\widetilde{\nabla W})_i^{n+1} \cdot \overrightarrow{C_i C_f} - \frac{1-\omega_i}{2}(\widetilde{\Delta_t W})_i^{n+1}\right]. \end{aligned} \tag{9.2}$$

The temporal limiter $(\widetilde{\Delta_t W})^{n+1}$ and the one of the TN scheme are equivalent. All details regarding this specific term and the proof of the TVD property are provided in App. A. For $\omega_j = \omega_i = 1$, the following reconstruction is obtained:

$$\begin{aligned} W^L &= \left[\frac{W_j^n + \widehat{W}_j}{2}\right] + \frac{1}{2}(\widetilde{\nabla W})_j^n \cdot \overrightarrow{C_j C_f} + \frac{1}{2}(\widetilde{\widetilde{\nabla W}})_j \cdot \overrightarrow{C_j C_f}, \\ W^R &= \left[\frac{W_i^n + \widehat{W}_i}{2}\right] + \frac{1}{2}(\widetilde{\nabla W})_i^n \cdot \overrightarrow{C_i C_f} + \frac{1}{2}(\widetilde{\widetilde{\nabla W}})_i \cdot \overrightarrow{C_i C_f}, \end{aligned} \tag{9.3}$$

and the hybrid part leads to the Heun's scheme for the one-dimension linear advection equation Eq. (6.30).

For time limiter designed as $\widetilde{\Delta_t W}^{n+1} = W^{n+1} - W^n$ and no gradient reconstruction, the reconstructed states have the following form:

$$\begin{aligned} W^L =& \omega_j \left[\frac{W_j^n + \widehat{W}_j}{2}\right] + (1-\omega_j)\left[\frac{W_j^{n+1} + W_j^n}{2} + \frac{\omega_j}{2}(\widetilde{\Delta_t W})_j^{n+1}\right], \\ =& \omega_j \left[W_{Heun}^L\right] + (1-\omega_j)\left[W_{IRK2}^L + \frac{\omega_j}{2}(\widetilde{\Delta_t W})_j^{n+1}\right], \\ W^R =& \omega_i \left[\frac{W_i^n + \widehat{W}_i}{2}\right] + (1-\omega_i)\left[\frac{W_i^{n+1} + W_i^n}{2} + \frac{\omega_i}{2}(\widetilde{\Delta_t W})_i^{n+1}\right], \\ =& \omega_i \left[W_{Heun}^R\right] + (1-\omega_i)\left[W_{IRK2}^R + \frac{\omega_i}{2}(\widetilde{\Delta_t W})_i^{n+1}\right]. \end{aligned} \tag{9.4}$$

with (W_{Heun}^L, W_{Heun}^R) the state reconstruction corresponding to Heun's scheme and (W_{IRK2}^L, W_{IRK2}^R) to the IRK2 scheme.

9.3 Space-Time Stability Analysis

The spectral analysis previously performed in Sec. 8.2 is now applied to the AION scheme. The spectral behaviour is illustrated in Figs. 9.1 and 9.2 for each cell index $1 \leq j \leq N$ and $k\Delta x \in [0, \pi]$. Regarding the isocontours of μ_j and ϕ_j, the spectral behaviour in terms of dissipation and dispersion is strongly dependent on the cell index j *via* the cell status ω_j as it was illustrated in previous spectral analysis of the HSC1 scheme.

As previously, the spectral behaviour at the six values of j introduced in Tab. 8.2 at CFL=0.1 and CFL=0.6 are still studied. As expected, Fig. 9.3 shows that the AION scheme and other time integrator have an equivalent evolution of dissipation for $k\Delta x \in [0, \pi]$ at CFL=0.1. Indeed the global spectral behaviour reveals that dissipation curves have equivalent behaviour at each cell index. The zoom for $k\Delta x \in [0, 0.6]$ does not reveal any numerical amplification (Fig. 9.3). Furthermore Fig. 9.4 shows that all schemes exhibit approximately the same dispersion properties. Finally the AION scheme allows to remove the spectral limitation of the initial HCS1 scheme at CFL=0.1. At CFL=0.6, the same conclusion is obtained in light of Figs. 9.5-9.6.

The stability of the AION scheme for linear advection has been demonstrated. The hybrid parameter ω_j is set to vary between 0 and 1. The reconstructed states at interface allow to recover the standard explicit scheme of Heun for the linear equation for $\omega_j = 1$. The main goal of AION scheme is to allow a smooth transition from explicit to implicit schemes thanks to hybrid region and it would be useful to switch as fast as possible to the implicit formulation. In the next section, attention is paid on the transition between implicit and hybrid cells.

9.3.1 Analysis of the Hyb/IRK2 and IRK2/Hyb Transitions

The following analysis is performed in order to define the suitable value of the hybrid parameter ω that allows to switch as fast as possible to the implicit formulation. The computational

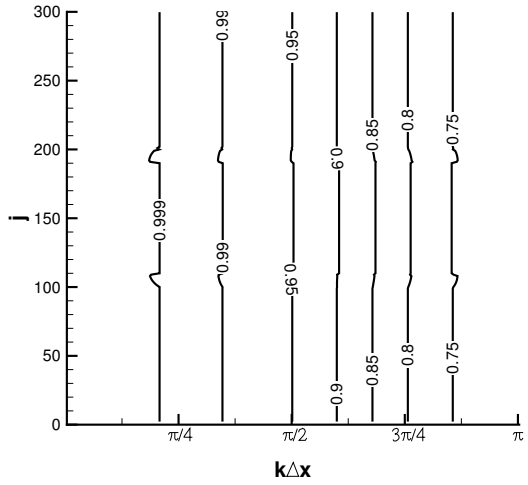

Fig. 9.1. Isocontours of the dissipation μ_j for the AION scheme and $1 \leq j \leq N$ at CFL=0.1

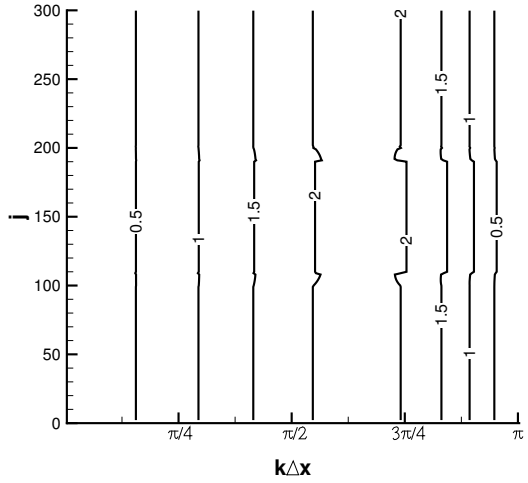

Fig. 9.2. Isocontours of the dispersion ϕ_j for the AION scheme and $1 \leq j \leq N$ at CFL=0.1

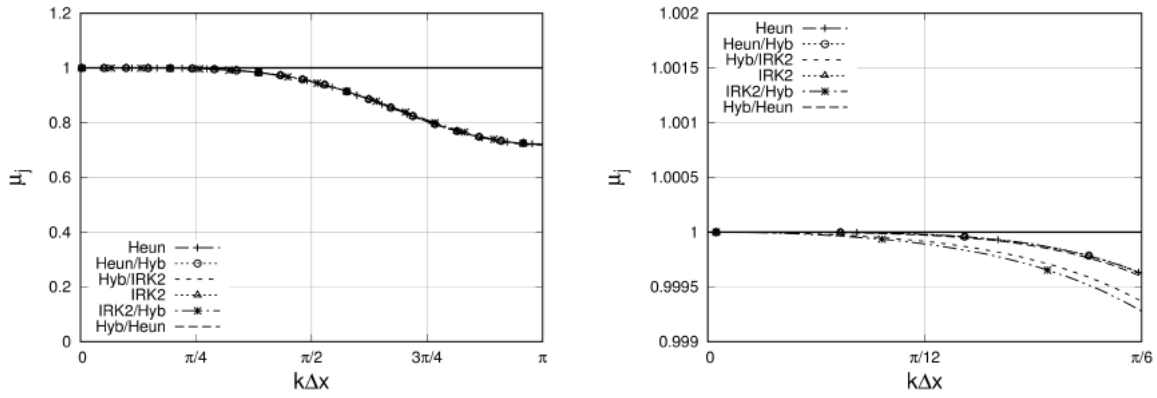

Fig. 9.3. Dissipation μ_j of the scheme AION depending on the kind of cell at CFL=0.1

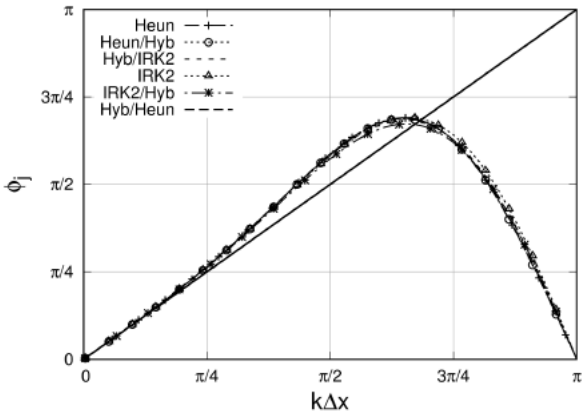

Fig. 9.4. Dispersion ϕ_j of the scheme AION depending on the kind of cell at CFL=0.1

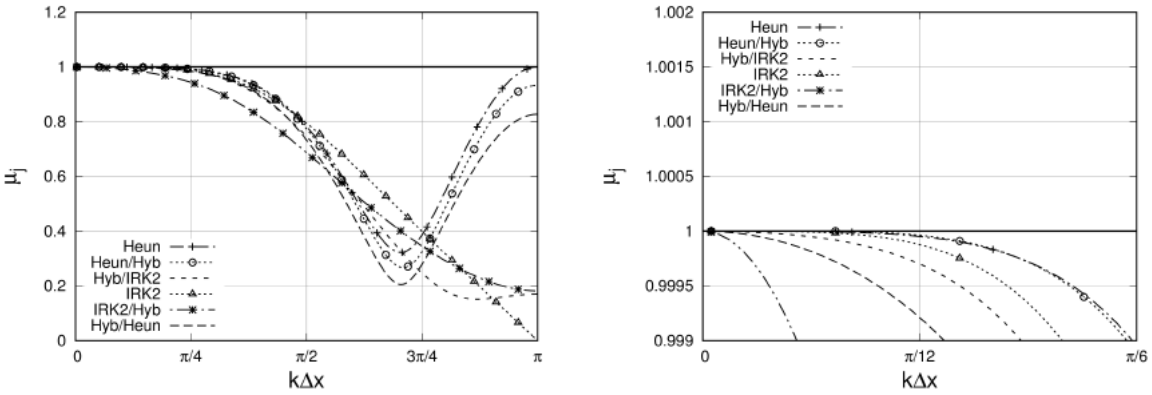

Fig. 9.5. Dissipation μ_j of the scheme AION depending on the kind of cell at CFL=0.6

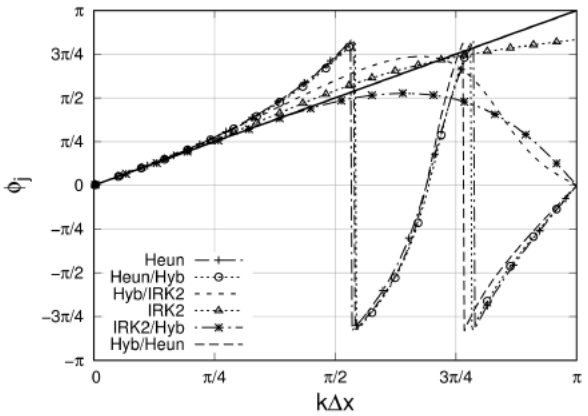

Fig. 9.6. Dispersion ϕ_j of the scheme AION depending on the kind of cell at CFL=0.6

domain with 300 cells is split into two parts. The 1-exact spatial scheme is used. Half of the domain is dedicated to the hybrid part of the AION scheme while the rest of the domain is dedicated to the IRK2 scheme. The study is focused on the transition between these two schemes. Two configurations are chosen for spectral analysis, one for the wave advected from the hybrid domain to the implicit domain, and one for the wave advected from the implicit domain to the hybrid domain.

Figs. 9.7 show the dissipation coefficient for CFL=0.5 and for CFL=0.6 at the transition from the hybrid scheme to the implicit scheme. Amplification may occur for this transition Hyb/IRK2. Figs. 9.8 show the dissipation coefficient for CFL=0.5 and for CFL=0.6 at the transition from the implicit scheme to the hybrid scheme. No amplification region appears. Nevertheless, a stable formulation up to CFL=0.6 is obtained for $\omega_j \leq 0.6$ for all transitions. This motivated our final choice to design the AION scheme to switch at $\omega_j = 0.6$ between the hybrid flux computation and the implicit Runge-Kutta scheme.

From now on, $\omega_j = 1$ will lead to the Heun's scheme, $\omega_j < 0.6$ will lead to the IRK2 scheme. The new hybrid reconstruction method based on the reconstructed states of Eq. (9.2) is applied for $0.6 \leq \omega_j \leq 1$.

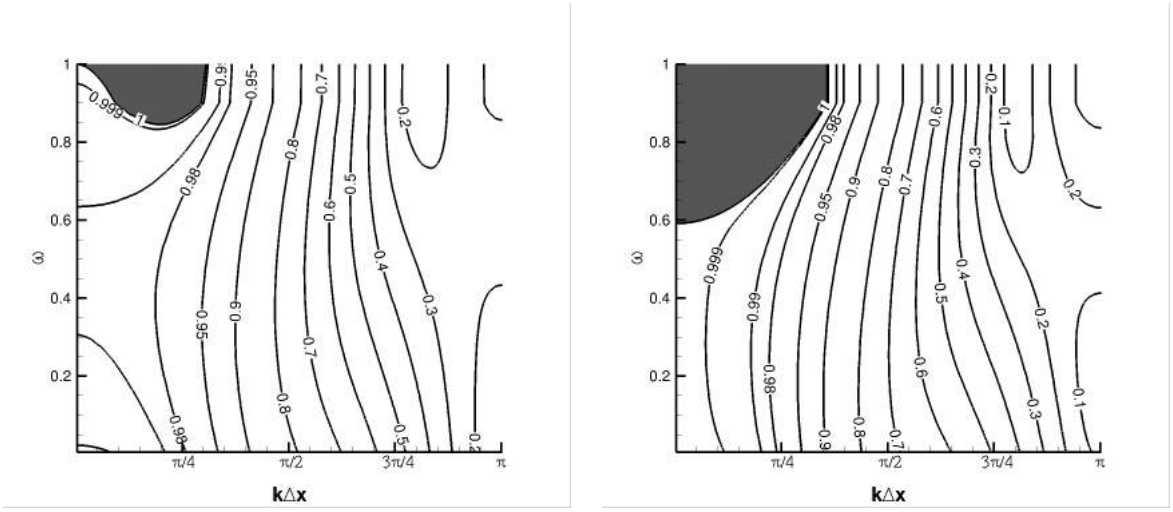

Fig. 9.7. Isocontours of the dissipation μ_j for Hyb/IRK2 transition at CFL=0.5 (left) and CFL=0.6 (right) as a function of ω_j and $k\Delta x$. The grey area represents the area of amplification.

9.3.2 Analysis of $q-$waves

In this section, the q-waves analysis previously performed for the temporal adaptive version of Heun's scheme in Sec. 6.2.4, is adapted to analyse the effect of coupling time integrators.

For this study, a mesh composed of 300 cells is considered with the same manufactured choice of ω_j used in Secs. 8.2 and 9.3. The numerical phase speed c_j^N and the numerical group velocity V_j^{gN} are obtained from G_j (Eq. (6.31)) for any cell j (and therefore for a given ω_j) time-integrated by the AION scheme. The analysis of q-waves is performed for CFL $\in [0, 1]$. The analysis will be focused on the computation of the group velocity V_j^{gN} for the different intersections of time integrators in AION scheme.

According to Figs. 9.9 and 9.10(a), the area of negative-V_j^{gN} group velocity is slightly more expanded for Heun/Hyb cells than for the pure Heun's scheme. Indeed the negative group-velocity zone is expanded until CFL=0.57 at Heun/Hyb cells while the full Heun's scheme negative-group-velocity zone is present up to CFL=0.47. Furthermore, Figs. 9.10(b) and 9.10(c) reveal that this negative group-velocity zone is larger for the other transitions. It appears that

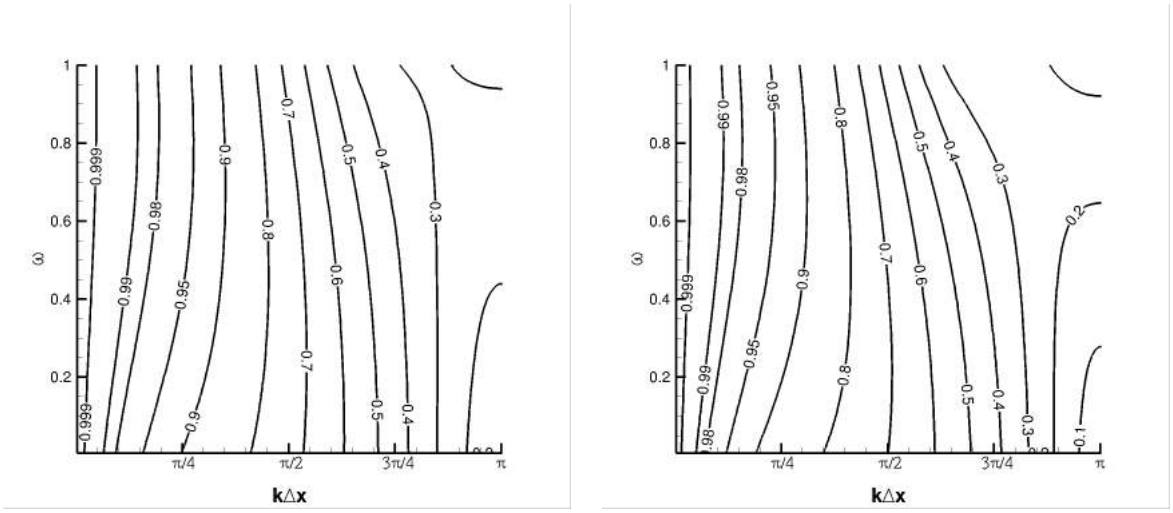

Fig. 9.8. Isocontours of the dissipation μ_j for IRK2/Hyb transition at CFL=0.5 (left) and CFL=0.6 (right) as a function of ω_j and $k\Delta x$. The coupled approach is always stable

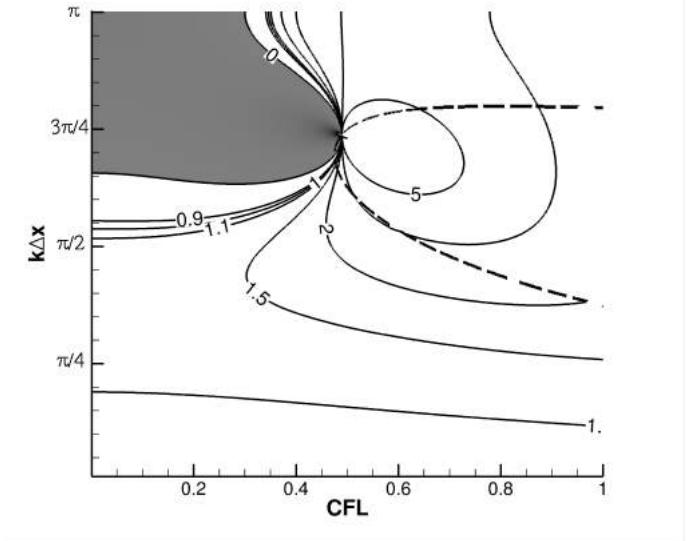

Fig. 9.9. Isocontours of V^{gN} for full Heun's scheme

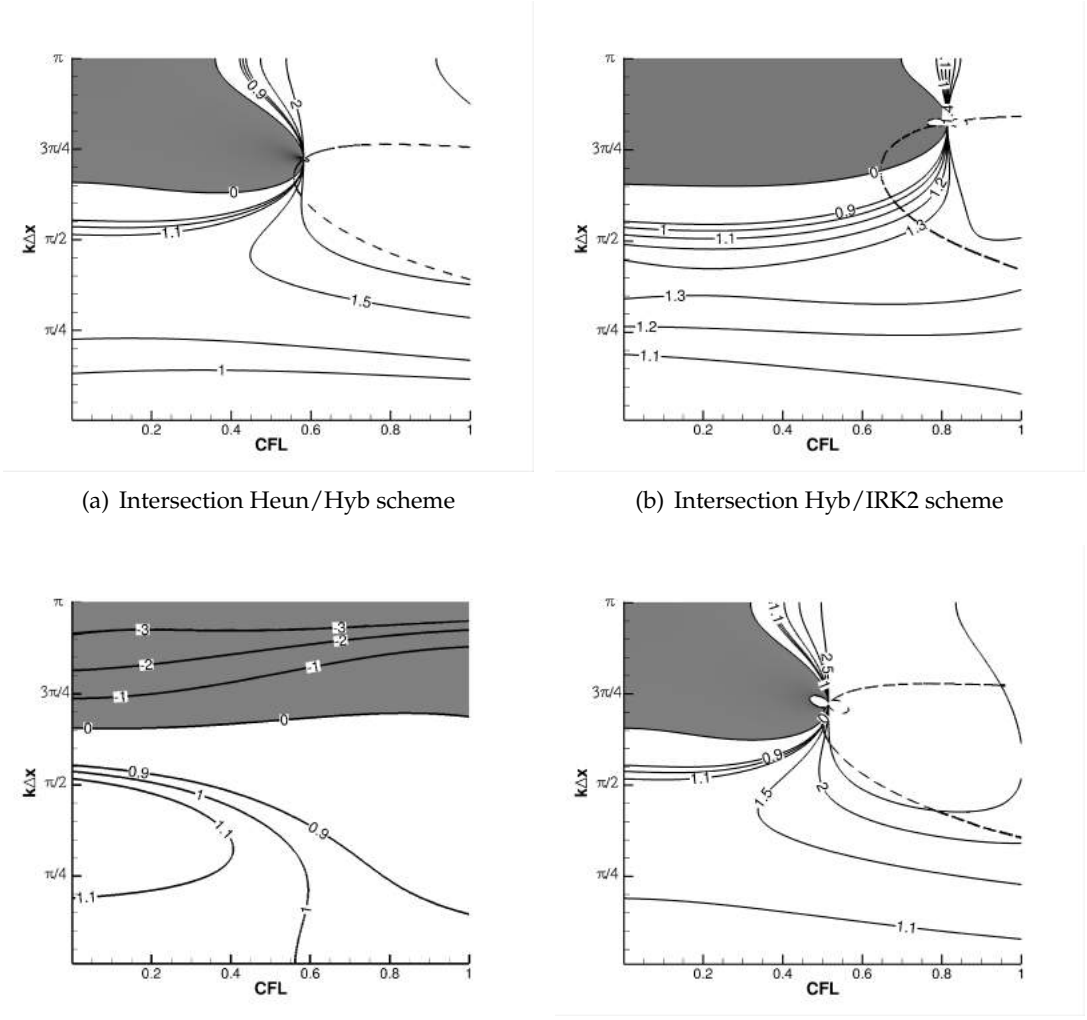

(a) Intersection Heun/Hyb scheme

(b) Intersection Hyb/IRK2 scheme

(c) Intersection IRK2/hyb scheme

(d) Intersection Hyb/Heun scheme

Fig. 9.10. Isocontours of V^{8N}.

the presence of q-waves is subject to a larger range of CFL in case of AION time integration compared with full standard explicit Heun's scheme.

It remains to discuss the capability of the AION scheme to dissipate possible q-waves that could appear. For our investigations, negative group velocity and dissipation properties of the AION scheme will be coupled and illustrated in Figs. 9.11-9.12(d).

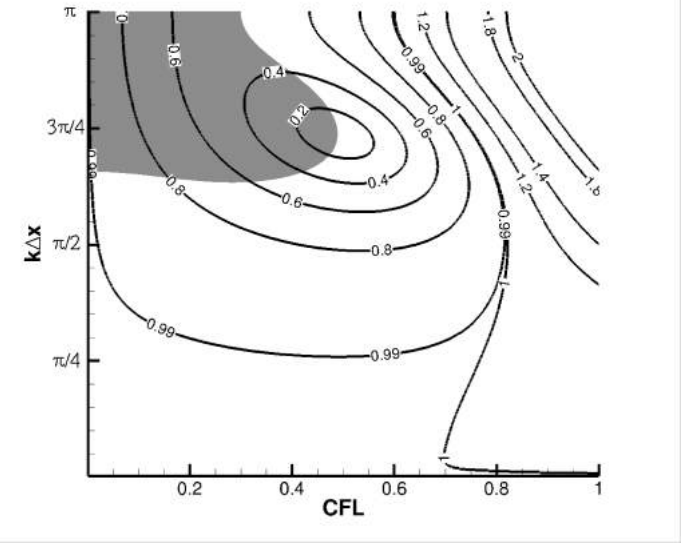

Fig. 9.11. Isocontours of the dissipation μ_j for the standard Heun's scheme and grey zone for negative group velocity

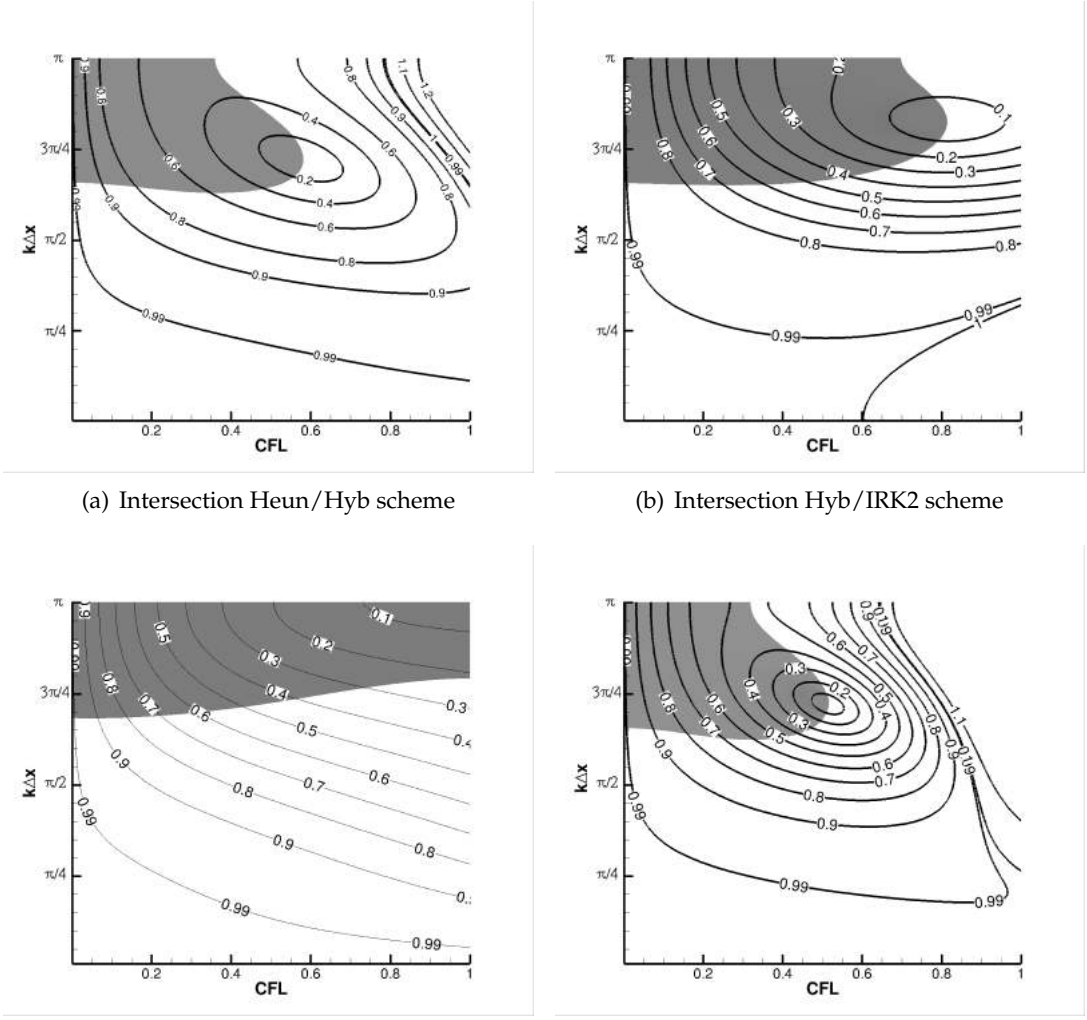

(a) Intersection Heun/Hyb scheme

(b) Intersection Hyb/IRK2 scheme

(c) Intersection IRK2/hyb scheme

(d) Intersection Hyb/Heun scheme

Fig. 9.12. Isocontours of the dissipation μ_j and grey zone for negative group velocity

It appears that, according to Fig. 9.11, the dissipation μ_j is lower than 0.2 at the CFL limit of the negative-V^{gN} zone (CFL=0.47) in case of Heun's time integration. While, for time integrator transitions of AION scheme, the dissipation at their own CFL limit of negative-V^{gN} zone corresponds to $\mu_j < 0.3$ for cell Heun/Hyb (Fig. 9.12(a)), $\mu_j < 0.5$ for hyb/IRK2 (Fig. 9.12(b)) and IRK2/Hyb cells (Fig. 9.12(c)), and finally $\mu_j < 0.2$ for cell Hyb/Heun cells (Fig. 9.12(d)). Fortunately it seems that the numerical dissipation can attenuate the extension of the q-waves zone due to our AION scheme.

9.4 Partial conclusion

To conclude, the proposed AION scheme seems to be as stable as the standard explicit Heun's scheme on uniform grid. In addition, q-waves could potentially be dissipated and the spectral behaviour agrees well with the one of the reference scheme (Heun's scheme). So, both spectral and q-waves analysis illustrate a good theoretical behaviour. In the following, numerical simulations will be performed in order to confirm the interest of our AION scheme.

9.5 Validation

In this section, the AION scheme will be validated on several numerical test cases of increasing complexity, from one-dimensional Euler solutions to three-dimensional Navier-Stokes computations and it will be compared to full explicit Heun's and full IRK2 time integrators.

9.5.1 Order of Accuracy

The accuracy of the AION scheme is evaluated with the advection (at velocity $c = 1$) of a sinus wave over a grid of length $L = 1$ ($x \in [0, 1]$) with periodic conditions. The initial state is given by Eq. (6.29).

Regular Grid

The grid size is first kept constant and the number of grid points is N. The parameter ω_j is defined as:

$$\begin{cases} \omega_j = \alpha\, \omega_{j-1} & \text{for } \dfrac{N}{2} - 50 \leq j \leq \dfrac{N}{2} \\ \omega_j = \dfrac{1}{\alpha}\, \omega_{j-1} & \text{for } \dfrac{N}{2} + 1 \leq j \leq \dfrac{N}{2} + 50 \\ \omega_j = 1 & \text{elsewhere.} \end{cases} \tag{9.5}$$

with $\alpha = 0.90$. This choice enables the use of several schemes over the computational domain through some parameters defined by the user. The computation is performed until $3\,s$ of physical time with a fixed time step $\Delta t = 5.10^{-5} s$. The accuracy of the AION is compared to the Heun's explicit scheme, the TN hybrid scheme, and Euler time integrators (explicit and implicit). As expected, the computed total errors E_{tot} in Tab. 9.1 reveal that the AION scheme is as accurate as Heun's and TN schemes. Paying attention to Fig. 9.13 and to Tab. 9.1, the computation of the error slopes needs explanations since it is not convenient to deduce any standard slope for explicit and implicit Euler's schemes. The data given in Tab. 9.1 are obtained by the "fit" function of the gnuplot software and the results gives the slopes that best fits the data using a least-square approximation.

In the following, a Takacs analysis (see Theorem 2.4.2) was performed to obtain the error relative to dissipation and to dispersion (respectively E_{diss} and E_{disp}). This analysis is also necessary to understand the reason why our first-order time accurate integrator (Euler explicit and implicit) gives a slope of total error lower than 1 (see Fig. 9.13). Indeed, the computational error in Eq. (2.50) corresponds to the dissipation error found with Takacs' method (see Fig. 9.14).

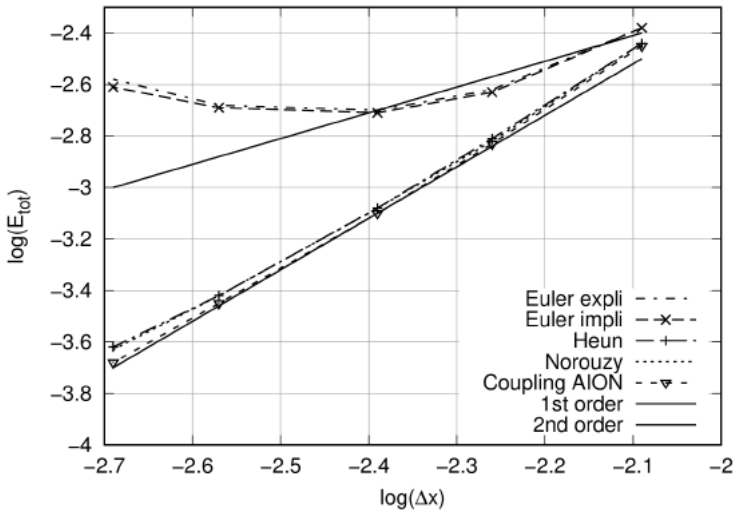

Fig. 9.13. Total error performed with second-order spatial scheme

Time integrator	E_{tot} slope
Euler explicit	0.31
Euler implicit	0.35
Heun	1.97
Norouzi	1.97
Coupling AION	2.04

Tab. 9.1. Total error slopes

For a refined spatial step Δx the dissipation error found with Takacs method is in agreement with the analytical error for (implicit and explicit) Euler time integrators. Note that the dissipation error decreases when the spatial step increases due to the fact that the spatial dissipation of the second-order spatial scheme compensates the negative diffusion of the Euler time integrators. Fig. 9.14 shows that the AION scheme dissipates more than the other second-order time integrators and also that the dissipation error slope of our coupling scheme is smaller than the other second-order schemes (see Tab. 9.2). Nevertheless, Fig. 9.15 demonstrates that the total error is driven by the dispersion and not by dissipation. For Euler's time integrators, the dissipation error drives the total error (see Tables 9.1, 9.2, and 9.3).

Time integrator	E_{diss} slope
Euler explicit	-1.05
Euler implicit	-0.95
Heun	4.81
Norouzi	4.89
Coupling AION	3.04

Tab. 9.2. Dissipation error slopes

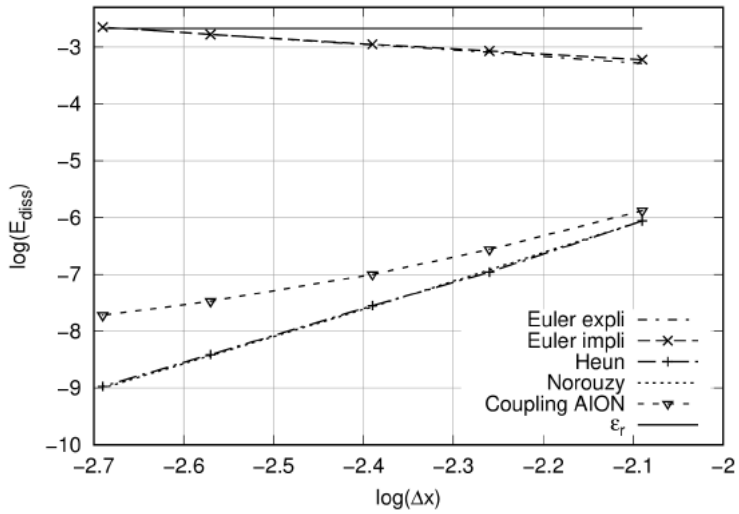

Fig. 9.14. Dissipation error performed with second-order spatial scheme

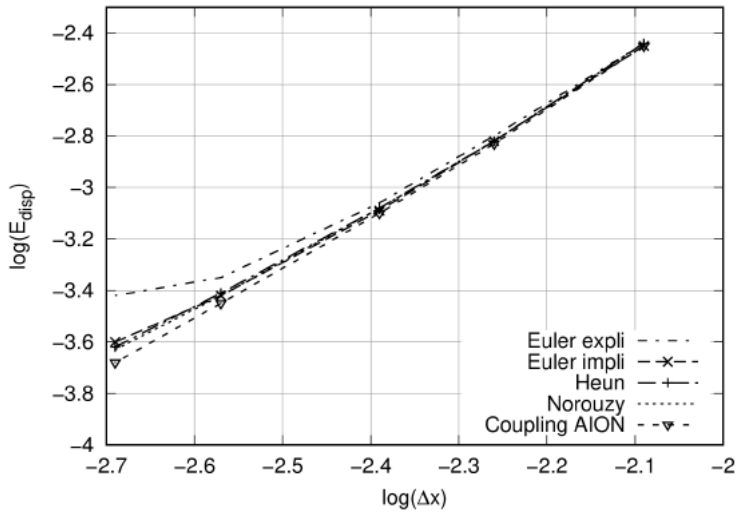

Fig. 9.15. Dispersion error performed with second-order spatial scheme

Time integrator	E_{disp} slope
Euler explicit	1.67
Euler implicit	1.92
Heun	1.96
Norouzi	1.96
Coupling AION	2.04

Tab. 9.3. Dispersion error slopes

Irregular Grid

Now, the same analysis is performed using an irregular grid size defined by:

$$\begin{cases} \Delta x_j = \alpha\, \Delta x_{j-1} & \text{for } \dfrac{N}{2} - \dfrac{N_I}{2} \leq j \leq \dfrac{N}{2} \\ \Delta x_j = \dfrac{1}{\alpha}\, \Delta x_{j-1} & \text{for } \dfrac{N}{2} + 1 \leq j \leq \dfrac{N}{2} + \dfrac{N_I}{2} \\ \Delta x_j = \Delta x_{max} & \text{elsewhere.} \end{cases} \tag{9.6}$$

The parameter N_I is introduced to define the switching area between the schemes, since the parameter ω_j is controlled by the local mesh size:

$$\omega_j = \frac{\Delta x_j}{\Delta x_{max}}. \tag{9.7}$$

This definition of ω_j leads to a fully explicit time integration on the regular part of the grid, where $\Delta x_j = \Delta x_{max}$. The influences of the parameter α and N_I on the order of accuracy will be studied. In this context, the Takacs' method will be performed (again) to analyse the influence of irregular grid and hybrid time integration on dissipation and dispersion error separately. The analysis will be performed for several values of $\alpha = (0.98, 0.95, 0.9)$ and $N_I = (100, 150, 200)$, in order to find if these parameters strongly influence the order of accuracy.

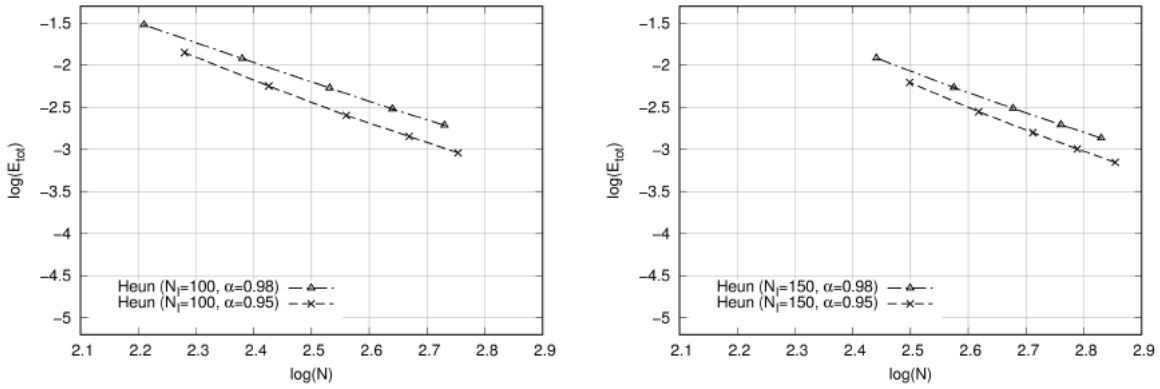

Fig. 9.16. Influence of α on total error of Heun's scheme for $N_I = (100, 150)$

In Figs. 9.16, 9.18 and 9.17, the analysis is focused on the influence of α for a fixed N_I. It appears that for the all time integrators, the parameter α has a little influence on the value of error as well as on the slope (Tab. 9.4). Note that the Heun's scheme does not converge for $\alpha = 0.9$ and $N_I = 200$ due to a too much restrictive CFL condition for our fixed time step ($\Delta t = 5.10^{-5} s$). For high number of hybrid/implicit cells ($N_I = 200$) the value α has a high influence on error value of the AION and IRK2 scheme. Indeed the decrease of α tends to increase the total error that converges for $\alpha = 0.95$ and $\alpha = 0.9$. But the value of the slope (which corresponds to the order of accuracy) is not influenced by this parameter. According to Tab. 9.4 the slope values vary between -2.3 and -2.9 and it appears that the increase of irregular cells (smaller than the reference ones) tends to improve accuracy of all the schemes. This is not really surprising since the error is controlled locally by the mesh size. The decrease of the parameter α, which corresponds to the decrease of cell size, tends also to improve accuracy of Heun's and AION schemes. Nevertheless the order of accuracy of the IRK2 scheme tends to slightly decrease with this parameter.

Figs. 9.19, 9.21 and 9.20 reveal the influence of N_I for a fixed value of α. It appears that for the all time integrators, the influence of N_I tends to decrease with the parameter α. Furthermore the values of error and slope are quite similar for all the schemes.

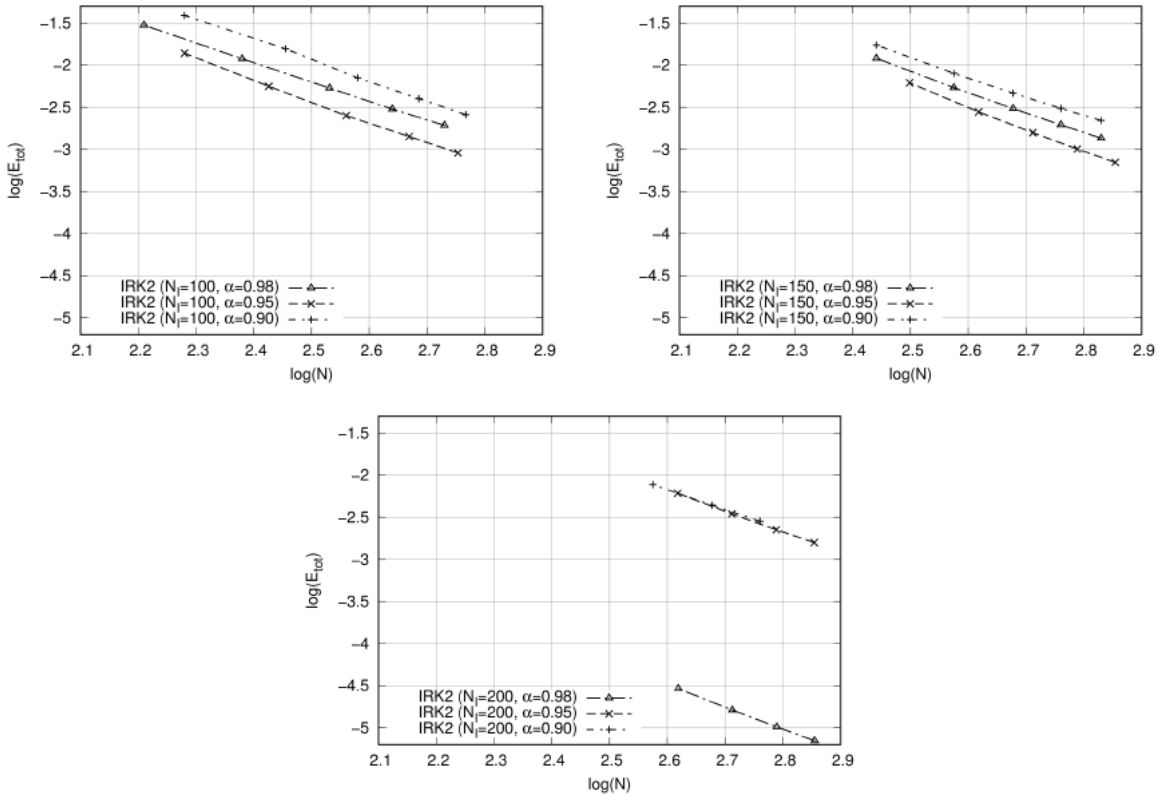

Fig. 9.17. Influence of α on total error of IRK2 scheme for $N_I = (100, 150, 200)$

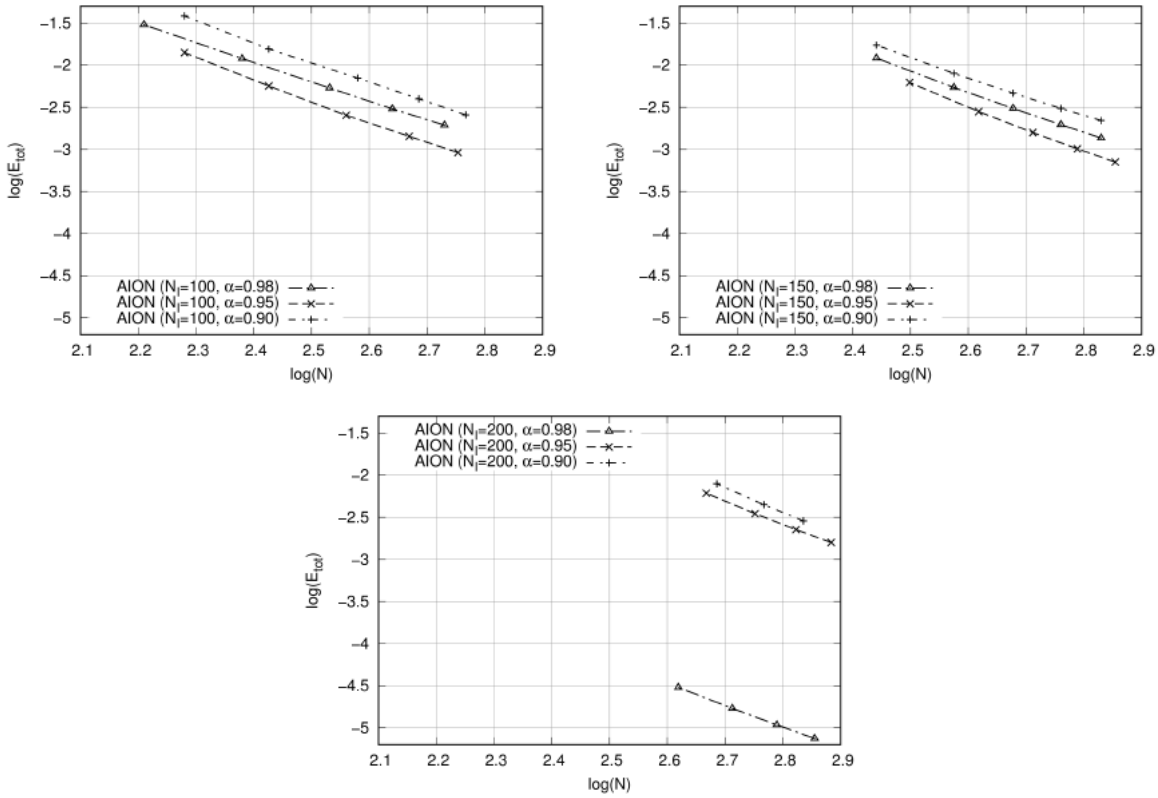

Fig. 9.18. Influence of α on total error of AION scheme for $N_I = (100, 150, 200)$

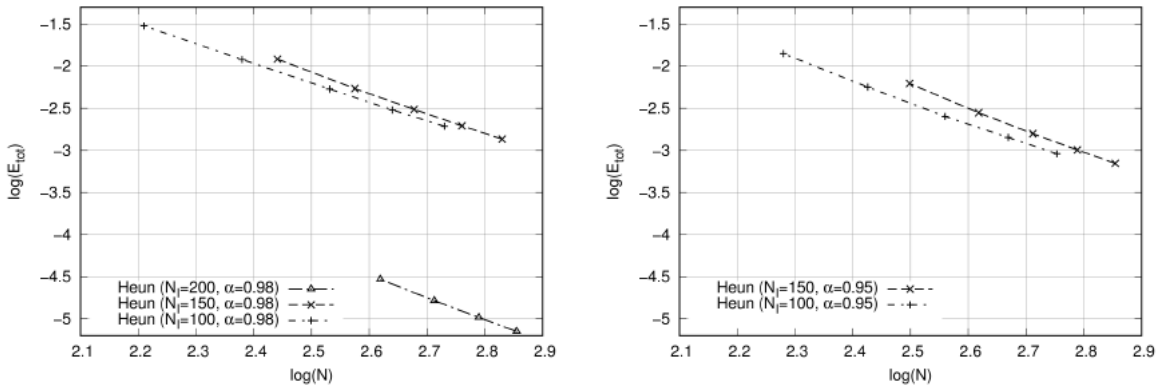

Fig. 9.19. Influence of N_i on total error of Heun's scheme for $\alpha = (0.98, 0.95)$

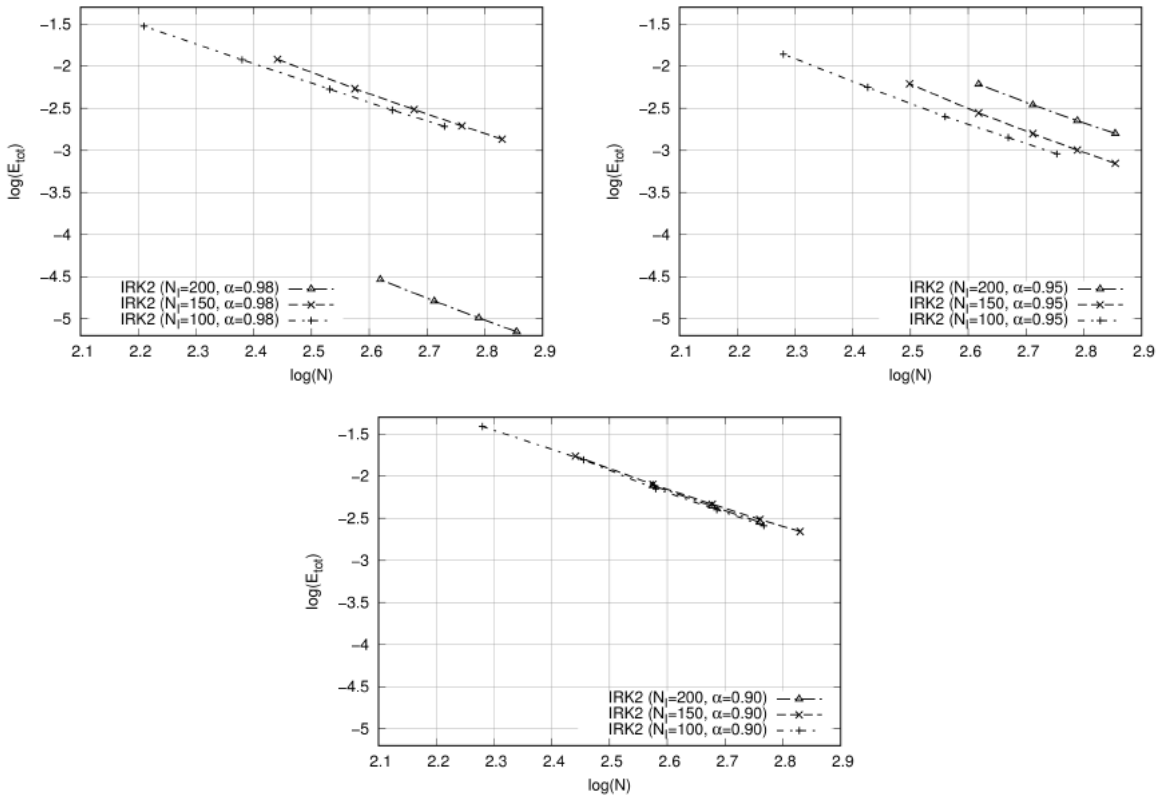

Fig. 9.20. Influence of N_I on total error of IRK2 scheme for $\alpha = (0.98, 0.95, 0.9)$

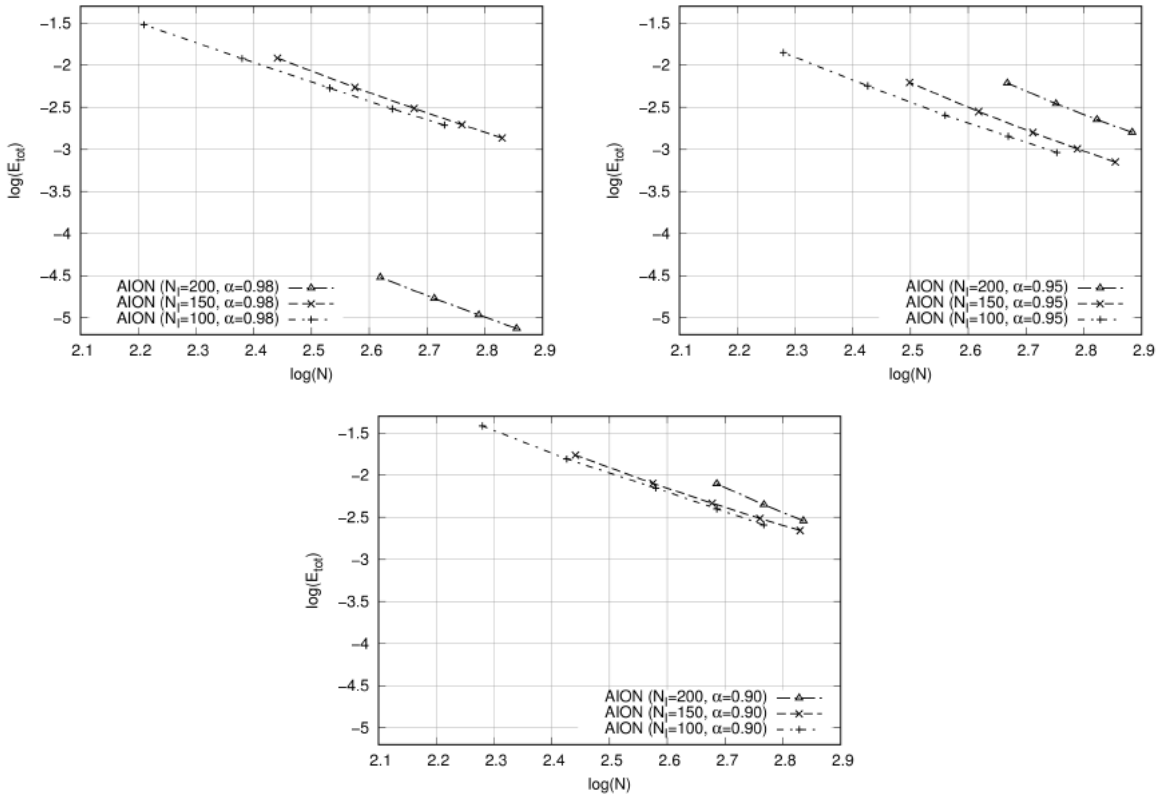

Fig. 9.21. Influence of N_I on total error of AION scheme for $\alpha = (0.98, 0.95, 0.9)$

In the following, the influence of α and N_I on the dissipation and dispersion errors will be analysed thanks to Takacs' method applied to irregular grids (Eq. (2.36)). As the analysis on regular grid, it appears that the dispersion error is predominant on total error even in case of irregular grids. Hence the following analysis will focused the dissipation error only.

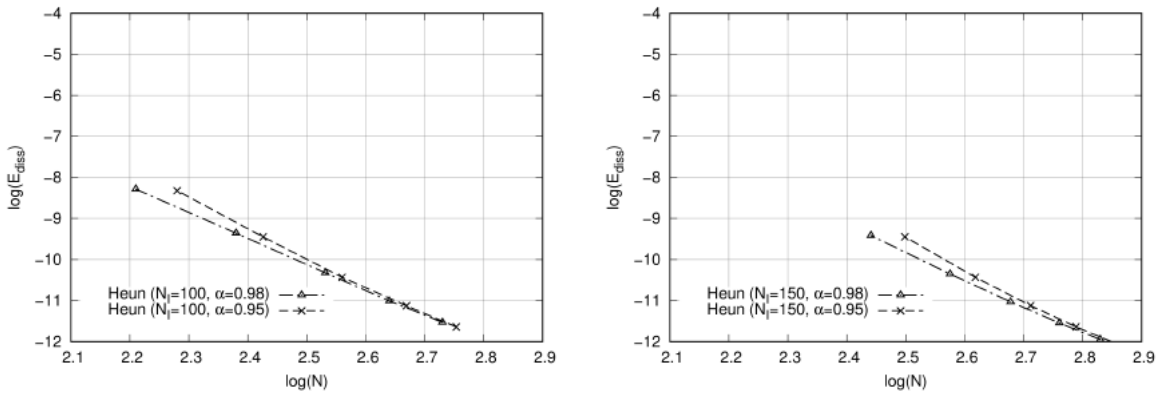

Fig. 9.22. Influence of α on dissipation error of Heun's scheme for $N_I = (100, 150)$

In Figs. 9.22, 9.24 and 9.23 the analysis is focused on the influence of α for a fixed N_I. It appears that the parameter α has a little influence for dissipation error of all the schemes and the same kind of slope is recovered (Tab. 9.5). The IRK2 scheme tends to have a dissipation error greater than AION and Heun's schemes. Figs. 9.25, 9.27 and 9.26 show that the parameter

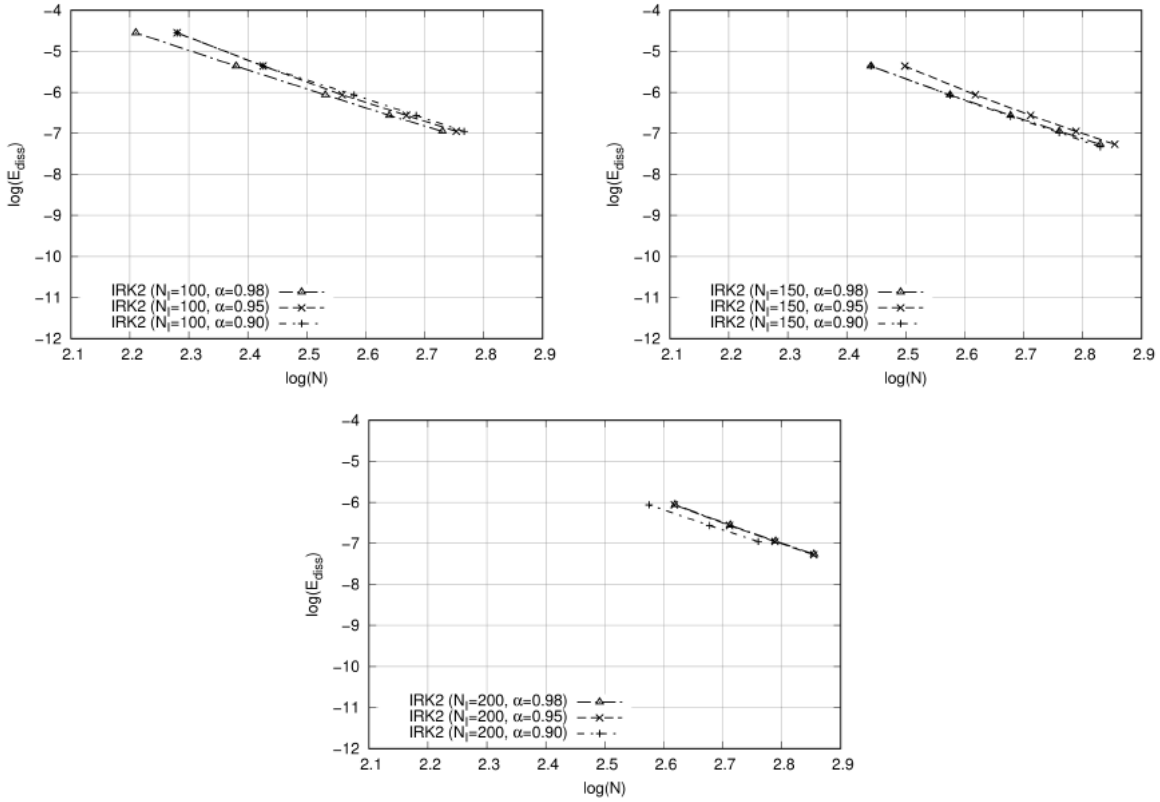

Fig. 9.23. Influence of α on dissipation error of IRK2 scheme for $N_I = (100, 150, 200)$

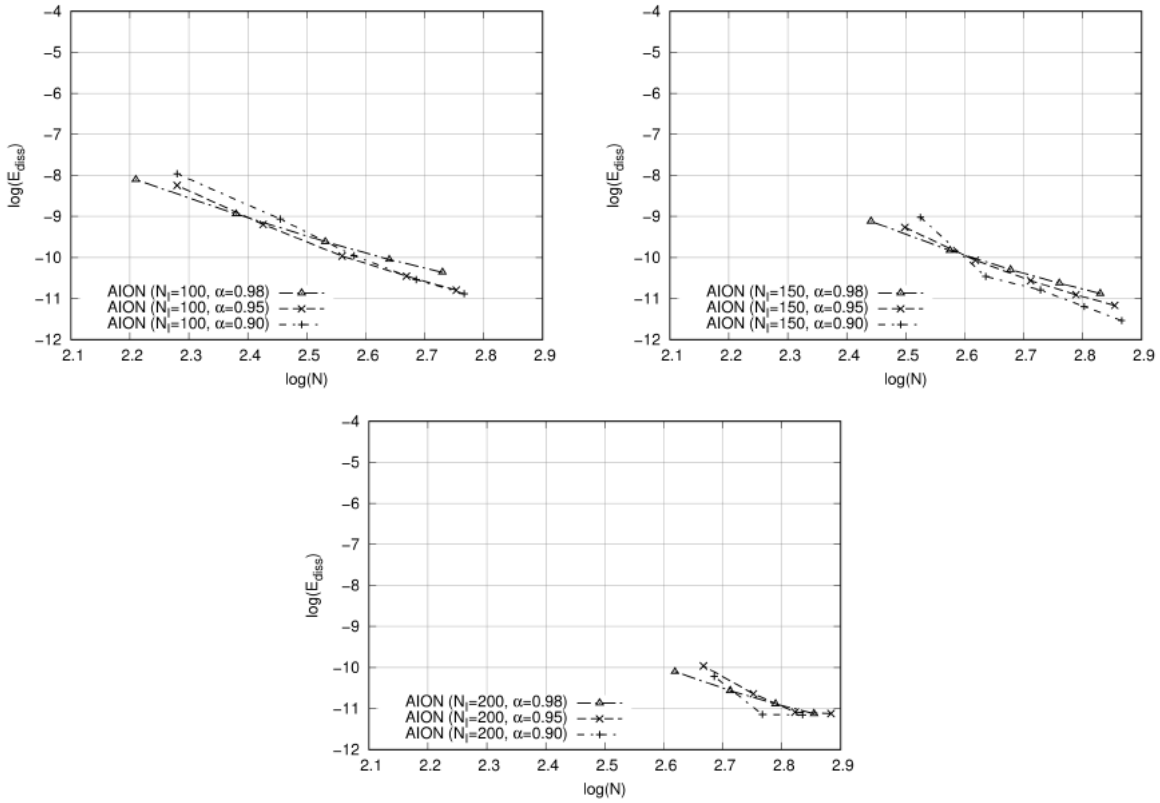

Fig. 9.24. Influence of α on dissipation error of AION scheme for $N_I = (100, 150, 200)$

N_I has a little influence on dissipation error for a fixed α. According to Tab. 9.5 the slope value of dissipation error vary between -4.3 and -7.3.

It appears that conclusion on the behaviour of dissipation and total error are equivalent. Indeed the increase of irregular cells (smaller than reference ones) tends to improve the slope of dissipation error of all the scheme. The decrease of the parameter α, which correspond to the decrease of cell size, tends also to improve slope of dissipation error of Heun's and AION scheme. Nevertheless the slope of dissipation error of the IRK2 tends to slightly decrease with this parameter. In the proposed analysis, the dispersion error takes the leadership on the global order of accuracy for the several time integrators.

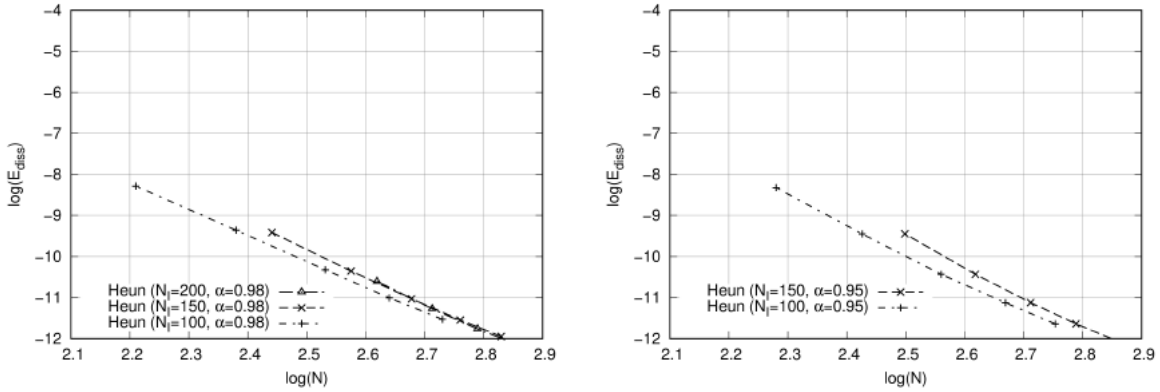

Fig. 9.25. Influence of N_I on dissipation error of Heun's scheme for $\alpha = (0.98, 0.95)$

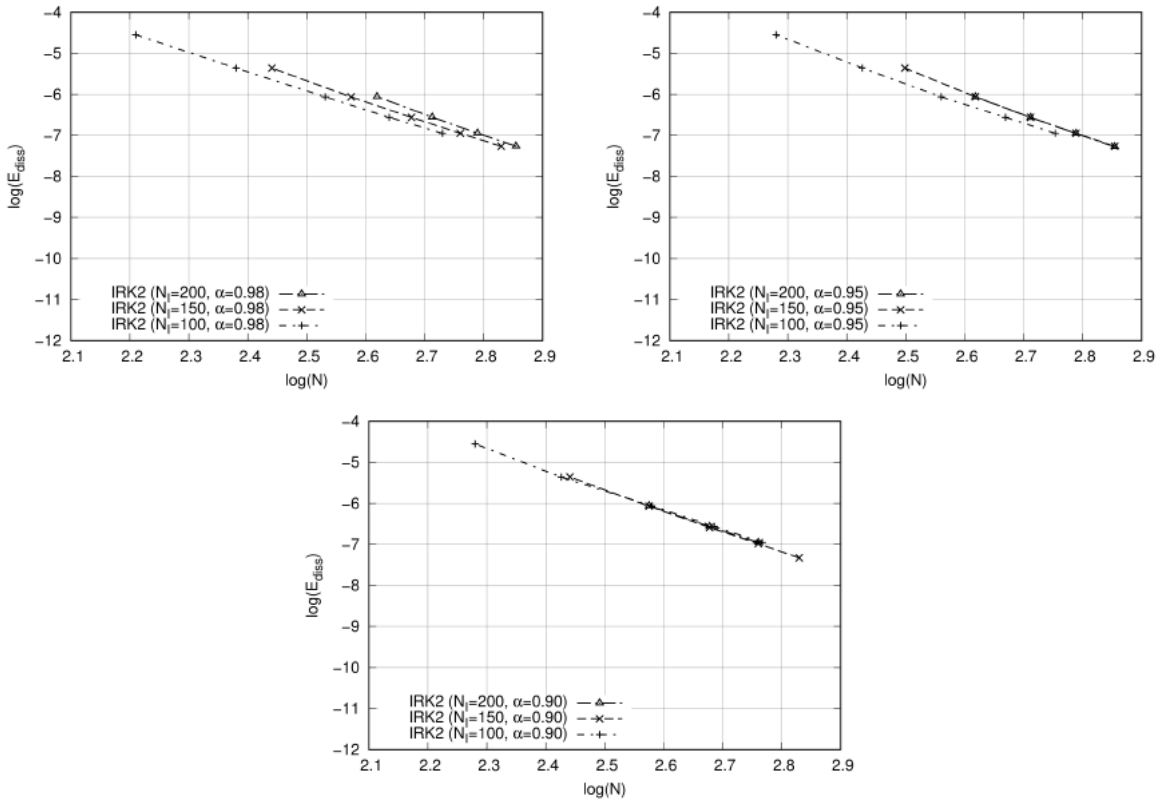

Fig. 9.26. Influence of N_I on dissipation error of IRK2 scheme for $\alpha = (0.98, 0.95, 0.9)$

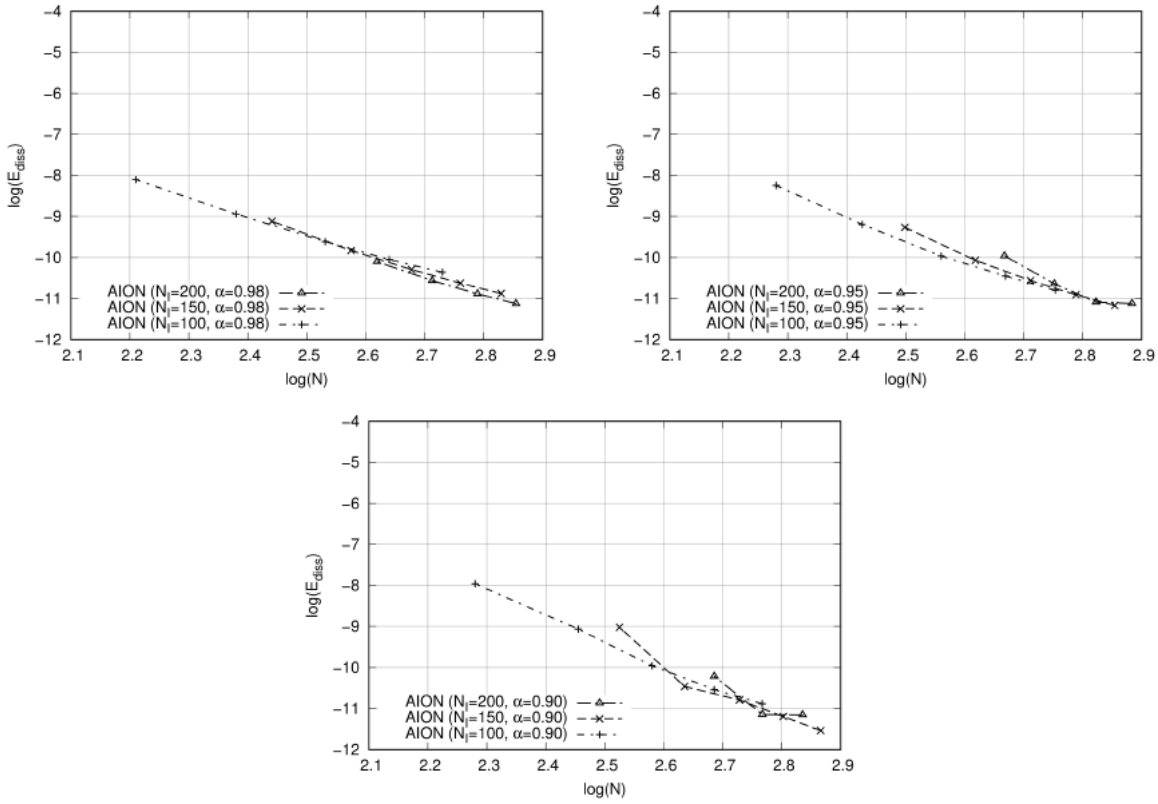

Fig. 9.27. Influence of N_I on dissipation error of AION scheme for $\alpha = (0.98, 0.95, 0.9)$

Tab. 9.4. Slopes of total error E_{tot}

	$N_I = 100$			$N_I = 150$			$N_I = 200$		
	$\alpha = 0.98$	$\alpha = 0.95$	$\alpha = 0.9$	$\alpha = 0.98$	$\alpha = 0.95$	$\alpha = 0.9$	$\alpha = 0.98$	$\alpha = 0.95$	$\alpha = 0.9$
Heun	-2.3	-2.51	x	-2.44	-2.66	x	x	x	x
AION	-2.29	-2.5	-2.38	-2.43	-2.65	-2.62	-2.57	-2.7	-2.9
IRK2	-2.29	-2.5	-2.44	-2.43	-2.65	-2.3	-2.62	-2.47	-2,35

Tab. 9.5. Slopes of dissipation error E_{diss}

	$N_I = 100$			$N_I = 150$			$N_I = 200$		
	$\alpha = 0.98$	$\alpha = 0.95$	$\alpha = 0.9$	$\alpha = 0.98$	$\alpha = 0.95$	$\alpha = 0.9$	$\alpha = 0.98$	$\alpha = 0.95$	$\alpha = 0.9$
Heun	-6.27	-7.02	x	-6.53	-7.27	x	x	x	x
AION	-4.53	-5.4	-6.12	-4.52	-5.33	-6.93	-4.33	-5.58	-6.41
IRK2	-4.62	-5.06	-4.87	-4.89	-5.34	-5.05	-5.11	-5.13	-4.82

9.5.2 Sod's Tube

The Sod's tube is an unsteady inviscid one-dimensional test case used to evaluate the properties of the numerical scheme to manage compressible effects. For a computational domain of length $L_x = 1\ m$, a membrane, located at $x = 0.5L_x$, splits into two parts the numerical domain. The initial flow is defined by

$$\begin{pmatrix} \rho_L \\ p_L \\ U_L \end{pmatrix} = \begin{pmatrix} 1.0 \\ 1.0 \\ 0.0 \end{pmatrix}, \begin{pmatrix} \rho_R \\ p_R \\ U_R \end{pmatrix} = \begin{pmatrix} 0.125 \\ 0.1 \\ 0.0 \end{pmatrix}, \tag{9.8}$$

where L refers to the left side and R to the right side of the membrane. At $t = 0$, the membrane breaks. Next, the physics of the flow is characterised by waves travelling inside the computational domain. At the final time $t = 0.2\,s$, the theoretical solution (solution of Euler equations) is composed of a rarefaction wave, a contact discontinuity and a shock.

A 1-exact (second-order) upwind scheme is used to solve Euler equations with the Roe approximate Riemann solver. To avoid spurious oscillation, the minmod slope limiter [105] is used to provide a TVD solution. The numerical domain is composed of $N = 300$ cells composed with regular parts with a uniform mesh size and an irregular part with non-uniform mesh size such as:

$$\begin{cases} \Delta x_j = \alpha\, \Delta x_{j-1} & \text{for } \dfrac{N}{2} - 50 \leq j \leq \dfrac{N}{2} \\ \Delta x_j = \dfrac{1}{\alpha}\, \Delta x_{j-1} & \text{for } \dfrac{N}{2} + 1 \leq j \leq \dfrac{N}{2} + 50 \\ \Delta x_j = \Delta x_{max} & \text{elsewhere.} \end{cases} \tag{9.9}$$

with $\alpha = 0.98$. Then the parameter ω_j is imposed as:

$$\omega_j = \frac{\Delta x_j}{\Delta x_{max}}. \tag{9.10}$$

This design of the hybrid parameter ω_j enables a fully explicit time integration on the regular part of the grid ($\omega_j = 1$), where $\Delta x_j = \Delta x_{max}$. In the following, ν_j is defined by $\nu_j = \frac{\Delta t}{\Delta x_j}$. Several computations are performed and the solutions analysed.

First Set of ν_j

For the minimal value of ν equal to 0.1 in the explicit part of the domain, the maximum value of ν in the implicit part reaches 0.3. The density and velocity profiles are illustrated in Figs. 9.28 and 9.29 with zooms in the region of the rarefaction wave and near the shock. The AION scheme is as accurate as the second-order time accurate standard schemes and also in agreement with the theoretical solution. Moreover, first-order accurate Euler time integrators show a greater dissipation near the compressible characteristics of the solution (rarefication wave and shock).

Second Set of ν_j

A second set of ν_j is chosen now: $\nu_{min} = 0.4$ is applied in the explicit part, which leads to a maximum value of $\nu = 1.01$ in the implicit part of the mesh. Figures 9.30 and 9.31 reveal that the AION and IRK2 schemes are still stable and solutions are very close. No solution is given using Heun's scheme since it is now unstable. Focusing on the velocity and density numerical solution near the shock, the AION scheme appears to slightly dissipate the overshoots compared to the IRK2 implicit scheme.

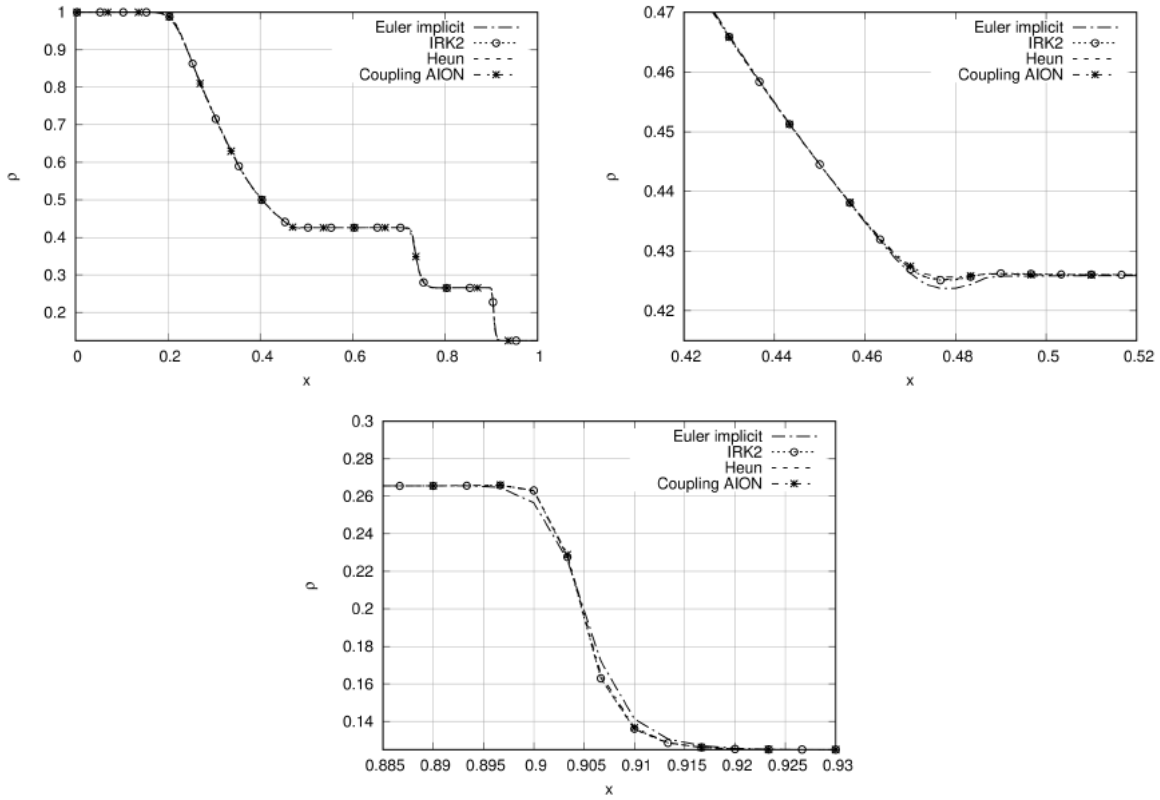

Fig. 9.28. Sod's shock tube at $\nu_{min} = 0.1$. Global view of the density profile at $t = 2s$ and close-up views near the rarefaction wave and near the shock.

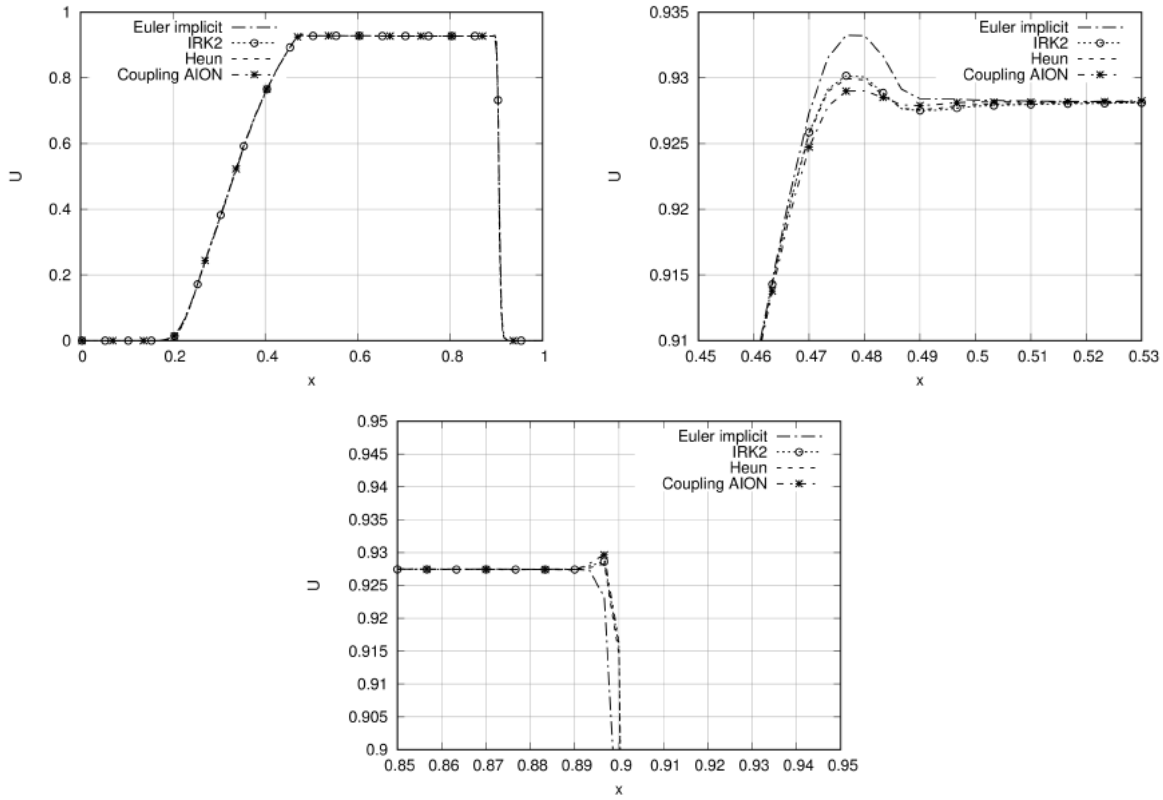

Fig. 9.29. Sod's shock tube at $\nu_{min} = 0.1$. Global view of the density profile at $t = 2s$ and close-up views near the rarefaction wave and near the shock.

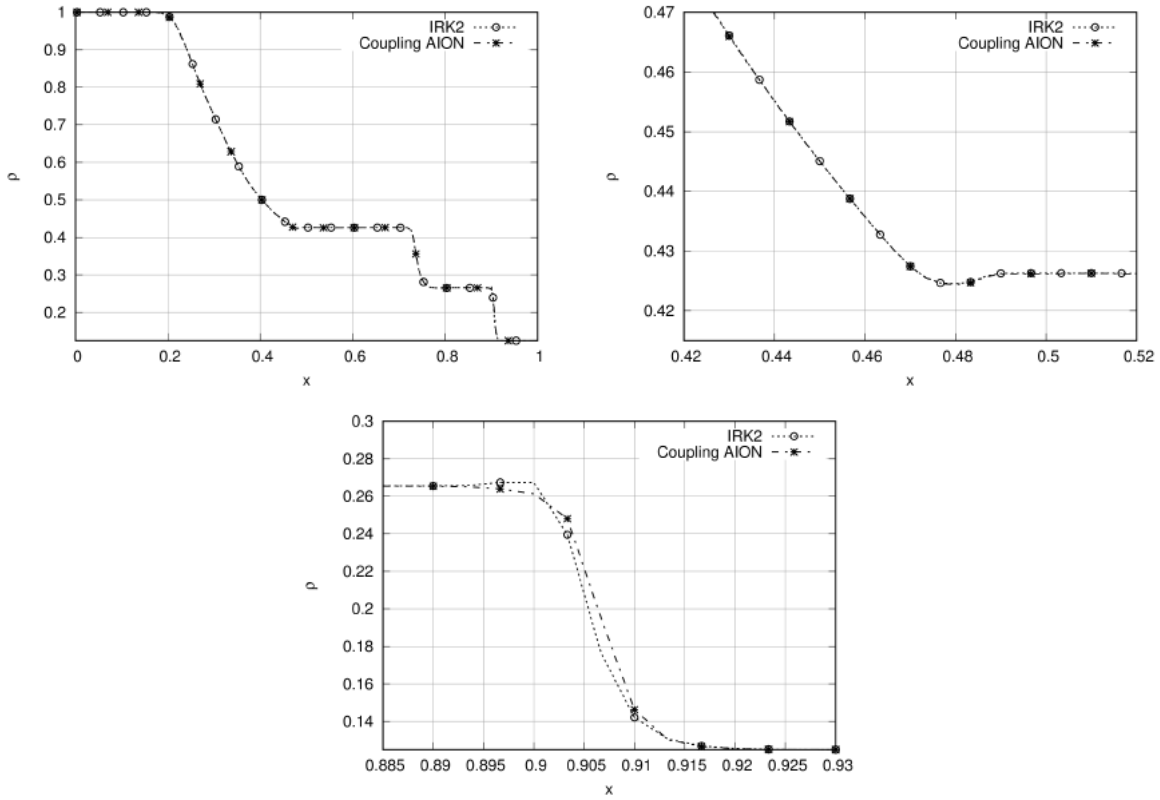

Fig. 9.30. Sod's shock tube at $\nu_{min} = 0.4$. Global view of the density profile at $t = 2s$ and close-up views near the rarefaction wave and near the shock.

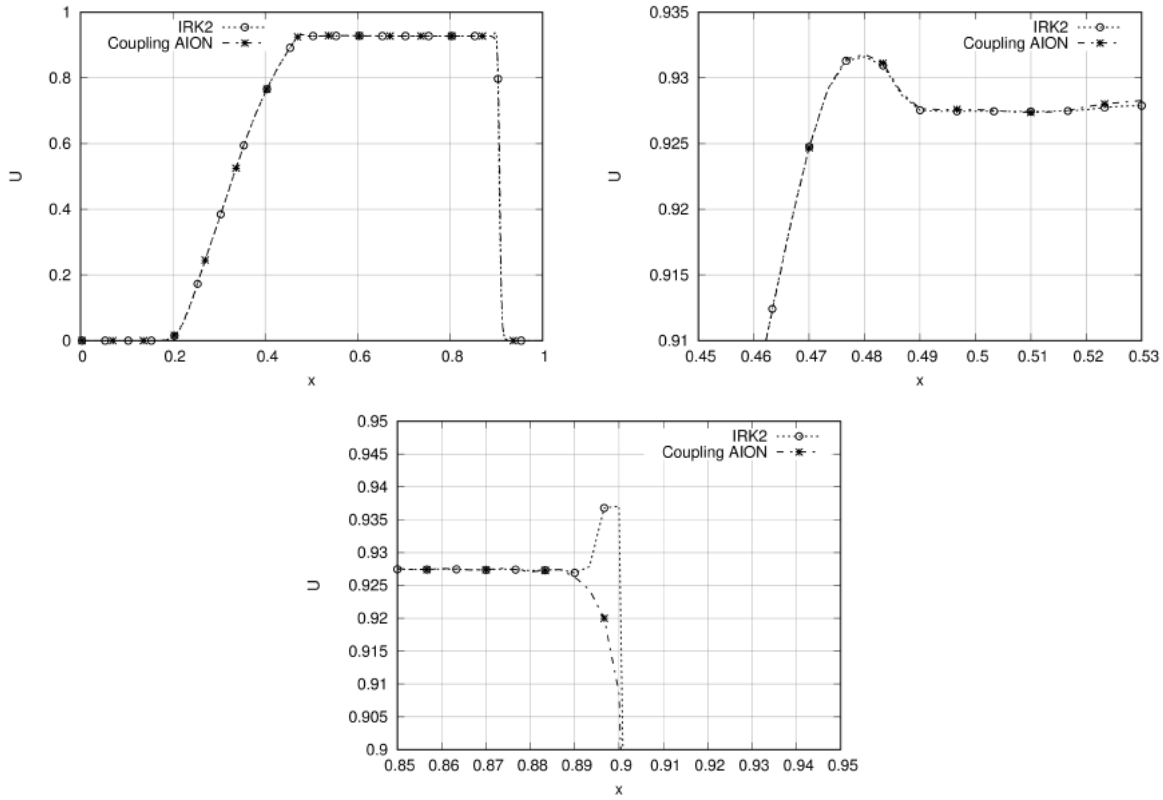

Fig. 9.31. Sod's shock tube at $\nu_{min} = 0.4$. Global view of the density profile at $t = 2s$ and close-up views near the rarefaction wave and near the shock.

Conclusion on Sod Test Case

According to this test case, the flux reconstruction procedure defined in AION scheme allows to manage compressible effects as shock, contact discontinuity and rarefaction wave. Furthermore, the AION procedure improves the Heun's explicit scheme with an enhanced stability and is more computationally efficient than the fully-implicit scheme. The next two dimensional test case is dedicated to the analysis of the scheme accuracy in **FLUSEPA**© solver.

9.5.3 Two-dimensional Linear Advection of an Isentropic Vortex

Thanks to the advection of an isentropic vortex solution of Euler's equations, it is possible to test the solver ability to preserve vorticity in an unsteady simulation. This test case is suitable for verifying total order of accuracy. For the total error E_{total} expressed as:

$$E_{total} = Ah^p + B\Delta t^q + O(h^{p+1}, \Delta t^{q+1}) \tag{9.11}$$

with $(A, B) \in \mathbb{R}^2$, the global order of accuracy is estimated as $min(p, q)$.

Mesh definition and initialization

The computational domain is limited to a square domain $[-\frac{L}{2}, \frac{L}{2}]^2$ ($L = 0.1$) with periodic boundary conditions. An isentropic vortex defined by its characteristic radius R and strength β is super-imposed onto a uniform flow of pressure P_∞, temperature T_∞ and Mach number M_∞. The vortex is initialized in the center of the computational domain $(x_c, y_c) = (0, 0)$. The initial state is defined by:

$$\begin{aligned}
\delta u &= -U_\infty \beta \frac{(y - y_c)}{R} e^{-\frac{r^2}{2}}, \\
\delta v &= U_\infty \beta \frac{(x - x_c)}{R} e^{-\frac{r^2}{2}}, \\
\delta T &= \frac{(U_\infty \beta)^2}{2} . e^{-\frac{r}{2}}, \\
u_0 &= U_\infty + \delta u, \\
v_0 &= \delta v,
\end{aligned} \tag{9.12}$$

with:

$$\begin{aligned}
r &= \frac{\sqrt{(x - x_c)^2 + (y - y_c)^2}}{R}, \\
U_\infty &= M_\infty \sqrt{\gamma \, R_{gas} \, T_\infty}.
\end{aligned} \tag{9.13}$$

with $R_{gas} = 287.15 \; J/kg/K$ the gas constant and a constant ratio of specific heats γ equal to 1.4. The isentropic relation leads to the complete set of initial solution:

$$\begin{aligned}
T_0 &= T_\infty - \delta T, \\
\rho_0 &= \frac{P_\infty}{R_{gas} \, T_\infty} \left(\frac{T_0}{T_\infty}\right)^{\frac{1}{\gamma - 1}}, \\
P_0 &= \rho_0 \, R_{gas} \, T_0
\end{aligned} \tag{9.14}$$

The uniform field is defined to perform the "fast vortex" test case defined by the High-Order Workshop committee:

$$P_\infty = 10^5 \; N/m^2, T_\infty = 300 \; K, M_\infty = 0.5, \beta = \frac{1}{5}, R = 0.005. \tag{9.15}$$

The numerical simulation is performed until three rotations of the vortex inside the periodic box. The computation is performed with a Successive-Correction 2-exact formulation for the

spatial scheme (order three) and time-integrated by Heun's, IRK2 and AION schemes on the baseline Cartesian grids of 64^2, 96^2, 128^2, 192^2 and 256^2 degrees of freedom (DOFs). The time integration of these computations was performed at CFL=0.1.

In order to use the AION time integration, it is mandatory to define the hybrid parameter ω_j. It is controlled according to the following equation:

$$\omega_j = 1 - e^{-\frac{r^2}{2}} \text{ with } r^2 = \frac{(x_j - x_c)^2 + (y_j - y_c)^2}{R^2}. \tag{9.16}$$

Figure 9.32 represents the distribution of ω_j on the 256^2 mesh.

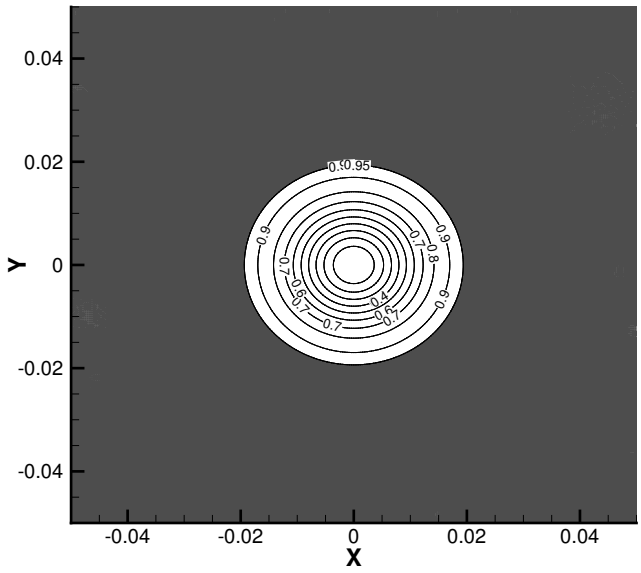

Fig. 9.32. Behaviour of ω_j for the manufactured solution ; the grey zone corresponds to $\omega_j = 1$

Analysis of the Solutions

Figures 9.33 and 9.34 illustrate pressure and velocity fields obtained with Heun's, AION and IRK2 time integrators with the grid of 256^2 DOFs. As it was shown with the previous Sod tube case, it seems that all time integrators have slightly the same spectral properties of dissipation and dispersion (through the definition of max and min pressure and velocity and phase lag of the solutions). The AION scheme tends to be less dissipative than the other second-order time integrators, all being coupled with the 2-exact formulation for the spatial scheme. This result was not obtained with Sod's tube.

Finally, the AION scheme coupled with the third-order accurate space reconstruction tends to improve the space-time spectral characteristics of the computation. Using the two velocity-vector components for computation of the L^2-norm of the error (see Fig. 9.33), it appears, as expected, that the AION time integrator keeps a second-order space-time accuracy (see Tab. 9.7) like Heun's and IRK2 scheme. Furthermore, according to the slope of $log(E_{total})$, it seems that the time integrator has an impact on the computational error. (see Tab. 9.7). Indeed slopes are quite different between $log(h) = [-2.4, -2.1]$ and $log(h) = [-2.1, -1.8]$, particularly in case of the Heun's scheme. Tab. 9.6 allows to compare computation cost of the AION and IRK2 time integrator at the same CFL for this isentropic convected vortex. The ratio between hybrid/implicit cells with $\omega < 1$ and explicit cells with $\omega = 1$ (ratio named "I/E cells" in

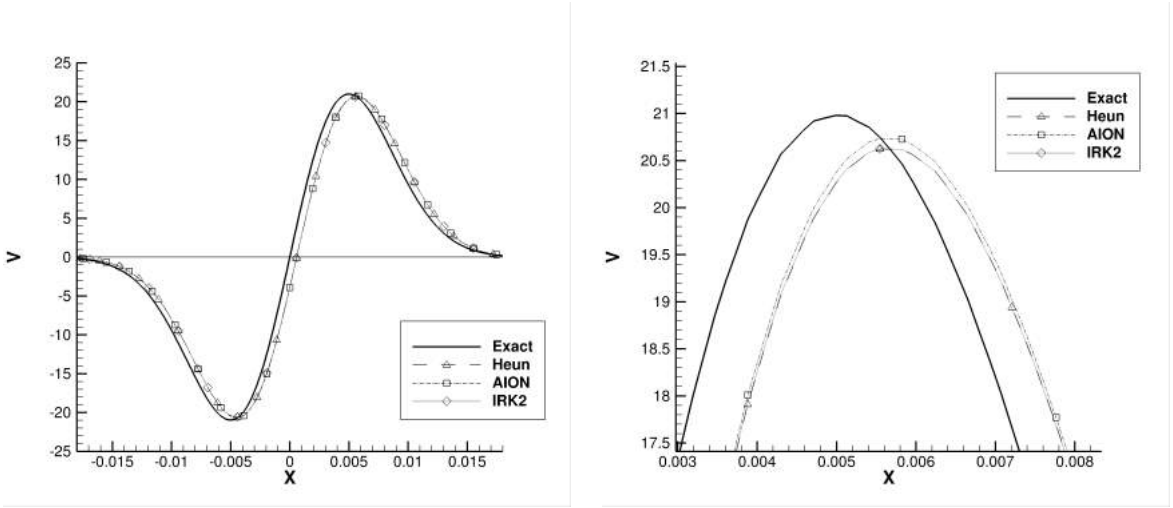

Fig. 9.33. Velocity field (CFL=0.1)

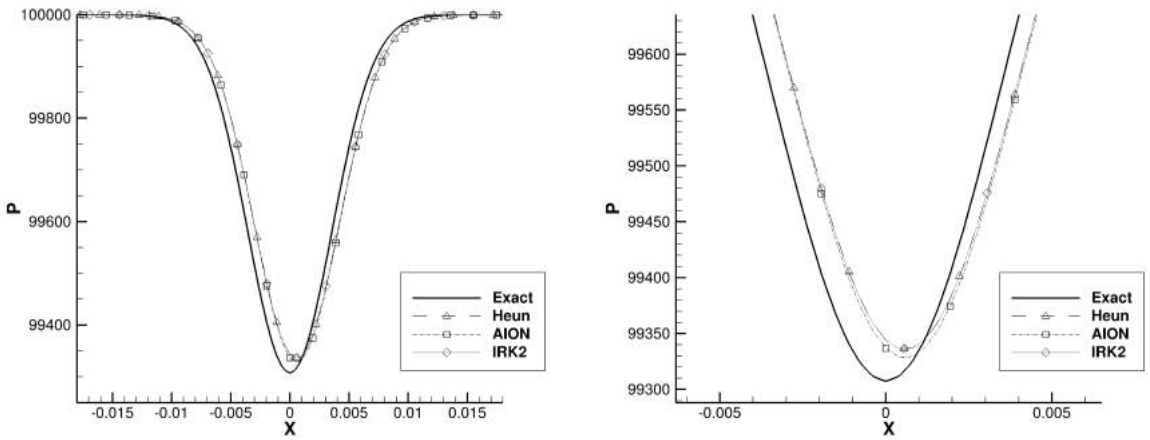

Fig. 9.34. Pressure field (CFL=0.1)

Tab. 9.6) is equal to 18% for all grids. At same CFL and for grid with 256^2 DOFs, the AION scheme seems to reach an overall cost that is about 50% lower than the pure implicit IRK2 scheme.

DOFs	64^2	128^2	256^2
I/E Cells	18%	18%	18%
AION/IRK2	0.75	0.66	0.52

Tab. 9.6. Elapsed CPU time to reach 3 time periods with AION and IRK2 time integrators

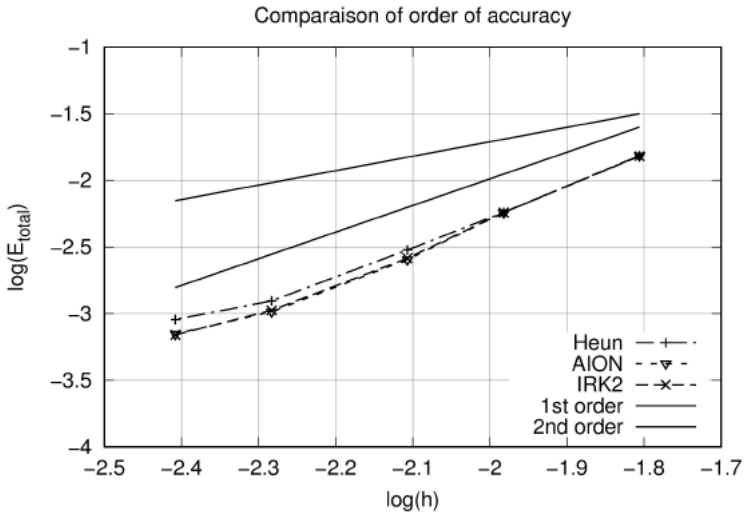

Fig. 9.35. Order of accuracy

Time integrator	$log(E_{total})$ slope
Heun	2.09
AION	2.22
IRK2	2.22

Tab. 9.7. Total error slopes

Analysis with an Irregular Grid

In order to test the stability of the AION scheme, an isentropic vortex convection, on an irregular grid of 260^2 DOFs is also performed. Here, the time integration is performed with a time step designed according to CFL condition of the biggest cells of the domain such as

$$\Delta t = CFL \frac{\max\limits_{j}(h)}{\|\vec{v}_j\|}, \tag{9.17}$$

leading to a ratio between the size of the largest and the smallest cell equal to 11 in this irregular domain. As a consequence, the Courant number is 11 times higher for the smallest cells than for the largest ones. Hence numerical computations during one time period of vortex convection, at several CFL values, allow to illustrate the stability characteristics of the several

time integrators. The parameter ω_j is defined according to the size of cells in the domain (see Fig. 9.36 with explicit cell of $\omega_j = 1$, coloured in grey) such as

$$\omega_j = \frac{|\Omega_j|}{\max_j(|\Omega_j|)}, \tag{9.18}$$

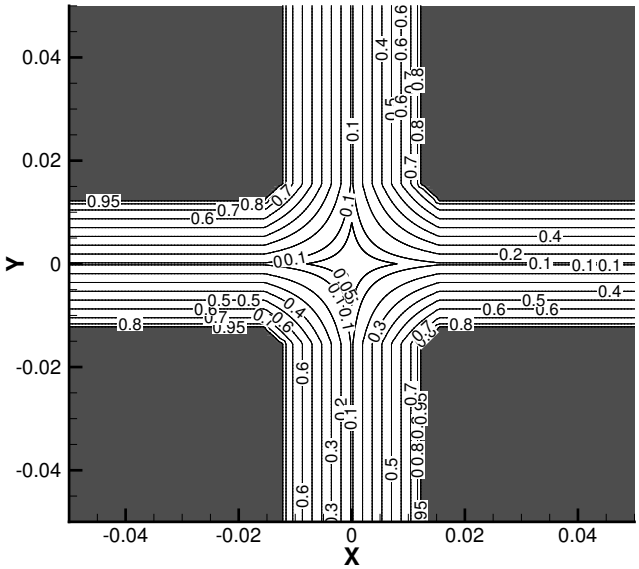

Fig. 9.36. Value of ω_j

In this configuration the proportion of hybrid and implicit cells (with $\omega_j < 1$) is equal to 73% The final computational times normalized by the computation cost of Heun's time integration at CFL=0.1 are provided, for several time integrator and CFL number, in Tab. 9.8. And, as expected, computations performed with explicit time integration become unstable for high CFL number due the violation of Courant stability condition in small cells (see Tab. 9.8). Our AION scheme provides stable solution thanks to Courant stability condition kept in small cells time-integrated with hybrid or implicit part of the AION scheme. Hence, the AION scheme, as expected, allows better stability properties than the standard time integrator proposed by Heun. It is important to notice that the computational gain compared to the full implicit computation is not really interesting (it is equal to 7%), due to high percentage of hybrid and implicit cells. But finally, the computation with AION scheme remains more efficient than a computation using an explicit time integration.

Tab. 9.8. Elapsed CPU time to reach 1 time period with AION and IRK2 time integrators on a 260^2 irregular mesh .

	CFL=0.1	CFL=0.4	CFL=0.9
Heun	1	×	×
AION	3.405	0.897	0.412
IRK2	3.64	0.948	0.434

The convected vortex computation allowed to test convected properties of our AION time integration. In order to test diffusion properties and the hybrid treatment of the gradient for the diffusion scheme, a three-dimensional Taylor Green vortex test case was proposed.

9.5.4 Three-dimensional Taylor Green Vortex

Indeed, in order to estimate the performance of the AION scheme for viscous test case, the TGV was implemented at Reynolds number ($Re = \frac{\rho_\infty U_\infty L}{\mu}$) equal to 1600 and Mach number equal to 0.1. This test case is also provided by the High-Order Workshop. The computational domain is a periodic cube $[-\pi L, \pi L]^3$ ($L = 1$) and the flow is initialized using:

$$\begin{aligned} u &= U_\infty sin(\frac{x}{L})cos(\frac{y}{L})sin(\frac{z}{L}), \\ v &= -U_\infty cos(\frac{x}{L})sin(\frac{y}{L})cos(\frac{z}{L}), \\ w &= 0, \\ p &= P_\infty + \frac{\rho_\infty U_\infty^2}{16}\left(cos(\frac{2x}{L}) + cos(\frac{2y}{L})\right)\left(cos(\frac{2z}{L}) + 2\right) \end{aligned} \tag{9.19}$$

A Direct Numerical simulation (DNS) of this test case allows to observe a vortex cascade often encountered in turbulent flow computation. For the computation, the fluid is assumed to be a compressible perfect gas with $\gamma = 1.4$ and the Prandtl number ($Pr = \frac{\mu.c_p}{\kappa}$) is equal to 0.71, with c_p and κ, respectively, the heat capacities at constant pressure and the heat conductivity. The initial temperature is kept constant $T_\infty = \frac{P_\infty}{R_{gas}\rho_\infty}$ with R_{gas} the perfect gas constant. Here the local pressure and temperature is deduced from the density $\rho = \frac{p}{R_{gas}T_\infty}$.

Our simulation is performed with laminar model until the physical time of $t = 20t_c$ with $t_c = \frac{L}{U_\infty}$ the characteristic convective time. The computation was performed with Heun's and AION time integrators on a 256^3 grid at CFL=0.9 coupled with a 2-exact formulation for the spatial discretisation (spatial order of accuracy is three). Thanks to these computations, the following outputs are performed:

- The temporal evolution of the kinetic energy integrated over the whole domain:

$$E_k = \frac{1}{\rho_\infty \Omega}\int_\Omega \rho \frac{U \cdot U}{2} d\Omega. \tag{9.20}$$

- The temporal evolution of the kinetic energy dissipation rate:

$$\varepsilon = -\frac{dE_k}{dt}. \tag{9.21}$$

- The temporal evolution of the dissipation rate on the whole domain computed from the enstrophy:

$$E = \frac{1}{\rho_\infty \Omega}\int_\Omega \rho \frac{w \cdot w}{2} d\Omega \text{ and } \epsilon = \frac{2\mu}{\rho_\infty} E \tag{9.22}$$

  with w the vorticity.

These outputs numerically obtained with our solver are compared with the DNS results obtained with a pseudo-spectral method on a 512^3 grid, taken as reference since the First International Workshop on High-Order CFD Methods held at the 50th AIAA Aerospace Meeting (https://www.grc.nasa.gov/hiocfd/).

According to E_k and ε (Fig. 9.37(a)- 9.37(b)), it appears that the AION scheme tends to fit better the DNS results than Heun's scheme for time range $t = [0t_c, 8t_c]$ and $t = [12t_c, 20t_c]$ while Heun's scheme seems to damp the solution in these time ranges. AION and Heun's schemes

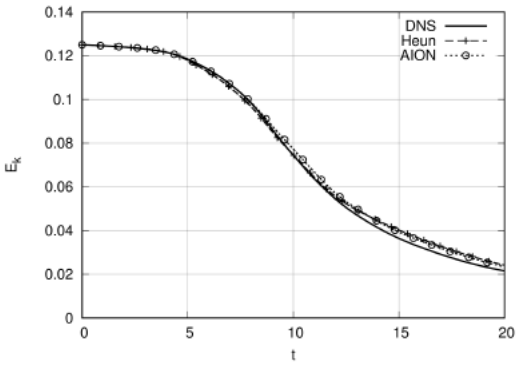

(a) The temporal evolution of the kinetic energy

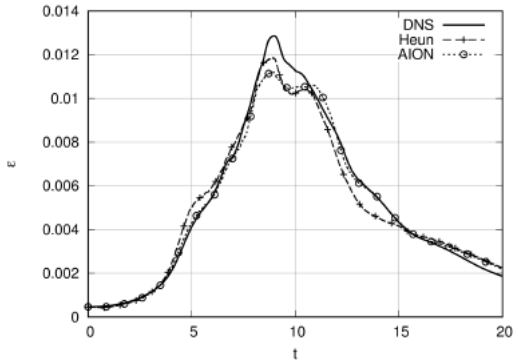

(b) The temporal evolution of the kinetic energy dissipation rate

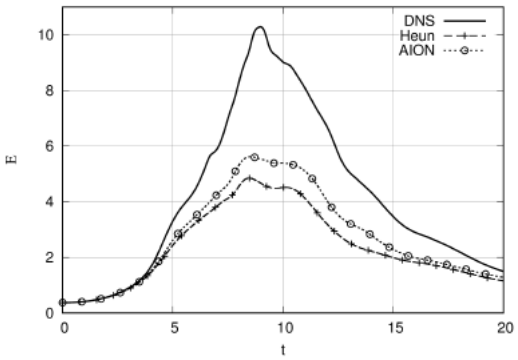

(c) The temporal evolution of the enstrophy

Fig. 9.37. Taylor Green Vortex outputs

do not reach the maximum of ϵ in the time range $t = [8t_c, 12t_c]$. Concerning to enstrophy E output and its associated ϵ, numerical computations reveal that solutions integrated with AION scheme lead to better results over the whole time range than computations with Heun's scheme (Fig. 9.37(c)).

According to these numerical results, it appears that the spectral behaviour of time integrators has significant consequences on the accuracy of our results. The importance of spectral behaviour was already observed on the slope of $log(E_{total})$ obtained in the previous case of the convected vortex. Finally this comparison of numerical results time-integrated with Heun's and AION scheme allows us to validate the definition of the hybrid gradients mandatory for the viscous terms with AION scheme.

9.6 Partial Conclusion

Finally our current study deals with the issues to spatially couple explicit and implicit time integrators. Here a smooth hybridization using a transition parameter ω allows to link two standard time integration schemes (Heun's explicit and implicit IRK2 schemes). Among the two proposed approaches based on the hybrid TN scheme, our approach named AION scheme gives the best spectral behaviour in agreement with the standard scheme proposed by Heun. Indeed spectral analysis on the coupled space / AION schemes enabled us to control the stability of the coupling procedure. This spectral analysis also allowed to reduce the transition area between time integrators thanks to the hybrid parameter ω. After the space-time spectral analysis, several test cases enabled to validate the proposed AION scheme and results were either as or more accurate than those with the standard schemes. Moreover,

the hybrid formulation enables to reduce the CPU time, taking the full implicit time integrator as reference.

In order to fill all the requirements of the PhD, the following study focuses on the behaviour of the AION scheme with a local time stepping approach. Indeed, previous local time stepping method (see Sec.6.1) deals only with explicit cells which are separated into several classes depending of their local maximum stable time step.

10 Temporal Adaptive Method with AION Scheme

As the AION time integrator is built using three underlying schemes applied either in the explicit, implicit or hybrid regions of a mesh, the time step in case of AION time integration for an irregular mesh is *de facto* limited by the CFL condition of the smallest explicit cells. The example of the numerical simulation of a backward facing step is provided in Fig. 10.1 to show the typical changes in cell size.

As presented previously, for explicit cells, the AION scheme was designed as a predictor-corrector scheme to match with the formulation of Heun's scheme. It was highlighted in Sec. 6 that the predictor-corrector formulation is useful for time synchronisation between temporal classes in the temporal adaptive approach implemented in **FLUSEPA**©. Hence this kind of temporal adaptive approach should be made compatible with the AION time integration. In such a case, implicit and hybrid cells will belong to highest ranked temporal class with highest time step limited by the CFL condition of the largest explicit cells. However, in several case it is possible to obtain the situation where hybrid cells belonging to highest ranked temporal class share a common interface with explicit cells of lowest ranked temporal classes (even though the approach forbids neighborhood cells with difference of temporal class's rank over 1). It is then mandatory to extend the time adaptive approach to the hybrid time integration of AION scheme.

The following section deals with finding a way to couple the AION scheme with time adaptation. Time adaptation should not be considered for the treatment of implicit cells since they are protected by the choice of the transition parameter. So, time synchronisation will be allowed only in hybrid and/or explicit cells.

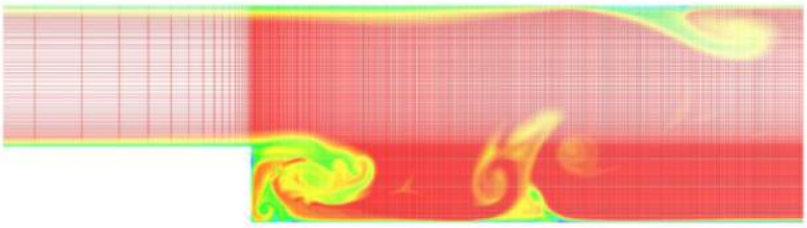

Fig. 10.1. Temperature field for backward facing step with irregular mesh (from Limare [6])

10.1 Update of the Solution for Hybrid Time Integration

For $\omega = 1$, the AION scheme coupled with the temporal adaptive approach is equivalent to the scheme presented in Sec. 6.1. The modifications of the scheme presented previously in Sec. 6 must be adapted in order to match with the hybrid time integration for AION scheme. Let us consider the same one-dimensional example represented in Sec. 6.1.2. So, for time integration

in the hybrid part of AION scheme until $t = 2\Delta t$, cells with class rank 1 will undergo only two stages:
a-1. $\widehat{W}^{2\omega\Delta t} = W^0 + 2\omega\Delta t R(W^0)$
b-1. $W^{2\Delta t} = W^0 + 2\Delta t\big(R^{Hybrid}(\widehat{W}^{2\omega\Delta t})\big)$,
and cells with class rank 0 will undergo four stages:
a-0. $\widehat{W}^{\omega\Delta t} = W^0 + \omega\Delta t R(W^0)$
b-0. $W^{\Delta t} = W^0 + \Delta t\big(R^{Hybrid}(\widehat{W}^{\omega\Delta t})\big)$
c-0. $\widehat{W}^{2\omega\Delta t} = W^{\Delta t} + \omega\Delta t R(W^{\Delta t})$
d-0. $W^{2\Delta t} = W^{\Delta t} + \Delta t\big(R^{Hybrid}(\widehat{W}^{2\omega\Delta t})\big)$.

The methodology for time synchronisation of the different temporal classes with different steps presented in Sec. 6.1.2 remains unchanged in case of the full explicit part of the hybrid time integration.

• **Steps 1 and 2:**
They are equivalent with the one presented in the full explicit case (Sec. 6.1.2)

• **Step 3:**
For the cells of class rank 0 sharing a face with a cell of class rank 1, the update of the solution associated with stage b-0 needs the definition of the flux at the interface $\beta + 1/2$,

$$F_{\beta+1/2}(\widehat{W}^{\omega\Delta t}) = \frac{1}{2}\big(F_{\beta+1/2}(W^0) + F^{Hybrid}_{\beta+1/2}(\widehat{W}^{2\omega\Delta t})\big). \tag{10.1}$$

• **Step 4:**
Also equivalent with the one presented in full explicit (see sec. 6.1.2), the parabolic interpolation of the residual is performed:

$$R^{\Delta t}_{\beta+1} = \frac{1}{4}R^{Hybrid}_{\beta+1}(\widehat{W}^{2\omega\Delta t}) + \frac{3}{4}R_{\beta+1}(W^0). \tag{10.2}$$

• **Step 5:**
The approach to time-integrate cells of class rank 0 from Δt to $2\Delta t$ is equivalent to the standard explicit one. Indeed the flux computed in Eq. (10.1) is imposed to compute residual in cell β for stages c-0 and d-0. Nevertheless, the time integration of cell β from Δt to $2\Delta t$ is as follows:

$$W^{2\Delta t}_{\beta} = W^{\Delta t}_{\beta} + \frac{\Delta t}{\Delta x}\left(\frac{3}{2}F^{Hybrid}_{\beta+\frac{1}{2}}(\widehat{W}^{2\omega\Delta t}) - \frac{1}{2}F_{\beta+\frac{1}{2}}(W^0) - F^{Hybrid}_{\beta-\frac{1}{2}}(\widehat{W}^{2\omega\Delta t})\right). \tag{10.3}$$

The modification introduced herein (compared with the full explicit Heun's method) is important to ensure the space-time conservation of the flux from 0 to $2\Delta t$ and the proof is provided in Sec. 10.2.1.

10.2 Conservation and Adaptive Time Accuracy

10.2.1 Conservation Property

In the following, attention will be paid on the demonstration of the space-time conservation of the flux between different temporal classes in case of temporal adaptive method in the hybrid part of the AION scheme.

For reminder, the spatial flux integrated in time during the duration $2\Delta t$ at an interface between cells of different temporal classes must be recovered on both sides of the interface, even if the cells do not belong to the same classes. The one-dimensional configuration presented in Sec. 10.1 is considered.

Class Rank 1

The time integration of cell $\beta+1$ of class rank 1 is simply:

$$\begin{aligned}\widehat{W}_{\beta+1}^{2\omega\Delta t} &= W_{\beta+1}^{0} + \frac{2\omega\Delta t}{\Delta x}\big(F_{\beta+\frac{3}{2}}(W^0) - F_{\beta+\frac{1}{2}}(W^0)\big)\\ W_{\beta+1}^{2\Delta t} &= W_{\beta+1}^{0} + \frac{2\Delta t}{\Delta x}\big(F^{Hybrid}_{\beta+\frac{3}{2}}(\widehat{W}^{2\omega\Delta t}) - F^{Hybrid}_{\beta+\frac{1}{2}}(\widehat{W}^{2\omega\Delta t})\big).\end{aligned} \tag{10.4}$$

Here too, as it was noticed in Sec. 6.1.3, all negative contribution of flux at the interface $\beta+\frac{1}{2}$ must be recovered for the flux balance of the cell β. To demonstrate conservation it is necessary to time integrate the solution at cell β until $t = 2\Delta t$.

Class Rank 0

For cell β of class rank 0, the time integration is:

$$\begin{aligned}\widehat{W}_{\beta}^{\omega\Delta t} &= W_{\beta}^{0} + \frac{\omega\Delta t}{\Delta x}\big(F_{\beta+\frac{1}{2}}(W^0) - F_{\beta-\frac{1}{2}}(W^0)\big),\\ W_{\beta}^{\Delta t} &= W_{\beta}^{0} + \frac{\Delta t}{\Delta x}\left(\frac{1}{2}\big(F^{Hybrid}_{\beta+\frac{1}{2}}(\widehat{W}^{2\omega\Delta t}) + F_{\beta+\frac{1}{2}}(W^0)\big) - F^{Hybrid}_{\beta-\frac{1}{2}}(\widehat{W}^{\omega\Delta t})\right).\end{aligned} \tag{10.5}$$

in a first time and

$$\begin{aligned}\widehat{W}_{\beta}^{2\omega\Delta t} &= W_{\beta}^{\Delta t} + \frac{\omega\Delta t}{\Delta x}\left(\frac{1}{2}\big(F^{Hybrid}_{\beta+\frac{1}{2}}(\widehat{W}^{2\omega\Delta t}) + F_{\beta+\frac{1}{2}}(W^0)\big) - F_{\beta-\frac{1}{2}}(W^{\Delta t})\right),\\ W_{\beta}^{2\Delta t} &= W_{\beta}^{\Delta t} + \frac{\Delta t}{\Delta x}\left(\frac{3}{2}F^{Hybrid}_{\beta+\frac{1}{2}}(\widehat{W}^{2\omega\Delta t}) - \frac{1}{2}F_{\beta+\frac{1}{2}}(W^0) - F^{Hybrid}_{\beta-\frac{1}{2}}(\widehat{W}^{2\omega\Delta t})\right).\end{aligned} \tag{10.6}$$

in a second time. If $W_{\beta}^{\Delta t}$ of Eq. (10.5) is replaced in the second equation of (10.6), and reminding that Eq. (10.1) holds, then

$$W_{\beta}^{2\Delta t} = W_{\beta}^{0} + \frac{\Delta t}{\Delta x}\left(2F^{Hybrid}_{\beta+\frac{1}{2}}(\widehat{W}^{2\omega\Delta t}) - F^{Hybrid}_{\beta-\frac{1}{2}}(\widehat{W}^{\omega\Delta t}) - F^{Hybrid}_{\beta-\frac{1}{2}}(\widehat{W}^{2\omega\Delta t})\right). \tag{10.7}$$

Fortunately the hybrid time integration at cells β and $\beta+1$ share the exact same flux at interface $\beta+\frac{1}{2}$. Hence, the procedure is conservative.

10.2.2 Time Accuracy

In the following section, the main goal is to perform the same analysis as the one introduced in Sec. 6.2.1 for Heun's scheme coupled with the time adaptation procedure. The configuration chosen in Sec. 6.2.1 is taken again and attention is paid on the time integration of hybrid cells for the AION scheme. As previously, the same finite-volume formulation is applied to the one-dimensional ODE (Eq. (6.11)) introduced in Sec. 6.2.1.

Considering a pth-order accurate spatial numerical scheme and the first-order time accurate predictor step of the hybrid part of AION time integrator (Eq. (9.1)), the finite-volume formulation Eq. (6.11) may be written as (omitting subscript j)

$$\widehat{W}^{\omega\Delta t} = W^0 + \omega\Delta t\big(\mathcal{R} + \mathcal{O}(\Delta x^{p-1})\big) + \mathcal{O}(\Delta t^2) = W^0 + \omega\Delta t\mathcal{R} + \mathcal{O}(\Delta t\Delta x^{p-1}, \Delta t^2). \tag{10.8}$$

In the following, the numerical error at cells of temporal classes rank 0 and 1 will be studied. Let us first study the local error performed at cells of class rank 1.

Local Numerical Error of Cells of Class Rank 1

By Taylor expansion of residual/flux around W, it is possible to reformulate the hybrid flux according to hybrid reconstruction states (Eq. (9.1)), the numerical error performed at predictor state (Eq. (10.8)) and the orders of accuracy of the space numerical scheme, such as:

$$\begin{aligned} R^{Hybrid}(\widehat{W}^{2\omega\Delta t}) &= R\bigg(\omega\bigg\{\frac{W^0+\widehat{W}^{2\omega\Delta t}}{2}\bigg\}+\mathcal{O}(\Delta x^p) \\ &\quad +(1-\omega)\bigg\{W^0+2\Delta t\frac{\partial \mathcal{W}}{\partial t}-\frac{1-\omega}{2}2\Delta t\frac{\partial \mathcal{W}}{\partial t}+\mathcal{O}(\Delta t^2,\Delta x^p)\bigg\}\bigg) \\ &= R\bigg(W^0+\Delta t\frac{\partial \mathcal{W}}{\partial t}+\mathcal{O}(\Delta t^2,\Delta x^p)+\frac{\omega}{2}\bigg\{\mathcal{O}(\Delta t^2,\Delta t\Delta x^{p-1})\bigg\}\bigg) \\ &= \mathcal{R}\bigg(W^0+\Delta t\frac{\partial \mathcal{W}}{\partial t}+\mathcal{O}(\Delta t^2,\Delta x^p)+\frac{\omega}{2}\bigg\{\mathcal{O}(\Delta t^2,\Delta t\Delta x^{p-1})\bigg\}\bigg)+\mathcal{O}(\Delta x^{p-1}). \end{aligned} \tag{10.9}$$

Considering an exact solution at the time instant $t=0$ (i.e. $W^0=\mathcal{W}^0$), the Taylor expansion of residual around W^0 gives:

$$R^{Hybrid}(\widehat{W}^{2\omega\Delta t})=\mathcal{R}+\Delta t\mathcal{R}\frac{\partial \mathcal{R}}{\partial \mathcal{W}}+\mathcal{O}(\frac{\Delta t^2}{\Delta x},\Delta t\Delta x^{p-2},\Delta x^{p-1}). \tag{10.10}$$

Then state W at cells of class rank 1 may be formulated such as:

$$\begin{aligned} W^{2\Delta t} &= W^0+2\Delta t\big(R^{Hybrid}(\widehat{W}^{2\omega\Delta t})\big). \\ &= W^0+2\Delta t\bigg(\mathcal{R}+\Delta t\mathcal{R}\frac{\partial \mathcal{R}}{\partial \mathcal{W}}+\mathcal{O}(\frac{\Delta t^2}{\Delta x},\Delta t\Delta x^{p-2},\Delta x^{p-1})\bigg). \end{aligned} \tag{10.11}$$

Hence it is possible to define the numerical error of $W^{2\Delta t}$ at cells of class rank 1:

$$e(W^{2\Delta t})=\mathcal{W}^0+2\Delta t\frac{\partial \mathcal{W}}{\partial t}+2\Delta t^2\frac{\partial^2 \mathcal{W}}{\partial t^2}+\mathcal{O}(\Delta t^3)-W^{2\Delta t}=\mathcal{O}(\Delta t^3,\frac{\Delta t^3}{\Delta x},\Delta t^2\Delta x^{p-2},\Delta t\Delta x^{p-1}). \tag{10.12}$$

Local numerical error due to time interpolation for cells of class rank 1

As mentioned, the flux at interface $\beta-\frac{1}{2}$ has the same special treatment for hybrid and explicit time integration. Indeed, according to the MUSCL reconstruction and its stencil, special treatment of cells of class rank 1 are necessary for computation of flux $\beta-\frac{1}{2}$ (see Step 4 in Sec. 6.1.2). Only cell $\beta+1$ of class rank 1 is considered here and the key point is the evaluation of the error performed during the parabolic interpolation. Thanks to Eq. (10.10), the state $\widehat{W}^{\omega\Delta t}_{\beta+1}$ may be formulated as:

$$\begin{aligned} \widehat{W}^{\omega\Delta t}_{\beta+1} &= W^0_{\beta+1}+\omega\Delta t\bigg(\frac{3}{4}R(W^0)+\frac{1}{4}R^{Hybrid}(\widehat{W}^{2\omega\Delta t})\bigg). \\ &= W^0_{\beta+1}+\omega\Delta t\bigg(\frac{3}{4}(\mathcal{R}+\mathcal{O}(\Delta x^{p-1}))+\frac{1}{4}(\mathcal{R}+\Delta t\mathcal{R}\frac{\partial \mathcal{R}}{\partial \mathcal{W}}+\mathcal{O}(\frac{\Delta t^2}{\Delta x},\Delta t\Delta x^{p-2},\Delta x^{p-1}))\bigg). \end{aligned} \tag{10.13}$$

Then the error $e(\widehat{W}_{\beta+1}^{\omega\Delta t})$ according to parabolic interpolation is:

$$\begin{aligned} e(\widehat{W}_{\beta+1}^{\omega\Delta t}) &= \mathcal{W}_{\beta+1}^{0} + \omega\Delta t\frac{\partial\mathcal{W}}{\partial t} + \frac{\omega^2\Delta t^2}{2}\frac{\partial^2\mathcal{W}}{\partial t^2} + \mathcal{O}(\Delta t^3) - \widehat{W}_{\beta+1}^{\omega\Delta t} \\ &= \frac{\omega^2\Delta t^2}{2}\frac{\partial^2\mathcal{W}}{\partial t^2} - \frac{\Delta t^2}{4}\mathcal{R}\frac{\partial\mathcal{R}}{\partial\mathcal{W}} + \mathcal{O}(\Delta t^3, \frac{\Delta t^3}{\Delta x}, \Delta t^2\Delta x^{p-2}, \Delta t\Delta x^{p-1}) \\ &= \mathcal{O}(\Delta t^2, \frac{\Delta t^3}{\Delta x}, \Delta t^2\Delta x^{p-2}, \Delta t\Delta x^{p-1}). \end{aligned} \tag{10.14}$$

The numerical flux at interface $\beta - \frac{1}{2}$ may be expressed, according to the formulation of the error $e(\widehat{W}_{\beta+1}^{\omega\Delta t})$ (Eq. (10.14)), as:

$$\begin{aligned} F_{\beta-\frac{1}{2}}^{Hybrid}(\widehat{W}^{\Delta t}) &= \mathcal{F}_{\beta-\frac{1}{2}} + \frac{\Delta t}{2}\mathcal{R}\frac{\partial\mathcal{F}_{\beta-\frac{1}{2}}}{\partial\mathcal{W}} + \mathcal{O}(\Delta t^2, \frac{\Delta t^3}{\Delta x}, \Delta t\Delta x^{p-2}, \Delta x^{p-1}). \\ F_{\beta-\frac{1}{2}}(W^0) &= \mathcal{F}_{\beta-\frac{1}{2}} + \mathcal{O}(\Delta x^p). \end{aligned} \tag{10.15}$$

Now the numerical error performed in case of cell β of class rank 0 is treated.

Local Numerical Error of Cells β of Class Rank 0

Thanks to the numerical error $e(\widehat{W}^{2\omega\Delta t})$ (Eq. (10.8)), Taylor's expansion of flux around W and expression of hybrid reconstruction states of AION scheme, it comes:

$$\begin{aligned} F_{\beta+\frac{1}{2}}^{Hybrid}(\widehat{W}^{2\omega\Delta t}) &= \mathcal{F}_{\beta+\frac{1}{2}} + \Delta t\mathcal{R}\frac{\partial\mathcal{F}_{\beta+\frac{1}{2}}}{\partial\mathcal{W}} + \mathcal{O}(\Delta t^2, \Delta t\Delta x^{p-1}, \Delta x^p). \\ F_{\beta+\frac{1}{2}}(W^0) &= \mathcal{F}_{\beta+\frac{1}{2}} + \mathcal{O}(\Delta x^p). \end{aligned} \tag{10.16}$$

The flux $F_{\beta+\frac{1}{2}}^{Hybrid}(\widehat{W}^{\omega\Delta t})$ is formulated such as:

$$\begin{aligned} F_{\beta+\frac{1}{2}}^{Hybrid}(\widehat{W}^{\omega\Delta t}) &= \frac{1}{2}\left(F_{\beta+\frac{1}{2}}(W^0) + F_{\beta+\frac{1}{2}}^{Hybrid}(\widehat{W}^{2\omega\Delta t})\right) \\ &= \mathcal{F}_{\beta+\frac{1}{2}} + \frac{\Delta t}{2}\mathcal{R}\frac{\partial\mathcal{F}_{\beta+\frac{1}{2}}}{\partial\mathcal{W}} + \mathcal{O}(\Delta t^2, \Delta t\Delta x^{p-1}, \Delta x^p) \end{aligned} \tag{10.17}$$

Thanks to Eq. (10.15), (10.17), (10.16), the state $W_\beta^{\Delta t}$ can be expressed as:

$$\begin{aligned} W_\beta^{\Delta t} &= W_\beta^0 + \frac{\Delta t}{\Delta x}\left(F_{\beta+\frac{1}{2}}^{Hybrid}(\widehat{W}^{\omega\Delta t}) - F_{\beta-\frac{1}{2}}^{Hybrid}(\widehat{W}^{\omega\Delta t})\right) \\ &= W_\beta^0 + \Delta t\Bigg(\mathcal{R} + \frac{\Delta t}{2}\mathcal{R}\frac{\partial\mathcal{R}}{\partial\mathcal{W}} \\ &\quad + \mathcal{O}(\frac{\Delta t^2}{\Delta x}, \frac{\Delta t^3}{\Delta x^2}, \Delta t\Delta x^{p-2}, \Delta t^2\Delta x^{p-3}, \Delta x^{p-1})\Bigg), \end{aligned} \tag{10.18}$$

and the error $e(W_\beta^{\Delta t})$ is:

$$\begin{aligned} e(W_\beta^{\Delta t}) &= \mathcal{W}_\beta^0 + \Delta t\frac{\partial\mathcal{W}}{\partial t} + \frac{\Delta t^2}{2}\frac{\partial^2\mathcal{W}}{\partial t^2} + \mathcal{O}(\Delta t^3) - W_\beta^{\Delta t} \\ &= \mathcal{O}(\Delta t^3, \frac{\Delta t^3}{\Delta x}, \frac{\Delta t^4}{\Delta x^2}, \Delta t\Delta x^{p-1}, \Delta t^2\Delta x^{p-2}, \Delta t^3\Delta x^{p-3}). \end{aligned} \tag{10.19}$$

Considering the local error of state W at cell β until $t = \Delta t$ (Eq. (10.19)) and the stencil of the MUSCL reconstruction technique (Eq. (10.14)), the fluxes $F_{\beta-\frac{1}{2}}(W^{\Delta t})$ and $F_{\beta-\frac{1}{2}}(\widehat{W}^{2\omega\Delta t})$ may be formulated as:

$$F_{\beta-\frac{1}{2}}^{Hybrid}(\widehat{W}^{2\omega\Delta t}) = \mathcal{F}_{\beta-\frac{1}{2}} + \Delta t\mathcal{R}\frac{\partial\mathcal{F}_{\beta-\frac{1}{2}}}{\partial\mathcal{W}} + \mathcal{O}(\Delta t^2, \frac{\Delta t^3}{\Delta x}, \frac{\Delta t^4}{\Delta x^2}, \Delta t\Delta x^{p-1}, \Delta t^2\Delta x^{p-2}, \Delta t^3\Delta x^{p-3}, \Delta x^p)$$

(10.20)

Thanks to Eqs. (10.20), (10.17), (10.16), (10.19), the state $W_\beta^{2\Delta t}$ is expressed as:

$$\begin{aligned} W_\beta^{2\Delta t} &= W_\beta^{\Delta t} + \frac{\Delta t}{\Delta x}\left(\frac{3}{2}F_{\beta+\frac{1}{2}}^{Hybrid}(\widehat{W}^{2\omega\Delta t}) - \frac{1}{2}F_{\beta+\frac{1}{2}}(W^0) - F_{\beta-\frac{1}{2}}^{Hybrid}(\widehat{W}^{2\omega\Delta t})\right). \\ &= \mathcal{W}_\beta^{\Delta t} + \mathcal{O}(\Delta t^3, \frac{\Delta t^3}{\Delta x}, \frac{\Delta t^4}{\Delta x^2}, \Delta t\Delta x^{p-1}, \Delta t^2\Delta x^{p-2}, \Delta t^3\Delta x^{p-3}) \\ &\quad + \Delta t\Bigg(\mathcal{R} + \frac{3}{2}\Delta t\mathcal{R}\frac{\partial \mathcal{F}_{\beta+\frac{1}{2}}/\Delta x}{\partial \mathcal{W}} - \frac{1}{2}\Delta t\mathcal{R}\frac{\partial \mathcal{F}_{\beta-\frac{1}{2}}/\Delta x}{\partial \mathcal{W}} \\ &\quad + \mathcal{O}(\frac{\Delta t^2}{\Delta x}, \frac{\Delta t^3}{\Delta x^2}, \frac{\Delta t^4}{\Delta x^3}, \Delta t\Delta x^{p-2}, \Delta t^2\Delta x^{p-3}, \Delta t^3\Delta x^{p-4}, \Delta x^{p-1})\Bigg). \end{aligned} \tag{10.21}$$

Finally, the local error $e(W_\beta^{2\Delta t})$ is:

$$\begin{aligned} e(W_\beta^{2\Delta t}) &= \mathcal{W}_\beta^{\Delta t} + \Delta t\frac{\partial \mathcal{W}}{\partial t} + \frac{\Delta t^2}{2}\frac{\partial^2 \mathcal{W}}{\partial t^2} + \mathcal{O}(\Delta t^3) - W_\beta^{2\Delta t} \\ &= \left(\frac{1}{2}\frac{\partial^2 \mathcal{W}}{\partial t^2} - \frac{3}{2}\mathcal{R}\frac{\partial \mathcal{F}_{\beta+\frac{1}{2}}/\Delta x}{\partial \mathcal{W}} + \frac{1}{2}\mathcal{R}\frac{\partial \mathcal{F}_{\beta-\frac{1}{2}}/\Delta x}{\partial \mathcal{W}}\right)\Delta t^2 \\ &\quad + \mathcal{O}(\Delta t^3, \frac{\Delta t^3}{\Delta x}, \frac{\Delta t^4}{\Delta x^2}, \frac{\Delta t^5}{\Delta x^3}, \Delta t\Delta x^{p-1}, \Delta t^2\Delta x^{p-2}, \Delta t^3\Delta x^{p-3}, \Delta t^4\Delta x^{p-4}) \\ &= \mathcal{O}(\Delta t^2, \frac{\Delta t^3}{\Delta x}, \frac{\Delta t^4}{\Delta x^2}, \frac{\Delta t^5}{\Delta x^3}, \Delta t\Delta x^{p-1}, \Delta t^2\Delta x^{p-2}, \Delta t^3\Delta x^{p-3}, \Delta t^4\Delta x^{p-4}). \end{aligned} \tag{10.22}$$

In case of resolution of hyperbolic equation, the CFL number allows to link Δt and Δx such as $\Delta x \simeq \Delta t$. This assumption leads to some simplification in the expression of numerical error performed until $t = 2\Delta t$ on cell β of class rank 0 and this error behaves as $O(\Delta t^2, \Delta x^p)$, which is exactly the local numerical error at cells of class rank 1. So the local time order of accuracy is kept constant at an interface between cells of different temporal classes in hybrid part of AION scheme. In the following section, the influence of local numerical error due to temporal adaptive method in hybrid of AION scheme is measured on the global error.

10.2.3 Numerical Assessment of the Theoretical Behaviour

We consider the same set of equations and grids as introduced in Sec. 6.2.2. Here, the parameter ω is chosen arbitrary to be equal to 0.72 for switching between cells of class rank 0 and those of class rank 1 for the time-adaptive AION scheme. For comparison, global numerical errors of Heun's scheme, time-adaptive Heun's scheme, AION scheme and time-adaptive AION scheme are provided in Tab. 10.1. As before, the time adaptive versions of the schemes are referred as "+TA". Fortunatly, it is demonstrated numerically that the temporal adaptive method recovers the expected order of accuracy.

Time integrator	E_{tot} slope
Heun	1.97
Heun + TA	1.93
AION	2.08
AION + TA	2.04

Tab. 10.1. Total error slopes

The analysis of the scheme accuracy is incomplete since for unsteady simulations, it is mandatory to estimate the effects of the scheme on dissipation and dispersion using a Von

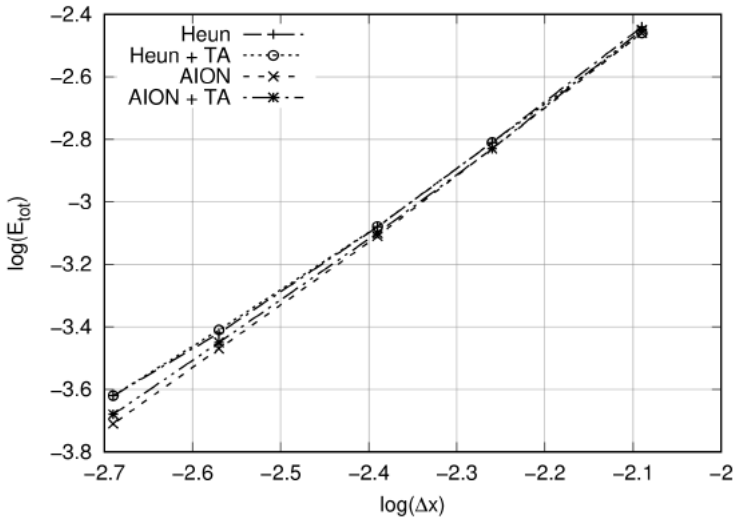

Fig. 10.2. Total error performed with second order spatial scheme

Neumann analysis. This is the main objective of Sec. 9.3 for the time-adaptive version of AION scheme.

10.2.4 Space-Time Von Neumann Analysis

The steps of the Von Neumann analysis of the time-adaptive AION scheme are equivalent to the ones for the time-adaptive Heun's scheme presented in Sec. 6.2.3. For the sake of clarity, all details are not presented but the main steps to derive mathematical expressions are introduced. Considering the same domain illustrated in Fig. 6.11 with the following ω configuration:

$$\begin{cases} \omega_j = \alpha\,\omega_{j-1} & \text{for } \dfrac{N}{2} - 50 \leq j \leq \dfrac{N}{2} \\ \omega_j = \dfrac{1}{\alpha}\,\omega_{j-1} & \text{for } \dfrac{N}{2} + 1 \leq j \leq \dfrac{N}{2} + 50 \\ \omega_j = 1 & \text{elsewhere.} \end{cases} \tag{10.23}$$

with $\alpha = 0.90$, N the number of cells and j the cell index. The analysis for the explicit part of the time-adaptive AION scheme recovers exactly the time adaptive version of Heun's scheme and it is not provided here. As a consequence, only the hybrid time integration (for $0.6 < \omega < 1$) is analysed. Moreover, the notions of Step UP and Step DOWN are used again, as in Sec. 6.2.3.

In the following, expressions of time integration of the different cells are theoretically recovered.

Step UP

The hybrid time integration at cell β until $t = 2\Delta t$ is performed as:

$$\begin{aligned} W_\beta^{\Delta t} &= W_\beta^0 - \frac{\Delta t}{\Delta x}\left[\frac{1}{2}\left(F_{\beta+\frac{1}{2}}(\Delta t, W^0) + F^{Hybrid}_{\beta+\frac{1}{2}}(2\Delta t, \widehat{W}^{2\omega\Delta t})\right) - F^{Hybrid}_{\beta-\frac{1}{2}}(\Delta t, \widehat{W}^{\omega\Delta t})\right] \\ W_\beta^{2\Delta t} &= W_\beta^{\Delta t} - \frac{\Delta t}{\Delta x}\left[\frac{3}{2}F^{Hybrid}_{\beta+\frac{1}{2}}(2\Delta t, \widehat{W}^{2\omega\Delta t}) - \frac{1}{2}F_{\beta+\frac{1}{2}}(\Delta t, W^0) - F^{Hybrid}_{\beta-\frac{1}{2}}(2\Delta t, \widehat{W}^{2\omega\Delta t})\right] \end{aligned} \tag{10.24}$$

Thanks to the following reconstruction for one-dimensional advection with a positive advection velocity $c > 0$ time integrated by hybrid scheme,

$$\begin{aligned} F^{Hybrid}(2\Delta t, W^{2\Delta t}) =& c\Big\{\omega\big(\frac{W^0 + \widehat{W}^{2\Delta t}}{2}\big) + \frac{1}{2}(\nabla W)^0 + (\omega - \frac{1}{2})(\widehat{\nabla W})^{2\omega\Delta t} \\ &+ (1-\omega)\big\{W_\beta^{2\Delta t} + (\nabla W)_\beta^{2\Delta t} - \frac{1-\omega}{2}(\Delta_t W)^{2\Delta t}\big\}\Big\} \end{aligned} \tag{10.25}$$

the following finite volume formulation in case of hybrid time integration is obtained:

$$\begin{aligned} W_\beta^{2\Delta t} = W_\beta^{\Delta t} - \frac{c\Delta t}{\Delta x}\Big[&\frac{3}{2}\Big\{\omega_\beta\big(\frac{W_\beta^0 + \widehat{W}_\beta^{2\omega\Delta t}}{2}\big) + \frac{1}{2}(\nabla W)_\beta^0 + (\omega_\beta - \frac{1}{2})(\widehat{\nabla W})_\beta^{2\omega\Delta t} \\ &+ (1-\omega_\beta)\big\{W_\beta^{\Delta t} + (\nabla W)_\beta^{\Delta t} - \frac{1-\omega_\beta}{2}(\Delta_t W)_\beta^{\Delta t}\big\}\Big\} \\ &- \frac{1}{2}\Big\{W_\beta^0 + (\nabla W)_\beta^0\Big\} \\ &- \Big\{\omega_{\beta-1}\big(\frac{W_{\beta-1}^0 + \widehat{W}_{\beta-1}^{2\omega\Delta t}}{2}\big) + \frac{1}{2}(\nabla W)_{\beta-1}^0 + (\omega_{\beta-1} - \frac{1}{2})(\widehat{\nabla W})_{\beta-1}^{2\omega\Delta t} \\ &+ (1-\omega_{\beta-1})\big\{W_{\beta-1}^{2\Delta t} + (\nabla W)_{\beta-1}^{2\Delta t} - \frac{1-\omega_{\beta-1}}{2}(\Delta_t W)_{\beta-1}^{2\Delta t}\big\}\Big\}\Big] \end{aligned} \tag{10.26}$$

Terms $\widehat{W}_\beta^{2\omega\Delta t}$ and $(\widehat{\nabla W})_\beta^{2\omega\Delta t}$, here too, are potential source of instability as for the time-adaptive Heun's scheme.

Step DOWN

For the step DOWN configuration (cell γ), the hybrid time integration leads to:

$$\begin{aligned} W_\gamma^{2\Delta t} = W_\gamma^{\Delta t} - \frac{c\Delta t}{\Delta x_\gamma}\Big[&\Big\{\omega_\gamma\big(\frac{W_\gamma^0 + \widehat{W}_\gamma^{2\omega\Delta t}}{2}\big) + \frac{1}{2}(\nabla W)_\gamma^0 + (\omega_\gamma - \frac{1}{2})(\widehat{\nabla W})_\gamma^{2\omega\Delta t} \\ &+ (1-\omega_\gamma)\big\{W_\gamma^{2\Delta t} + (\nabla W)_\gamma^{2\Delta t} - \frac{1-\omega_\gamma}{2}(\Delta_t W)_\gamma^{2\Delta t}\big\}\Big\} \\ &- \frac{3}{2}\Big\{\omega_{\gamma-1}\big(\frac{W_{\gamma-1}^0 + \widehat{W}_{\gamma-1}^{2\omega\Delta t}}{2}\big) + \frac{1}{2}(\nabla W)_{\gamma-1}^0 + (\omega_{\gamma-1} - \frac{1}{2})(\widehat{\nabla W})_{\gamma-1}^{2\omega\Delta t} \\ &+ (1-\omega_{\gamma-1})\big\{W_{\gamma-1}^{\Delta t} + (\nabla W)_{\gamma-1}^{\Delta t} - \frac{1-\omega_{\gamma-1}}{2}(\Delta_t W)_{\gamma-1}^{\Delta t}\big\}\Big\} \\ &+ \frac{1}{2}\Big\{ + W_{\gamma-1}^0(\nabla W)_{\gamma-1}^0\Big\}\Big]. \end{aligned} \tag{10.27}$$

Mathematical expressions

To study the spectral behaviour of the sub-cycling approach in the hybrid time integration, all the terms in the previous expressions Eqs. (10.26) (10.27) need to be expressed according to the state $W^{\Delta t}$ to obtain the amplification factor G between $W^{2\Delta t}$ and W^0:

$$\begin{aligned} W^0 &= \frac{1}{G_0}W^{\Delta t} \\ \widehat{W}^{2\omega\Delta t} = G_1 W^0 &= \frac{G_1}{G_0}W^{\Delta t} \\ (\nabla W)^0 &= \frac{G_3}{G_0}W^{\Delta t} \\ &\dots \end{aligned} \tag{10.28}$$

According to presence of term of state $W^{2\Delta t}$ at the right of Eqs. (10.26)-(10.27), the following final expression is obtained:

$$W^{2\Delta t} = GW^{\Delta t} = GG_0W^0 \tag{10.29}$$

The analysis of hybrid time integration is provided for four values of the transition parameter ω_j: 0.9, 0.81, 0.72 and 0.65. The dissipation is illustrated as a function of $k\Delta x$ for the step DOWN and UP configurations respectively at CFL=0.1 in Figs 10.3 and 10.4. Focusing on low normalised wavenumbers ($0 < k\Delta x < \pi/6$) it appears that amplification occurs for both configurations, something which was not found for the Heun+TA scheme. Furthermore the amplification increases with CFL number as shown in Fig. 10.5 for the step DOWN configuration and in Fig. 10.6 for the step UP configuration.

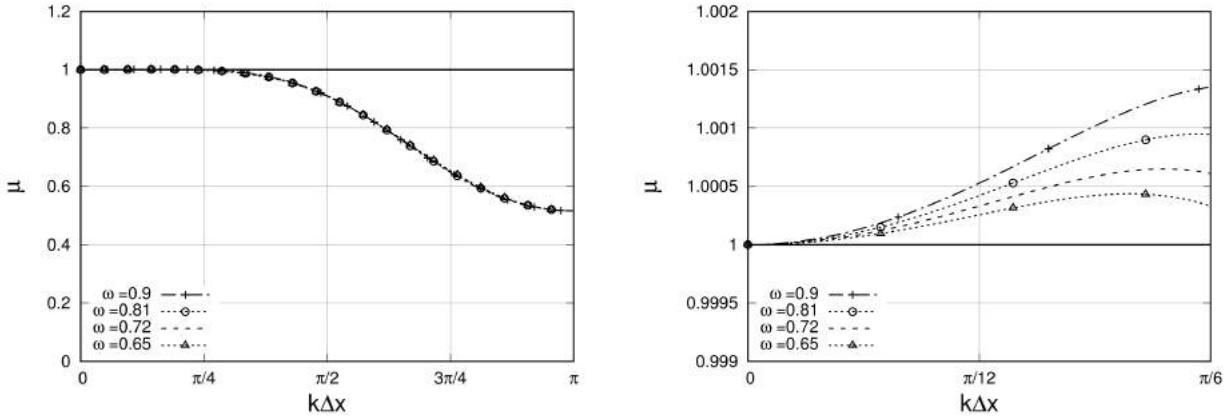

Fig. 10.3. Step DOWN configuration time integrated with Hybrid part of AION scheme at several values of ω ($CFL = 0.1$)

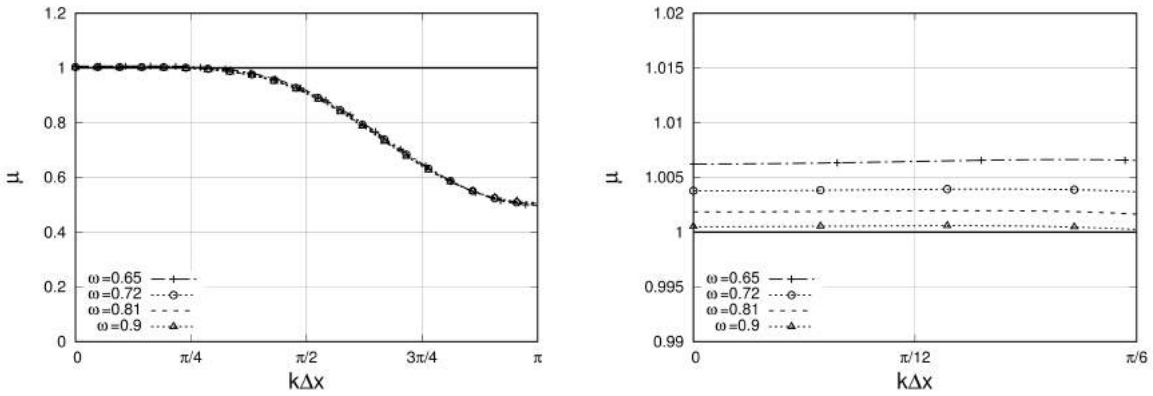

Fig. 10.4. Step UP configuration time integrated with Hybrid part of AION scheme at several values of ω ($CFL = 0.1$)

Concerning dispersion behaviour, it appears that the value of ω has a very small influence on the dispersion behaviour at CFL=0.1 (Fig. 10.7). This statement seems to change at CFL=0.6 according to Fig. 10.8 but the shape of the analysis is more complex, due to discontinuities in phases. Such discontinuities in phase were also encountered in Sec. 8.2 and correspond to a specific shape of the transfer function between the parameter $k\,\Delta x$ and the dispersion Φ. The spectral behaviour for AION+TA and Heun+TA schemes is illustrated in Figs. 10.9-10.11 for

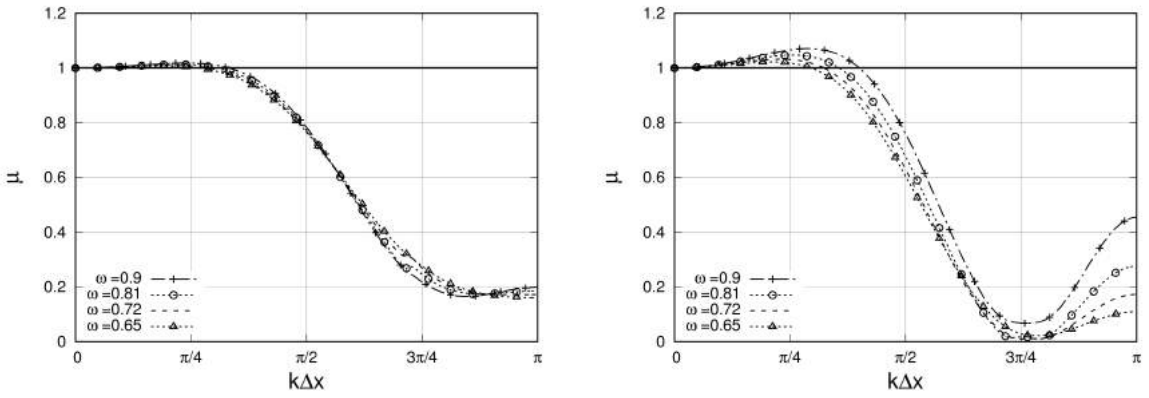

Fig. 10.5. Step DOWN configuration time integrated with Hybrid part of AION scheme at several values of ω ($CFL = 0.3$ at the left, $CFL = 0.6$ at the right)

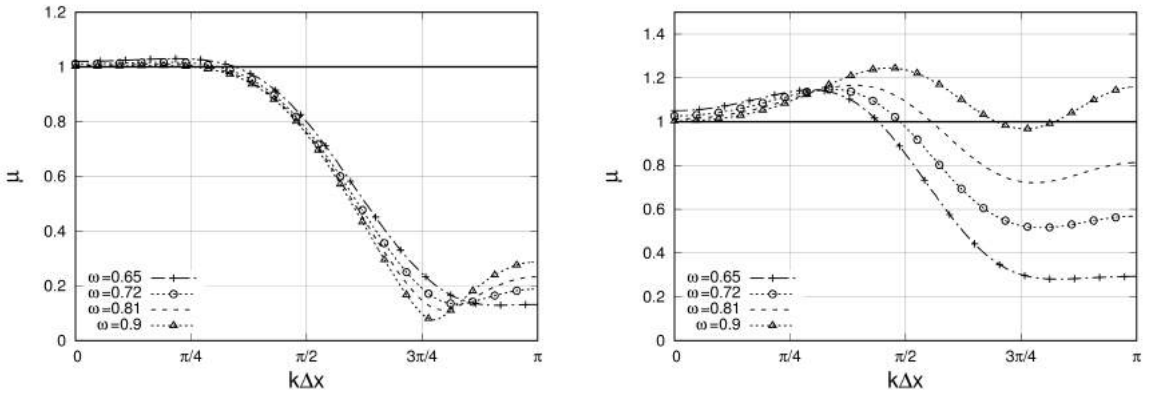

Fig. 10.6. Step UP configuration time integrated with Hybrid part of AION scheme at several values of ω ($CFL = 0.3$ at the left, $CFL = 0.6$ at the right)

two values of the CFL number and for the specific choice $\omega = 0.72$. Fig. 10.11 reveals that amplification only occurs in a short range of wavenumbers for the AION scheme while an amplification of the Heun's scheme occurs for any wavenumber.

To conclude, the stability limitation of CFL$\leq$ 0.5 with Heun's time integration is overcome thanks to the hybrid time integration.

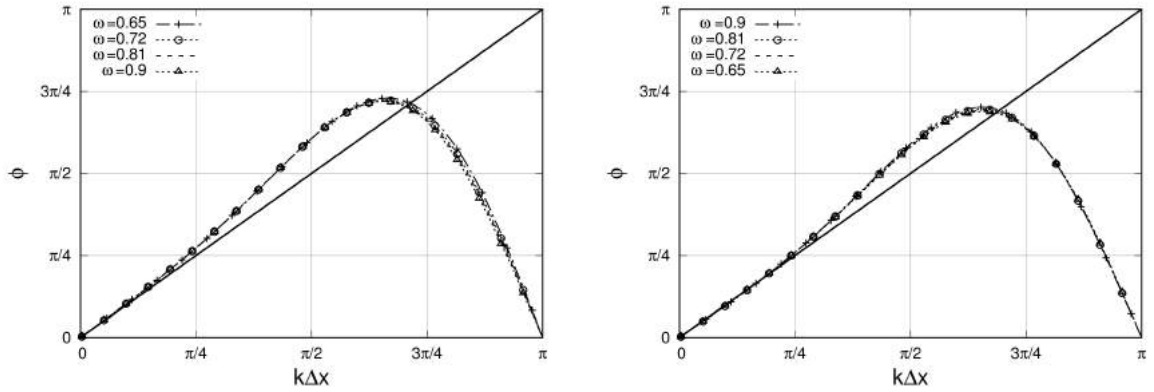

Fig. 10.7. Dissipation of the hybrid time integration for several values of ω for the Step UP (left) and DOWN (right) configurations at CFL=0.1

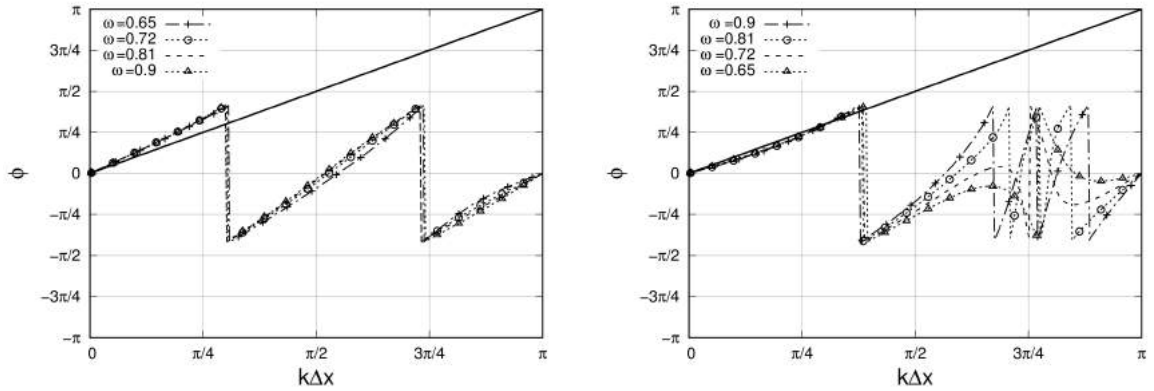

Fig. 10.8. Dissipation of the hybrid time integration for several values of ω for the Step UP (left) and DOWN (right) configurations at CFL=0.6

10.2.5 Analysis of $q-$Waves

The analysis of $q-$waves provided in Sec. 6.2.4 is now applied to the AION+TA configuration in order to study the effect of the hybrid time integration for configurations UP and DOWN on the occurrence of $q-$waves. Again, the definition of the group velocity and areas of negative group velocity are computed. The areas of negative-V^{gN} group velocity for the AION+TA configuration and steps UP and DOWN are illustrated by grey zone in Fig. 10.12. The negative group velocity waves appear essentially for large wavenumbers compared to Heun+TA configuration. Furthermore, the area is larger for the step DOWN configuration than for the step UP and the associated CFL values differ. Indeed the CFL limit of the negative-V^{gN} group velocity zone is CFL$=$ 0.65 in case of hybrid time integration of Step DOWN whereas the CFL limit is 0.3 in Heun part (Fig. 6.16). The last question concerns the damping of these $q-$waves using the dissipation of the scheme.

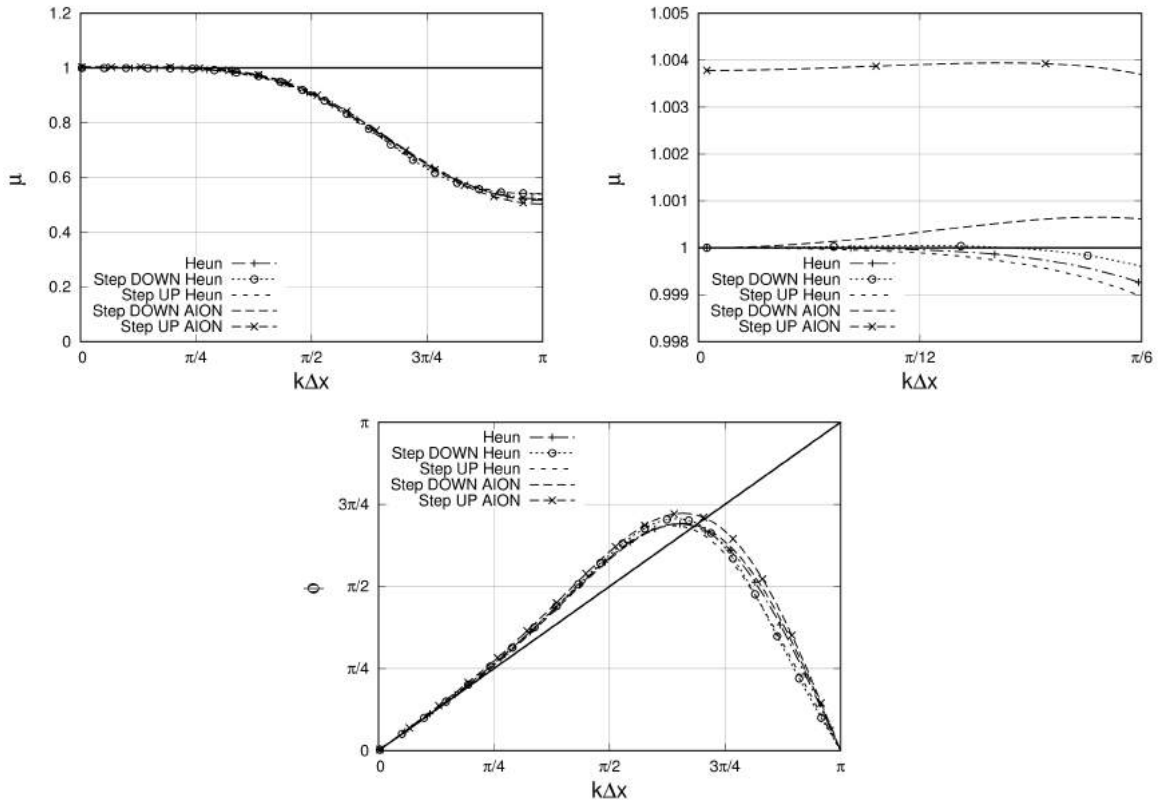

Fig. 10.9. Dissipation μ and dispersion ϕ behaviour at step configurations for AION+TA and Heun+TA integration with CFL=0.1

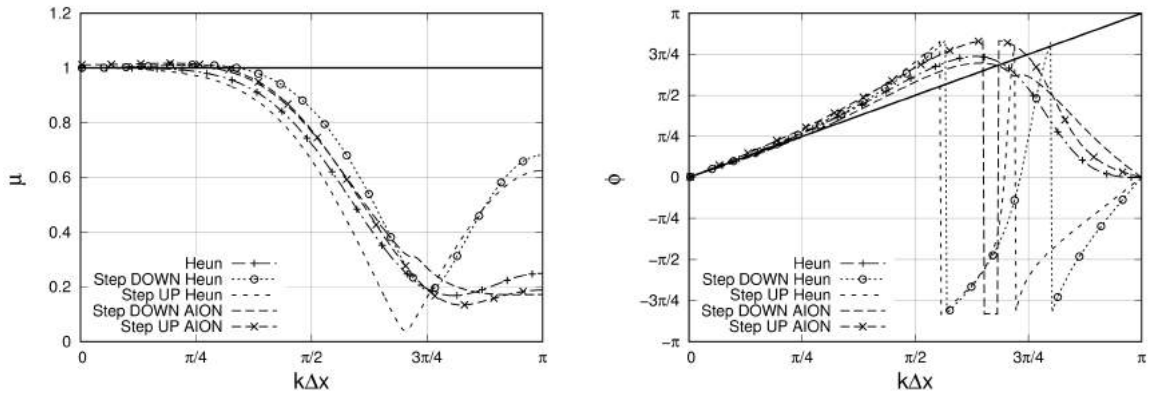

Fig. 10.10. Dissipation μ and dispersion ϕ behaviour at step configurations for AION+TA and Heun+TA integration with CFL=0.3

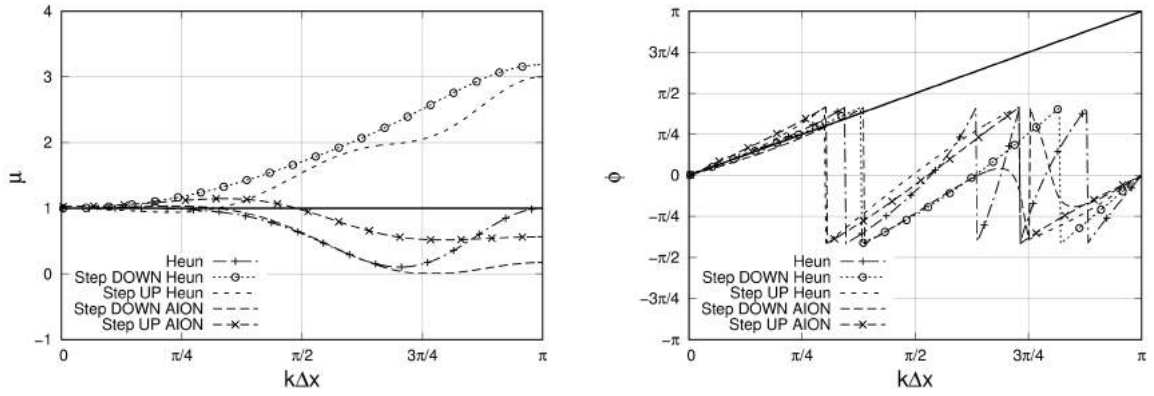

Fig. 10.11. Dissipation μ and dispersion ϕ behaviour at step configurations for AION+TA and Heun+TA time integration with CFL=0.6

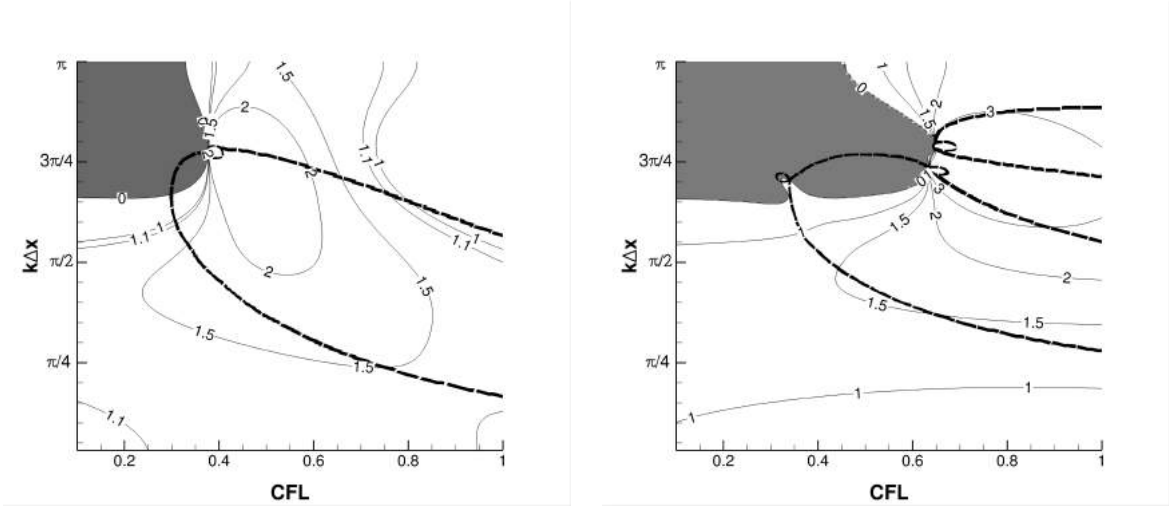

Fig. 10.12. Isocontours of V^{gN} for step UP and step DOWN with AION+TA time integration scheme

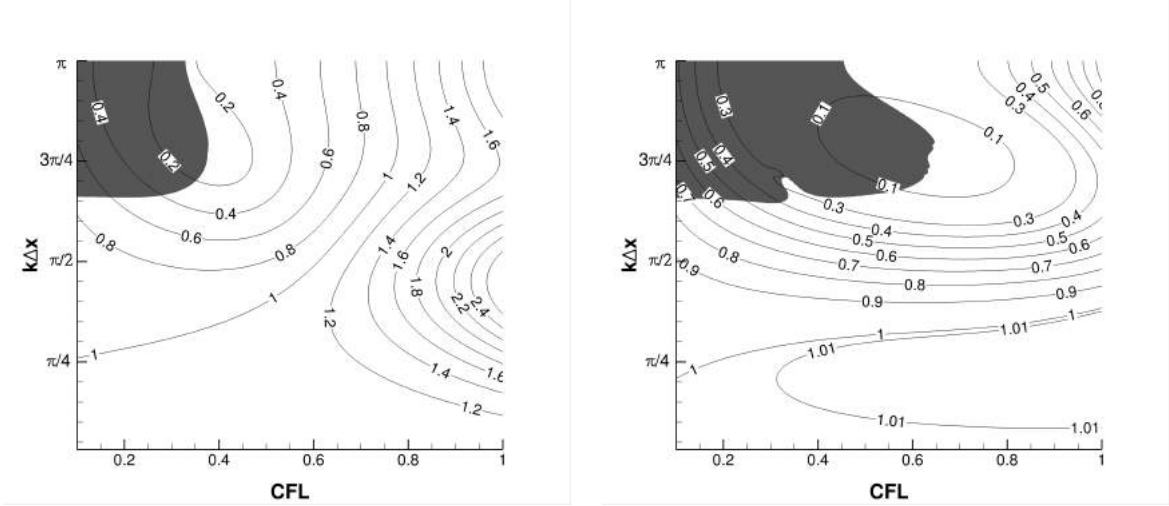

Fig. 10.13. Isocontours of the dissipation μ_β and μ_γ with grey zone for negative group velocity

Fortunately Fig. 10.13 reveals that for hybrid time integration, the CFL limit of the negative-V^{gN} zone corresponds to a dissipation $\mu > 0.2$ for step UP and $\mu > 0.1$ for STEP DOWN. Indeed, numerical dissipation can help in attenuating the $q-$waves.

The proposed theoretical analysis is validated for a regular grid only and it remains relevant to provide an analysis of the time-adaptive AION scheme ability for irregular grid. To answer this question, several configurations are analysed in Sec. 10.3

10.3 Validation of Temporal Adaptive Method with AION Scheme

This section is devoted to the validation of the temporal adaptive method with AION scheme using several test cases of increasing complexity, starting from 1D propagation problem to 2D Euler computation.

10.3.1 Wave Propagation Problem

The previous theoretical analysis provided in Secs. 6.2 and 10.2 reveals that Heun+TA and AION+TA schemes do not have a similar behaviour at an interface between different temporal classes in case of regular grids. The theoretical analysis for irregular grid is difficult (see Vichnevetsky [103]). The goal of the current section is to perform a numerical analysis of Heun+TA and AION+TA time integration in case of irregular meshes. To do so, first, a wave packet is propagated in a domain in order to introduce a frequency content and analyse it behaviour for any wave number. In this test case, a non-periodic computational domain of length $L_x = 270\ m$ composed of $N = 1024$ cells with irregular size, is initialized thanks to:

$$y(x,0) = \cos\left[2\pi f_e(x - x_c)\right] \exp(-\frac{(x - x_c)}{K}) \tag{10.30}$$

with $K = 200$, $f_e = 1/\pi$ and $x_c = 90\ m$. The wave packet will be advected at velocity $c = 1\,m/s$. While the theoretical analysis was performed with two temporal classes of cells with same size (see Secs. 6.2 and 10.2), here, two temporal classes of cells with different sizes are introduced. In the temporal class 0, the space size Δx is designed such as

$$\Delta x_j = \frac{1}{2}\Delta x_{max} \text{ for } \frac{N}{2} - 100 \leq j \leq \frac{N}{2} + 100 \tag{10.31}$$

with $\Delta x_{max} = 0.29\,m$. Step configurations are localised at $x = 120.2\,m$ (step DOWN) and $x = 149.5\,m$ (step UP) and two cell classes are introduced. The computation is integrated until $t = 100\,s$ with Δt in cells of class rank 1 and $\Delta t/2$ in cells of class rank 0, such as Δt corresponds to the time step associated with the largest cells, at CFL= 0.6, which means that:

$$\text{CFL} = \frac{\Delta t}{c\Delta x_{max}}.$$

The computation is first performed using Heun+TA scheme. It appears that, a sinusoidal with a certain wavenumber ($p-$waves) is amplified when the wave-packet is advected through the time synchronisation configuration (at $t = 25s$ in the Fig. 10.14) and this result was previously provided in the theoretical analysis (with constant Δx) in Sec. 6.2.3. In order to highlight the phenomena, a Fast Fourier Transformation (FFT) of the numerical solution y is performed. The FFT is performed with sampling frequencies equal to $1Hz$.

According to Fig. 10.15 it appears that the main frequency observed from FFT of y (called $\Psi(y)$ in the following) is equal to $0.1Hz$ at initial instant $t = 0s$. This obtained frequency is linked to the discretisation of the signal according to Δx_{max}. At instant $t = 25s$ a second dominant frequency appears, corresponding to the discretisation of the signal according to the space size of the finest part of the domain ($\Delta x_{max}/2$). The amplified $p-$waves observed at instant $t = 25s$ is characterized by an overshoot of FFT with a frequency near $0.46Hz$. Indeed,

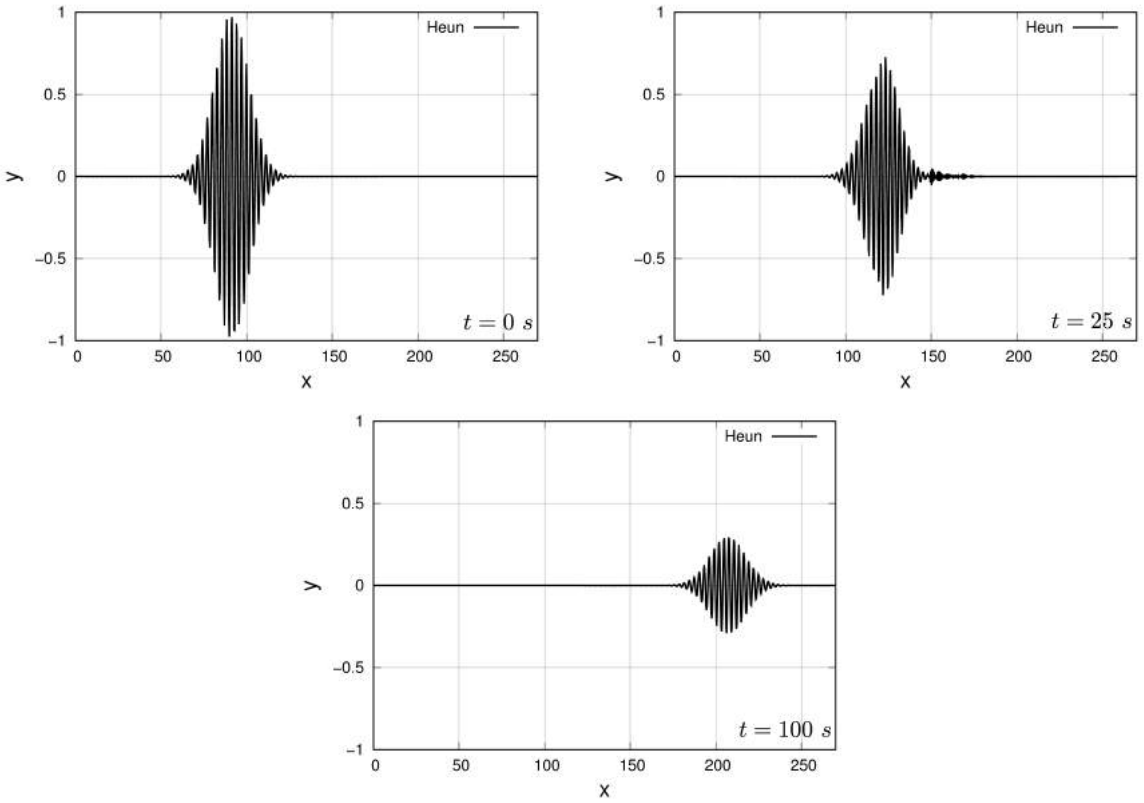

Fig. 10.14. Propagation of wavepacket with Heun's scheme with temporal adaptive method until $t = 100s$ ($CFL = 0.6$).

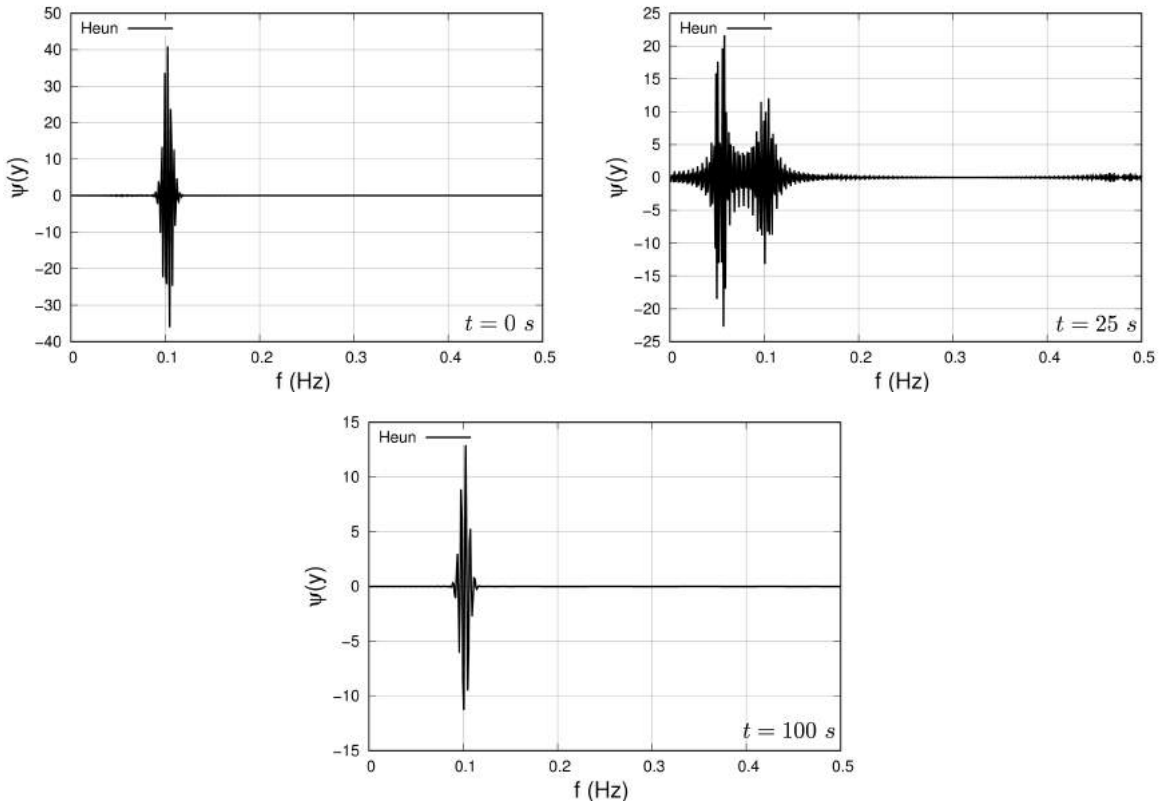

Fig. 10.15. Fast Fourrier transformation $\Psi(y)$ of the numerical solution obtained thanks to Heun's scheme couple with temporal adaptive method at $t = 0s$, $25s$, $100s$.

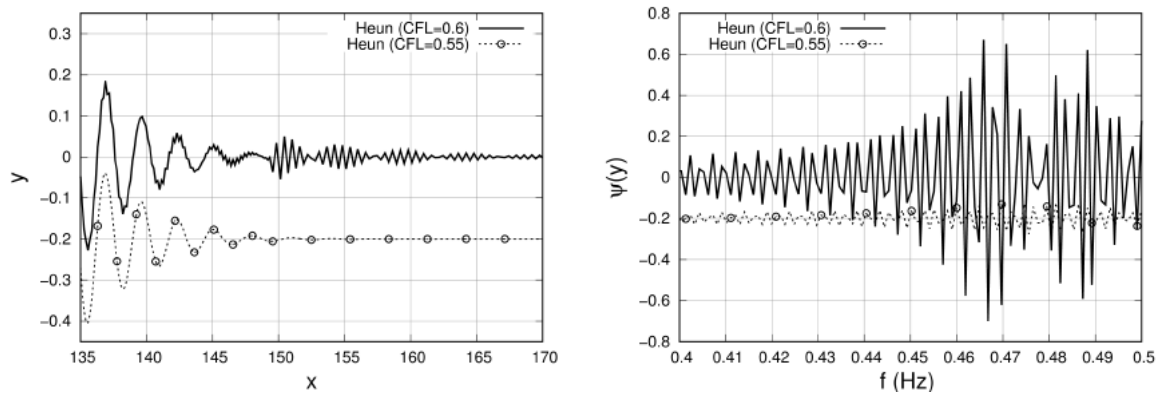

Fig. 10.16. Comparaison of numerical solution time integrated by Heun+TA scheme with CFL=0.55 and CFL=0.6 at $t = 25s$.

as it is observed in Fig. 10.14, the frequency corresponding to amplified $p-$waves is strongly higher than the main frequency that composes the signal.

For a computation at CFL=0.6, near the stability limit of Heun's scheme, amplification occurs. If amplification appears because of local instability of the space/time scheme, a lower value of CFL could reduce amplified spectrum. In order to justify our assumption, a similar simulation is performed at CFL=0.55 until $t = 25s$. The two solutions with CFL=0.6 and CFL=0.55 are provided in Fig.10.16. For readiness, the numerical solution for CFL=0.55 is translated by -0.2 in y-axis. As expected, the amplification present at CFL=0.6 disappears at CFL=0.55, which confirms that amplification of $p-$waves at CFL=0.6 is due to global stability properties of the Heun+TA scheme.

The same computation is time-integrated thanks to AION+TA scheme. For hybrid time synchronisation, the parameter ω is configured such as:

$$\begin{cases} \omega_j = \alpha\,\omega_{j-1} & \text{for } \dfrac{N}{2} - 102 \leq j \leq \dfrac{N}{2} \\ \omega_j = \dfrac{1}{\alpha}\,\omega_{j-1} & \text{for } \dfrac{N}{2} + 1 \leq j \leq \dfrac{N}{2} + 102 \\ \omega_j = 1 & \text{elsewhere.} \end{cases} \tag{10.32}$$

with $\alpha = 0.90$.

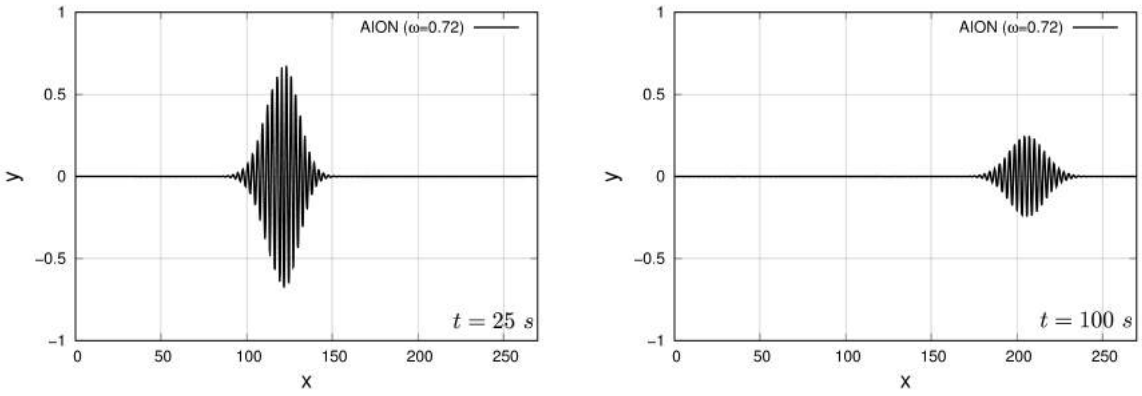

Fig. 10.17. Propagation of wavepacket with AION scheme with temporal adaptive method (step configuration in hybrid part) until $t = 100s$ ($CFL = 0.6$).

Fig. 10.17 reveals that the AION+TA approach does not lead to the same amplification of $p-$waves as the ones observed with Heun+TA scheme. Fig. 10.18 reveals that the second frequency $0.46Hz$ observed in Heun+TA configuration is no longer present with the AION+TA scheme.

Thus even if the AION+TA approach shares many characteristics with Heun+TA one, it appears to be more stable and to allow time integration with higher CFL number: AION+TA can be qualified as enhancement of Heun+TA time integrator.

The following test case is dedicated to illustrate how AION+TA deals with compressible effects of Euler equations solution.

10.3.2 Sod's Tube

The standard space/time analysis was performed assuming a local regularity of the flow. Here, our goal is to analyse the scheme behaviour on an academic case with discontinuities. The same physical initialisation introduced in Sec.9.5.2 is chosen in order to test temporal adaptive method coupled with Heun's and AION time integrators in a more complex test case with

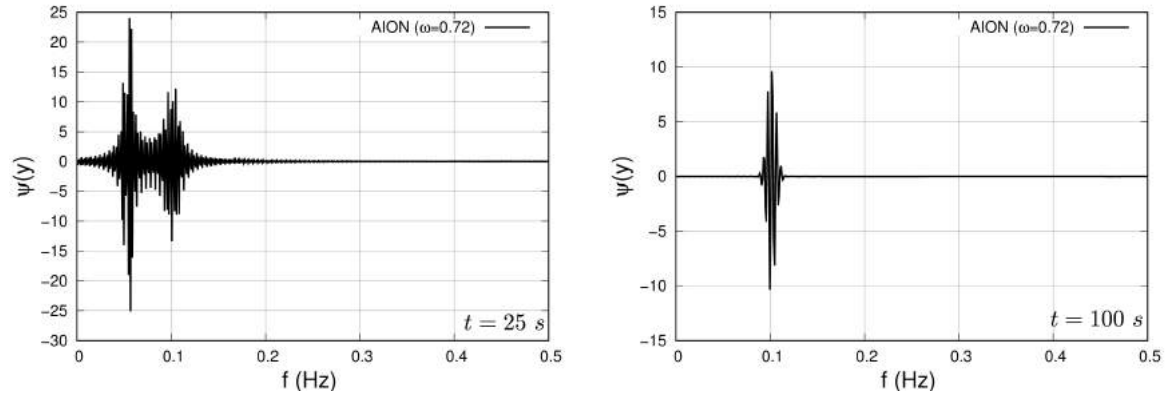

Fig. 10.18. Fast Fourrier transformation $\Psi(y)$ of the numerical solution obtained thanks to AION with temporal adaptive method at $t = 25s,\ 100s$ (step configuration in hybrid part).

compressible effect. The computational domain is composed of a regular part with $N = 300$ cells (with uniform size) and an irregular part with non-uniform mesh size designed such as:

$$\begin{cases} \Delta x_j = \alpha\, \Delta x_{j-1} & \text{for } \dfrac{N}{2} - 45 \leq j \leq \dfrac{N}{2} \\ \Delta x_j = \dfrac{1}{\alpha}\, \Delta x_{j-1} & \text{for } \dfrac{N}{2} + 1 \leq j \leq \dfrac{N}{2} + 45 \\ \Delta x_j = \Delta x_{max} & \text{elsewhere.} \end{cases} \tag{10.33}$$

with $\alpha = 0.973$. In order to perform temporal adaptive procedure, the cells are ranked in temporal class of number K, such as:

$$K = int\left[\frac{\ln(\Delta t_j / \Delta t_{min})}{\ln(2)}\right] \tag{10.34}$$

with $\Delta t_j = CFL.\frac{\Delta x_j}{\|\vec{v}_j\| + c_j}$. Here, two classes of cells are obtained such as the local time step of the computation is equal to $\Delta t_{max}/2$ in cells of class 0 and Δt_{max} in cells of class 1. The time step Δt_{max} is designed as the maximal time step allowed for the whole domain. Then the parameter ω_j is controlled as:

$$\begin{cases} \omega_j = \alpha\, \omega_{j-1} & \text{for } \dfrac{N}{2} - 37 \leq j \leq \dfrac{N}{2} \\ \omega_j = \dfrac{1}{\alpha}\, \omega_{j-1} & \text{for } \dfrac{N}{2} + 1 \leq j \leq \dfrac{N}{2} + 37 \\ \omega_j = 1 & \text{elsewhere.} \end{cases} \tag{10.35}$$

For CFL= 0.1, the Heun+TA scheme will be compared to the AION+TA scheme, the density and velocity profiles are illustrated in Figs. 10.19 and 10.20, with zooms in the critical region of the rarefaction wave and near the shock. It appears that AION+TA approach is as accurate as Heun+TA and leads to results in agreement with the theoretical behaviour (with global time stepping at $\Delta t = \Delta t_{max}$). Furthermore it appears that the AION time integration has a stronger dissipative effect on the overshot of solution near the rarefaction waves than the other time integrators.

A second set of computations is performed at $CFL = 0.45$. Here, the Heun+TA scheme is unstable and AION+TA results will be compared with those of the standard implicit IRK2 scheme (Figs 10.21 and 10.22). It appears that both time integrators allow to obtain solution of

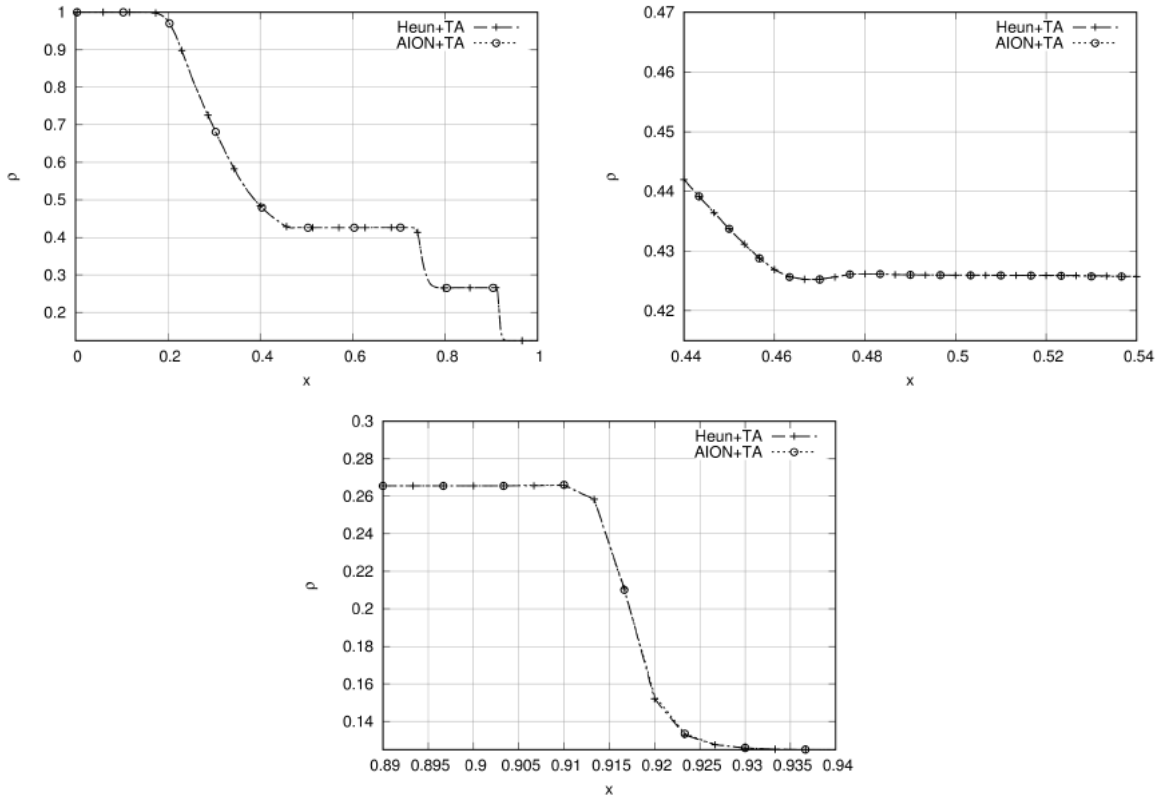

Fig. 10.19. Sod's shock tube at $CFL = 0.1$. Global view of the density profile at $t = 0.2s$ and close-up views near the rarefaction wave and near the shock.

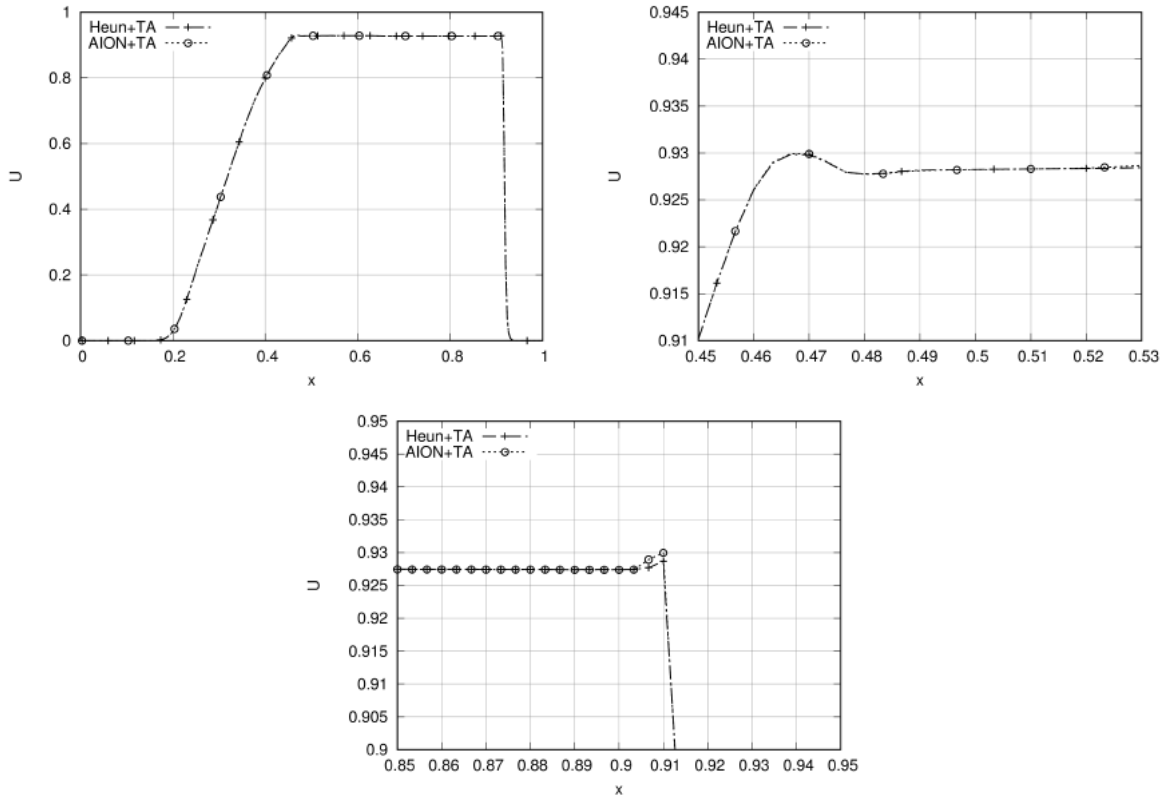

Fig. 10.20. Sod's shock tube at $CFL = 0.1$. Global view of the density profile at $t = 0.2s$ and close-up views near the rarefaction wave and near the shock.

same accuracy. At this CFL condition too, the AION scheme seems to slightly dissipate the overshoots given by the IRK2 implicit scheme, according to the numerical solution of velocity and density near the shock.

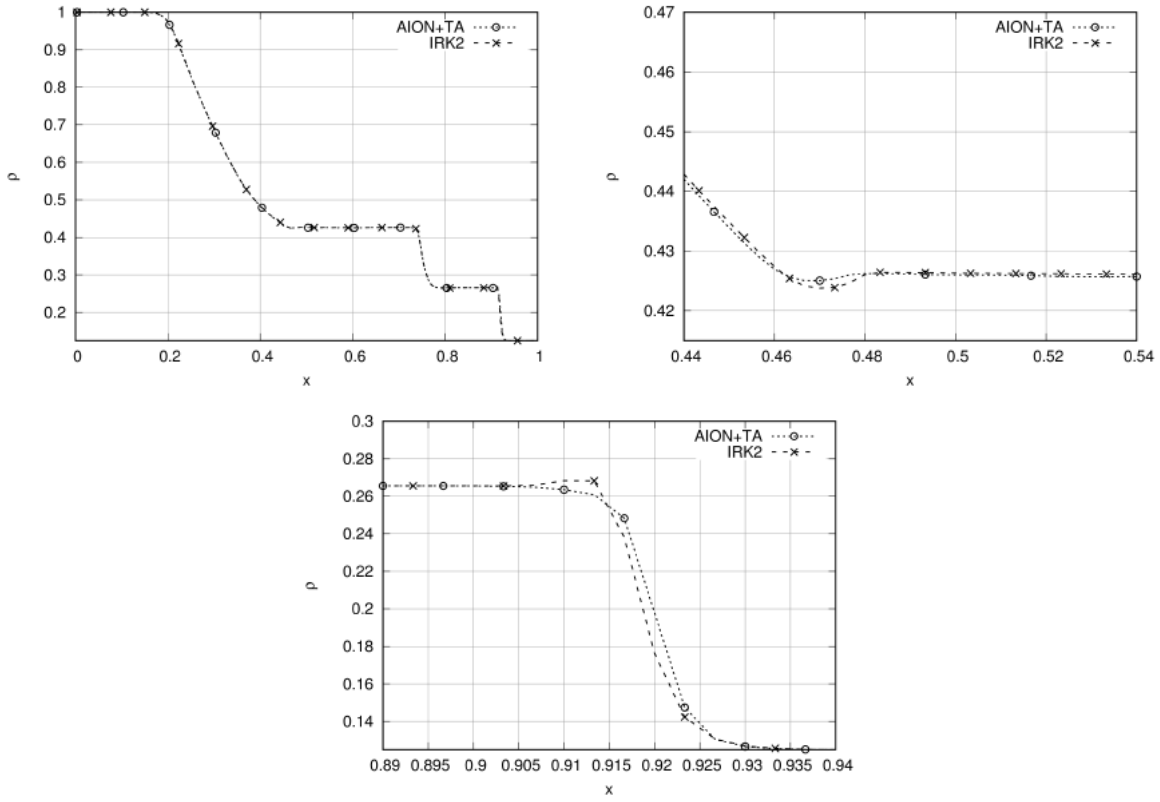

Fig. 10.21. Sod's shock tube at $CFL = 0.45$. Global view of the density profile at $t = 0.2s$ and close-up views near the rarefaction wave and near the shock.

According to numerical computation performed for resolution of Euler equation, it appears that the AION+TA approach is able to handle shock, contact discontinuity and rarefaction waves coupled with temporal adaptive approach. And here too, the AION scheme improves stability of the explicit scheme coupled with temporal adaptive method thanks to hybrid flux reconstruction. The next two dimensional test case is dedicated to the analysis of global accuracy of AION+TA for two-dimensional test case

10.3.3 Two-dimensional Linear Advection of an Isentropic Vortex

The same physical initialisation introduced in Sec. 9.5.3 is performed in order to estimate the accuracy of the temporal adaptive method coupled with Heun's and AION time integrators and with several temporal classes for a two-dimensional test case. The vortex is advected for three rotations inside the periodic box. Here again, a Successive-Correction 2-exact formulation for the spatial scheme (order three) is performed, and the time integration is provided by several schemes for comparison (Heun's scheme with temporal adaptive method, standard IRK2 scheme and AION scheme with temporal adaptive method). An irregular domain of 260^2 degrees of freedom (DOF) is designed in order to obtain several temporal classes and use temporal adaptive method. The ratio between the size of the largest and the smallest cells is equal to 11 in this irregular domain. In our previous computations in Sec. 9.5.3, it was highlighted that standard Heun's scheme was unable to perform such test case configuration for a time step Δt imposed according to CFL of the biggest cells contrary to AION scheme. Here, the numerical computation is performed with four temporal classes of cells, with a Δt_{min}

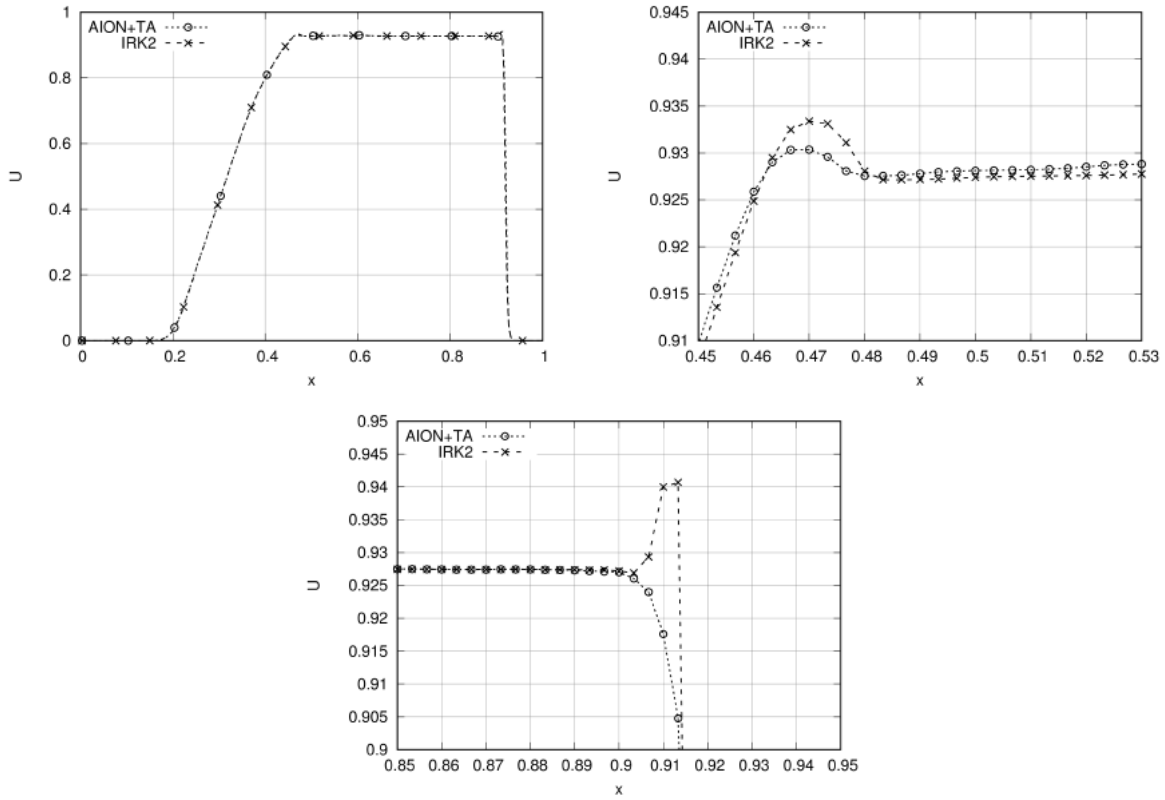

Fig. 10.22. Sod's shock tube at $CFL = 0.45$. Global view of the density profile at $t = 0.2s$ and close-up views near the rarefaction wave and near the shock.

of the temporal classes 0 corresponding to a $CFL = \frac{U_\infty \Delta t_{min}}{\min\limits_j(h_j)} = 0.9$. The parameter ω_j is defined according to the size of cells in the domain (see Fig. 9.36 with explicit cell of $\omega_j = 1$, coloured in grey with the proportion of cells with $\omega_j < 1$ corresponding to hybrid and implicit cells is equal to 73%.

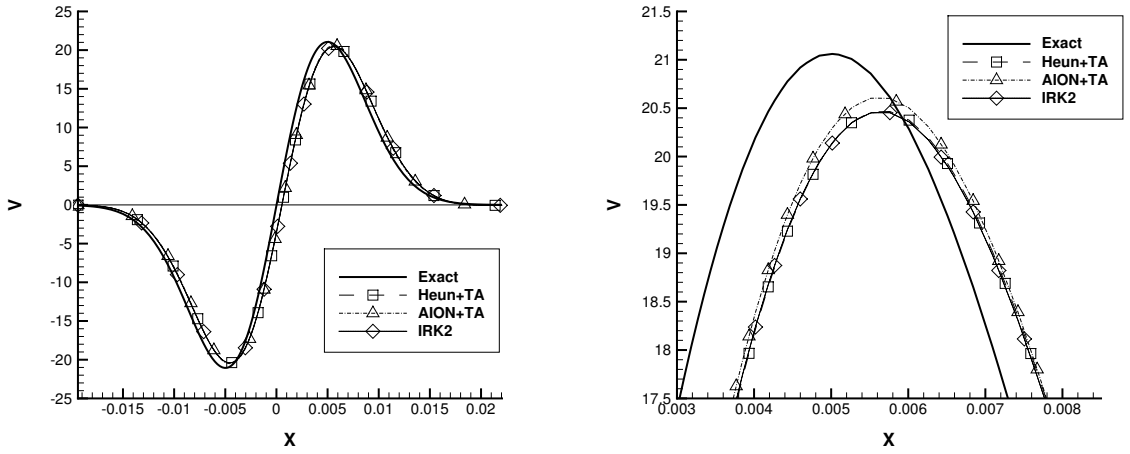

Fig. 10.23. Velocity field (CFL=0.1)

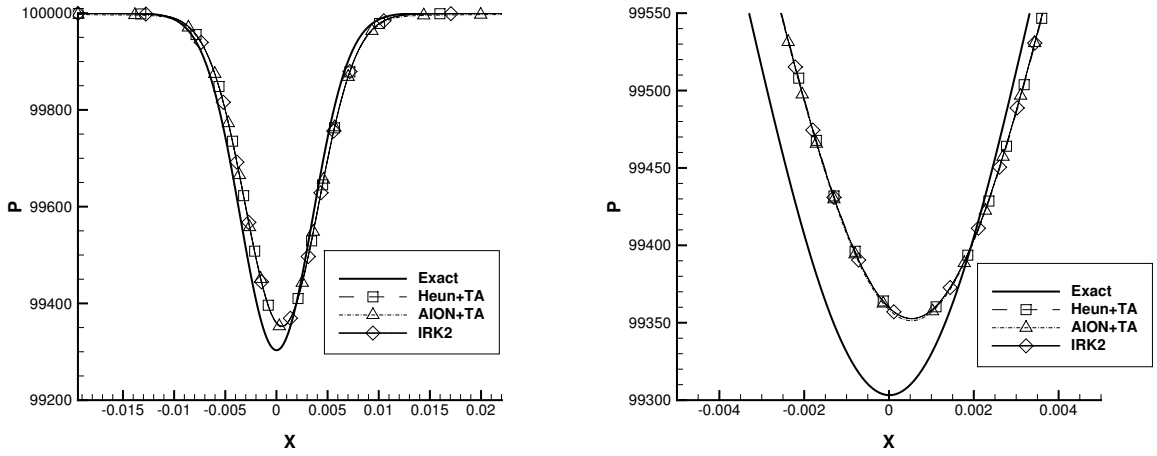

Fig. 10.24. Pressure field (CFL=0.1)

The pressure and velocity fields obtained with the several time integrators on the irregular grid (260^2) are illustrated in Figs. 10.23 and 10.24. They reveal that time integrators have slightly same properties of dissipation and dispersion. The AION scheme coupled with temporal adaptive method seems to be slightly more accurate as it was already illustrated in validation test cases for global time step computation (Sec. 9.5) and for the one-dimensional sinus-wave advection (Sec. 10.2.3).

The spectral behaviour of our AION scheme provided by space-time von Neumann analysis demonstrated optimistic characteristics and capability. This is confirmed by validation test cases. The same spectral analysis and several test case realised with temporal adaptive approach, reveals that, as expected, the AION scheme keeps time accuracy and interesting spec-

tral behaviour even when time synchronisation occurs in hybrid part of AION time integration. Finally, it remains to validate our coupling approach of time integrator (the AION scheme) with hybrid RANS/LES simulation. Indeed, in following, a methodology that provides the coupling between AION scheme and HRL (Hybrid RANS LES) simulation will be introduced and validated.

11 AION Time Integration with RANS/LES Simulation

11.1 Introduction

The Hybrid RANS/LES (HRL) coupling technique available in **FLUSEPA**© was implemented by Pont *et al.* [19] and largely used at ArianeGroup for massively detached flows. This model is similar to the DDES-SA model of Spalart *et al.* [106] and Deck [107]. A shielding function f_d that protects the modelling of the boundary layers is designed:

$$f_d = 1 - \tanh\left((8r_d)^3\right) \tag{11.1}$$

with,

$$r_d = \frac{\nu + \nu_t}{\sqrt{\frac{\partial u_i}{\partial x_j}\frac{\partial u_i}{\partial x_j}}\kappa^2 d_w^2} \tag{11.2}$$

with ν and ν_t the viscosity and turbulence viscosity, $\kappa = 0.41$ a closure coefficient from SA model [108] and d_w the distance from the nearest wall. According to this definition of shielding function of HRL simulation, RANS modelisation is activated for $f_d = 0$ in the boundary layers while LES simulation is performed for $f_d = 1$ elsewhere. Given that the physics is quasi-stationary in boundary layers and unstationary elsewhere. The hybrid parameter ω is defined as,

$$\begin{aligned} &\beta = 1 - (1+\alpha)\tanh\left((8r_d)^3\right) \text{ with } 0 < \alpha < 1 \\ &\omega = \begin{cases} 1+\beta & \text{if } \beta < 0, \\ 1 & \text{if } \beta \geq 0, \end{cases} \end{aligned} \tag{11.3}$$

with $\alpha = 0.5$ in the following. The function f_d may pass through 0 to 1 in one cell (in certain zones of the mesh). If ω is imposed as equal to f_d, it may be critical to pass through implicit to explicit in one cell. In this context, May and Berger [84] analysed the effect of switching from explicit to implicit (and vice-versa) for their flux bounding approach and found that an order of accuracy is lost locally for irregular grids. The shielding function ω of Eq. (11.3) is designed to avoid such situation.

Usually in such Hybrid RANS/LES simulation, the mesh is defined such that $y^+ \approx 1$ near the wall in order to obtain the best accuracy for the turbulent model (Fig. 11.3). The interest of RANS modelling near the wall is to decrease the computational cost with less cells near the wall (using strongly stretched cells). Cells in LES part of the domain are quite isotropic. Unfortunately the temporal adaptive method of **FLUSEPA**© becomes ineffective in case of strong stratification near the wall. In such configuration, most of the cells are among time levels of small rank value. Hence the computational CPU gain obtained by Brenner [95] is no more ensured. In order to circumvent this limitation, any usual mesh domain defined with **FLUSEPA**© was designed with $y^+ \approx 50$. Such a configuration imposes a wall model in HRL simulation and the minimal time step constrained by the characteristic size of cells in RANS

part is equivalent to the minimal time step constrained by the characteristic size of cells in LES part of the turbulent modelling ($\Delta t_{min}^{RANS} = \Delta t_{min}^{LES}$). The AION time integration is useless in such configuration, a more useful configuration will be with $\Delta t_{min}^{RANS} << \Delta t_{min}^{LES}$ where RANS equations are time integrated with hybrid and implicit part of AION scheme and a LES part of turbulent model time integrated with full explicit part of AION scheme.

Furthermore a possible configuration of interest would be to perform also implicit/hybrid time integration in steady (or physically uninteresting) zone out of the boundary layers (where $f_d = 1$) where the size of cells may be smaller than size of interesting and LES cells. In this situation, a much higher minimal time step is obtained in zone explicitly time-integrated than zone implicitly time-integrated ($\Delta t_{min}^{Implicit} << \Delta t_{min}^{Explicit}$).

In the following, a validation test case of 2D Backward Facing step with $y^+ \approx 1$ is time integrated with AION scheme (with and without temporal adaptive approach) in order to validate the shielding ω function in HRL modelling.

11.2 Two-dimensional Backward Facing Step

The two-dimensional Backward facing step is part of validation base of **FLUSEPA**© solver. Indeed the physics flows is quite similar to the one from Launcher shrinkage characterised by massive detachment of the boundary layers. An experimental study was performed by Moreau *et al.* [109] who assimilate the case to the configuration of a combustion chamber. Driver *et al.* [110] and Hall *et al.* [12] also performed experimental studies on this configuration. The geometry of the test case is represented in Fig. 11.1. The step size is characterised by h and the physic flows is represented in Fig. 11.2 . The stationary upstream boundary layer is formed for negative abscissa. The unsteady detachment of the boundary layer occurs after at $x = 0$ which involves formation of a recirculation bubble in the corner of the step. Near the detachment zone, the time integrations shall not dissipate the capture nor delay the formation of Kelvin Helmholtz instability. The red zone in Fig. 11.2 is strongly unsteady and needs to be simulated by LES in order to correctly capture structures. The other green zone represents steady or quasi-steady flows that should be modelled by RANS equations.

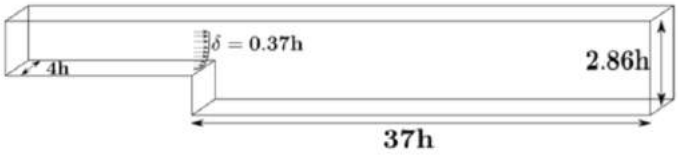

Fig. 11.1. Schematic of the geometry of the 2D backward facing step

The spatial scheme is of order three. First, the AION time integration with global time step approach is compared to Heun's scheme with temporal adaptive approach. The mesh is composed of $6 \cdot 10^6$ cells with $\Delta t_{min}^{Explicit} = 4\Delta t_{min}^{Implicit} = 4.6 \cdot 10^{-6} s$ and $y^+ \approx 1$. For a computation performed until the non-dimensional time computation $t_{final} = \frac{TU_{max}}{h} = 150$, with T the physical computation time and h the step size. The AION time integration performed with $\Delta t = \Delta t_{min}^{Explicit}$ (with 20% of implicit/hybrid cells) is equivalent in terms of CPU cost to Heun's time integration performed with $\Delta t_{min} = \Delta t_{min}^{Implicit}$ and 5 temporal classes (there is no interest, in terms of computational CPU gain, to increase the number of temporal classes over 5).

Fig. 11.6 illustrates pressure lines and contours in the shear-layer of the backward facing step with the Heun's scheme (left) and the AION scheme (right) and Fig. 11.5 shows temperature distribution. It is clear that the AION time integrator dissipates less the recirculation and better

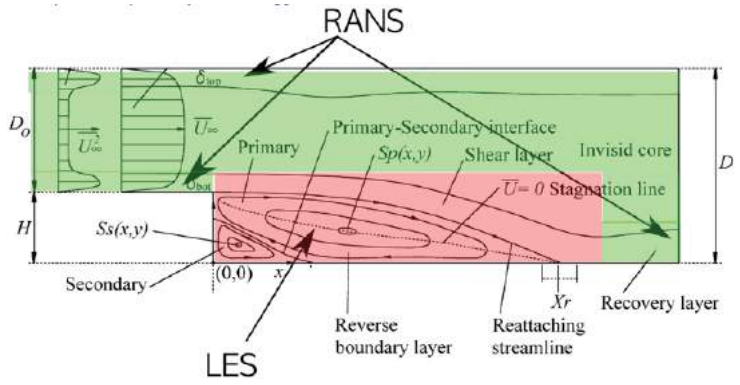

Fig. 11.2. Mean flow regions of a turbulent backward facing step flow in the longitudinal plane (from Hall *et al.* [12])

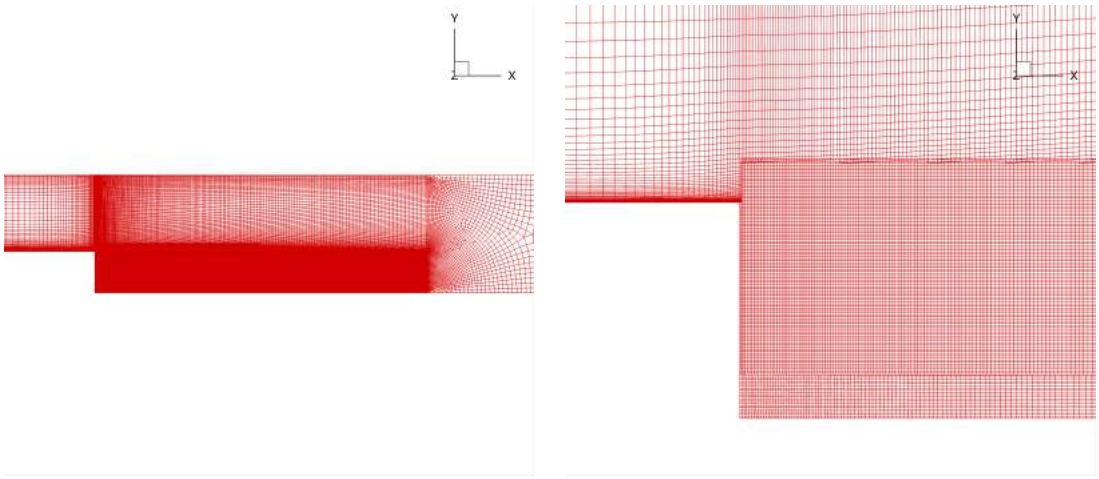

Fig. 11.3. irregular mesh of 2D backward facing step ($y^+ \approx 1$ near the wall $x < 0$)

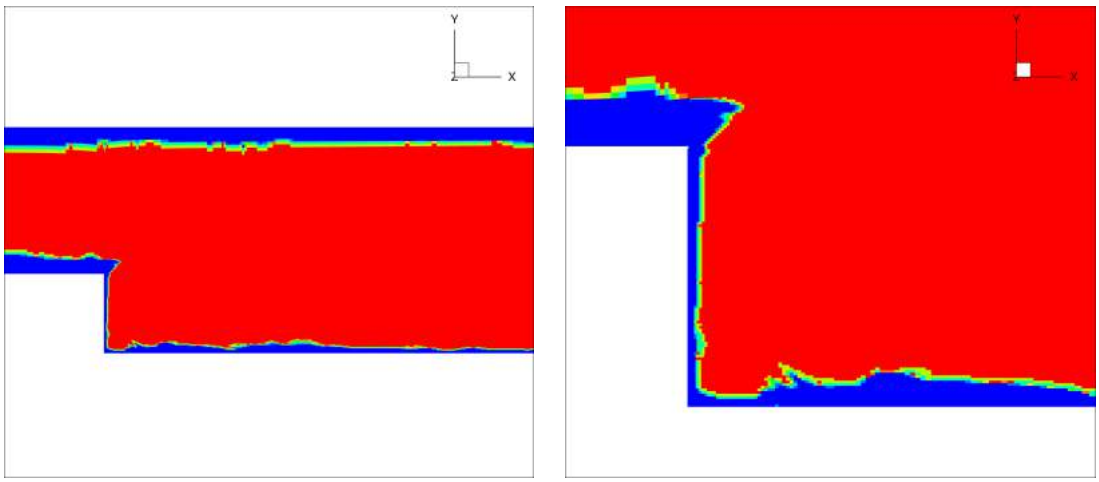

Fig. 11.4. Hybrid parameter ω for the 2D backward facing step ($\omega = 1$ out of the boundary layers)

captures the triggering of Kelvin-Helmholz instabilities than the Heun's scheme. In addition, Heun's time integrator captures recirculation with delay.

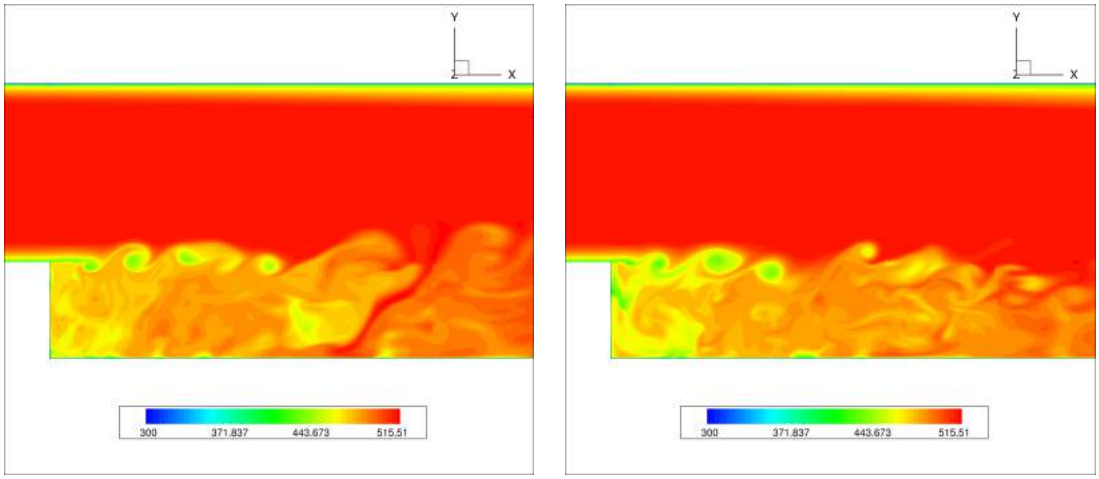

Fig. 11.5. Temperature field (with 2-exact spatial scheme) time integrated by Heun+TA and AION scheme

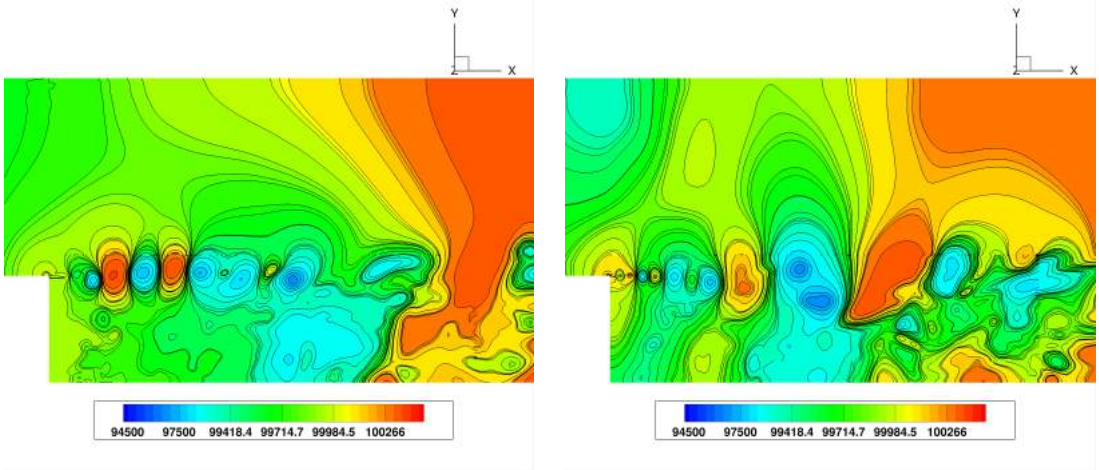

Fig. 11.6. Pressure field (with 2-exact spatial scheme) time integrated by Heun+TA and AION scheme

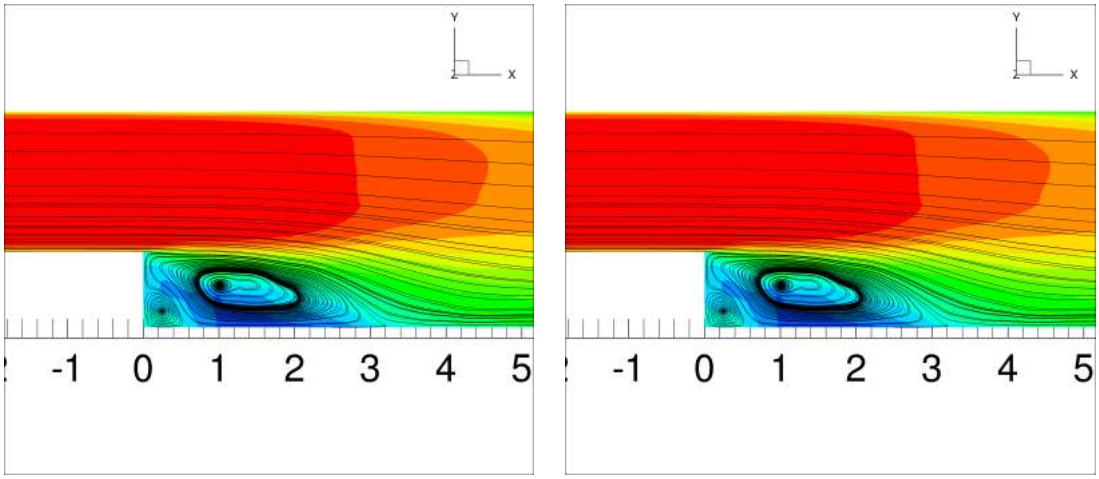

Fig. 11.7. Contour of mean longitudinal velocity with Heun+TA and AION time integrator

The computed mean flow is characterized by a main recirculation bubble with a secondary corner vortex and with solid reattachment point as it can be seen in figure 11.7. For both time integrations, the main recirculation, the corner vortex and position of reattachment point are slightly equivalent. As it was previously observed in 3D Taylor Green vortex it appears that, with implicit time integration of steady physics, the AION time integration allows to better capture unsteady physics than Heun's scheme.

Now, attention is paid on the AION+TA scheme. The AION+TA scheme is used with $\Delta t_{min} = \Delta t_{min}^{Explicit}$ and 3 temporal classes.

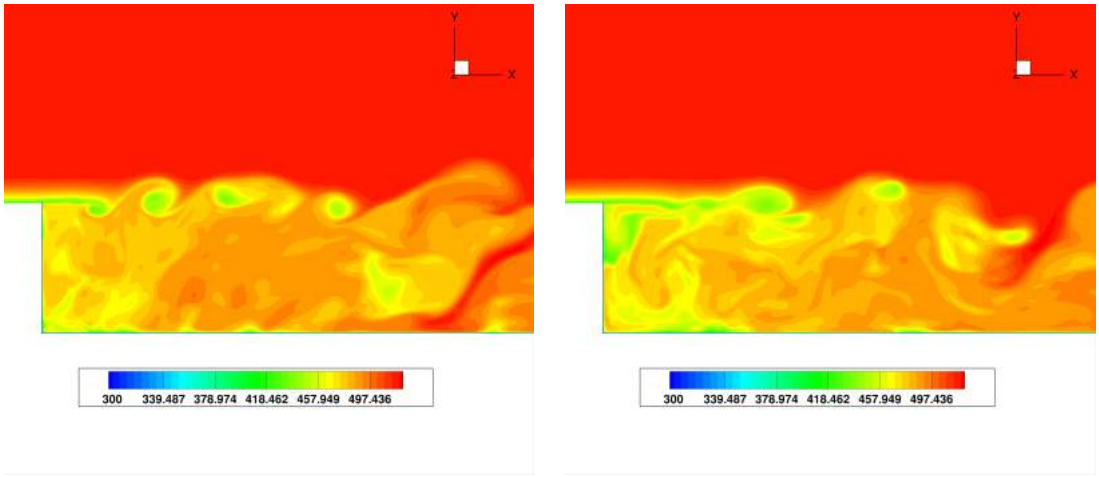

Fig. 11.8. Temperature field (with 2-exact spatial scheme) time integrated by Heun+TA and AION+TA scheme

Pressure and temperature contours in the shear-layer of the backward facing step using Heun+TA (left) and AION+TA schemes (right) are illustrated in Figs. 11.9-11.8. It appears that both time integrators enable to capture the recirculation with delay. This is not surprising since the temporal adaptive approaches showed dispersion in Sec. 6.2.1 and 10.2.2. Nevertheless the AION+TA scheme captures smaller vortices than the Heun+TA scheme. Thanks to good properties of accuracy, dissipation and dispersion, the AION+TA scheme is able to capture smaller vortices with a delay. In a practical point of view, it seems that the AION time

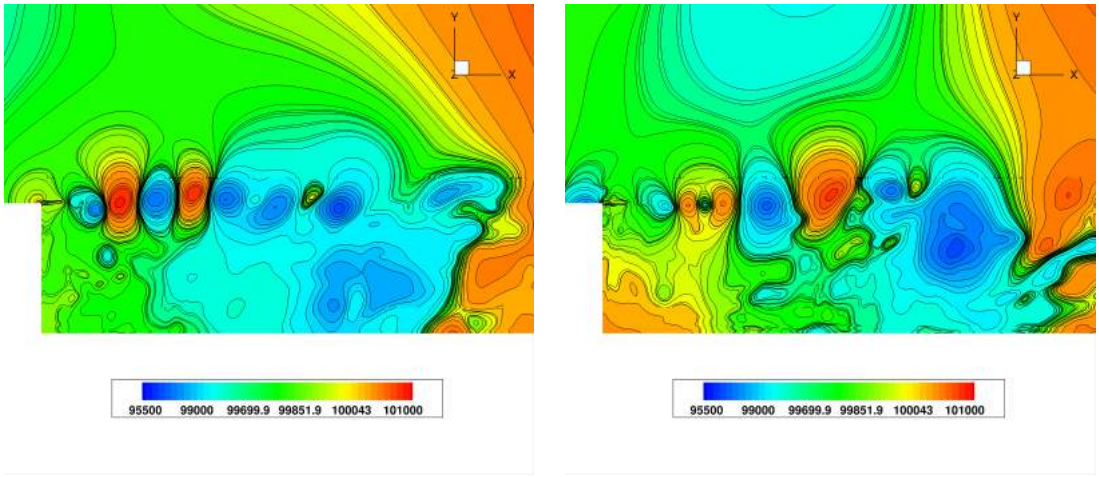

Fig. 11.9. Pressure field (with 2-exact spatial scheme) time integrated by Heun+TA and AION+TA scheme

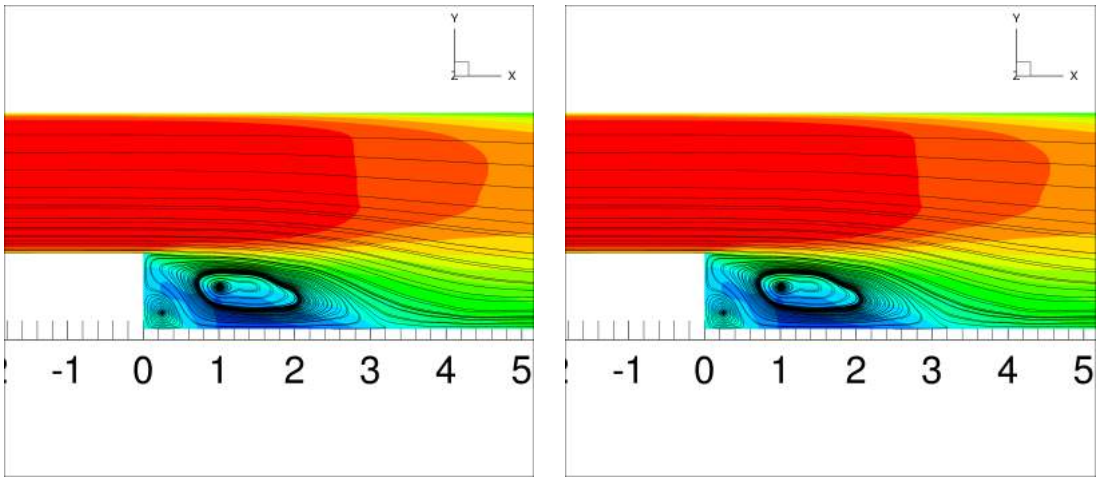

Fig. 11.10. Contour of mean longitudinal velocity with Heun+TA and AION+TA time integrator

integration can be an essential ingredient in order to less dissipate structures generated by convective instabilities. Many other simulations must be performed to confirm this behaviour on industrial configurations.

V Conclusion & Perspectives

12 Conclusion 149

13 Perspectives 151

12 Conclusion

The objective of this PhD work was to find an efficient (in terms of HPC) and accurate (to capture the flow physics) time integration technique that allows larger time step while dealing with complex geometries and convection of unsteady flow over a long distance. It relied on the different techniques implemented in the industrial solver of ArianeGroup called **FLUSEPA**©. This latter solver deals with time integration of hybrid RANS/LES simulation thanks to an explicit temporal adaptive method based on predictor-corrector Heun's scheme. But the numerical simulations performed by ArianeGroup tend to have strong stratification in order to capture flows physics near the wall and in this case the explicit temporal adaptive approach appears to suffer from high computational time cost. It was decided to investigate several kinds of time integration method to overcome this issue.

In chapters 3 and 4, a literature review on standard explicit and implicit time integrators was carried out offering a theoretical background on possible candidates that allow larger time step than Heun's scheme. This study was performed with a special emphasis on second order accurate method, with interesting spectral behaviour and stability property. For the simulation of the quasi-steady flows near walls (modelled by RANS equations), it is preferable to advance in time with large time steps thanks to an implicit time integration. But for unsteady flows (modelled by LES equations), an explicit time integration is preferable to control simply and efficiently spectral properties (dissipation and dispersion). In this context, it was decided to develop a hybrid approach to be able to couple spatially explicit and implicit time integration approaches. Finally, the explicit scheme designed by Heun and the implicit IRK2 scheme were chosen as best options for future applications.

In chapter 5, the attention was focused on a hybrid approach. To summarize, several methods have been designed to allow different ways to take advantage of both types of temporal integration schemes (explicit or implicit). Two families seem to emerge, such as the IMEX coupling technique which time-integrates, in all cells but separately, the stiff part and the non-stiff part of the equations and the techniques that use specific integration schemes according to the zonal characteristics of flow physics. The transition parameter ω used by the method of Timofeev and Norouzi [81] was the corner stone of the our coupling between Heun's and Crank-Nicolson's schemes.

In chapter 6, the temporal adaptive approach implemented in **FLUSEPA**© was introduced and analysed. This approach sorts cells in temporal classes according to their own maximal time step available and uses sub-cycling for time integration of temporal classes until the biggest time step. The technique maintains a conservative behaviour during time synchronisation of temporal classes and the local time accuracy is demonstrated in case of explicit time integration. The space-time spectral behaviour of the approach and its ability to damp spurious waves was also analysed. Such results were not found by the literature review.

The chapters 8 and 9 deal with how explicit and implicit time integrators can be coupled spatially. Here, two standard time integration schemes (Heun's and second order implicit Runge-Kutta schemes -IRK2-) are hybridized / blended using a transition function ω, while keeping the standard expected properties (spectral behaviour). In the first part (chapter 8), a way to couple the proposed schemes, adapted from the literature, was first introduced but lead to instability for some wavenumbers and CFL values. A new alternative approach (chapter

9), named AION scheme, was proposed and designed in order to correct the unexpected behaviour of the first coupling procedure. The spectral analysis performed on the coupled space / AION schemes enabled us to check the stability of the coupling procedure. In addition, in order to minimize the CPU cost, transition to explicit and implicit schemes was performed by reducing the transition area, playing with the values of ω. After the spectral analysis, attention was paid on simulations of increasing complexity, from one-dimensional shock tube to three-dimensional Taylor Green Vortex. The results with the new scheme were shown to have same or better quality than the standard basic schemes. In addition, starting from the reference fully-implicit time integration, the hybrid formulation enables to reduce the CPU cost while advancing in time with larger time step than standard Heun's scheme and maintains accuracy.

In chapter 10 the extension of our AION scheme with the temporal adaptive approach implemented in our industrial solver was validated. Conservation and local time accuracy are demonstrated on regular grid. Spectral analysis reveals that the extension to AION time integration does not influence dissipation and dispersion behaviour of the temporal adaptive approach. The theoretical results are then confirmed numerically. Propagation of an one-dimensional wave packet confirm that the AION scheme improves the stability properties of the temporal adaptive approach. An one-dimensional shock tube test case reveals that the time-adaptive AION scheme can handle compressible effect and finally two-dimensional convected vortex confirm that the global time accuracy is kept for AION scheme coupled with temporal adaptive approach for irregular grid. Finally, the AION scheme was validated on a basic RANS/LES simulation. The transition parameter ω was designed in such turbulent case to match with the shielding function that switches between RANS and LES models. Simulation performed on two-dimensional backward facing step reveals that the AION time integration is able to capture turbulent physics flows while being efficient in term of computational cost.

It is important to mention that additional activity was performed during the thesis and was not included into the document:

- Expertise on time integration for stiff phenomena for the Plasma team at CERFACS: IMEX time integrators appear to be an interesting option of investigation for time integration of stiffness in case of Plasma simulation [75].
- Expertise for trainees on implementation of implicit time integration on Spectral differences prototype, following the reference [111]
- Design of one-dimensional prototype (with finite volume and Spectral differences formulation) with several type of time integrators with global and local time stepping for resolution of advection, diffusion and Euler equations.

13 Perspectives

In this Ph.D. work, an approach that couples explicit and implicit time integration depending of the local physics of flows of the turbulent model employed (RANS or LES) was designed and validated. Nevertheless several suggestions of improvement and perspectives might be possible.

- **Optimisation in terms of CPU cost:** First, two main optimisations (in terms of CPU cost) may be interesting. The solver for linear systems of equations implemented in **FLUSEPA**© (GMRES/QR) is performed only in case of AION time integration for hybrid or implicit cells. It will be more interesting in terms of effectiveness to implement and validate a Jacobian-free Newton-Krylov method (JFNK) [112, 113] since it avoids the computation of the Jacobian matrix. Secondly, usual time integrators implemented in **FLUSEPA**© are Euler's backward scheme (implicit one) and Heun's scheme coupled with time adaptive approach (explicit one). Each time integrator was optimised for multiprocessors (thesis of Couteyen [5]). Nevertheless, the coupling between AION scheme and temporal adaptive approach represents a high CPU cost (in case of hybrid time integration of different temporal classes) due to non-optimised approach in term of multiprocessing. Indeed too many cores treat too few hybrid and implicit cells. It will be necessary to design a methodology that leads to task equilibrium.
- **Coupling with AMR technique:** The Adaptive Mesh Refinement technique implemented by Limare [6] use physical criterion in order to better capture unsteady physics by fine cells while optimising the amount of cells in the grid. A way to couple AMR criterion with the hybrid time integration parameter of the AION scheme may also be studied in the future in order to perform hybrid and implicit time integration in the zone defined as steady by AMR criterion.
- **Investigation on time limiter:** Our AION scheme is designed with a time limiter that ensures TVD property in one-dimensional case. The extension of TVD property for multi-dimensional case was widely investigated, **FLUSEPA**© use method with MND (Maximal Norm Diminishing) property to deal with compressible phenomena while other method as Multi-dimensional Optimal Order Detection (MOOD) [114, 115] downgrade locally the order of accuracy of the reconstruction. In future investigation it will be mandatory to design a time limiter that matches with the space limiter defined in **FLUSEPA**©.
- **Spectral discontinuous methods:** This report deals only with the finite volume formulation of Navier-Stokes equation, and high order k-exact reconstruction. Other high order methods as Spectral difference (SD) [116, 117], Discontinus Galerkin (DG) [97, 118, 119] or Flux Reconstruction (FR) [120, 121, 122] methods can be investigated for time integration with AION scheme. The SD and FR formulations impose a Riemann solver at junction between cells (as for flux computation in a finite volume formulation) that allows to fit the hybrid reconstruction of the AION scheme with this scheme methodology. An one-dimensional prototype of the AION scheme with SD method was designed for resolution of advection equation. Results and conclusion obtained with advection of Gaussian hump by SD formulation with explicit Heun, implicit IRK2 and AION time

integrations are equivalent with finite volume reconstruction.

- **Improvement of the temporal adaptive approach:** Temporal adaptive technique appears to be an approach widely studied and with many improvement [123]. A first improvement would be to change the methodology introduced previously in chapter 6, a second reflection will be to substitute temporal adaptive approach with exponential time integrators according to their A-stable property.

VI Appendices

A TVD property of hybrid part of AION scheme 155

A

TVD property of hybrid part of AION scheme

The proof that the hybrid part of the AION scheme is TVD follows the procedure for the TN scheme [82]. It is applied to the linear one-dimensional advection equation Eq. (1.23) time-integrated by the hybrid part of the AION scheme Eq. (9.2):

$$W^{n+1} = W^n - \nu_j(W_{j+1/2} - W_{j-1/2}) \tag{A.1}$$

with $\nu_j = \frac{c\Delta t}{\Delta x_j}$. The faces values of the hybrid part of AION scheme Eq. (9.2) for the one-dimensional advection Eq. (1.23) are formulated as:

$$\begin{aligned} W_{j+1/2} =& \omega_i W_j + \frac{1-\omega_j\nu_j}{2}\phi_j(\nabla_x)^n_{j+1/2} + \left(\omega_j - \frac{1}{2}\right)\phi_j(\widehat{\nabla}_x)_{j+1/2} \\ & (1-\omega_j)\left[W^{n+1}_j + \frac{1}{2}\phi_j(\nabla_x)^{n+1}_{j+1/2} - \frac{1-\omega_j}{2}\psi_j(\Delta_t)^{n+1}_j\right] \end{aligned} \tag{A.2}$$

with:

$$\begin{aligned} (\nabla_x)^n_{j+1/2} &= W^n_{j+1} - W^n_j \\ (\nabla_x)^{n+1}_{j+1/2} &= W^{n+1}_{j+1} - W^{n+1}_j \\ (\widehat{\nabla}_x)_{j+1/2} &= \widehat{W}_{j+1} - \widehat{W}_j \\ (\Delta_t)^{n+1}_j &= W^{n+1}_j - W^n_j, \end{aligned} \tag{A.3}$$

The functions ϕ_j and ψ_j are respectively the spatial and temporal limiter, functions of $q_j = \frac{(\nabla_x)_{j-1/2}}{(\nabla_x)_{j+1/2}}$ and $s_j = \frac{(\Delta_t)_{j+1}}{(\nabla_x)_j}$. By substitution of above Eq. (A.2) into Eq. (A.1), the following formulation of the hybrid time integration is obtained:

$$\begin{aligned} W^{n+1}_j =& W^n_j - \nu_j\Big[\omega_j(\nabla_x)^n_{j-1/2} + (1-\omega_j)(\nabla_x)^{n+1}_{j-1/2} - \frac{(1-\omega_j)^2}{2}\big[\psi_j - \frac{\psi_{j-1}}{s_{j-1}}\big](\Delta_t)^{n+1}_j \\ & + \frac{1-\omega_j^2\nu_j}{2}\big[\frac{\phi_j}{q_j} - \phi_{j-1}\big]^n(\nabla_x)^n_{j-1/2} + (\omega_j - \frac{1}{2})\big[\frac{\phi_j}{q_j} - \phi_{j-1}\big]\widehat{(\widehat{\nabla}_x)}_{j-1/2} \\ & + \frac{1-\omega_j}{2}\big[\frac{\phi_j}{q_j} - \phi_{j-1}\big]^{n+1}(\nabla_x)^{n+1}_{j-1/2}\Big] \end{aligned} \tag{A.4}$$

With some rearrangement, it leads to:

$$\begin{aligned} (W^{n+1}_j - W^n_j)\left[1 + \frac{\nu_j(1-\omega_j)^2}{2}\big[\frac{\psi_{j-1}}{s_{j-1}} - \psi_j\big]\right] =& -\nu_j\left[\omega_j + \frac{1-\omega_j^2\nu_j}{2}\big[\frac{\phi_j}{q_j} - \phi_{j-1}\big]^n\right](\nabla_x)^n_{j-1/2} \\ & -\nu_j\left[(\omega_j - \frac{1}{2})\big[\frac{\phi_j}{q_j} - \phi_{j-1}\big]\widehat{\ }\right](\widehat{\nabla}_x)_{j-1/2} \\ & -\nu_j(1-\omega_j)\left[1 + \frac{1}{2}\big[\frac{\phi_j}{q_j} - \phi_{j-1}\big]^{n+1}\right](\nabla_x)^{n+1}_{j-1/2} \end{aligned}$$

(A.5)

Defining the parameter β as:

$$\beta = 1 + \frac{\nu_j(1-\omega_j)^2}{2}\big[\frac{\psi_{j-1}}{s_{j-1}} - \psi_j\big], \tag{A.6}$$

and substituting Eq. (A.6) into Eq. (A.5):

$$\begin{aligned} W_j^{n+1} + \frac{\nu_j(1-\omega_j)}{\beta}\left[1+\frac{1}{2}\big[\frac{\phi_j}{q_j} - \phi_{j-1}\big]^{n+1}\right](\nabla_x)_{j-1/2}^{n+1} =& W_j^n - \frac{\nu_j}{\beta}\left[(\omega_j - \frac{1}{2})\widehat{\big[\frac{\phi_j}{q_j} - \phi_{j-1}\big]}\right](\widehat{\nabla}_x)_{j-1/2} \\ & - \frac{\nu_j}{\beta}\left[\omega_j + \frac{1-\omega_j^2\nu_j}{2}\big[\frac{\phi_j}{q_j} - \phi_{j-1}\big]^n\right](\nabla_x)_{j-1/2}^n. \end{aligned} \tag{A.7}$$

The previous relation Eq. (A.7) may be reformulated as:

$$W_j^{n+1} - A(\nabla_x)_{j-1/2}^{n+1} = W_j^n - B(\nabla_x)_{j-1/2}^n - C(\widehat{\nabla}_x)_{j-1/2} \tag{A.8}$$

Finally, according to Harten's theorem, the sufficient conditions for the previous scheme Eq. (A.8) to be TVD are:

$$\begin{cases} A \le 0 \\ 0 \le B + C \le 1 \end{cases} \tag{A.9}$$

with:

$$\begin{aligned} A &= -\frac{\nu_j(1-\omega_j)}{\beta}\left[1+\frac{1}{2}\big[\frac{\phi_j}{q_j} - \phi_{j-1}\big]^{n+1}\right] \\ B &= \frac{\nu_j}{\beta}\left[\omega_j + \frac{1-\omega_j^2\nu_j}{2}\big[\frac{\phi_j}{q_j} - \phi_{j-1}\big]^n\right] \\ C &= \frac{\nu_j}{\beta}\left[(\omega_j - \frac{1}{2})\widehat{\big[\frac{\phi_j}{q_j} - \phi_{j-1}\big]}\right] \end{aligned} \tag{A.10}$$

Applying the condition (A.9) and considering $A \le 0$ then

$$A \le 0 \Rightarrow \begin{cases} 1 + \frac{1}{2}\big[\frac{\phi_j}{q_j} - \phi_{j-1}\big]^{n+1} \ge 0 \\ \frac{(1-\omega_j)\nu_j}{\beta} \ge 0 \end{cases} \tag{A.11}$$

Fortunately, the first inequality in Eq. (A.11) is satisfied by conventional space limiter as the minmod one [105]. Then according to second inequality in (A.11), the first condition on time limiter to be TVD is:

$$\frac{\psi_{j-1}}{s_{j-1}} - \psi_j \ge -\frac{2}{\nu_j(1-\omega_j)^2} \tag{A.12}$$

Another condition to be TVD according to Eq. (A.9) leads to:

$$B + C \ge 0 \Rightarrow \begin{cases} \nu_j\left(\omega_j + \frac{1-\omega_j^2\nu_j}{2}\big[\frac{\phi_j}{q_j} - \phi_{j-1}\big]^n + (\omega_j - \frac{1}{2})\widehat{\big[\frac{\phi_j}{q_j} - \phi_{j-1}\big]}\right) \ge 0 \\ 1 + \frac{(1-\omega_j)^2\nu_j}{2}\big[\frac{\psi_{j-1}}{s_{j-1}} - \psi_j\big] \ge 0 \end{cases} \tag{A.13}$$

The first inequality in the previous expression Eq. (A.13) is satisfied for any space limiter (e.g. minmod limiter) as long as $\nu_j\omega_j \leq 1$ and $0.6 < \omega_j < 1$. Second inequality results in the same condition on time limiter (see eq. (A.12)). The last condition for having a TVD scheme leads to:

$$B + C \leq 1 \Rightarrow \frac{\nu_j\left(\omega_j + \frac{1-\omega_j^2\nu_j}{2}\left[\frac{\phi_j}{q_j} - \phi_{j-1}\right]^n + (\omega_j - \frac{1}{2})\widehat{\left[\frac{\phi_j}{q_j} - \phi_{j-1}\right]}\right)}{1 + \frac{(1-\omega_j)^2\nu_j}{2}\left[\frac{\psi_{j-1}}{s_{j-1}} - \psi_j\right]} \leq 1 \tag{A.14}$$

According to the fact that the maximum value for $\left[\frac{\phi_j}{q_j} - \phi_{j-1}\right]^n$ and $\widehat{\left[\frac{\phi_j}{q_j} - \phi_{j-1}\right]}$ for a spatial limiter is 2, the time limiter of the hybrid part of the AION scheme is TVD and the proof is the same as for the TN scheme [82]:

$$\frac{\psi_{j-1}}{s_{j-1}} - \psi_j \geq -\frac{2}{\nu_j}\frac{1 - \omega_j\nu_j(2 - \omega_j\nu_j)}{(1-\omega_j)^2} \tag{A.15}$$

The condition resulting from Eq. (A.15) is more restrictive than the condition from Eq. (A.12) so it is the only necessary condition to satisfy for the proof of the TVD property in the hybrid part of the AION scheme.

VII Bibliography

[1] P. Brenner. Three-dimensional aerodynamics with moving bodies applied to solid propellant. 27th AIAA Joint Propulsion Conference. AIAA. (1991). (Cited on page 3).

[2] P. Brenner. Unsteady flows about bodies in relative motion. First AFOSR Conference on Dynamic Motion CFD. (1996). (Cited on pages 3, 57, 59).

[3] G. Pont. Self adaptive turbulence models for unsteady compressible flows. PhD thesis. École Nationale Supérieure d'Arts et Métiers ParisTech, (2015). (Cited on pages 3, 5).

[4] L. Charrier, G. Pont, S. Marié, P. Brenner, and F. Grasso. Hybrid RANS/LES Simulation of a Supersonic Coaxial He/Air Jet Experiment at Various Turbulent Lewis Numbers. Progress in Hybrid RANS-LES Modelling. Springer International Publishing (2018), 337–346. (Cited on page 3) http://dx.doi.org/10.1007/978-3-319-70031-1_28.

[5] J.M. Couteyen Carpaye. Contribution à la parallélisation et au passage à l'échelle du code FLUSEPA. PhD thesis. Université de Bordeaux, (2016.) (Cited on pages 3, 151).

[6] A. Limare. Adaptation par enrichissement de maillages ointersectant, dans un contexte Volume Finis d'ordre élévé, pour la simulation des écouleemnts ccompressible instationnaires. PhD thesis. Université de Technologie de Troyes, (2017). (Cited on pages 4, 117, 151).

[7] A. Menasria, P. Brenner, P. Cinnella, and G. Pont. Toward an improved wall treatment for multiple-correction k-exact schemes. 2018 Fluid Dynamics Conference, AIAA AVIATION Forum, (AIAA Paper 2018-4164). (2018). (Cited on page 4) http://dx.doi.org/10.2514/6.2018-4164.

[8] D.R. Chapman. Computational Aerodynamics Development and Outlook. *AIAA Journal* 17 (12) (1979), 1293–1313. (Cited on page 4). http://dx.doi.org/10.2514/3.61311.

[9] P. Sagaut. Large Eddy Simulation for Incompressible Flows: An introduction. Springer Science & Business Media (2006). (Cited on page 5).

[10] E. Garnier, N. Adams, and P. Sagaut. Large Eddy Simulation for Compressible Flows. Springer Science & Business Media (2009). (Cited on page 5).

[11] C. Moussaed, M.V. Salvetti, S. Wornom, B. Koobus, and A. Dervieux. Simulation of the flow past a circular cylinder in the supercritical regime by blending RANS and variational-multiscale LES models. *Journal of Fluids and Structures* 47 (2014), 114–123. (Cited on page 5). http://dx.doi.org/10.1016/j.jfluidstructs.2013.11.006.

[12] S.D. Hall, M. Behnia, C.A.J. Fletcher, and G.L. Morrison. Investigation of the secondary corner vortex in a benchmark turbulent backward-facing step using cross-correlation particle imaging velocimetry. *Experiments in Fluids* 35 (2) (2003), 139–151. (Cited on pages 5, 142, 143). http://dx.doi.org/10.1007/s00348-003-0626-9.

[13] G. Dahlquist. Convergence and stability in the numerical integration of ordinary differential equations. *Mathematica Scandinavica* 4 (1956), 33–53. (Cited on page 6). http://dx.doi.org/10.7146/math.scand.a-10454.

[14] M. Catchirayer, J.-F. Boussuge, P. Sagaut, M. Montagnac, D. Papadogiannis, and X. Garnaud. Extended integral wall-model for large-eddy simulations of compressible wall-bounded turbulent flows. *Physics of Fluids* 30 (6) (2018), 065106. (Cited on page 6). http://dx.doi.org/10.1063/1.5030859.

[15] P.R. Spalart. Detached-Eddy Simulation. *Annual Review of Fluid Mechanics* 41 (1) (2009), 181–202. (Cited on page 6). http://dx.doi.org/10.1146/annurev.fluid.010908.165130.

[16] P. Sagaut, S. Deck, and M. Terracol. Multiscale and Multiresolution Approaches in Turbulence. (2006). (Cited on page 6).

[17] C. Ollivier Gooch and M. Van Altena. A High-Order-Accurate Unstructured Mesh Finite-Volume Scheme for the Advection–Diffusion Equation. *Journal of Computational Physics* 181 (2) (2002), 729–752. (Cited on page 9). http://dx.doi.org/10.1006/jcph.2002.7159.

[18] F. Haider, P. Brenner, B. Courbet, and J.P. Croisille. Parallel Implementation of k-Exact Finite Volume Reconstruction on Unstructured Grids. Lecture Notes in Computational Science and Engineering. Springer International Publishing (2014), 59–75. (Cited on page 9). http://dx.doi.org/10.1007/978-3-319-05455-1_4.

[19] G. Pont, P. Brenner, P. Cinnella, B. Maugars, and J.-C. Robinet. Multiple-correction hybrid k-exact schemes for high-order compressible RANS-LES simulations on fully unstructured grids. *Journal of Computational Physics* (350) (2017), 45–83. (Cited on pages 9, 141). http://dx.doi.org/10.1016/j.jcp.2017.08.036.

[20] D.J. Higham and L.N. Trefethen. Stiffness of ODEs. *BIT Numerical Mathematics* 33 (2) (1993), 285–303. (Cited on page 17). http://dx.doi.org/10.1007/bf01989751.

[21] R. Abgrall, D. Aregba, C. Berthon, M. Castro, and C. Parés. Numerical approximations of hyperbolic systems with source terms and applications: Preface. Volume 48. (1-3). J. Sci. Comput volume 48 (2011), 1–2. (Cited on page 17). http://dx.doi.org/10.1007/s10915-011-9497-z.

[22] E. Süli and D.F. Mayers. An Introduction to Numerical Analysis. Cambridge University Press (2003). (Cited on page 18). http://dx.doi.org/10.1017/CBO9780511801181.

[23] E. Hairer, S. P. Nørsett, and G. Wanner. Solving Ordinary Differential Equations I (2Nd Revised. Ed.): Nonstiff Problems. Berlin, Heidelberg. Springer-Verlag (1993). (Cited on pages 18, 32, 40).

[24] T.K. Sengupta, Y.G. Bhumkar, M.K. Rajpoot, V.K. Suman, and S. Saurabh. Spurious waves in discrete computation of wave phenomena and flow problems. *Applied Mathematics and Computation* 218 (18) (2012), 9035–9065. (Cited on pages 20–22). http://dx.doi.org/10.1016/j.amc.2012.03.030.

[25] T.K. Sengupta, M.J. Rajpoot, and Y.G. Bhumkar. Space-time discretizing optimal DRP schemes for flow and wave propagation problems. *Journal of Computational Physics* 47 (2011), 144–154. (Cited on page 20). http://dx.doi.org/10.1016/j.compfluid.2011.03.003.

[26] T.K. Sengupta, G. Ganeriwal, and S. De. Analysis of central and upwind compact schemes. *Journal of Computational Physics* 192 (2003), 677–694. (Cited on page 20). http://dx.doi.org/10.1016/j.jcp.2003.07.015.

[27] L.L. Takacs. A Two-Step Scheme for the Advection Equation with Minimized Dissipation and Dispersion Errors. *Monthly Weather Review* 113 (6) (1985), 1050–1065. (Cited on page 20). http://dx.doi.org/10.1175/1520-0493(1985)113<1050:atssft>2.0.co;2.

[28] T. Poinsot and D. Veynante. Theoretical and Numerical Combustion. Edited by Philadelphia. second ed. R.T. Edwards Inc. (2005). (Cited on page 21).

[29] L.N. Trefethen. Group velocity in finite difference schemes. *SIAM Review* 24 (2) (1982). (Cited on page 21). http://dx.doi.org/10.1137/1024038.

[30] R. Vichnevetsky and J.B. Bowles. Fourier Analysis of Numerical Approximations of Hyperbolic Equations. Society for Industrial and Applied Mathematics (1982). (Cited on page 21). http://dx.doi.org/10.1137/1.9781611970876.

[31] A. Harten. High resolution schemes for hyperbolic conservation laws. *Journal of Computational Physics* 49 (3) (1983), 357–393. (Cited on page 22). http://dx.doi.org/https://doi.org/10.1016/0021-9991(83)90136-5.

[32] R. Anguelov, J.M.-S. Lubuma, and F. Minani. Total variation diminishing nonstandard finite difference schemes for conservation laws. *Mathematical and Computer Modelling* 51 (3) (2010) Proceedings of the International Conference of Computational Methods in Sciences and Engineering 2005, 160–166. (Cited on page 22). http://dx.doi.org/https://doi.org/10.1016/j.mcm.2009.08.038.

[33] R.J. LeVeque. Finite Volume Methods for Hyperbolic Problems. Cambridge University Press (2002). (Cited on page 22). http://faculty.washington.edu/rjl/book.html.

[34] J.P. Demailly. Analyse numérique et équations différentielles. EDP Sciences, coll. « Grenoble Sciences » (2006). (Cited on page 27).

[35] E. Hairer and G. Wanner. Solving Ordinary Differential equation II. Stiff and Differential Algebraic Problems. 2nd ed. Springer-Verlag (1996). (Cited on pages 29, 31, 32, 40, 42, 44).

[36] C. Runge. 0ber die numerisehe Aufltising yon Differentialgleichungen. *Mathematische Annalen* 46 (1895), 167–178. (Cited on page 29).

[37] W. Kutta. Beitrag zur näherungsweisen Integration totaler Differentialgleichungen. *Zeitschrift für angewandte Mathematik und Physik* 46 (1901), 435–453. (Cited on page 29).

[38] J.C. Butcher. A history of Runge-Kutta methods. *Applied Numerical Mathematics* 20 (1996), 247–260. (Cited on page 30). http://dx.doi.org/10.1016/0168-9274(95)00108-5.

[39] A. Jameson, W. Schmidt, and E. Turkel. Numerical solution of the Euler equations by finite volume methods using Runge-Kutta time stepping schemes. 14th Fluid and Plasma Dynamics Conference. AIAA (1981). (Cited on pages 31, 32, 37) http://dx.doi.org/10.2514/6.1981-1259.

[40] K. Heun. Neue Methoden zur approximativen Integration der Differentialgleichungen einer unabhängigen Veränderlichen. *Zeitschrift für angewandte Mathematik und Physik* 45 (1900), 23–38. (Cited on pages 31, 60).

[41] J.C. Butcher. Numerical Methods for Ordinary Differential Equations, Second Edition. John Wiley & Sons, Ltd (2008). (Cited on page 32). http://dx.doi.org/10.1002/9780470753767.

[42] J.H. Williamson. Low-storage Runge-Kutta schemes. *Journal of Computational Physics* 35 (1) (1980), 48–56. (Cited on page 32). http://dx.doi.org/10.1016/0021-9991(80)90033-9.

[43] C.-W. Shu and S. Osher. Efficient implementation of essentially non-oscillatory shock-capturing schemes. *Journal of Computational Physics* 77 (2) (1988), 439–471. (Cited on page 32). http://dx.doi.org/10.1016/0021-9991(88)90177-5.

[44] J. Certaine. The solution of ordinary differential equations with large time constants, in Mathematical methods for digital computers. A. Ralston and H.S. Wilf (1960). (Cited on page 32).

[45] S.P. Norsett. An A-stable modification of the Adams-Bashforth methods. Lecture Notes in Mathematics. Springer Berlin Heidelberg (1969), 214–219. (Cited on page 34). http://dx.doi.org/10.1007/bfb0060031.

[46] G. Beylkin, J.M. Keiser, and L. Vozovoi. A New Class of Time Discretization Schemes for the Solution of Nonlinear PDEs. *Journal of Computational Physics* 147 (2) (1998), 362–387. (Cited on page 34). http://dx.doi.org/10.1006/jcph.1998.6093.

[47] B. L. Ehle and J. D. Lawson. Generalized Runge-Kutta Processes for Stiff Initial-value Problems. *IMA Journal of Applied Mathematics* 16 (1) (1975), 11–21. (Cited on page 34). http://dx.doi.org/10.1093/imamat/16.1.11.

[48] P.J. van der Houwen. Construction of integration formulas for initial value problem. Edited by North-Holland Series in Applied Mathemtaics and Mechanics. Volume 19. North-Holland Publishing Co. volume 19 (1977). (Cited on page 34).

[49] J.G. Verwer. S-Stability properties for generalized Runge-Kutta methods. *Numerische Mathematik* 27 (4) (1976), 359–370. (Cited on page 34). http://dx.doi.org/10.1007/BF01399599. https://doi.org/10.1007/BF01399599.

[50] B.V. Minchev and W.M. Wright. A review of exponential integrators for first order semi-linear problems. (2005). (Cited on pages 34, 35).

[51] J. Huang and C.-W. Shu. Bound-preserving modified exponential Runge–Kutta discontinuous Galerkin methods for scalar hyperbolic equations with stiff source terms. *Journal of Computational Physics* 361 (2018), 111–135. (Cited on page 34). http://dx.doi.org/https://doi.org/10.1016/j.jcp.2018.01.051.

[52] J.C. Schulze, P.J. Schmid, and J.L. Sesterhenn. Exponential time integration using Krylov subspaces. *International Journal for Numerical Methods in Fluids* 60 (6) (2009), 591–609. (Cited on page 35). http://dx.doi.org/10.1002/fld.1902.

[53] M. Hochbruck, C. Lubich, and H. Selhofer. Exponential Integrators for Large Systems of Differential Equations. *SIAM Journal on Scientific Computing* 19 (5) (1998), 1552–1574. (Cited on page 35). http://dx.doi.org/10.1137/s1064827595295337.

[54] M. Caliari and A. Ostermann. Implementation of exponential Rosenbrock-type integrators. *Applied Numerical Mathematics* 59 (3-4) (2009), 568–581. (Cited on page 35). http://dx.doi.org/10.1016/j.apnum.2008.03.021.

[55] H.Montanelli and N.Bootland. Solving periodic semilinear stiff PDEs in 1D, 2D and 3D with exponential integrators. (2016). eprint: arXiv:1604.08900 (cited on page 35).

[56] H. Hollanders, A. Lerat, and R. Peyret. Three-dimensional calculation of transonic viscous flows by an implicit method. *AIAA Journal* 23 (11) (1985), 1670–1678. (Cited on page 36). http://dx.doi.org/10.2514/3.9150.

[57] P. Cinnella and C. Content. High-order implicit residual smoothing time scheme for direct and large eddy simulations of compressible flows. *Journal of Computational Physics* 326 (2016), 1–29. (Cited on pages 37, 38). http://dx.doi.org/10.1016/j.jcp.2016.08.023.

[58] C. Bogey and C. Bailly. A family of low dispersive and low dissipative explicit schemes for flow and noise computations. *Journal of Computational Physics* 194 (1) (2004), 194–214. (Cited on page 37). http://dx.doi.org/10.1016/j.jcp.2003.09.003.

[59] L.A. Catalano and V.S.E. Daloiso. Upwinding and implicit residual smoothing on cell-vertex unstructured grids. *International Journal for Numerical Methods in Fluids* 47 (8-9) (2005), 895–902. (Cited on page 38). http://dx.doi.org/10.1002/fld.896.

[60] C.W. Gear. Numerical Initial Value Problems in Ordinary Differential Equations. Upper Saddle River, NJ, USA. Prentice Hall PTR (1971). (Cited on page 40).

[61] J. Crank and P. Nicolson. A practical method for numerical evaluation of solutions of partial differential equations of the heat conduction type. *Advances in Computational Mathematics* 6 (1) (1996), 207–226. (Cited on page 41). http://dx.doi.org/10.1007/BF02127704.

[62] J. Kuntzmann. Neure Entwicklungen der Methoden von Runge und Kutta. *Zeitschrift für angewandte Mathematik und Physik* 41 (1961), 29–31. (Cited on page 42). http://dx.doi.org/10.1002/zamm.19610411317.

[63] J.C. Butcher. Implicit Runge-Kutta Processes. *Mathematics of Computation* 18 (85) (1964), 50–64. (Cited on pages 42, 44). http://dx.doi.org/10.1090/s0025-5718-1964-0159424-9.

[64] P.C. Hammer and J.W. Hollingsworth. Trapezoidal Methods of Approximating Solutions of Differential Equations. *Mathematical Tables and Other Aids to Computation* 9 (51) (1955), 92. (Cited on page 43). http://dx.doi.org/10.2307/2002064.

[65] B.L. Ehle. On Pade approximations to the exponential function and A-stable methods for the numerical solution of initial value problems. PhD thesis. University of Waterloo, (1969). (Cited on pages 44, 45).

[66] O. Axelsson. A class of A-stable methods. *BIT Numerical Mathematics* (1969). (Cited on pages 44, 45). http://dx.doi.org/10.1007/BF01946812.

[67] C. Schneider. ROW-method adapted to differential algebraic systems. *Mathematics of Computation* VI-3 (1990). (Cited on page 46). http://dx.doi.org/10.2307/2008537.

[68] Y. Saad and M.H. Schultz. GMRES: A generalized minimal residual algortihm for solving nonsymmetric linear systems. *SIAM J. Sci. Stat. Comput.*. 7 (3) (1986). (Cited on page 46). http://dx.doi.org/10.1137/0907058.

[69] Y. Saad. Analysis of some Krylov subspace approximations to the matrix exponential operator. *SIAM J. Numer. Anal.* 29 (1) (1992), 209–228. (Cited on page 46). http://dx.doi.org/10.1137/0729014.

[70] P.N. Brown and Y. Saad. Hybrid Krylov methods for nonlinear systems of equations. *SIAM J. Sci. Stat. Comput.* 11 (3) (1990), 450–481. (Cited on page 46). https://doi.org/10.1137/0911026.

[71] C.A. Kennedy and M.H. Carpenter. Additive Runge–Kutta schemes for convection – diffusion – reaction equations. *Applied Numerical Mathematics* 44 (1-2) (2003), 139–181. (Cited on page 47). http://dx.doi.org/10.1016/s0168-9274(02)00138-1.

[72] M. Crouzeix. Une méthode multipas implicite-explicite pour l'approximation des équations d'évolution paraboliques. *Numerische Mathematik* 35 (1980), 257–276. (Cited on page 49). http://dx.doi.org/10.1007/BF01396412.

[73] J. Kim and P. Moin. Application of a fractional-step method to incompressible Navier-Stokes equations. *Journal of Computational Physics* 59 (2) (1985), 308–323. (Cited on page 49). http://dx.doi.org/10.1016/0021-9991(85)90148-2.

[74] U. Ascher, S. Ruuth, and B. Wetton. Implicit-explicit Methods for time-dependent partial differential equations. *SIAM J. Numer. Anal.* 32 (3) (1995), 797–823. (Cited on page 50). http://dx.doi.org/10.1137/0732037.

[75] V.T. Luan, M. Tokman, and G. Rainwater. Preconditioned implicit-exponential integrators (IMEXP) for stiff PDEs. *Journal of Computational Physics* 335 (2017), 846–864. (Cited on pages 50, 150). http://dx.doi.org/10.1016/j.jcp.2017.01.054.

[76] B.A. Fryxell, P.R. Woodward, P.Colella, and K.-H. Winkler. An implicit-explicit hybrid method for Lagrangian hydrodynamics. *Journal of Computational Physics* 63 (2) (1986), 283–310. (Cited on page 51). http://dx.doi.org/https://doi.org/10.1016/0021-9991(86)90195-6.

[77] P.R. Woodward W. Dai. A Second-Order Iterative Implicit–Explicit Hybrid Scheme for Hyperbolic Systems of Conservation Laws. *Journal of Computational Physics* 128 (1) (1996), 181–196. (Cited on page 51). http://dx.doi.org/10.1006/jcph.1996.0202.

[78] J.P. Collins, P. Colella, and H.M. Glaz. An Implicit-Explicit Eulerian Godunov Scheme for Compressible Flow. *Journal of Computational Physics* 116 (2) (1995), 195–211. (Cited on page 51). http://dx.doi.org/10.1006/jcph.1995.1021.

[79] I. Men'Shov and Y. Nakamura. Hybrid Explicit-Implicit, Unconditionally Stable Scheme for Unsteady Compressible Flows. *AIAA Journal* 42 (3) (2004), 551–559. (Cited on page 51). http://dx.doi.org/10.2514/1.9109.

[80] A. Harten, P. D. Lax, and B. van Leer. On Upstream Differencing and Godunov-Type Schemes for Hyperbolic Conservation Laws. *SIAM Review* 25 (1) (1983), 35–61. (Cited on page 51). http://dx.doi.org/10.1137/1025002.

[81] E. Timofeev and F. Norouzi. Hybrid, explicit-implicit, finite-volume schemes on unstructured grids for unsteady compressible flows. *AIP Conference Proceedings* (2016). (Cited on pages 52, 53, 55, 79, 149). http://dx.doi.org/10.1063/1.4951758.

[82] F. Norouzi. A hybrid, explicit-implicit, second-order TVD method on adaptive unstructured grids for unsteady compressible flows. PhD thesis. McGill, (2015). (Cited on pages 53, 155, 157).

[83] G. Tóth, D.L. De Zeeuw, T.I. Gombosi, and K.G. Powell. A Parallel Explicit/Implicit Time Stepping Scheme on Block-adaptive Grids. *Journal of Computational Physics* 217 (2) (2006), 722–758. (Cited on page 55). http://dx.doi.org/10.1016/j.jcp.2006.01.029.

[84] S. May and M.J. Berger. An Explicit Implicit Scheme for Cut Cells in Embedded Boundary Meshes. *Journal of Scientific Computing* 71 (3) (2016), 919–943. (Cited on pages 55, 141). http://dx.doi.org/10.1007/s10915-016-0326-2.

[85] S. Osher and R. Sanders. Numerical Approximations to Nonlinear Conservation Laws With Locally Varying Time and Space Grids. *Mathematics of Computation* 41 (164) (1983), 321–336. (Cited on page 57). http://dx.doi.org/10.2307/2007679.

[86] C. Dawson. High resolution upwind-mixed finite element methods for advection-diffusion equations with variable time-stepping. *Numerical Methods for Partial Differential Equations* 11 (5), 525–538. (Cited on page 57). http://dx.doi.org/10.1002/num.1690110508.

[87] C. Dawson and R. Kirby. High Resolution Schemes for Conservation Laws with Locally Varying Time Steps. *SIAM Journal on Scientific Computing* 22 (6) (2001), 2256–2281. (Cited on page 57). http://dx.doi.org/10.1137/S1064827500367737.

[88] E.M. Constantinescu and A. Sandu. Multirate Timestepping Methods for Hyperbolic Conservation Laws. *Journal of Scientific Computing* 33 (3) (2007), 239–278. (Cited on page 57). http://dx.doi.org/10.1007/s10915-007-9151-y.

[89] A. Sandu and E.M. Constantinescu. Multirate Explicit Adams Methods for Time Integration of Conservation Laws. *Journal of Scientific Computing* 38 (2) (2009), 229–249. (Cited on page 57). http://dx.doi.org/10.1007/s10915-008-9235-3.

[90] M.J. Berger and J. Oliger. Adaptive mesh refinement for hyperbolic partial differential equations. *Journal of Computational Physics* 53 (3) (1984), 484–512. (Cited on pages 57, 59). http://dx.doi.org/10.1016/0021-9991(84)90073-1.

[91] M.J. Berger and P. Colella. Local adaptive mesh refinement for shock hydrodynamics. *Journal of Computational Physics* 89 (1) (1989), 64–84. (Cited on pages 57, 59). http://dx.doi.org/10.1016/0021-9991(89)90035-1.

[92] J.B. Bell, P. Colella, and H.M. Glaz. A second-order projection method for the incompressible Navier-Stokes equations. Journal of Computational Physics. (1989), 789–794. (Cited on page 58) http://dx.doi.org/10.1016/0021-9991(89)90151-4.

[93] J. Bell. AMR for low Mach number reacting flow. Adaptive Mesh Refinement - Theory and Applications. Springer Berlin Heidelberg (2005), 203–221. (Cited on page 59). http://dx.doi.org/10.1007/3-540-27039-6_14. https://doi.org/10.1007%2F3-540-27039-6_14.

[94] W.L. Kleb, J.T. Batina, and M.H. Williams. Temporal adaptive Euler/Navier-Stokes algorithm involving unstructured dynamic meshes. *AIAA Journal* 30 (8) (1992), 1980–1985. (Cited on page 59). http://dx.doi.org/10.2514/3.11169.

[95] P. Brenner. Numerical Simulations of Three-Dimensional and Unsteady Aerodynamics About Bodies in Relative Motion Applied To A TSTO Separation. 5th International Aerospace Planes and Hypersonics Technologies Conference, International Space Planes and Hypersonic Systems and Technologies Conferences. (5142). AIAA. (1993). (Cited on pages 59, 63, 141) http://dx.doi.org/10.2514/6.1993-5142.

[96] L. Krivodonova. An Efficient Local Time-stepping Scheme for Solution of Nonlinear Conservation Laws. *Journal of Computational Physics* 229 (22) (2010), 8537–8551. (Cited on page 59). http://dx.doi.org/10.1016/j.jcp.2010.07.037.

[97] B. Cockburn, S.-Y. Lin, and C.-W. Shu. TVB Runge-Kutta local projection discontinuous Galerkin finite element method for conservation laws III: One-dimensional systems. *Journal of Computational Physics* 84 (1) (1989), 90–113. (Cited on pages 59, 151). http://dx.doi.org/https://doi.org/10.1016/0021-9991(89)90183-6.

[98] L. Liu, X. Li, and F. Q. Hu. Nonuniform time-step Runge–Kutta discontinuous Galerkin method for Computational Aeroacoustics. *Journal of Computational Physics* 229 (19) (2010), 6874–6897. (Cited on page 59). http://dx.doi.org/https://doi.org/10.1016/j.jcp.2010.05.028.

[99] L. Liu, X. Li, and F.Q. Hu. Nonuniform-time-step explicit Runge–Kutta scheme for high-order finite difference method. *Computers & Fluids* 105 (2014), 166–178. (Cited on page 59). http://dx.doi.org/https://doi.org/10.1016/j.compfluid.2014.09.008.

[100] T. Unfer. An asynchronous framework for the simulation of the plasma/flow interaction. *Journal of Computational Physics* 236 (2013), 229–246. (Cited on page 59). http://dx.doi.org/10.1016/j.jcp.2012.11.018.

[101] A. Toumi, G. Dufour, R. Perrussel, and T. Unfer. Asynchronous numerical scheme for modeling hyperbolic systems. *Comptes Rendus Mathematique* 353 (9) (2015), 843–847. (Cited on page 59). http://dx.doi.org/10.1016/j.crma.2015.06.010.

[102] V.A. Semiletov and S.A. Karabasov. Cabaret Scheme for Computational Aero Acoustics: Extension to Asynchronous Time Stepping and 3D Flow Modelling. *International Journal of Aeroacoustics* 13 (3-4) (2014), 321–336. (Cited on page 59). http://dx.doi.org/10.1260/1475-472X.13.3-4.321.

[103] R. Vichnevetsky. Energy and group velocity in semin discretizations of hyperbolic equations. *Mathematics and Computers in Simulation* 23 (1981), 333–343. (Cited on pages 68, 80, 130). http://dx.doi.org/10.1016/0378-4754(81)90020-3.

[104] L. Muscat, G. Puigt, M. Montagnac, and P. Brenner. A coupled implicit-explicit time integration method for compressible unsteady flows. *submitted to Journal of Computational Physics* (2018). (Cited on page 85).

[105] P. L. Roe. Characteristic-Based Schemes for the Euler Equations. *Annual Review of Fluid Mechanics* 18 (1) (1986), 337–365. (Cited on pages 104, 156). http://dx.doi.org/10.1146/annurev.fl.18.010186.002005.

[106] P.R. Spalart, S. Deck, M.L. Shur, K.D. Squires, M.Kh. Strelets, and A. Travin. A new version of detached-eddy simulation, resistant to ambiguous grid densities. *Theorical and Computational FLuid Dynamics* (20) (2006), 181–195. (Cited on page 141). http://dx.doi.org/10.1007/s00162-006-0015-0.

[107] S. Deck. Recent improvements in the Zonal Detached Eddy Simulation (ZDES) formulation. *Theoretical and Computational Fluid Dynamics* 26 (6) (2012), 523–550. (Cited on page 141). http://dx.doi.org/10.1007/s00162-011-0240-z.

[108] P.R. Spalart and S. Allmaras. A one-equation turbulence model for aerodynamic flows. American Institute of Aeronautics and Astronautics (1992). http://dx.doi.org/10.2514/6.1992-439. (Cited on page 141).

[109] P. Moreau, J. Labbé, F. Dupoirieux, and R. Borghi. Experimental and Numerical Study of a Turbulent Recirculation Zone with Combustion. Turbulent Shear Flows 5. Edited by Franz Durst, Brian E. Launder, John L. Lumley, Frank W. Schmidt, and James H. Whitelaw. Berlin, Heidelberg. Springer Berlin Heidelberg (1987), 337–346. (Cited on page 142) http://dx.doi.org/10.1007/978-3-642-71435-1_28.

[110] D.M. Driver, H.L. Seegmiller, and J.G. Marvin. Time-dependent behavior of a reattaching shear layer. *AIAA Journal* 25 (7) (1987), 914–919. (Cited on page 142). http://dx.doi.org/10.2514/3.9722.

[111] F.M. Moreira, E. Jourdan, C. Breviglieri, A.R. Aguiar, and J.L.F. Azevedo. Implicit Spectral Difference Method Solutions of Compressible Flows Considering High-Order Meshes. *American Institute of Aeronautics and Astronautics* (2016). (Cited on page 150). http://dx.doi.org/10.2514/6.2016-3352.

[112] D.A. Knoll and D.E. Keyes. Jacobian-free Newton-Krylov methods: a survey of approaches and applications. *Journal of Computational Physics* 193 (2004), 357–397. (Cited on page 151). http://dx.doi.org/10.1016/j.jcp.2003.08.010.

[113] R. Turpault. An Implicit Preconditioned JFNK Method for Fully Coupled Radiating Flows. Application to Superorbital Re-Entry Simulations. Computational Fluid Dynamics 2004. Edited by Clinton Groth and David W. Zingg. Springer Berlin Heidelberg (2006), 263–269. (Cited on page 151) http://dx.doi.org/10.1007/3-540-31801-1_35.

[114] S. Clain, S. Diot, and R. Loubère. A high-order finite volume method for systems of conservation laws—Multi-dimensional Optimal Order Detection (MOOD). *Journal of Computational Physics* 230 (10) (2011), 4028–4050. (Cited on page 151). http://dx.doi.org/10.1016/j.jcp.2011.02.026.

[115] T.-H. Nguyen Bui R. Turpault. A High Order MOOD Method For Compressible Navier-Stokes Equations : Application To Hypersonic Viscous Flows. *Progress in Computational Fluid Dynamic* (2018). (Cited on page 151).

[116] Y. Liu, M. Vinokur, and Z.J. Wang. Spectral difference method for unstructured grids I: Basic formulation. *Journal of Computational Physics* 216 (2) (2006), 780–801. (Cited on page 151). http://dx.doi.org/10.1016/j.jcp.2006.01.024.

[117] Z. J. Wang, Y. Liu, G. May, and A. Jameson. Spectral Difference Method for Unstructured Grids II: Extension to the Euler Equations. *Journal of Scientific Computing* 32 (1) (2007), 45–71. (Cited on page 151). http://dx.doi.org/10.1007/s10915-006-9113-9.

[118] B. Cockburn and C.-W. Shu. TVB Runge-Kutta Local Projection Discontinuous Galerkin Finite Element Method for Conservation Laws II: General Framework. *Mathematics of Computation* 52 (186) (1989), 411–435. (Cited on page 151). http://dx.doi.org/10.2307/2008474.

[119] B. Cockburn, S. Hou, and C.-W. Shu. The Runge-Kutta Local Projection Discontinuous Galerkin Finite Element Method for Conservation Laws. IV: The Multidimensional Case. *Mathematics of Computation* 54 (190) (1990), 545–581. (Cited on page 151). http://dx.doi.org/10.2307/2008501.

[120] H.T. Huynh. A Flux Reconstruction Approach to High-Order Schemes Including Discontinuous-Galerkin Methods. 18th AIAA Computational Fluid Dynamics Conference, 25 - 28 June, Miami, FL, AIAA Paper 2007-4079. (2007). (Cited on page 151).

[121] Z.J. Wang and H. Gao. A unifying lifting collocation penalty formulation including the discontinuous Galerkin, spectral volume / difference methods for conservation laws on mixed grids. *Journal of Computational Physics* 228 (21) (2009), 8161–8186. (Cited on page 151).

[122] P.E. Vincent, P. Castonguay, and A. Jameson. A New Class of High-Order Energy Stable Flux Reconstruction Schemes. *Journal of Scientific Computing* 47 (1) (2011), 50–72. (Cited on page 151).

[123] L. Mieussens G. Jeanmasson I. Mary. Explicit local time stepping scheme for the unsteady simulation of turbulent flows. (2018) (cited on page 152).



Abstract: This work deals with the design of a hybrid time integrator that couples spatially explicit and implicit time integrators. In order to cope with the industrial solver of Ariane Group called **FLUSEPA**©, the explicit scheme of Heun and the implicit scheme of Crank-Nicolson are hybridized using the transition parameter ω: the whole technique is called AION time integration. The latter is studied into details with special focus on spectral behaviour and on its ability to keep the accuracy. It is shown that the hybrid technique has interesting dissipation and dispersion properties while maintaining precision and avoiding spurious waves. Moreover, this hybrid approach is validated on several academic test cases for both convective and diffusive fluxes. And as expected the method is more interesting in term of computational time than standard time integrators. For the extension of this hybrid approach to the temporal adaptive method implemented in **FLUSEPA**©, it was necessary to improve some treatments in order to maintain conservation and acceptable spectral properties. Finally the hybrid time integration was also applied to a RANS/LES turbulent test case with interesting computational time while capturing the flow physics.

Keywords: Finite Volume, Hybrid time integration, Space-time spectral analysis, Spurious Waves, Temporal adaptive method, Compressible unsteady flows.

Résumé : Dans ce travail, on s'intéresse au développement d'une méthode hybride qui couple spatialement les schémas d'intégration temporelle explicite et implicite. Afin de répondre aux contraintes du solveur industriel **FLUSEPA**©, les schémas explicite Heun et implicite Crank-Nicolson ont été hybridés via un paramètre de transition ω : l'approche mise en place est appelée schéma AION. Cette dernière est étudiée en détails avec une attention particulière sur son comportement spectral et sa capacité à maintenir l'ordre de précision. On montre que le traitement hybride a d'intéressants comportements dissipatif et dispersif tout en empêchant la réflexion d'ondes parasites et en maintenant la précision attendue. De plus, l'approche hybride est validée sur plusieurs cas académiques à la fois pour les flux convectifs et pour les flux diffusifs. Et comme espéré, la méthode est plus intéressante en terme de temps de calcul que les méthodes standards d'intégration temporelle. Pour l'extension de cette approche à la méthode temporelle adaptative présente dans **FLUSEPA**©, il a été nécessaire d'améliorer le traitement qui permet à la méthode d'être conservative tout en obtenant des propriétés spectrales acceptables. Finalement l'approche hybride a été aussi étendue pour la modélisation RANS/LES de la turbulence avec des temps de calcul intéressants tout en capturant la physique de l'écoulement.

Mots-clefs : Volumes Finis, Intégration temporelle hybride, Analyse Spectrale spatio-temporelle, Ondes Parasites, Méthode temporelle adaptative, Écoulement compressible et instationnaire.